University of Bath

PHD

Self-consistent modelling of buried heterostructure lasers

Gurney, Phillip C. R.

Award date:
1992

Awarding institution:
University of Bath

Link to publication

Alternative formats
If you require this document in an alternative format, please contact:
openaccess@bath.ac.uk

Copyright of this thesis rests with the author. Access is subject to the above licence, if given. If no licence is specified above, original content in this thesis is licensed under the terms of the Creative Commons Attribution-NonCommercial 4.0 International (CC BY-NC-ND 4.0) Licence (https://creativecommons.org/licenses/by-nc-nd/4.0/). Any third-party copyright material present remains the property of its respective owner(s) and is licensed under its existing terms.

Take down policy
If you consider content within Bath's Research Portal to be in breach of UK law, please contact: openaccess@bath.ac.uk with the details. Your claim will be investigated and, where appropriate, the item will be removed from public view as soon as possible.

Download date: 05. May. 2023

SELF-CONSISTENT MODELLING OF BURIED HETEROSTRUCTURE LASERS

submitted by Phillip C.R. Gurney
for the degree of PhD
of the University of Bath
1992

COPYRIGHT

'Attention is drawn to the fact that the copyright of this thesis rests with its author. This copy of the thesis has been supplied on condition that anyone who consults it is understood to recognise that its copyright rests with its author and that no quotation from the thesis and no information derived from it may be published without the prior written consent of the author'.

'This thesis may be made available for consultation within the University Library and may be photocopied or lent to other libraries for the purposes of consultation'.

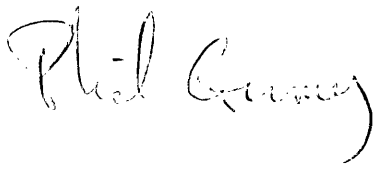

UMI Number: U601612

All rights reserved

INFORMATION TO ALL USERS
The quality of this reproduction is dependent upon the quality of the copy submitted.

In the unlikely event that the author did not send a complete manuscript
and there are missing pages, these will be noted. Also, if material had to be removed,
a note will indicate the deletion.

UMI U601612
Published by ProQuest LLC 2013. Copyright in the Dissertation held by the Author.
Microform Edition © ProQuest LLC.
All rights reserved. This work is protected against
unauthorized copying under Title 17, United States Code.

ProQuest LLC
789 East Eisenhower Parkway
P.O. Box 1346
Ann Arbor, MI 48106-1346

UNIVERSITY OF BATH
LIBRARY
19 JUL 1993
PHD
572346

SUMMARY

This thesis is concerned with the self-consistent modelling of the static electrical properties of buried heterostructure lasers. The model developed has been applied to examine the current leakage and optical mode structures of two particular laser structures, the buried ridge structure (BRS) and constricted mesa (CM) lasers, which are used in high frequency applications.

In order to model the electrical and optical properties in a self-consistent fashion, separate models of the current spreading and optical waveguiding are developed. These models are then linked by the carrier density in the active layer, which sets the active layer voltage and refractive index distributions, and the active layer carrier density is treated in a self-consistent fashion between the two models.

The electrical model is developed in chapter 3, and used to study the current leakage around the active region in above threshold buried heterostructure lasers. Results are presented showing the effect on the leakage current of changes in laser geometry and upper cladding layer doping density. The optical model solves for the waveguiding in the laser structure in two dimensions. The Weighted Index method is used to obtain the modes of the waveguide, and the method is extended to handle the case of complex permittivity. Using this model, the effects of changing the laser geometry and active layer carrier density are studied.

The self-consistent model is used to examine the effects of the cladding layer doping density, and changes in the laser geometry, on the lasing characteristics of BRS and CM lasers. The effects of two lasing modes are included in a self-consistent fashion. The model is used to predict the light-current and current-voltage characteristics, and the proportion of current flowing around the active layer is calculated. It is also possible to predict the photon densities of each lasing mode, the optical field profile and the current and carrier density distributions.

ACKNOWLEDGEMENTS

I would like to thank all those who have helped me in the production of this thesis. In particular, I would like to thank my supervisor, Dr. R.F.Ormondroyd, whose help and encouragement has saved me from despair and pointed me in the right direction when everything appeared to be falling down around me. I would like to thank my parents, without whom all this would not have been possible, and my wife Debbie, without whom none of it would have been worthwhile.

I would also like to thank all of those whose support I have enjoyed during my time at Bath. In particular, Hazim Abdullah, who has been a good friend, and whose encouragement and help has been invaluable. I would like to thank Kathy Kwan who came to my aid in my hour of need in donating some of the paper (on a Saturday evening) on which this thesis is printed, and Rob Noyes. I am also indebted to Marconi Defence systems at Stanmore for their help and financial support during this work. Finally, I would like to dedicate this thesis to my hamster, Hamlet.

TABLE OF CONTENTS

LIST OF SYMBOLS

ENGLISH SYMBOLS

a	gain parameter, normalised waveguide parameter
A	active layer width
A_{12},A_{21}	spontaneous transition rate
b	gain parameter, normalised waveguide parameter
$\overline{B}$	magnetic flux vector
B_{12},B_{21}	Einstein coefficients
B_0,B_1	spontaneous radiative coefficients
c	speed of light
C	Auger coefficient, contact width
d	upper cladding region depth
$\overline{D}$	electric displacement vector
D_e	effective ambipolar diffusion coefficient
$D_{n,p}$	electron, hole diffusivity
$\overline{E}$	electric field vector
Ej	energy of state j
E_c,E_v	electron and hole quasi-Fermi levels
F_c,F_v	conduction and valence band edge energy
$F_{1/2}$	Fermi integral
g	optical gain
g_{th}	threshold optical gain
G	total optical gain
h	Planck's constant
h_x,h_y	mesh spacing in horizontal and vertical directions
$\overline{H}$	magnetic field vector
I	current
j	square root of -1
$J(x,y)$	current density
k	Boltzmann's constant, wavenumber
K	extinction coefficient
L_n	device/cavity length
$L_{n,p}$	effective diffusion length
$n(x),N$	electron concentration
n_i	intrinsic carrier concentration
n_j	refractive index of medium j
N_c,N_v	conduction and valence band density of states

$p(x)$	hole concentration
p_a, p_o	p-doping of active, cladding layer
P	time averaged power flow
q	electronic charge
R	ratio of real to imaginary part of refractive index
R_j	reflectance of mirror j
R_{spon}	spontaneous recombination coefficient
R_{stim}	stimulated recombination coefficient
R_{NR}	non-radiative recombination coefficient
s, S	photon density
S_z	Poynting vector
t	time, active region depth
T	temperature
$V(x,y)$	voltage distribution

GREEK SYMBOLS

α	optical absorption coefficient
α_T	effective absorption coefficient
β	propagation constant
δ	waveguide parameter
η	ideality factor
η_a	active layer refractive layer
ε	relative permittivity/dielectric constant
γ	waveguide parameter
Γ	confinement factor
κ	waveguide parameter
λ	wavelength
μ	magnetic permittivity
ν	frequency
ω	frequency
Ω	over-relaxation parameter
ω_R	relaxation oscillation frequency
ρ	charge density
ρ_ν	energy density at frequency ν
σ	conductivity
τ_{21}	transition lifetime from state 2 to sate 1
$\mu_{n,p}$	hole mobility

CHAPTER 1: INTRODUCTION

1.1 Semiconductor lasers

Semiconductor lasers, due to their small physical dimensions and ease of production, have found many applications in areas as diverse as optical storage devices, compact disk players and laser printers. One application for which the semiconductor laser is particularly suited is in high bandwidth communications systems, due to their high electro/optical conversion efficiency, the high directly modulated bandwidths attainable, and an active layer size compatible with that of optical fibres.

Lasers which are directly modulated, i.e. the current injected into the laser itself is modulated, must have a low capacitance and resistance to reduce the parasitic frequency roll-off, and a high power output, since the intrinsic bandwidth is related to the square root of the cavity power [1]. The buried-heterostructure geometry is most often used because of the high optical confinement which leads to high photon densities in the active region. These devices are generally fabricated from the InP/InGaAsP material system, due to the wavelength and high power requirements.

Two laser structures which have been used in high bandwidth applications are the buried ridge structure (BRS) and constricted mesa (CM) lasers shown in figure 1.1. The constricted mesa laser in particular has been used to obtain direct modulation bandwidths in excess of 24GHz at room temperature [2], and 26.5 GHz when cooled [3]. The buried ridge structure, whilst not capable of quite such high bandwidth operation, has the advantage of a planar construction which makes it ideal for integration with other optoelectronic components. This thesis is concerned with the modelling of the static properties of these two laser structures. The following sections describe the various topics that are covered by the thesis.

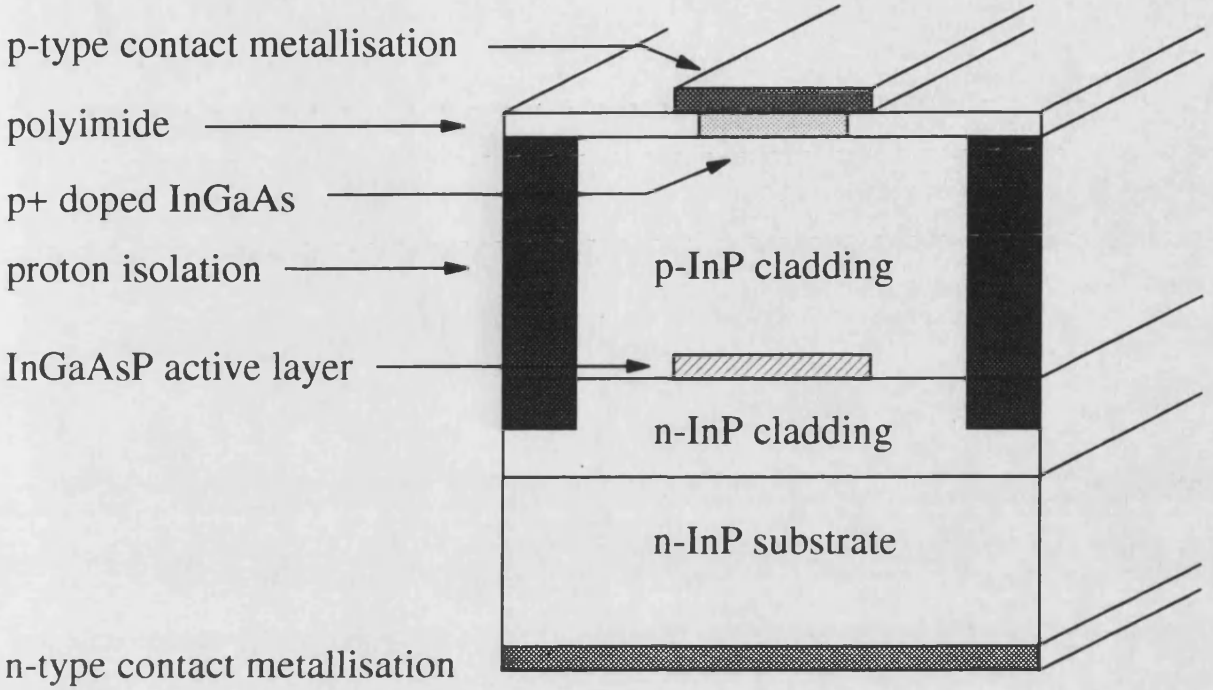

Figure 1.1(a) The buried ridge structure laser

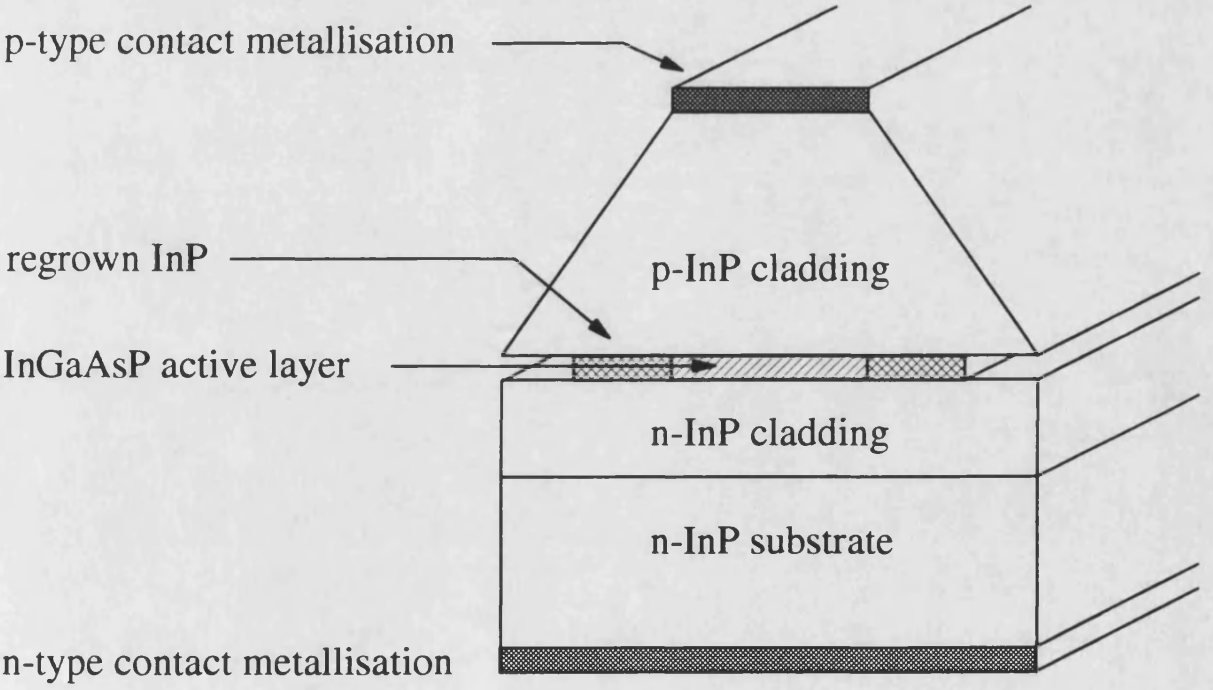

Figure 1.1(b) The constricted mesa laser

1.2 The buried ridge structure laser

The buried ridge structure laser [4-6] is shown in figure 1.1(a). The device uses the buried heterostructure geometry, and the InGaAsP active layer is completely buried by the upper p-type and lower n-type InP cladding layers. A stripe contact is used to the upper p-type cladding region and a broad area contact made to the substrate. Such lasers have been fabricated by many groups, mainly due to the simple fabrication process, which is compatible with all epitaxy techniques presently used.

Unlike many other buried heterostructure lasers, the BRS laser does not incorporate reverse biased junctions for current confinement. Instead, current confinement is by InP homojunction regions on either side of the active layer, and the design relies on the difference in turn on voltage between the active layer heterojunction and the homojunction regions. Further current confinement is achieved either by limiting the width of the device, either by proton bombarding or Fe doping the InP material on either side of the active region.

1.3 The constricted mesa laser

The constricted mesa structure [7-11] shown in figure 1.1(b) is currently credited with the highest modulation bandwidth for bulk lasers, and has been designed specifically for high bandwidth operation. The CM and BRS lasers are similar in construction, however with the CM laser the physical dimensions of the device have been minimized to reduce parasitics. The main differences between the CM and BRS lasers are the sloping mesa sidewalls, and the undercut region on either side of the active layer. The sloping sidewalls are formed by etching through the upper cladding layer using a wet chemical etchant. The active layer is then etched away to the required width using a second wet etch, and InP material regrown around the active layer by either mass transport [7] or vapour phase epitaxy [8-10], leaving an undercut region.

The narrow regrown regions that can be achieved by this process limit the current leakage path around the active layer (current can by-pass the active region through the forward biased p-n homojunction regions on either side). It might be thought that lasers fabricated without the regrown InP regions would have the advantage of eliminating this leakage path altogether. Devices with this structure (called mushroom stripe lasers) have been manufactured [12-15], however there appears to be a degradation mechanism which causes lasers with no regrown region to fail after only a short operational period [16,17], and so they are no longer produced.

1.4 Design considerations

Whilst the design of the constricted mesa and buried ridge structure lasers is in many ways ideal for high speed operation, unless the design is optimized these lasers can suffer from two effects which will limit their ultimate performance. These are current leakage around the active layer, and lasing in several lateral modes. The implications of these phenomena are discussed in the following sections

1.4.1 Leakage current

Leakage current in buried heterostructure lasers in which transverse current confinement is achieved by forward biased p-n homojunctions can be a serious problem [6,18,19]. With reference to figure 1.1, it can be seen that on either side of the active layer there is an InP p-n homojunction region. It is through these two homojunction regions that the leakage current flows, by-passing the active layer, and therefore not contributing to light production. The current does, however, add to the ohmic heating of the device, and increases in proportion to the drive current, eventually dominating the injected current and thus limiting the output light power of the device.

The reasons for this leakage current can be understood by considering a simple, but somewhat analogous situation, where the active region and homojunction regions are

replaced by discrete diodes, with the homojunction diode having a higher turn on voltage. As the voltage applied to the top contact is increased, both diodes are forward biased, but the heterojunction diode starts to conduct first. As the applied voltage is further increased, the homojunction diode becomes turned on and starts to conduct. Due to the lasing action at the heterojunction, the voltage here becomes pinned near to its value at the laser threshold. A further increase in the applied voltage therefore leads to a greater proportion of the injected current flowing through the homojunction diode. Although this is a simplification of the actual situation, it provides a basis for an understanding of the problem.

The problem of current leakage is common to many devices, and a fuller understanding of the problem is becoming increasingly important as devices are designed for higher power outputs. Such devices are constantly finding applications, one area of current interest being in optical pumps for fibre amplifiers. The self consistent model presented in this thesis examines the problem of current leakage in the class of lasers which have a buried heterostructure geometry, and use forward biased heterojunctions for current confinement. Such lasers are attractive to build because of their simplicity of fabrication against other current confinement schemes.

1.4.2 Multi-lateral mode operation

The problem of multi-lateral mode operation is well known in the context of buried heterostructure lasers [5,15], however, it is more complex to explain than that of current leakage. The design of the active region of most buried heterostructure lasers is often such that the waveguide formed by the active and cladding regions will permit several lateral modes to propagate. It is possible to fabricate active regions with dimensions such that only one mode may propagate, however, this requires a very narrow active region, with consequent problems of beam divergence and coupling the light output to fibres. It is therefore often desirable to have a relatively wide active layer, but to still be able to confine the laser to single mode operation.

Single lateral mode lasing is possible because although a mode may be allowed to propagate by the waveguiding structure of the laser, it may not have sufficient gain to enable it to lase. For a mode to lase it must have enough gain to overcome the losses in the cavity. The gain of an optical mode in a waveguide is related to the imaginary part of the propagation constant of the mode. This in turn is determined by the complex refractive indices of the various sections of the guide.

The carrier density in the active layer alters the real and imaginary parts of the refractive index of the active material, and thus the waveguiding properties of the structure. The carrier density distribution is related to the current injected into the active layer. If the current is well confined to the active region then considerable current crowding can occur at the edges of the region. Such current crowding alters the carrier distribution and thus the waveguiding properties, altering the gains experienced by the propagating modes. In many cases this will lead to sufficient gain experienced by the second and subsequent modes to enable them to lase.

Such multi-lateral mode outputs are undesirable because of the effect which they have on the device output. Often, the commencement of the second lasing mode is associated with a kink in the output light-current curve, which will cause distortion of the modulated output. The coupling of light out of the device is affected by beam width, which is altered if a second mode is lasing, and the high speed performance may be affected by the turn on transient of the higher order modes. The self consistent model has been used to examine the point at which the transition between single and multiple mode operation occurs, with a view to limiting the laser output to a single mode.

1.5 Semiconductor laser modelling

There are many reasons why one may wish to model a laser diode, and many purposes to which such a model may be put. For example, when designing a fibre optic link one may wish to model the laser component in order to simulate the output power levels and

frequency, and its sensitivity to back reflections from the link. Or one may wish to model the electrical characteristics of the laser to ensure that the power consumed falls within the power budget of the system under consideration. Because of the complexity of the laser diode, it is not possible to produce one model which will accurately simulate all characteristics over all possible situations. The purpose of modelling must be to provide a sufficiently accurate model of the characteristics which one is interested in.

The model presented in this thesis is of the current spreading and optical mode characteristics of bulk Fabry-Perot semiconductor lasers. It is intended to help provide a better understanding of the device operation and help in the design of the physical characteristics of the laser, such as contact width and active layer depth, which it is difficult, and expensive, to vary experimentally. This requires a detailed model of the physical characteristics of the laser, together with a self-consistent model of the electrical and optical properties.

Device modelling has been carried out since before the first semiconductor lasers were produced, indeed the practical demonstration of laser action in semiconductors required a detailed theoretical background. Since that time much effort has been expended on the modelling of semiconductor laser devices, and a review paper by Buus [20] in 1985 gives the development of modelling up to that time. However, relatively few authors have attempted to model more than one laser characteristic (e.g. current spreading, optical properties, temperature sensitivity) simultaneously.

In common with this work, many of the more recent self-consistent laser models [21-26] have examined both electrical and optical properties in two dimensions, rather than the one dimensional or quasi-two dimensional models summarised in Buus's paper. Several of more recent models have been applied to devices with strong index guiding structures, e.g. [24,25], however, because of the assumptions made about the active layer they cannot be applied to buried heterostructure geometries. Also, although most claim to be able to solve for several optical modes simultaneously, very few have done so in a fully self-consistent fashion. It is believed, therefore, that this is the first published model to

handle the buried heterostructure geometry in a fully self-consistent fashion, and also the only model to handle the superposition of optical modes self-consistently for such devices.

1.6 Layout of thesis

This thesis is concerned with the development of a self-consistent model of the optical and electrical properties of buried heterostructure lasers such as the buried ridge and constricted mesa lasers. It covers the various aspects required to model both the static electrical and optical characteristics of semiconductor lasers, and shows how the two are linked. This leads on to the generation of a fully self-consistent model for buried heterostructure lasers.

Chapter 2 is an introduction to the concepts required to understand semiconductor lasers, and covers the basics of laser theory. Laser action in a two level system is examined, and the condition for laser action derived. It is seen that this theory can be extended to cover semiconductor lasers, and laser structures are examined. Finally, the requirements of directly modulated lasers are investigated, and it is shown that one of the main requirements is for high power operation.

In chapter 3 the electrical model is explained. The equations which are used to construct the model of current flow are developed, and the solution scheme discussed. The equations are solved using a numerical scheme, and the numerical equations are derived. Results are presented assuming a fixed active layer carrier distribution to model the current leakage effects above threshold. The model is used to examine the effects on the leakage current of changing the device dimensions and active layer carrier density.

Chapter 4 consists of a review of the theory used in the optical section of the self consistent model. From Maxwell's equations the equations describing light propagation in one dimensional waveguides are developed. These are used to show how the propagation

constant is linked to the loss or gain of the guide when the guide is formed of a conducting medium. Power flow of the optical mode is examined, and the confinement factor is defined. The differences between TE and TM modes are considered.

The optical model is developed in chapter 5. This considers two dimensional waveguides, and the methods of solution available. The weighted index method is presented, and the reasons for its adoption for the optical model explained. The extension of the weighted index method to waveguides of complex permittivity is developed. Results are given for the use of the weighted index method in waveguides of real and complex permittivity, examining the effects of device dimensions and active layer carrier density.

In chapter 6 the method of combining the two separate sections of the model into a self consistent scheme is presented. The solution of the carrier diffusion equation and its crucial effect in linking the electrical and optical models is explained. The full optical model is described, and the scheme for adjusting the gain of the modes via the photon densities is given. The self consistent model is used to examine the twin problems of current leakage and multi-lateral mode operation of lasers. Results are presented showing the change in output of the lasers in a variety of situations. In particular the effects of dimensional changes and of the p-type doping of the upper cladding layer are examined.

The final chapter, chapter 7, discusses the implications of the results of the model to device design, and examines possible extensions to the model. The attempts made so far to fabricate constricted mesa lasers are detailed, and finally some suggestions for further work are given.

References

[1] A.Yariv, "Quantum electronics", 2nd edition, John Wiley and Sons, section 11.6

[2] E.Meland, R.Holstrom, J.Schlafer, R.B.Lauer and W.Powazinik, "Extremely high-frequency (24GHz) InGaAsP diode lasers with excellent modulation efficiency", Electron.Lett., vol. 26, no 21, pp.182-184, 1990

[3] J.E.Bowers, "Millimeter-wave response of InGaAsP lasers", Elect.Lett., vol 21, no. 25/26, pp.1195-1197, 1985

[4] M.Krakowski, R.R.Blondeau, K.Kazmierski and M.Razeghi "High yield manufacture of very low threshold, high reliablility, 1.30μm buried heterostructure laser diodes grown by metal organic chemical vapour deposition," J.Lightwave Technol., vol. 4, pp.1470-1474, 1986

[5] J.P.van der Ziel, R.A.Logan and T.Tabun-Ek, "InGaAsP ($\lambda = 1.3\mu m$) strip buried heterostructure lasers grown by MOCVD," IEEE J.Quantum Electron., vol 27, no. 11, pp.2378-2385, 1991

[6] M.C.Amann and W.Thulke, "Current confinement and leakage currents in planar buried-ridge structure laser diodes on n-substrate," IEEE J.Quantum Electron., vol. QE-25, no. 7, pp.1595-1602, 1989

[7] Z.L.Liau, J.N.Walpole and D.Z.Tsang, "Fabrication, characterisation, and analysis of mass-transported GaInAsP/InP buried heterostructure lasers," IEEE J.Quantum Electron., vol. QE-20, no. 8, pp.855-865, 1984

[8] T.L.Koch and L.A.Coldren, "Low-threshold high speed 1.55μm vapour phase transported buried heterostructure lasers (VPTBH)," Elect.Lett., vol. 20, pp.856-857, 1984

[9] J.E.Bowers, B.R.Hemmingway, A.H.Gnauk and D.P.Wilt, "High speed InGaAsP constricted mesa lasers," IEEE J.Quantum Electron., vol. QE-22, no. 6, pp.833-843, 1986

[10] R.Olshansky and W.Powazinik, "InGaAsP buried heterostructure laser with 22GHz bandwidth and high modulation effiency," Elect.Lett., vol. 23, no. 16, pp.839-841, 1987

[11] Y.Hirayama and H.Furuyama, "High speed 1.5μm self-aligned constricted mesa lasers grown entirely by MOCVD," Elect.Lett., vol. 24, no. 8, pp.452-454, 1988

[12] R.Blondeau and J.Ricciardi, "Low threshold CW operation GaInAsP/InP mushroom stripe (MSL) emitting at 1.27μm," J.J.Appl.Phys., vol. 21, no. 11, pp.1655, 1982

[13] U.Koren and T.R.Chen, "InGaAsP/InP undercut laser with planar polyimide passivation," Appl.Phys.Lett., vol. 42, no. 5, pp.403-405, 1983

[14] H.Burkhard and E.Kuphal, "InGaAsP/InP mushroom stripe lasers with low cw threshold and high output power," J.J.Appl.Phys., vol. 22, no. 11, pp.L721-723, 1983

[15] H.Burkhard and E.Kuphal, "Three-and four-layer LPE InGaAsP mushroom stripe lasers for 1.30,1.54 and 1.66 μm," IEE J.Quantum Electron., vol. QE-21, vol. 6, pp.650-657, 1986

[16] H.Jung and P.Marschall, "Localisation of degradation in InP/InGaAsP mushroom stripe lasers," Appl.Phys.Lett., vol. 51, no. 2, pp.72-73, 1987

[17] H.Jung, E.G.Burkhardt and W.Pfister, "Reduction of degradation in vapour phase transported InP/InGaAsP stripe lasers," Appl.Phys.Lett., vol. 53, no. 14, pp.1230-1232, 1988

[18] Z.L.Liau and J.N.Walpole "Characterisation of mass transported p-substrate GaInAsP/InP buried heterostructure lasers with analytical solutions for electrical and thermal resistances," IEEE J.Quantum Electron., vol. QE-24, no. 1, pp.36-42, 1988

[19] Z.L.Liau and J.N.Walpole, "Prevention of current leakage in mass transported GaInAsP/InP buried heterostructure lasers with narrow transported regions," IEEE J.Quantum Electron., vol. QE-23, no. 3, pp.313-319, 1987

[20] J.Buus, "Principles of semiconductor laser modelling", IEE Proc.J. Feb 1985, vol 132, no 1, pp.42-51

[21] K.B.Kahen, "Two-dimensional simulation of laser diodes in the steady state," IEEE J.Quantum.Electron., vol 24, no. 4, pp.641-651, 1988

[22] T.Kumar, R.F.Ormondroyd and T.E.Rozzi, "A self-consistent model of the lateral behaviour of a twin-stripe injection laser," IEEE J.Quantum Electron., vol. QE-22, no. 10, pp.1975-1985, 1986

[23] M.Ueno, S.Asada and S.Kumashiro, "Two-dimensional numerical analysis of lasing characteristics for self-aligned structure semiconductor lasers", IEEE. J.Quantum Electron., vol. 26, no. 6, pp.972-981, 1990

[24] P.Meissner, E.Patzak and B.Yevic, "A self-consistent model of stripe geometry lasers based on the beam propagation method", IEEE J.Quantum.Electron., vol QE-20, pp.899-905, 1984

[25] A.Shimizu and T.Hara, "A self-consistent analysis of DH lasers over the gain-guiding and index guiding regions", IEEE J.Quantum.Electron., vol QE-23, pp.293-302, 1987

[26] T.Ohtoshi and K.Yamaguchi "A two dimensional device simulator of semiconductor lasers", Solid-State Electron., vol 22, pp.627-638, 1987

CHAPTER 2: LASER BASICS

2.1 Introduction

The laser is a source of coherent radiation at optical wavelengths, the word "laser" being an acronym for "light amplification by stimulated emission of radiation". This indicates that the light generated comes from stimulated emission, although to fabricate a laser rather than an optical amplifier some form of resonant cavity is also required. The first semiconductor lasers were produced in 1962, and in the ensuing three decades there has been a great deal of research carried out in this field.

The theory of semiconductor lasers has been covered in detail by many authors [e.g. 1-6]. This chapter will concentrate on the most important aspects, to give an understanding of the semiconductor laser, and as an introduction to the rest of the thesis. The chapter begins by examining the basic concepts of laser action, using the simple two level system as an example. The semiconductor laser is then examined, and it is shown that although the situation in semiconductors is more complex than with the simple two level system, the concepts developed for the two level system can be kept, provided they are appropriately modified.

2.2 Laser action in a two level system

Some important relationships concerning laser action can be obtained from consideration of the energy system shown schematically in figure 2.1, with has just two electronic states E_1 and E_2. Although the energy diagrams for all laser systems are necessarily more complex than this, it is useful to illustrate the basic concepts using this system, and then to extend the theory as necessary to cover the practical situation.

2.2.1 Emission and absorption

The electrons in an atom may change state by exchange of energy. These transitions may be radiative, in which case a photon is emitted, or non-radiative, where the energy is converted into lattice vibrations or kinetic energy of free carriers. In this section, only direct radiative recombination in the two level system of figure 2.1 is considered. When an electron undergoes transitions between the energy states it will either emit or absorb a photon whose frequency ν is given by $\nu = (E_2 - E_1)/h$, where h is Planck's constant.

The electron may change state in three distinct ways, as illustrated in figure 2.2. It may fall from the upper level to the lower level, emitting a photon in a process called spontaneous emission. Alternatively, by absorbing a photon of energy E_2-E_1 from an incident optical field, the electron will be excited from the lower energy level 1 to the upper level 2. In the presence of an incident optical field, it is also possible for an electron to be stimulated to make a transition from the upper to lower states by a photon of energy E_2-E_1, in turn emitting a photon of this energy. This is called stimulated emission, and the radiation produced by this process is coherent with the stimulating optical field, i.e. it has the same frequency, polarisation, phase and travels in the same direction.

The stimulated emission process adds coherently to the incident wave, and therefore the amplitude of an electromagnetic wave of the correct frequency will grow as it passes through a collection of excited atoms. It is this process that provides the amplification in laser systems. However, in most circumstances the probability of the spontaneous emission process is several orders of magnitude greater than the probability of the stimulated emission process, and thus net stimulated emission is not observed. In order to obtain laser action the circumstances must be altered so that the probability of a stimulated transition is greater than that of the spontaneous transition.

The number of electrons per unit volume, N_1 and N_2, which at any given instant are at the energy levels E_1 and E_2 respectively, is given by the Boltzmann equation

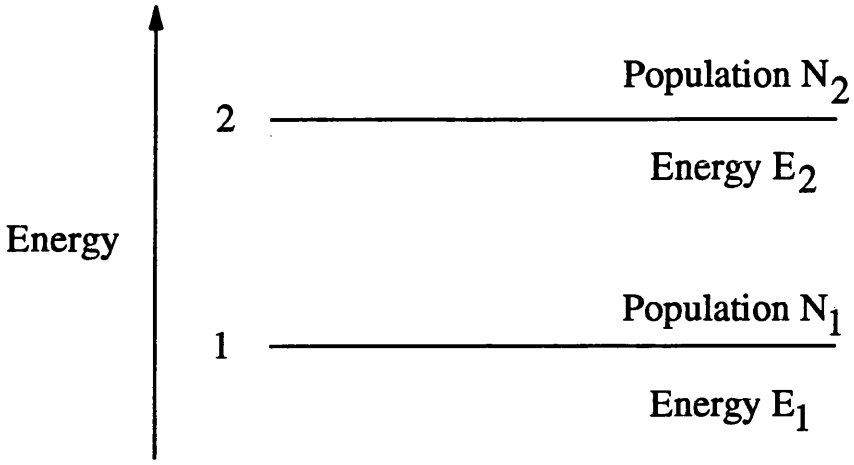

Figure 2.1 Schematic diagram of the two level energy system

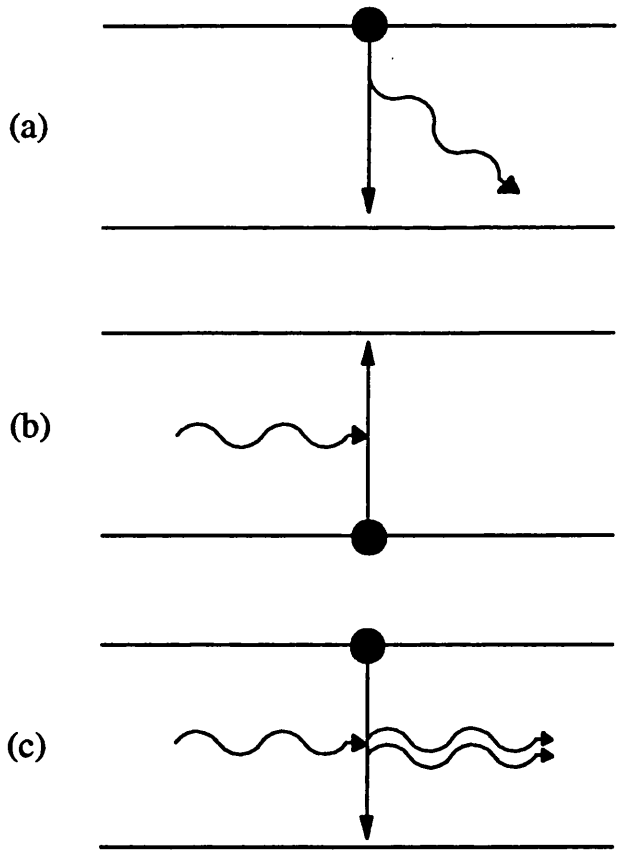

Figure 2.2 Schematic diagrams of the three emission processes.
(a) Spontaneous emission; (b) stimulated apsorption; (c) stimulated emission

$$\frac{N_1}{N_2} = \exp\left[\frac{E_2 - E_1}{kT}\right] \qquad (2.2.1.1)$$

where k is the Boltzmann constant and T is the temperature.

The average time an electron exists in the upper, or excited state, before making a transition to the lower state is called the lifetime, τ_{21} of the excited state, where the subscript '21' indicates a transition from state 2 to state 1. The probability that an electron will undergo a spontaneous transition within a given time period is given by $A_{21} = 1/\tau_{21}$. If there are N_2 electrons per unit volume at energy E_2, then the spontaneous emission rate will be given by N_2A_{21}.

The stimulated emission and absorption processes require the presence of an optical field of the correct wavelength, and so the rates at which these stimulated processes occur will be related to ρ_ν, the photon energy density at frequency ν. The rate of stimulated emission may thus be calculated as $N_2\rho_\nu B_{21}$, where B_{21} is a constant. If there are N_1 electrons in the lower state, then the stimulated recombination rate may be found in a similar fashion as $N_1\rho_\nu B_{12}$, where again B_{12} is a constant.

For a system in thermal equilibrium, the upward and downward transition rates must be equal, such that

$$N_1\rho_\nu B_{12} = N_2\rho_\nu B_{21} + N_2A_{21} \qquad (2.2.1.2)$$

which may be re-arranged, using (2.2.1.1) to give

$$\rho_\nu = \frac{A_{21}/B_{21}}{\frac{B_{12}}{B_{21}}\frac{N_1}{N_2} - 1} = \frac{A_{21}/B_{21}}{\frac{B_{12}}{B_{21}}\exp\left(\frac{E_2 - E_1}{kT}\right) - 1} \qquad (2.2.1.3)$$

The energy system under consideration is in thermal equilibrium, and will therefore give rise to radiation identical to that of blackbody radiation, for which the radiation density is known to be given by

$$\rho_\nu = \frac{8\pi h\nu^3}{c^3}\left(\frac{1}{\exp(h\nu/kT)-1}\right) \qquad (2.2.1.4)$$

where c is the speed of light. Comparing terms between equation (2.2.1.3) and (2.2.1.4) it can be seen that

$$B_{12} = B_{21} = B \qquad (2.2.1.5)$$

and

$$\frac{A_{21}}{B_{21}} = \frac{A}{B} = \frac{8\pi h\nu^3}{c^3} \qquad (2.2.1.6)$$

These two equations, (2.2.1.5) and (2.2.1.6) are known as the Einstein relations, and give the relationships between the emission and absorption parameters.

2.2.2 The condition for laser action

In order to obtain the necessary condition for optical gain, it is useful to consider a collimated beam of light passing in the z-direction through an assembly of two level atoms. The beam of light carries a power density P, and extends over a narrow range of frequencies around ν_{21} as shown in figure 2.3. Its normalized spectral distribution $\xi(f)$ is defined by

$$\int_0^\infty \xi(f)df = 1 \qquad (2.2.2.1)$$

so the spectral electromagnetic energy density in the beam is

$$\rho(f) = \frac{P\xi(f)}{c} \qquad (2.2.2.2)$$

As the beam passes through the medium it will suffer net absorption, and the power loss is equal to the energy absorbed per second per unit volume by the atoms, hence

$$-\frac{dP}{dz} = B\rho(\nu_{21})(N_1 - N_2)h\nu_{21} \qquad (2.2.2.3)$$

The attenuation of the beam may be described in terms of an attenuation coefficient per unit length, α_{12}, which is defined as

$$\alpha_{12} = -\frac{1}{P}\frac{dP}{dz} = \frac{B(N_1 - N_2)h\nu_{21}\xi(\nu_{21})}{c} \qquad (2.2.2.4)$$

$P(z)$ may thus be found in terms of the intensity of the incident beam, P_0, by integrating the above equation to give

$$P(z) = P_0 \exp(-\alpha_{12}z) \qquad (2.2.2.5)$$

This equation assumes that any spontaneous emission at frequency ν_{21} can be neglected as being small. If the beam is to be amplified instead of absorbed by the medium, then the attenuation coefficient defined in equation (2.2.2.4) must be positive. The attenuation coefficient is now termed a gain coefficient, g_{12}, and may be written using the previously defined expression for spontaneous lifetime as

$$g_{12} = \frac{c^2}{8\pi}\frac{(N_2 - N_1)\xi(\nu_{21})}{\nu_{21}^2\tau_{sp}} \qquad (2.2.2.6)$$

This parameter will only be positive when

$$N_2 > N_1 \qquad (2.2.2.7)$$

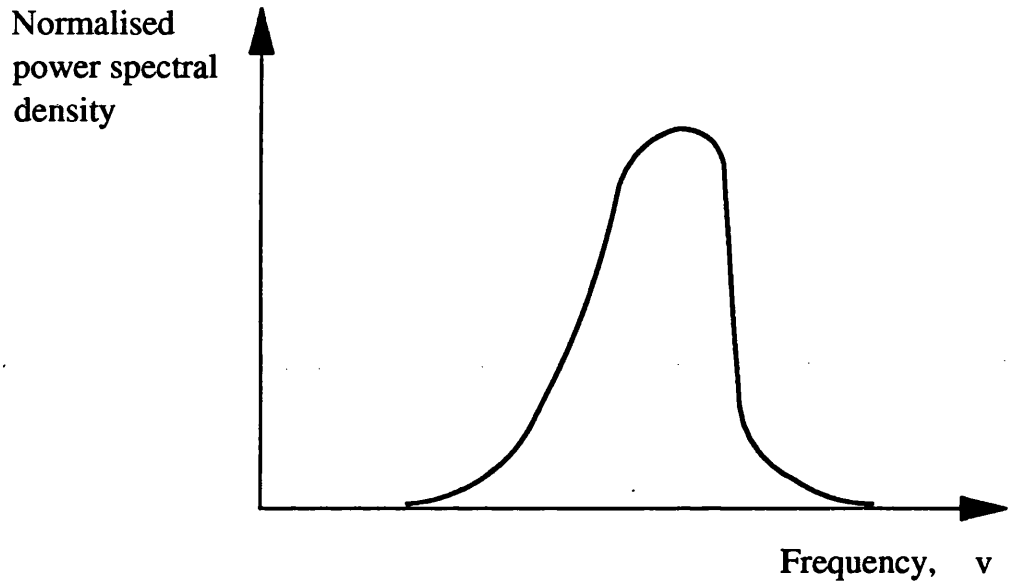

Figure 2.3 Power spectral density function of a beam of radiation

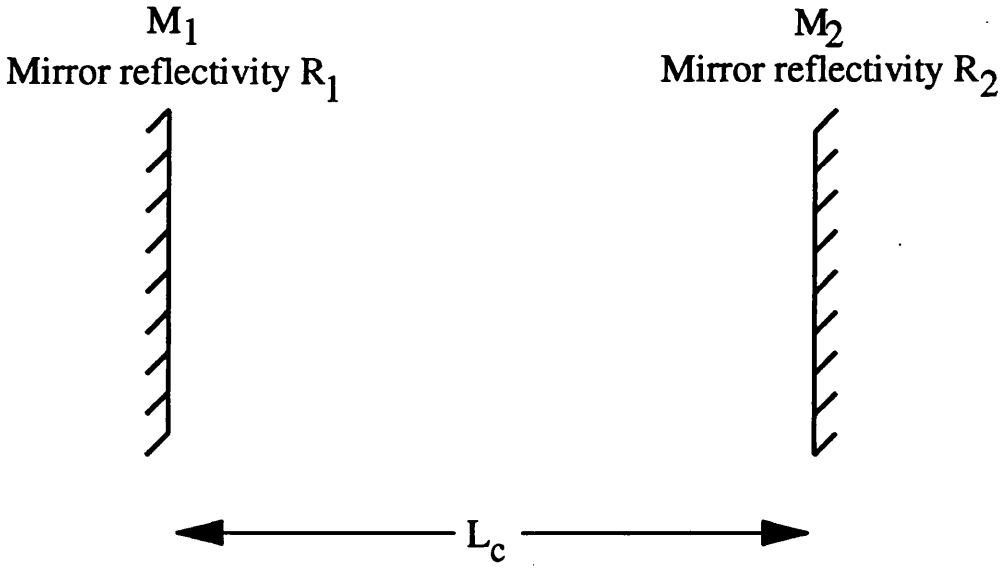

Figure 2.4 The laser cavity

This condition is a requirement for net stimulated emission, and is known as population inversion, since the populations of the two states are reversed compared to the rest state. To achieve this condition energy must be put into the system (called pumping) to excite atoms into the upper energy level.

Amplification of light by stimulated emission is the first step to producing a laser, the second step requires that there be some form of positive feedback to turn the optical amplifier into a laser oscillator. The positive feedback is often provided by a pair of mirrors at either end of the material, forming an optical cavity. These mirrors will reflect the light back and forth in the cavity, and each time the light passes through the cavity it is amplified. The cavity has a particular set of resonant frequencies, and the radiation emitted from the cavity is characterised by these rather than by the continuous emission spectrum of the amplifying medium. The type of cavity described above is called a Fabry-Perot resonator and is shown in figure 2.4. Other forms of feedback have been developed, and these include Bragg reflectors, distributed feedback cavities, and external cavities.

Some form of initial stimulus must be applied in order to initiate the laser action, and this may be provided, for example, by spontaneous emission at the correct frequency. The spontaneously emitted photon travels down the cavity, causing stimulated transitions, and leading to amplification of the signal. This amplified signal is "fed back" into the cavity by the mirrors. A steady state condition will occur when the gain provided by the medium is exactly equal to the losses in the cavity over a round trip. At the point at which this occurs the gain is said to have achieved its threshold value, and this specifies the minimum (threshold) value of population inversion necessary for lasing. The losses in the cavity arise from several sources, the most important of which include:-

1. Mirror losses. These are made up of several components:

a) The mirrors generally transmit quite a large proportion of the incident light. This provides the useful light output from the device, but also constitutes a large proportion of the cavity loss.

b) Absorption and scattering at the mirrors, due to mirror imperfections.

c) Diffraction of light at the mirror interfaces.

2. Absorption of light in the laser medium due to energy transitions other than the desired transitions.

3. Scattering at optical inhomogeneities in the laser medium.

The losses from the phenomena mentioned in 2 and 3 above are distributed along the length of the cavity, and it is convenient to include them as a single effective loss parameter per unit length, α_T. The gain experienced by light in the cavity per unit length is therefore $g_{12} - \alpha_T$. The threshold gain may be found by considering the round trip loss of light in the cavity. For a cavity of length L_c, as shown in figure 2.4, the variation in power along the cavity of a beam of light now becomes

$$P(z) = P_0 \exp | (g_{12} - \alpha_T) z | \qquad (2.2.2.8)$$

The reflectances of mirrors M_1 and M_2 are R_1 and R_2 respectively. After reflection at mirror M_1 the beam will have a power given by

$$P = R_1 P_0 \exp\{(g_{12} - \alpha_T) L_c\} \qquad (2.2.2.9)$$

To complete the round trip the light must again traverse the cavity, and be reflected from mirror M_2. The net gain in power over the round trip is therefore

$$G = R_1 R_2 \exp\{2(g_{12} - \alpha_T) L_c\} \qquad (2.2.2.10)$$

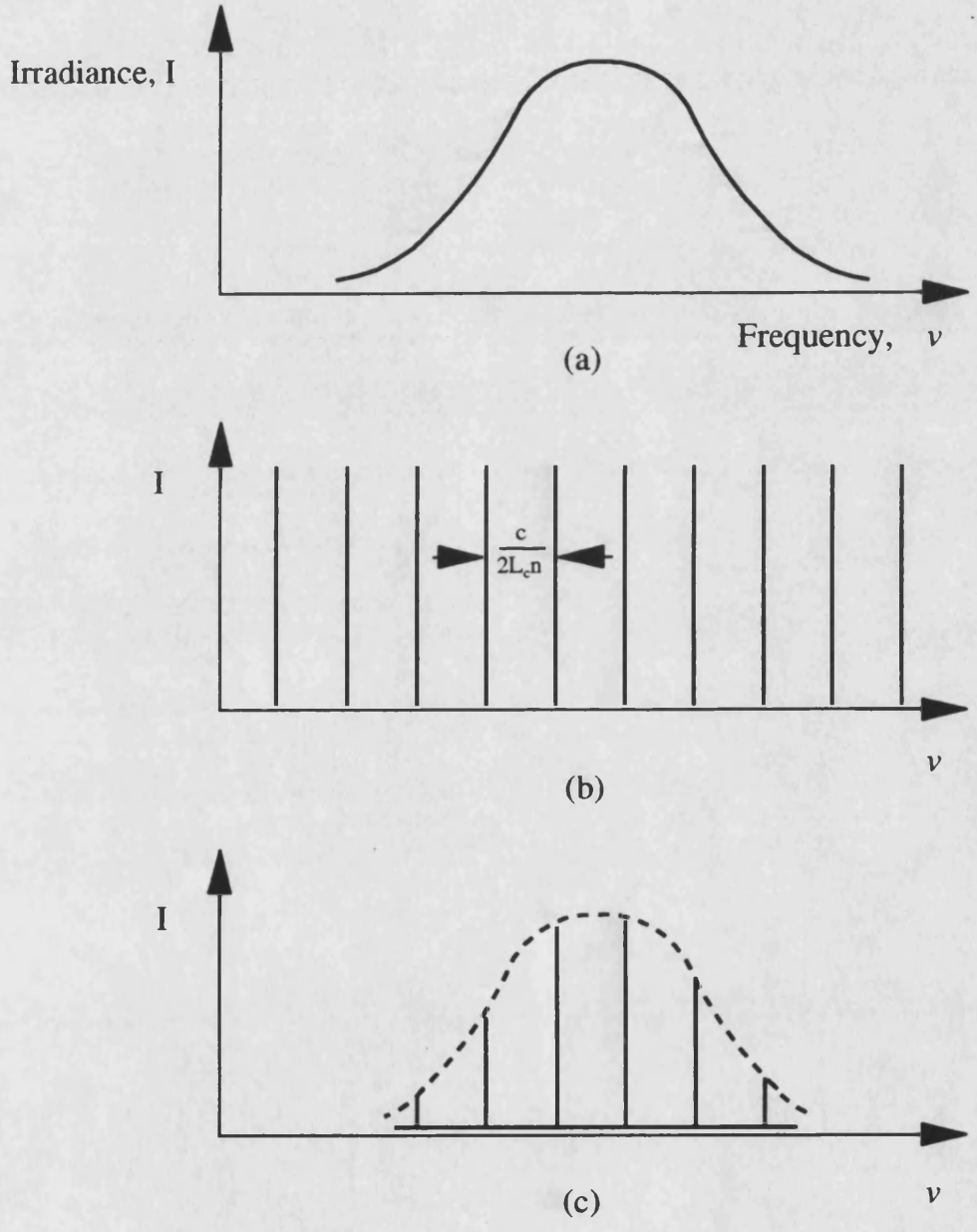

Figure 2.5 (a) The laser gain curve; (b) axial cavity modes; (c) axial modes in the laser output.

For G less than unity the oscillations will eventually die out, whereas for G greater than unity the oscillations will continue to grow until gain saturation occurs. This happens because the gain process is limited by the rate at which carriers are supplied to the laser to provide the gain. The threshold condition is therefore

$$G = R_1 R_2 \exp\{2(g_{th} - \alpha_T)L_c\} \qquad (2.2.2.11)$$

where g_{th} is the threshold gain and may be obtained from

$$g_{th} = \alpha_T + \frac{1}{2L_c}\ln\left(\frac{1}{R_1 R_2}\right) \qquad (2.2.2.12)$$

It is worth noting that when the laser is operating under steady state conditions, then the gain must always be equal to its threshold value, since the gain G may not exceed unity for physical situations. This implies that there is a threshold value of population inversion, N_2 - N_1 which cannot be exceeded during lasing.

2.3 Laser modes

The active material of the laser has optical gain over a range of frequencies as shown in figure 2.5a, which would seem to imply that the output of the laser would be a continuous function of frequency. However, as mentioned in the previous section, this is not the case, due to the cavity in which the active material is placed. The cavity only allows certain frequencies, called the longitudinal, or axial, laser modes to propagate.

2.3.1 Axial modes

The two mirrors at the end of the cavity form a resonant cavity in which standing wave patterns are set up. In a cavity of length L_c, the standing waves must satisfy the condition

$$\nu = \frac{pc}{2L_c n} \qquad (2.3.1.1)$$

where p is an integer and n is the refractive index of the material in the cavity. The integer p is generally large, and for each value of p there is an axial mode of the cavity. The laser modes have a separation given by

$$\delta\nu = \frac{c}{2L_c n} \qquad (2.3.1.2)$$

as illustrated in figure 2.5b. However, only those modes which are at frequencies that fall within the gain curve have the possibility of lasing. A possible laser spectral output is shown in figure 2.5c.

2.3.2 Lateral modes

The distribution of light in the laser cavity is found from the solutions of Maxwell's equations for the particular waveguide formed by the laser structure. Waveguiding in laser structures is discussed in detail in Chapters 4 and 5, and semiconductor lasers all incorporate some waveguiding mechanism to confine the light to the active material. As with the waveguide formed in the axial direction, the solutions in the transverse (y-direction) and lateral (x-direction) directions only allows a set of discrete modes to propagate. These include the fundamental mode which has only one intensity maximum, and other off-axis modes which have more than one intensity maximum. Under certain conditions there may be sufficient gain for the off-axis modes to lase. In the laser structures under study in this thesis the waveguide is such that only a single transverse mode is guided, however more than one lateral mode may be guided and may in some cases lase.

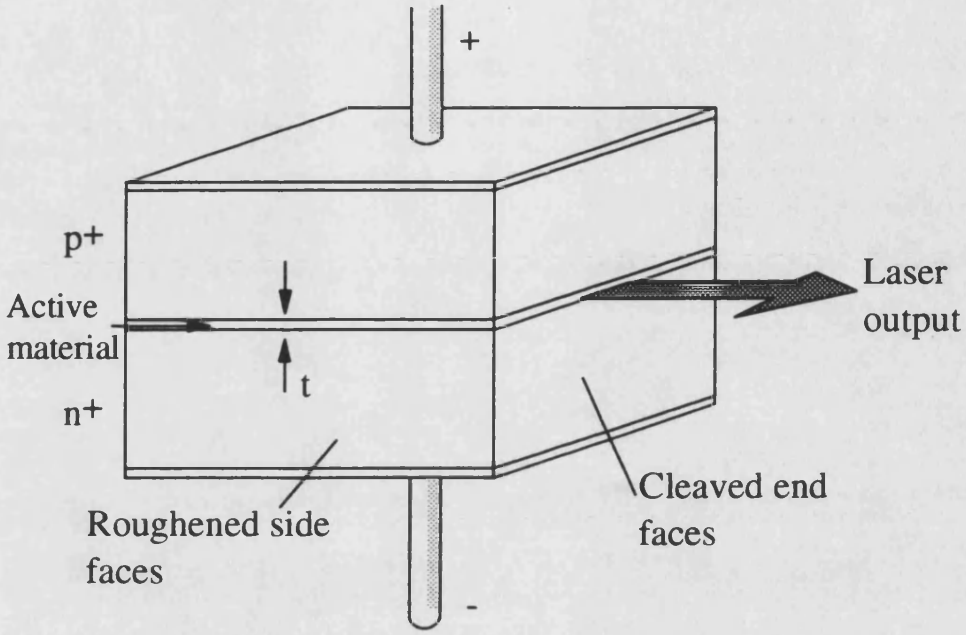

Figure 2.6 Schematic diagram of a double heterostructure semiconductor laser

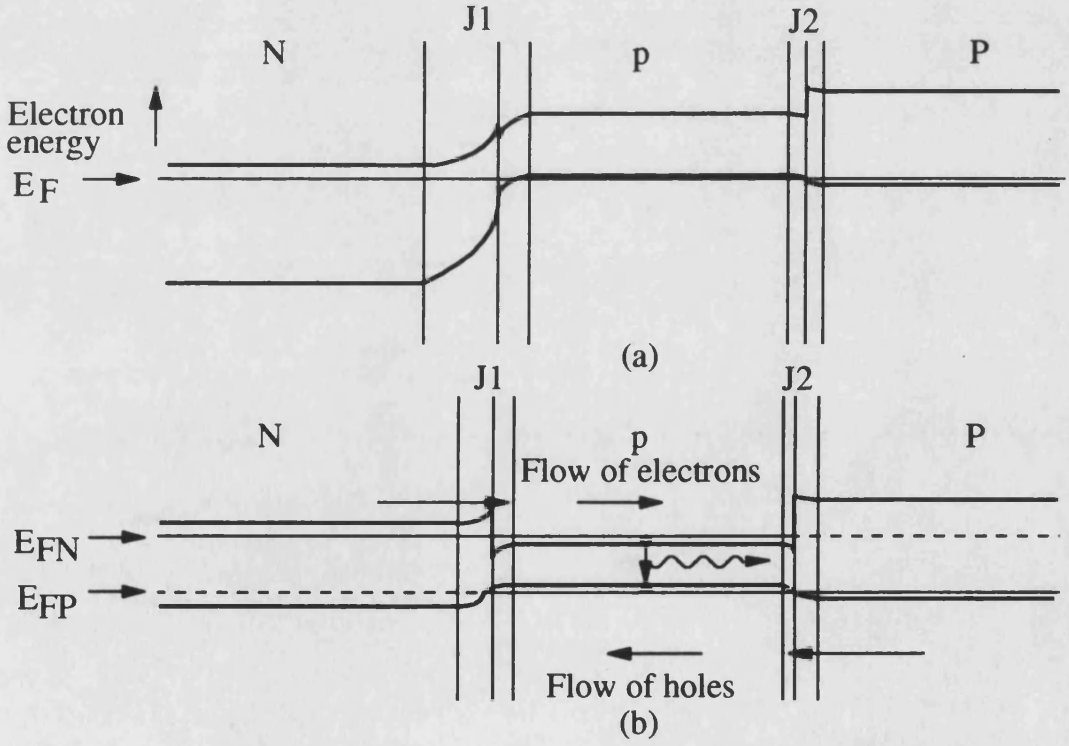

Figure 2.7 Energy band diagram across an N-p-P double heterostructure (a) equilibrium energy levels, (b) strongly forward biased

2.4 The semiconductor laser

The semiconductor laser is most often formed using a forward biased p-n diode structure, enclosed between two reflecting surfaces. A very simple laser diode structure is shown in figure 2.6. This shows an N-p-P double heterostructure diode, across which a voltage is applied via contacts to the top and bottom surfaces. The material has been cleaved along crystal planes to form partially reflecting front and back facets which are parallel with each other, providing the optical cavity. The other sidewalls have been roughened, to provide a waveguide structure in the lateral direction, transverse waveguiding being provided by the change in refractive index between the active medium and the cladding layers. Population inversion is achieved by injection of carriers into the active region to create an excess of carriers out of thermal equilibrium. It is in this region that the radiative recombination takes place.

The choice of materials for useful semiconductor lasers is limited to those semiconductors that have a direct band gap, in order that the radiative transition is the most probable one. Other considerations are whether the material can be obtained in a sufficiently pure form, and the value of the band gap of the material, since this sets the wavelength of the emission. Currently the most popular material systems are those based on GaAs and InP.

2.4.1 Optical amplification in semiconductor material

In section 2.2.2 the ideas of population inversion and threshold conditions were introduced using the simple two level atomic system. However, in the semiconductor laser the energy level structure is considerably more complex than in the two level system. Nevertheless, the ideas derived in the previous section can be applied almost exactly, notably there is a simple condition that can be derived for population inversion.

Consider the forward biased N-p-P double heterostructure illustrated in figure 2.7, where the active region is p doped. The probability that an energy state in the conduction band of the active region is occupied is determined by the energy of the state, E_2, relative to the Fermi energy of the N region, E_{FN}. The probability, F_2, is given by

$$F_2 = F_N(E_2) = \frac{1}{\exp(E_2 - E_{FN})/kT + 1} \qquad (2.4.1.1)$$

Likewise, for holes the probability that an energy level, E_1, in the valence band is unoccupied (i.e that there is a hole there) is determined by the difference between E_1 and the Fermi energy of the P region, E_{FP}. This probability is given by (1 - F_1), where

$$F_1 = F_P(E_1) = \frac{1}{\exp(E_1 - E_{FP})/kT + 1} \qquad (2.4.1.2)$$

This is a highly non-equilibrium situation, which is shown by the fact that there are separate Fermi levels for electrons and holes, referred to as quasi-Fermi levels. It will now be shown that stimulated emission will only exceed absorption for photons whose energy is less than the separation of the quasi-Fermi levels. Since the photon energy must also be greater than the band gap energy, then at least one of the quasi-Fermi levels in the active region must lie outside the band gap and within the conduction or valence bands.

This is not possible for lightly doped p-n homojunctions, and such devices will not lase. It is possible for this condition to exist in a degenerately doped homojunction laser, but the gain is generally too low. Consequently the most effective method of achieving this situation is to use a heterojunction structure such as the one shown in figure 2.7(b). For such a structure the quasi-Fermi levels in the cladding layers fall within the band gap, but due to the heavy forward biasing of the junction and the high doping levels used, the quasi-Fermi levels are beyond the band gap edges in the active layer.

There are four factors which will determine the rate, r_{12}, at which electrons in an energy state E_1 in the valence band can be excited up to an energy state E_2 in the conduction band:

(a) The probability that the transition can occur, B_{12} $(=B_{21} = B)$

(b) The electromagnetic energy density at the frequency $\nu_{21} = (E_2 - E_1)/h$, represented as $\rho(\nu_{21})$

(c) The probability that the state E_1 is occupied, F_1

(d) The probability that the state E_2 is unoccupied, $1 - F_2$

Thus

$$r_{12} = B\rho(\nu_{21})F_1(1 - F_2) \qquad (2.4.1.3)$$

A similar argument may be used to obtain the rate, r_{21}, at which stimulated emission from level E_2 to E_1 may occur

$$r_{21} = B\rho(\nu_{21})(1 - F_1)F_2 \qquad (2.4.1.4)$$

Stimulated emission will exceed absorption when $r_{21} > r_{12}$, that is

$$(1 - F_1)F_2 > F_1(1 - F_2) \qquad (2.4.1.5)$$

which may be reduced to

$$F_2 > F_1 \qquad (2.4.1.6)$$

Using the substitutions

$$x = \frac{E_1 - E_{FP}}{kT}, \qquad y = \frac{E_2 - E_{FN}}{kT} \qquad (2.4.1.7)$$

and using the definitions of F_2 and F_1 (equations (2.4.1.1) and (2.4.1.2)), condition (2.4.1.6) becomes

$$\frac{1}{e^{y}+1} > \frac{1}{e^{x}+1} \tag{2.4.1.8}$$

or $x > y$. In terms of the quasi-Fermi levels, this implies that, for net stimulated emission

$$E_1 - E_{FP} > E_2 - E_{FN} \tag{2.4.1.9}$$

or

$$E_{ph} = E_2 - E_1 < E_{FN} - E_{FP} \tag{2.4.1.10}$$

The semiconductor material will thus act as an amplifier for radiation whose photon energy exceeds the band gap, but is less than the difference between the quasi-Fermi levels. This implies, as previously noted, that at least one of the quasi-Fermi levels must lie in the conduction or valence bands. The net rate of stimulated emission between the two levels at E_1 and E_2 may be written as

$$\begin{aligned} r_{st} = r_{21} - r_{12} &= B\rho(\nu_{21})\{(1-F_1)F_2 - F_1(1-F_2)\} \\ &= B\rho(\nu_{21})(F_2 - F_1) \end{aligned} \tag{2.4.1.11}$$

and finally the spontaneous emission rate, r_{sp}, between the two levels is

$$r_{sp} = AF_2(1-F_1) \tag{2.4.1.12}$$

2.4.2 Laser structures

Initial laser designs used a simple p-n homojunction structure, but this structure has very limited confinement of carriers or light to the active region. Therefore, when using such devices very high current injection, in the range 30-100kA/cm^{-2}, was required to achieve

lasing. These lasers were not only extremely inefficient, but had to be both cooled and run in pulsed mode in order to limit the ohmic heating produced by the large currents used.

One of the major advances in semiconductor laser design was the use of the double heterostructure. Using a double heterostructure has distinct advantages in confining both the carriers and the optical field, and enables lasers to be produced which can operate continuously at room temperatures. The energy diagram of a forward biased heterostructure is shown in figure 2.7, and from this it can be seen how the carriers are confined by potential barriers to a narrow region. The potential barriers are formed by the differing energy gaps of the layers forming the regions of the laser.

A second advantage in using the double heterostructure is the waveguide structure is formed in the transverse (y) direction by the difference between the refractive indices of the active and cladding layers. This confines the light to the active layer, and therefore a greater part of the optical field is available for interaction with the active layer carriers.

There are two main considerations in choosing the material from which the heterostructure is formed. First, there must be a good lattice match between the two materials in order to achieve good electrical characteristics and device lifetimes, and secondly that the refractive indices of the materials must be such as to form a waveguiding structure. For the GaAs system, the heterostructure barriers are generally formed from $Al_xGa_{x-1}As$, with a light output at about 850nm. For the InP system the active layer is $In_{x-1}Ga_xAs_{y-1}P_y$, which can be exactly lattice matched to InP to provide a range of output wavelengths from 1.1μm to 1.7μm, covering the important communications wavelengths of 1.3μm and 1.55μm

It is possible to increase the efficiency of the laser further by limiting the current spreading in the cladding layer, providing the greatest current injection to the area of light production. One common method to achieve this is to use a stripe contact to the upper,

p-type cladding layer. Provided the upper confining region is not too thick there will be limited current spreading in this region, and thus current (and carrier) injection into the active layer will be over a narrow area. The carrier injection causes a change in the complex refractive index which in turn leads to an optically guiding structure, although the waveguiding is relatively weak.

A further improvement on this structure uses not only a stripe contact, but some form of materially induced waveguiding in the lateral direction. The guiding structure may take several forms, as shown in figure 2.8. The most common structure is the ridge waveguide, which provides an effective index step between the region under the strip and the regions on either side, thus generating a waveguiding structure.

The buried heterostructure laser, some examples of which are shown in figure 2.9, takes the ideas of the heterostructure laser one step further. The structure uses a narrow strip of active material, surrounded on all sides of the cross section by cladding material. This provides a structure which confines carriers and light in two dimensions. Using this structure, very low threshold currents and high optical output powers may be obtained.

2.4.3 The laser as a source for optical communications systems

The lasers under consideration in this thesis are designed mainly for use as sources in high bit rate fibre optic optical communications systems. In a typical optical communications system the light source may be a laser or an LED, and the light output may be directly or indirectly modulated. For short distances and bandwidths up to a few MHz then LEDs are often used, since they are far cheaper than lasers. However, for longer distance, or higher bit rate communications systems, it is necessary to use lasers. This is because the laser produces more power, can be modulated at higher frequencies, and has a much narrower optical bandwidth than an LED.

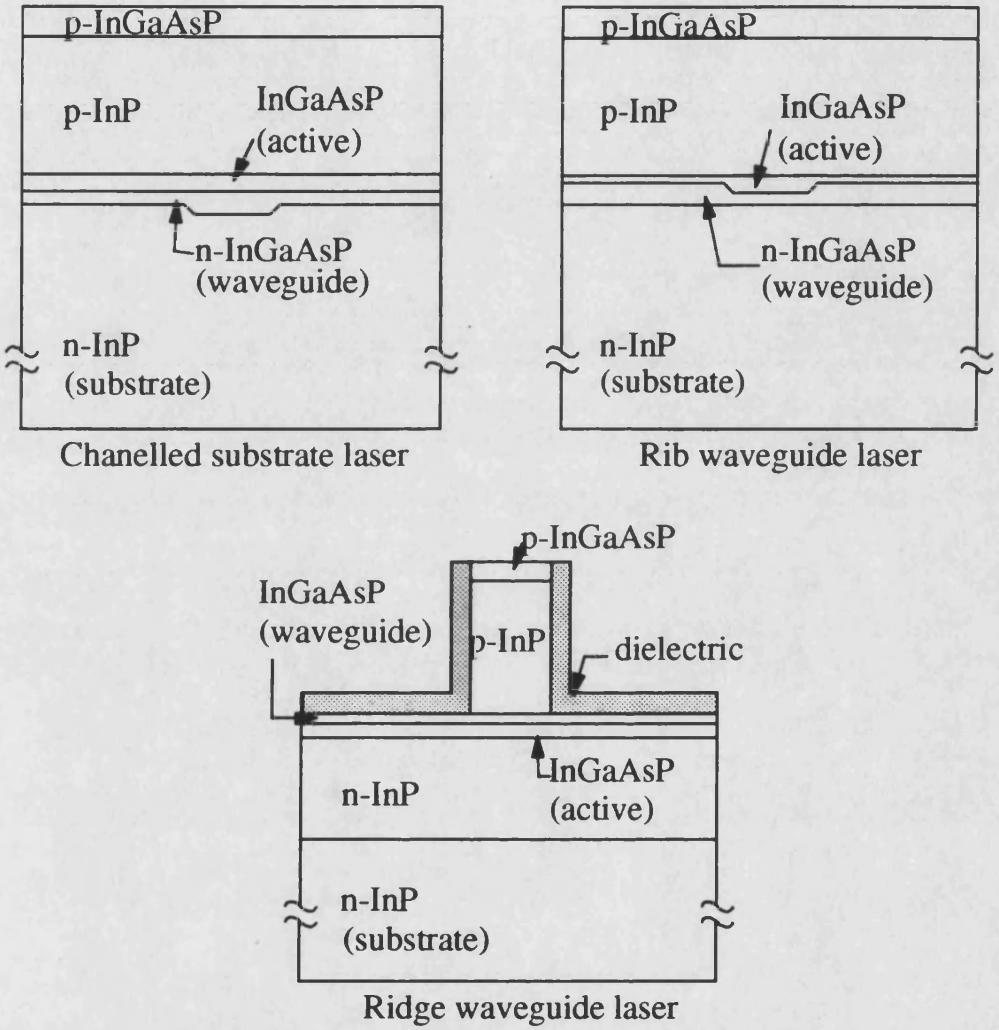

Figure 2.8 Schematic cross sections of different types of index guided lasers

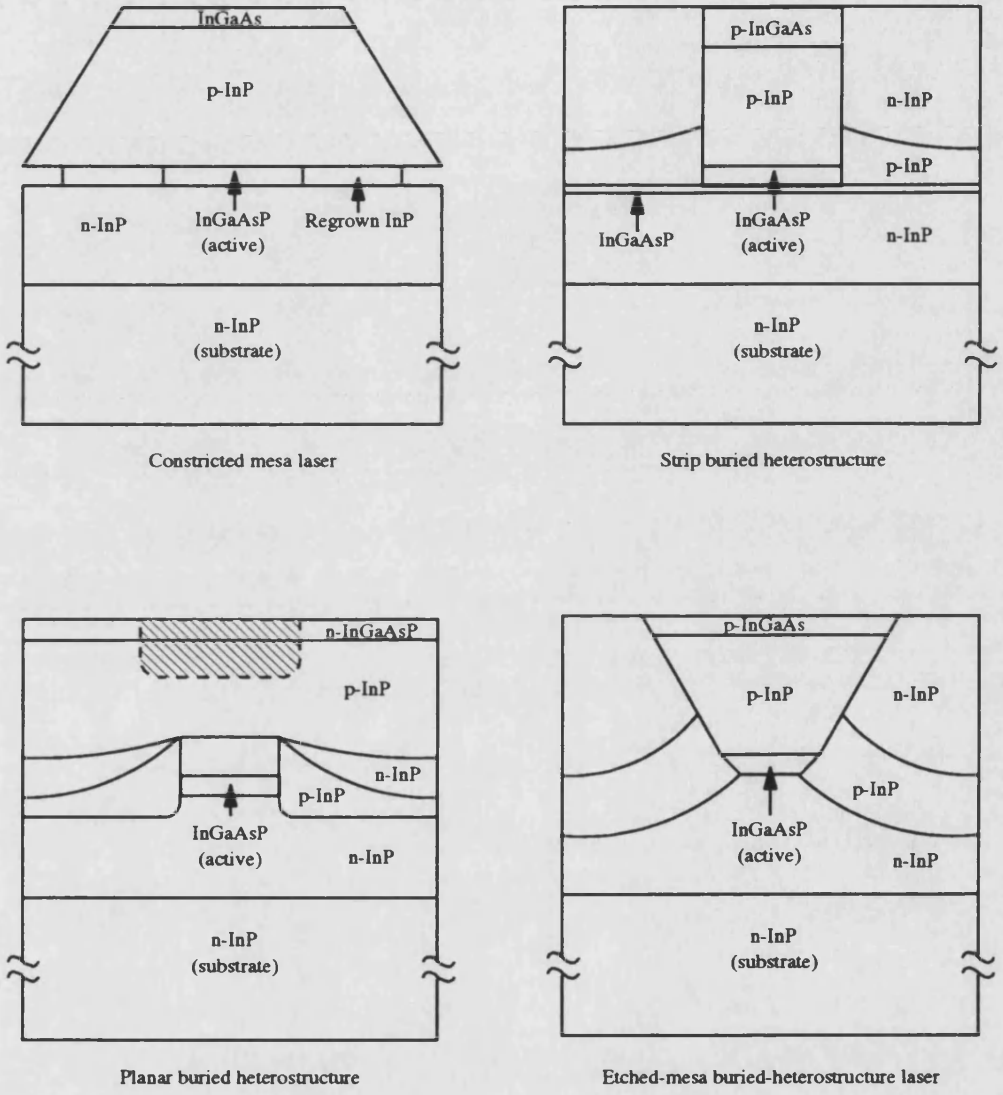

Figure 2.9 Schematic cross sections of different types of buried heterostructure lasers

There are two possible schemes of light modulation, direct modulation of the laser output by modulating the laser drive current, and external modulation where the laser produces a constant power output, and the light is modulated using a device coupled to the laser. External modulation has the advantage of having a basically flat frequency response, and is capable of on-off modulation of the light without the chirp caused by direct on-off modulation. However, it adds to the system complexity and therefore increases system cost and decreases reliability.

A typical light current characteristic for a laser is shown in figure 2.10. The figure shows how, by modulation of the drive current to the laser, the output light from the device may be modulated. Such a scheme is called direct modulation. The figure also shows that, as the drive current to the laser is increased, above a certain point the curve becomes sub-linear. This is due to a number of mechanisms. In the lasers studied in this thesis, the most important of these mechanisms is leakage of current around the active layer of the device. This leakage current does not supply carriers to the active region, and thus does not contribute to light production. As the drive current is increased, the proportion of leakage current to useful current increases, and hence the curve becomes more sub-linear.

A sub-linear light current characteristic will obviously have adverse effects on the modulation performance of the laser, causing harmonic distortion of the modulated signal and reducing the modulation bandwidth. A second factor affecting the laser's modulation performance is its frequency characteristic. This may be obtained from the rate equations describing the generation and recombination of carriers and photons, which are given by

$$\frac{dN}{dt} = \frac{I}{qV} - \frac{N}{\tau} - (aN - b)S \qquad (2.4.3.1)$$

$$\frac{dS}{dt} = (aN - b)S\Gamma_a - \frac{S}{\tau_s} \qquad (2.4.3.2)$$

where N is the injected electron density, I the total current, q the electronic charge, V the volume of the active region, τ the spontaneous recombination lifetime, and S is the photon density inside the active region. Γ_a is the confinement factor of the light to the active region, τ_s the photon lifetime and a and b are the gain parameters of the material.

The steady state solutions for carriers and photons, denoted N_0 and S_0, are obtained by setting the left hand sides of equations (2.4.3.1) and (2.4.3.2) to zero, giving

$$0 = \frac{I_0}{qV} - \frac{N_0}{\tau} - (aN_o - b)S_0 \qquad (2.4.3.3)$$

$$(aN_0 - b) = 1/(\Gamma_a \tau_s) \qquad (2.4.3.4)$$

If the current is made up of a.c. and d.c. components, such that

$$I = I_0 + i_1 e^{j\omega t} \qquad (2.4.3.5)$$

this will give rise to a modulation of the carriers and photons given by

$$N = N_0 + n_1 e^{j\omega t} \qquad (2.4.3.6)$$

$$S = S_0 + s_1 e^{j\omega t} \qquad (2.4.3.7)$$

Using equations (2.4.3.4) to (2.4.3.7) in equations (2.4.3.1) and (2.4.3.2), the small signal equations describing the fluctuations of carriers and photons may be written

$$-j\omega n_1 = -\frac{i_1}{qV} + \left(\frac{1}{\tau} + aS_0\right)n_1 + \frac{1}{\tau_s \Gamma_a} s_1 \qquad (2.4.3.8)$$

$$j\omega s_1 = aS_0\Gamma_a n_1 \qquad (2.4.3.9)$$

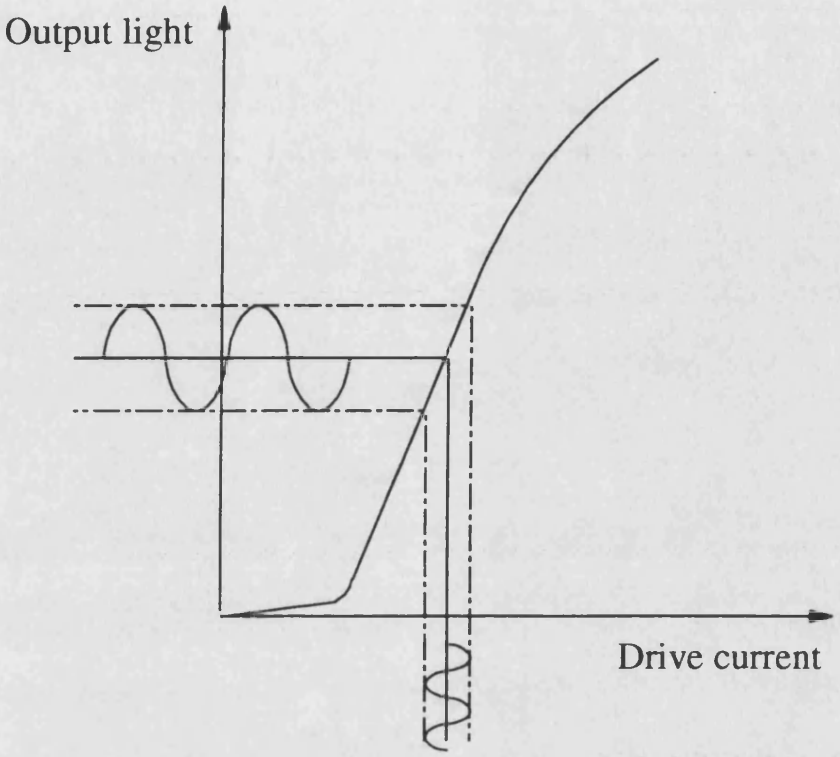

Figure 2.10 A typical light current curve for a laser showing the possibility of direct modulation

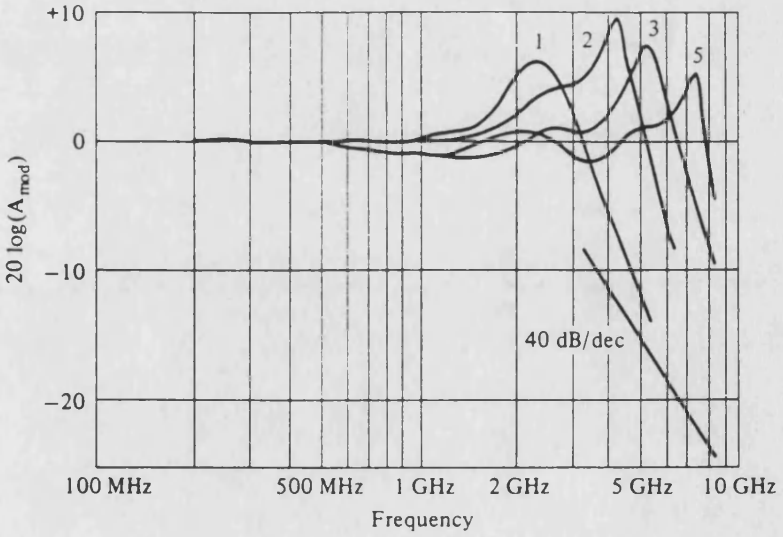

Figure 2.11 Experimental laser frequency characteristics

The frequency response, $s_1(\omega)$, may be obtained from the above as

$$s_1(\omega) = \frac{-(i_1/qV)aS_0\Gamma_a}{\omega^2 - j\omega/\tau - j\omega aS_0 - aS_0/\tau_s} \qquad (2.4.3.10)$$

This shows a flat response at low frequencies, with a peak at

$$\omega_R = \sqrt{\frac{aS_0}{\tau_s} - \frac{1}{2}\left(\frac{1}{\tau} + aS_0\right)^2} \qquad (2.4.3.11)$$

followed by a steep decline. The frequency at which this peak occurs is called the relaxation oscillation frequency. The first term under the square root in equation (2.4.3.11) is dominant, so that to a first approximation

$$\omega_R = \sqrt{\frac{aS_0}{\tau_s}} \qquad (2.4.3.12)$$

i.e. the relaxation oscillation frequency of the intrinsic laser, which is an indicator of the laser bandwidth, is proportional to the square root of the optical output power.

The overall laser frequency characteristic is a combination of this intrinsic laser response with the frequency response of the parasitic components of the laser, comprising mainly of spreading resistance, junction and layer capacitance, and bondwire inductance. Some experimental laser frequency characteristics are shown in figure 2.11.

To improve the bandwidth of the laser, the internal photon density must be increased, as shown by equation (2.4.3.12). This means that the leakage current in the device must be minimised, in order that the IL characteristic be linear at higher output powers. A second requirement is that the threshold current of the device be low, so that ohmic heating is minimised, and finally the device parasitics must be made as low as possible. The lasers considered in this thesis are small, thus limiting parasitics, and employ buried heterostructure designs, thus providing low thresholds and high power outputs. They are

therefore well suited to high bandwidth applications. However, they are subject to possible problems of current leakage around the active layer and multi-lateral mode operation, which may limit the operating characteristics of the lasers, and the work of this thesis has been carried out in order to gain further understanding of these problems.

REFERENCES

[1] G.H.B.Thompson, "Physics of semiconductor laser devices", John Wiley and sons, Chichester, 1980

[2] H.C.Casey, and M.B.Panesh, "Heterostructure lasers" Parts A and B, Academic Press Inc, New York, 1978

[3] G.P.Agrawal, and N.K.Dutta, "Long-wavelength semiconductor laser devices", Van Nostrand Reinhold, New York, 1986

[4] J.Wilson, and J.F.B.Hawkes, "Optoelectronics, an introduction", Prentice Hall, New York, 1983

[5] A.Yariv, "Optical electronics", 3rd Edition, CBS Colege Publishing, New York, 1985

[6] J.Gowar, "Optical communications systems", Prentice Hall, New York, 1984

CHAPTER 3: THE ELECTRICAL MODEL

3.1 Introduction

The self-consistent model presented in this thesis has been designed to examine the lasing characteristics of buried heterostructure lasers. The overall model can be split into two sub-problems, an electrical problem and an optical problem. This chapter deals with the model of the electrical characteristics of the device, and the following two chapters deal with the model of the optical properties. The electrical and optical sub-problems are coupled by the carrier density via the radiative recombination coefficient and the complex dielectric constant in the active layer, and are treated in a self-consistent fashion in chapter 6.

In this chapter, the equations and solution techniques used in the electrical model are presented, and results are given showing the effect of varying the device geometry. The focus of the electrical model is to obtain the current distribution in the laser for a given cross-sectional geometry, and thus to be able to find the carrier density in the active region. The carrier density can then be used as an input to the optical section of the overall model. The optical field obtained from the optical model distorts the carrier distribution by locally increasing the carrier recombination rate, and must be included in the electrical modelling. The two models are therefore coupled in a complex fashion.

The present work is limited to buried heterostructure devices which use forward-biased homojunction regions either side of the active layer for current confinement. Two such lasers are the constricted mesa (CM) and buried ridge structure (BRS) lasers which are

shown schematically in figures 3.1(a) and 3.1(b). Although there are slight variations on the basic geometry, the overall physical characteristics of both types of laser remain the same. These are:-

a) a stripe anode contact to the top, p-type cladding layer, and a broad area cathode contact to the n-type substrate.

b) lateral current confinement, achieved either by proton isolation (for example) in the case of the buried ridge structure laser, or by etching away the cladding layer material in the case of the constricted mesa laser.

c) InP p-n homojunction regions on either side of the narrow InGaAsP active layer.

e) highly doped n-type cladding and substrate regions.

Current spreading in buried heterostructure lasers can be a serious problem, leading to the leakage of current around the active layer heterojunction, with consequent sublinearity of the light-current characteristic and loss of differential external quantum efficiency. Leakage can be especially serious in lasers such as the CM and BRS lasers, where current confinement is by homojunction regions on either side of the active layer which are forward biased under the operating conditions of the laser.

In these devices, at high current injection the current spreading in the upper cladding region may be such that the homojunction regions have sufficient bias across them to enable them to become conducting. The current flowing through these homojunction regions will not contribute to light production, but as the current injection into the laser is increased, the proportion of current flowing through them increases. This in turn means that both the gain and the photon density at any particular drive current is less than that

achievable with perfect current and carrier confinement, and ultimately this has the effect of reducing the maximum achievable direct modulation bandwidth of the device, as was shown in chapter 2.

Although there have been previous investigations of the electrical properties of various lasers structures [e.g. 1-9], many of these are not applicable because they have been formulated for different device geometries and structures to the ones studied in this thesis. Of those that have been formulated for CM or BRS lasers [6-9], two papers consider only p-side down structures [6,7] and all ignore the effect of the lateral heterojunction, which blocks the lateral flow of carriers out of and into the active layer.

Two studies are noteworthy, and both are motivated by the need to look at ways of reducing the leakage of current around the active layer. The first of these investigations, by Liau and Walpole [8], uses analytical techniques, and examines the voltage distribution in the laser. The voltage spreading in the cladding layer is described in terms of a Schwarz-Christoffel transformation, assuming for this that there is no current leakage through the homojunction regions. The calculated voltage distribution is then used in a fairly crude fashion to determine the proportion of the homojunction region that is "turned on" and thus conducting. Finally, the leakage current is determined using an analytic expression relating the voltage to the current flowing through this part of the homojunction region.

The second investigation, by Amman and Thulke [9], examined the effects of current leakage in BRS lasers. The method used assumes a uniform active layer carrier density, pinned at the threshold value, and the fixed active layer voltage is calculated. The voltage distribution is obtained from a solution of Laplace's equation in the p-type confining region. The boundary conditions for Laplace's equation are simplified by assuming that the hole current through the homojunction regions can be ignored, implying that for the

holes all boundaries are insulating apart from the contact and active layer, which are held at fixed voltages. The hole and electron current densities are obtained from the voltage distribution thus calculated. Since the hole current through the homojunctions has been ignored, the proportion of the overall current flowing through the homojunctions is obtained by integrating the electron current over these regions.

Both of these investigations, however, ignore the effects of the lateral carrier confinement due to the lateral heterojunctions, and assume that in the active layer the lasing action clamps the carrier density at a fixed level, implying a fixed active layer voltage, and thus the active layer is treated as an equipotential surface. This simplifying assumption cannot be used in a self-consistent model, since it is the active layer carrier density that links the optical and electrical components of the model, and the distribution of these carriers has a great effect in determining the lasing characteristics of the device.

It was therefore necessary to construct a model different to those described above. The important considerations were to be able to determine the homojunction current, and to obtain the carrier density consistently with the optical field. If the current density injected into the active layer is known, it is possible to calculate the active layer carrier density from the carrier diffusion equation. In the past, several authors [2,6-8] have used conformal mapping techniques to obtain the current spreading in the cladding layers, whereas others [4,5] have used simplifying approximations to obtain analytic expressions. However, this thesis deals with buried heterostructure devices, in which carrier confinement in the active region is in two dimensions, and with devices which incorporate lateral insulating boundaries, so that it is necessary to examine the current spreading problem in two dimensions, and the above mentioned simplifying techniques cannot be used.

There are two main lines of approach which have been taken by other authors when tackling the two dimensional current and carrier problems self-consistently with the optical field problem [10-13]. The first [10-12] is to obtain a solution of Poisson's equation and the current continuity equations for electrons and holes. From these solutions, the active layer carrier densities are obtained. This approach suffers from the fact that, due to the number of equations that must be solved, it is very slow to converge even for the case of a reverse biased junction. Solution of Poisson's equations for heavily forward biased junctions, which are used in semiconductor lasers, is fraught with numerical complexities and questions over convergence and singularity of solution [14].

A second approach to the problem [13] is to assume that the cladding layer is electrically neutral (the junction depletion region is ignored), and that Laplace's equation may therefore be applied subject to appropriate boundary conditions at the edges of the region. The solution of Laplace's equation gives the voltage distribution, and this is directly related to the current distribution via the material resistivity. Knowledge of the current distribution then allows calculation of the current injected into the active layer, and from the active layer current and optical field distribution (obtained elsewhere) the active layer carrier density may be found from the carrier diffusion equation. This approach also allows calculation of the current injected into any other region. The Laplace equation method has been applied to other laser geometries by several other authors [1-3,13] and is the approach that has been taken in this thesis.

3.2 The model

The physical laser structures to be modelled, the CM and BRS devices, are shown schematically in figures 3.1(a) and (b). A stripe contact is made to the top p-type InP layer and a broad area contact to the n-type substrate. The active layer is completely

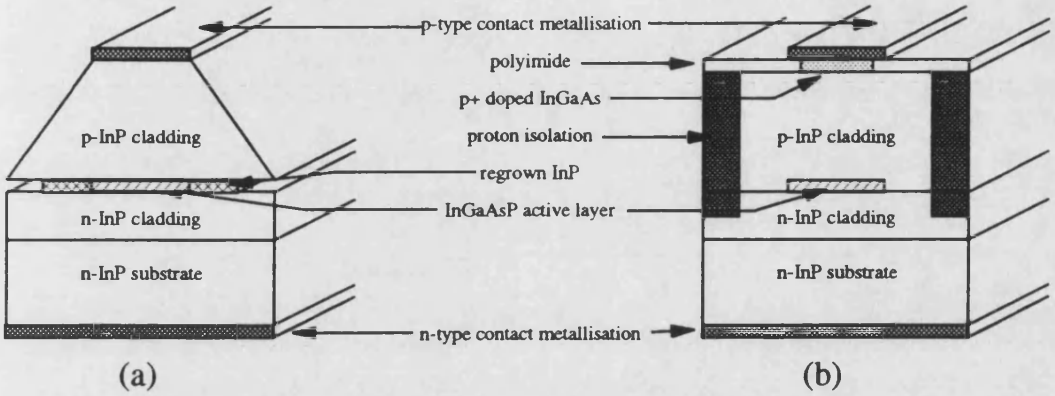

Figure 3.1 Schematic diagrams of (a) the constricted mesa laser and (b) the buried ridge laser

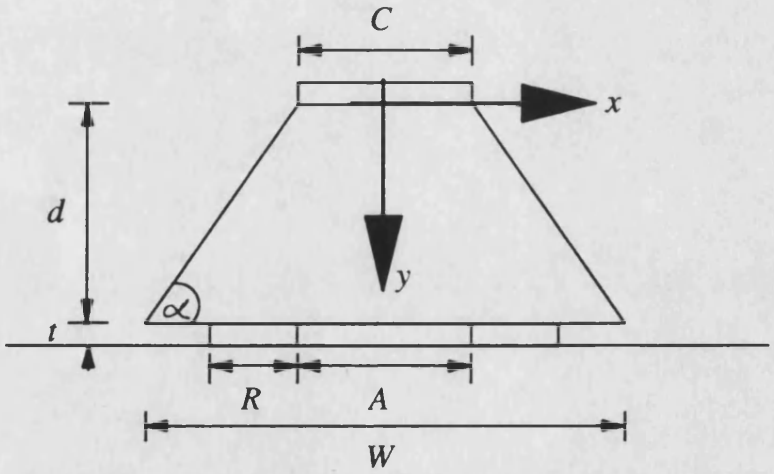

Figure 3.2 Schematic diagram of the structure to be modelled

buried by InP material. The BRS laser is formed by growth of p-type material over a non-planar region consisting of the n-type cladding layer and active region. The CM laser is fabricated from an 'as-grown' double heterostructure wafer. In this case the material at the sides of the active region is grown by mass-transport [8], or by vapour phase epitaxy [15], and may not have exactly the same crystal structure as the wafer material [16].

The exact nature and location of the p-n homojunction formed by the regrown InP of the CM laser is therefore unknown, although both experiment [16], and to some extent theory [6-8], suggests that the I-V characteristics resemble those of a normal p-n InP/InP abrupt junction. In contrast, the material composition of the BRS laser is closely controlled and known during growth. The junction for both devices is assumed to be abrupt and located just below the plane at $y=d$ (see figure 3.2).

For the laser to have a usable characteristic, the leakage current must be limited to a small percentage of the overall current. This implies that the homojunction current must be limited, at most, to a few mA and the homojunction regions are therefore operating in the low injection regime. In this model the homojunction regions are represented by a series of closely spaced discrete diodes, each having identical characteristics. In the low injection regime the carrier density may be described by the Boltzmann approximation, and this is used to obtain the diode characteristics.

In the active region, the Boltzmann approximation may no longer be used, due to the very high carrier concentrations. The lasing action at the heterojunction pins the carrier density near to its threshold value, and the carrier density is determined by the generation and recombination of carriers. The active region is very thin, and the variation of carriers across the depth of the active layer is invariably ignored. It is assumed that the variation of carriers in the longitudinal direction may also be averaged over, and the distribution

of carriers in the active region can therefore be described by a one dimensional diffusion equation operating in the lateral direction [17]. From the carrier concentrations, the quasi-Fermi level separations can be calculated, and thus the voltage distribution across the active layer found.

The lasers have a broad area cathode contact to the heavily doped n-type substrate, and in common with others [1-9,11-13] the assumption is made that the current spreading and voltage drop in the n-type layers is negligible, and thus the substrate and passive n-type layer are replaced in the model by an earth plane. The top contact is assumed to be ideal, such that the contact and any (heavily doped) capping layers may be assumed to be an equipotential surface.

The two structures to be modelled are basically similar, and the BRS laser may be considered to be a CM laser with full width regrown region and a 90° mesa angle. The equations derived in the following section are therefore equally applicable to both laser structures if the appropriate boundary conditions are used. The simplified structure used in the electrical model is shown in figure 3.2. The active layer has a thickness, t, and width A. The regrown region has width R, and the contact width is C. The upper cladding depth is d, and the mesa angle α. A cartesian coordinate system is adopted with the origin at the centre of the top contact.

3.3 Theory

In the electrically neutral p-type upper cladding region, the current spreading problem is related to the voltage spreading by the conductivity, σ, of the region, such that

$$J(x,y) = -\sigma \nabla V(x,y) \qquad (3.3.1)$$

where $J(x,y)$ is the current density at any point in the cladding region. In the heavily p-doped upper cladding region the conductivity is related to the electronic charge, q, the hole mobility μ_p and the p-type doping density p_0 by

$$\sigma = q\mu_p p_0 \tag{3.3.2}$$

where the effect of the minority carriers is ignored in comparison to the majority carriers. The upper cladding layer is taken to be homogeneous and passive, and thus the two dimensional potential distribution is given by a solution of Laplace's equation

$$\nabla^2 V(x,y) = 0 \tag{3.3.3}$$

subject to the boundary conditions at the edges of the region. There are broadly four different types of boundary conditions; (i) equipotential surfaces, i.e. the contacts, and those representing (ii) the insulating boundaries, (iii) the homojunction boundaries, and (iv) the heterojunction boundary. The total current injected into the device may be obtained by integrating the current density injected across the contact, or equivalently by integrating the current flowing through any plane parallel to the contact (e.g. the heterojunction/homojunction boundary).

The boundary conditions at all of the boundaries are related to the current flowing across them, and thus to the derivative of the voltage. At the insulating boundaries the condition is for zero current flow, i.e.

$$J(x,y).\bar{n} = 0 \tag{3.3.4}$$

where $\bar{n}$ is the unit vector in the direction perpendicular to the interface.

The homojunction regions are modelled by a row of InP/InP p-n homojunction diodes, each of which is assumed to have an abrupt junction, and to operate in the low injection

regime. Under these conditions, the carrier density is adequately described by Boltzmann statistics, and the current density injected into any point on the homojunction boundary may be obtained from the Shockley equation [18]

$$J(x,d)\,|_{homojunction} = J_{sat}\left[\exp\left(\frac{qV(x,d)}{\eta kT}\right)-1\right] \tag{3.3.5}$$

where

$$J_{sat} = \frac{qD_n n_i^2}{L_n p_0} + \frac{qD_p n_i^2}{L_p n_0} \tag{3.3.6}$$

In the above equations D_n and L_n, D_p and L_p are the electron and hole diffusivity and effective diffusion length respectively, n_i is the intrinsic carrier concentration, η is the ideality factor, k is the Boltzmann constant and T the temperature. p_0 is the p-type doping level in the upper cladding region, and n_0 is the doping level in the lower cladding region.

At the heterojunction boundary, the boundary conditions are somewhat more complex than at either the insulating or the homojunction boundaries. The carrier density at the active layer cannot be described in terms of Boltzmann statistics (as was the case for the homojunction regions) because, under lasing conditions, the carrier density is too high. The boundary conditions here may be found from considering the properties of the semiconductor material. The carrier continuity equations for electrons, n, and holes, p, are given by [18]

$$\frac{\partial n}{\partial t} = G_n - U_n + \frac{1}{q}\nabla . J_n \tag{3.3.7a}$$

$$\frac{\partial p}{\partial t} = G_p - U_p - \frac{1}{q}\nabla . J_p \tag{3.3.7b}$$

where G and U are the generation rate and recombination rate respectively, and the electron and hole current densities are given by the equations

$$J_n = q\mu_n nE + qD_n \nabla n \tag{3.3.8a}$$

$$J_p = q\mu_p pE - qD_p \nabla p \tag{3.3.8b}$$

Here, E is the electric field. If charge neutrality holds approximately, such that $n + N_a \approx p + N_d$, (where N_a is the number of ionised acceptor impurities and N_d the number of ionised donor impurities) and if the electrons and holes are generated and recombine in pairs, with no trapping or other effects, then the recombination and generation rates for electrons and holes are identical. Combining these relationships and limiting the solution to the steady state, one obtains the equations

$$G - U + \mu_n E \nabla n + \mu_n n \nabla E + D_n \nabla^2 n = 0 \tag{3.3.9a}$$

$$G - U - \mu_p E \nabla p - \mu_p p \nabla E + D_p \nabla^2 p = 0 \tag{3.3.9b}$$

Multiplying (3.3.9a) by $\mu_p p$ and (3.3.9b) by $\mu_n n$ and combining with the Einstein relation $D = (kT/q)\mu$ gives, after some rearrangement

$$D_a \nabla^2 n + G - \frac{n - p}{n/\mu_p + p/\mu_n} E \nabla n = U \tag{3.3.10}$$

where D_a is called the ambipolar diffusion coefficient, and is defined as

$$D_a = \frac{n + p}{n/D_p + p/D_n} \tag{3.3.11}$$

Equation (3.3.10) is called the ambipolar diffusion equation. In the active layer the generation of carriers is described by $G=J(x)/qt$, where $J(x)$ is the current injected into

the active region and t the active layer thickness. The variation of carriers in the longitudinal and transverse directions can be averaged over, and thus the diffusion equation is limited to the lateral direction only. Neglecting the active layer electric field, the equation may be written

$$D_a \frac{d^2 n(x)}{dx^2} + \frac{J|_{active}(x,d)}{qt} = R_{Stim}(n) + R_{Spon}(n) + R_{NR}(n) \qquad (3.3.12)$$

where the terms on the right hand side of the equation represent the recombination of carriers due to stimulated, spontaneous and non-radiative processes.

In the above derivation of equation (3.3.12) the active layer electric field has been neglected. Whilst this greatly simplifies the equation because the electric field does not need to be calculated, it is not a valid assumption in the active layer of a semiconductor laser. However, it has been shown by Joyce [17] that this term can indeed be neglected if an effective value of the diffusion constant is used in place of the ambipolar diffusion coefficient.

Under conditions where the voltage drop in the substrate can be neglected, Joyce shows that the electric field in the active layer is such that, whilst holes are transported in the active layer under the effects of both drift and diffusion, the movement is identical to that of pure diffusion. For devices fabricated on n-type substrates, the effective diffusion coefficient lies near to the electron diffusion coefficient, whereas for p-substrates it is near to the value of the hole diffusion coefficient. It is thus possible to apply the simplified equation to account for both drift and diffusion of carriers for devices based on either n or p doped substrates, as long as the effective diffusion coefficient D_e replaces D_a.

At the edges of the active region, lateral heterojunctions are formed. The voltage across these lateral heterojunctions is insufficient to cause them to become conducting, and

thus equation (3.3.12) must be solved subject to the boundary conditions of zero lateral carrier flow, i.e. $dn/dx = 0\,|_{x=\pm A/2}$ where A is the active layer width. The solution of this equation in the presence of an optical field is considered in chapter 6.

Assuming complete ionisation of impurity atoms, and ignoring the effect of minority carriers, the hole concentration, $p(x)$, for an active layer with a p-type doping of p_a is given by

$$p(x) = n(x) + p_a \tag{3.3.13}$$

The electron and hole concentrations set the quasi-Fermi level separation, and from knowledge of these quasi-Fermi levels it is possible to calculate the active layer voltage distribution. The quasi-Fermi levels for electrons, F_c, and for holes, F_v, are determined by the expressions

$$F_{1/2}\left[\frac{F_c(x) - E_c(x)}{kT}\right] = \frac{n(x)}{N_c} \tag{3.3.14}$$

$$F_{1/2}\left[\frac{E_v(x) - F_v(x)}{kT}\right] = \frac{p(x)}{N_v} \tag{3.3.15}$$

where $F_{1/2}[\phi]$ is the Fermi integral, E_c and E_v are the energies of the conduction and valence band edges in the active region, and N_c and N_v the conduction and valence band density of states in the active layer. The solution of the Fermi integral is found using an approximate analytic expansion [19]. For electrons this is given by

$$F_c(x) - E_c(x) = kT\left\{\ln\left(\frac{n(x)}{N_c}\right) + K_1\left(\frac{n(x)}{N_c}\right) + K_2\left(\frac{n(x)}{N_c}\right)^2 + K_3\left(\frac{n(x)}{N_c}\right)^3 + \cdots\right\} \tag{3.3.16}$$

and for holes

$$E_v(x) - F_v(x) = kT\left\{\ln\left(\frac{p(x)}{N_v}\right) + K_1\left(\frac{p(x)}{N_v}\right) + K_2\left(\frac{p(x)}{N_v}\right)^2 + K_3\left(\frac{p(x)}{N_v}\right)^3 + \cdots\right\} \quad (3.3.17)$$

The values of the constants K_1, K_2, K_3 are given in table 1. The potential difference across the active region may thus be found from the electron and hole densities and the bandgap, E_g, of the material, as

$$V(x,d) = \frac{1}{q}[(F_c - E_c) + (E_v - F_v) + E_g] \quad (3.3.18)$$

3.4 Solution

The above system of equations describes the electrical model used in this thesis. This electrical model is used to obtain the current density injected into the active layer, which can then be used to determine the active layer carrier density distribution. The equations describing the boundary conditions at the hetero- and homo- junction interfaces are non-linear in nature. Due to the complexity of the series of equations a numerical solution technique is required, and it was decided to use the method of finite differences. This method is simpler to implement than the other commonly used solution technique, the finite element method, and it has been shown that for the similar case of the twin stripe laser [3] the method of solution (finite difference or finite element) has no effect on the results.

The upper cladding region and boundaries were discretised into a rectangular mesh, and finite difference forms of the equations were written describing the voltage at each node of the grid. Due to the left-right symmetry, only half the device, the left half, is modelled in the electrical solution, and equations are only given here for this half. A non-uniform mesh was used in the solution, such that the grid size was smaller near critical boundaries,

in order to improve the accuracy of the solution (see section 3.5). However, to derive the equations for such a mesh adds complexity without aiding understanding, and so the finite difference equations are derived here assuming a regular rectangular mesh.

3.4.1 Internal nodes

For an interior node in the cladding region, as shown in figure 3.3a, Laplace's equation (3.3.3) may be written in finite difference form, using the standard five node central difference expansion, as

$$\frac{V(p-1,q)+V(p+1,q)-2V(p,q)}{h_x^2} + \frac{V(p,q-1)+V(p,q+1)-2V(p,q)}{h_y^2} = 0 \qquad (3.4.1.1)$$

where $V(p,q)$ is the voltage at node (p,q) in the mesh, h_x is the mesh spacing in the x direction and h_y is the mesh spacing in the y direction. This equation has an error of the order h^2. The equation may be rearranged to give the voltage at the pq_{th} node in terms of the voltages at the surrounding nodes

$$V(p,q) = \frac{1}{2}\frac{h_x^2 h_y^2}{h_x^2+h_y^2}\left[\frac{V(p-1,q)+V(p+1,q)}{h_x^2} + \frac{V(p,q-1)+V(p,q+1)}{h_y^2}\right] \qquad (3.4.1.2)$$

3.4.2 Insulating boundaries

The voltage at nodes lying on the insulating boundaries must satisfy equation (3.3.4). The most general case is that of nodes located on the sloping mesa boundary, which is shown in figure 3.3b. Here, the boundary lies at an angle α to the horizontal. The boundary condition that must be satisfied is that the component of current perpendicular to the

interface must be zero. One means of imposing this boundary condition is to extend the mesh past the boundary to produce an imaginary set of nodes outside the region of interest. The boundary condition can then be considered to imply that the currents flowing normally into the boundary on either side are equal in magnitude, and the voltage at the node (p,q) can be written in terms of the internal and external nodes as

$$\frac{V(p-1,q)-V(p,q)}{h_x}\sin(\alpha)+\frac{V(p,q-1)-V(p,q)}{h_y}\cos(\alpha) \qquad (3.4.2.1)$$

$$=\frac{V(p+1,q)-V(p,q)}{h_x}\sin(\alpha)+\frac{V(p,q+1)-V(p,q)}{h_y}\cos(\alpha)$$

and thus

$$\frac{V(p-1,q)-V(p+1,q)}{h_x}\sin(\alpha)=\frac{V(p,q+1)-V(p,q-1)}{h_y}\cos(\alpha) \qquad (3.4.2.2)$$

For the mesa sidewalls, the angle is fixed by the crystallographic direction in which the laser is grown. This is because the mesa is most often formed from the double heterostructure wafer using a wet etchant which cuts along the crystal planes. Thus for a laser with the stripe oriented along the $(01\bar{1})$ plane, the mesa angle is 53° [8], whereas for a laser with the stripe parallel to the (011) plane, the mesa angle will be 40° [20]. The sensitivity of the solution to mesa angle is considered in Appendix 1, and it is shown that for possible mesa angles found in practice, the solution is fairly insensitive to angle, and thus an angle of 45° is chosen for all CM laser simulations presented in the body of this thesis. This choice of angle is made because it is close to both possible mesa angles, and it simplifies calculations (since $\sin(\alpha) = \cos(\alpha)$), thus enabling a more rapid solution of the voltage spreading problem. From (3.4.2.2) it can be seen that, for $\alpha = 45°$

$$V(p-1,q)+V(p,q-1)=V(p+1,q)+V(p,q+1) \qquad (3.4.2.3)$$

which is satisfied (c.f. Appendix 1) for

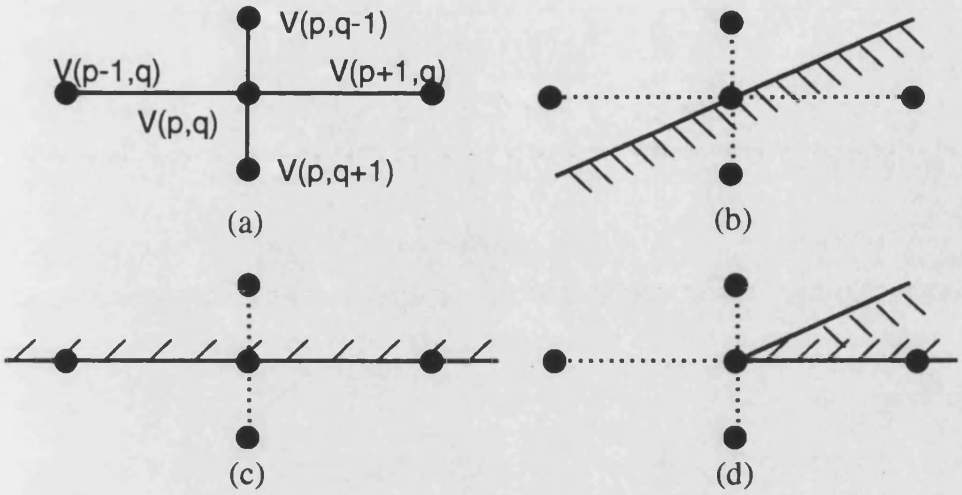

Figure 3.3 The node patterns. (a) An interior node, showing the numbering scheme (b) a node on the left hand sloping boundary (c) a node on the horizontal boundary (d) the bottom left hand corner node

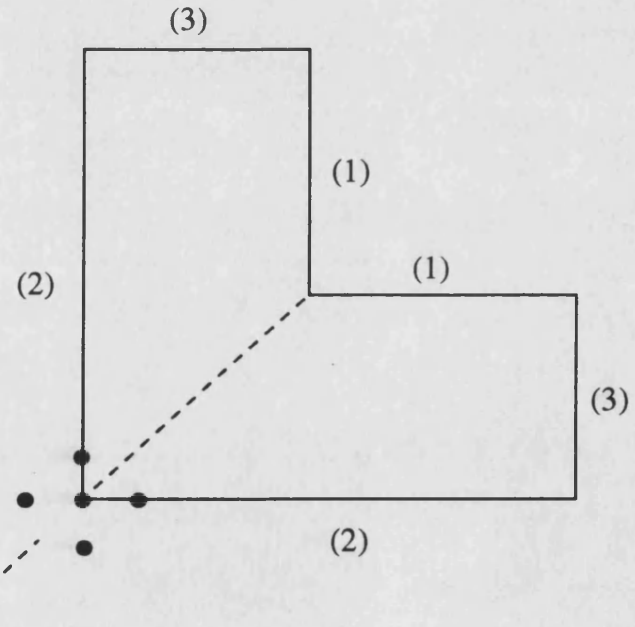

Figure 3.4 This L shaped region is symmetric about the dotted line and thus the voltage distribution would be unaltered by assuming that the dotted line is a current blocking boundary. This allows an easy visualisation of the equation for the bottom left hand corner node.

$$V(p,q+1) = V(p-1,q) \tag{3.4.2.4}$$

$$V(p+1,q) = V(p,q-1) \tag{3.4.2.5}$$

Thus the finite difference Laplace equation for a point lying on a left-sloping boundary may be written in terms of the internal nodes as

$$\frac{V(p,q+1)-2V(p,q)+V(p+1,q)}{h_x^2} \tag{3.4.2.6}$$

$$+\frac{V(p,q+1)-2V(p,q)+V(p+1,q)}{h_y^2} = 0$$

The voltage at the node *(p,q)* on the left-sloping boundary is therefore

$$V(p,q) = \frac{1}{2}\frac{h_x^2 h_y^2}{h_x^2+h_y^2}\left[\frac{V(p,q+1)+V(p+1,q)}{h_x^2}+\frac{V(p+1,q)+V(p,q+1)}{h_y^2}\right] \tag{3.4.2.7}$$

For a vertical sidewall ($\alpha = 90°$) or a horizontal sidewall ($\alpha = 0°$) the situation is somewhat simplified. For the case of a horizontal insulating boundary (which occurs at the mesa base outside the heterojunction/homojunction region) it can be seen that the boundary condition becomes

$$V(p,q+1) = V(p,q-1) \tag{3.4.2.8}$$

For the horizontal boundaries (figure 3.3c), the node at (p,q+1) lies outside the boundary, and thus Laplace's equation on this boundary may be written in terms of the inside nodes

$$\frac{V(p+1,q)-2V(p,q)+V(p-1,q)}{h_x^2}+\frac{2V(p,q-1)-2V(p,q)}{h_y^2} = 0 \tag{3.4.2.9}$$

The voltage at a node on the horizontal insulating boundaries can therefore be written as

$$V(p,q)=\frac{1}{2}\frac{h_x^2h_y^2}{h_x^2+h_y^2}\left[\frac{V(p+1,q)+V(p-1,q)}{h_x^2}+\frac{2V(p,q-1)}{h_y^2}\right] \qquad (3.4.2.10)$$

Similar equations exist for the top facing horizontal boundaries and vertical sidewalls found in the BRS laser.

The final type of boundary point on the insulating boundaries is the point at the bottom left mesa corner, shown in figure 3.3d. For the bottom corner it is initially difficult to see how an equation may be obtained, since only two of the five nodes are inside the region. Consider the L-shaped region shown in figure 3.4. The dotted boundary lies at 45° to the horizontal, the regions marked (1) and (2) have voltages V_1 and V_2 applied to them, and the regions marked (3) are subject to the boundary condition of zero current flow across them. Due to the symmetry of the region, there will be no current flow across the dotted boundary, so the region could be separated into two by an insulating boundary along this line without affecting the voltage distribution. For the corner node of the L-shaped region, the boundary condition is of zero current flow along the line given by the dotted arrow, and the boundary condition can thus be written

$$V(p-1,q)+V(p,q-1)=V(p+1,q)+V(p,q+1) \qquad (3.4.2.11)$$

Laplace's equation may then be written for this point as

$$\frac{V(p+1,q)-2V(p,q)+V(p,q-1)}{h_x^2} \qquad (3.4.2.12)$$

$$+\frac{V(p+1,q)-2V(p,q)+V(p,q-1)}{h_y^2}=0$$

Now, since the region can be split into two separate regions along the dotted line without altering the voltage distribution, and since therefore $V(p+1,q)=V(p,q-1)$, the equation for a left hand corner node of the separated region may be written

$$\frac{2V(p+1,q)-2V(p,q)}{h_x^2}+\frac{2V(p+1,q)-2V(p,q)}{h_y^2}=0 \qquad (3.4.2.13)$$

This situation is analogous to that of the CM laser bottom left hand corner node, and the voltage may thus be calculated as

$$V(p,q)=\frac{1}{2}\frac{h_x^2h_y^2}{h_x^2+h_y^2}\left[\frac{2V(p+1,q)}{h_x^2}+\frac{2V(p+1,q)}{h_y^2}\right] \qquad (3.4.2.14)$$

3.4.3 The homojunction boundary

The nodes which lie on the heterojunction and homojunction boundaries are subject to non-linear boundary conditions on the current flow, which is determined from the voltage distribution by equation (3.3.1). At the homojunction interface, the current injected into the homojunction is obtained from equation (3.3.5) as

$$J(x,d)\,|_{homojunction}=J_{sat}\left[\exp\left(\frac{qV(x,d)}{\eta kT}\right)-1\right] \qquad (3.4.3.1)$$

If an imaginary node is added, as before, then the current boundary condition may be written

$$-\sigma\frac{dV}{dy}=-\sigma\left(\frac{V(p,q-1)-V(p,q+1)}{2h_y}\right)=J_{sat}\left[\exp\left(\frac{qV(p,q)}{\eta kT}\right)-1\right] \qquad (3.4.3.2)$$

Thus, Laplace's equation may be written for a node on the homojunction boundary as

$$\left(\frac{V(p-1,q)-2V(p,q)+V(p+1,q)}{h_x^2}\right)+\left(\frac{2V(p,q-1)-2V(p,q)}{h_y^2}\right) \qquad (3.4.3.3)$$

$$-\frac{2J_{sat}}{\sigma h_y}\left[\exp\left(\frac{qV(p,q)}{\eta kT}\right)-1\right]=0$$

or

$$2V(p,q)\left(\frac{1}{h_y^2}+\frac{1}{h_x^2}\right)+\frac{2J_{sat}}{\sigma h_y}\left[\exp\left(\frac{qV(p,q)}{\eta kT}\right)-1\right]= \qquad (3.4.3.4)$$

$$\frac{V(p-1,q)+V(p+1,q)}{h_x^2}+\frac{2V(p,q-1)}{h_y^2}$$

3.4.4 The heterojunction boundary

At the heterojunction boundary the current density injected into the active region becomes a source term in the carrier diffusion equation (3.3.12). If the optical field distribution is known, this equation can be solved, and the solution technique for this equation will be presented in chapter 6. This chapter, however, is concerned with the non self-consistent electrical model. Consequently, it is assumed that a good estimate of the carrier distribution is available, either as an initial guess, or from a previous iteration of the self-consistent model.

The problem at the heterojunction boundary is therefore reduced to simply obtaining the active layer voltage distribution from the carrier distribution. This is achieved by use of the analytic expression of equation (3.3.18), applying the results of equations (3.3.13-17), at every point on the heterojunction boundary.

3.4.5 Solution technique

The system of finite difference equations presented in sections 3.4.1 to 3.4.4 will define the voltage distribution in the passive upper cladding region for a given active layer carrier distribution and applied voltage. The electrical solution is, in effect, the solution of Laplace's equation over a region, subject to non-linear boundary conditions at the edges of that region. During the solution of Laplace's equation, the carrier density distribution is not re-calculated. The first step in the solution is to assume an active layer carrier density distribution, or, in the overall model, to use the carrier distribution from the previous iteration, and calculate the active layer voltage that this implies using the methods of section 3.4.4.

Once the voltage distribution across the active layer has been obtained, all the boundary conditions at the edges of the cladding region are specified, and it is therefore possible to solve Laplace's equation. Because of the non-linear boundary conditions, the overall system of equations is non-linear. For nodes not lying on the heterojunction/homojunction boundary the chosen method of solution is the method of Successive Over-Relaxation (SOR).

This is an iterative technique, which means that computer storage requirements are minimised, at the expense of speed of solution. The method can, however, still provide a rapid solution provided a good initial estimate of the voltage distribution is available. In the overall self-consistent model, this is often the case, since the voltage distribution from the previous iteration of the model can be used as an initial estimate for the present SOR solution. According to the SOR technique, a better estimate of the value of the voltage at any node on the mesh at the $(k+1)^{th}$ iteration, $V^{k+1}(p,q)$, can be obtained from its previous value on the k^{th} iteration, $V^{k}(p,q)$, as

$$V^{k+1}(p,q)=V^{k}(p,q)-\Omega\{V^{k}(p,q)-\left[\frac{1}{2}\frac{h_x^2h_y^2}{h_x^2+h_y^2}\right] \tag{3.4.5.1}$$

$$\left[\frac{V^{k}(p+1,q)+V^{k}(p-1,q)}{h_x^2}+\frac{V^{k}(p,q+1)+V^{k}(p,q-1)}{h_y^2}\right]\}$$

where the constant Ω is called the over-relaxation parameter which takes a value in the range 1 to 2 which gives the fastest solution. The equation is modified according to the principles outlined in section 3.4.2 for nodes lying on the insulating boundaries. Ω is chosen manually, by carrying out a number of trial computer runs.

For nodes lying on the passive/homojunction boundary the Newton-Raphson method is used to handle the non-linear boundary condition. This method states that if $f(V)$ is a function of V, and $f'(V)$ is its derivative with respect to V, then a better estimate of the roots of the equation $f(V) = 0$ can be obtained from the previous value at the kth iteration, V^k, as

$$V^{k+1}=V^{k}-\frac{f(V^{k})}{f'(V^{k})} \tag{3.4.5.2}$$

in this case

$$f(V(p,q))=2V(p,q)\left(\frac{1}{h_y^2}+\frac{1}{h_x^2}\right)+\frac{2J_{sat}}{\sigma h_y}\left[\exp\left(\frac{qV(p,q)}{\eta kT}\right)-1\right] \tag{3.4.5.3}$$

$$-\frac{V(p-1,q)+V(p+1,q)}{h_x^2}-\frac{2V(p,q-1)}{h_y^2}$$

and

$$f'(V(p,q))=2\left(\frac{1}{h_y^2}+\frac{1}{h_x^2}\right)+\frac{2J_{sat}}{\sigma h_y}\left[\exp\left(\frac{qV(p,q)}{\eta kT}\right)-1\right] \tag{3.4.5.4}$$

Since the method is iterative, the solution is required to converge to within a pre-defined tolerance. The convergence criterion is

$$\sum_{p,q} | V^{k+1}(p,q) - V^{k}(p,q) | \leq Tol \qquad (3.4.5.5)$$

i.e. the sum of the absolute values of the difference of the previous and current iterations at all nodes is less than a tolerance. The value of the tolerance parameter is chosen, along with the grid size, to provide a rapid and sufficiently accurate solution. Convergence was not found to be a problem, provided that the value of Ω was chosen carefully. The optimum value of Ω depends on the geometry of the structure and the number of nodes used, but for good convergence with the structures studied, the value lay in the range of 1.8 to 1.95. Within this range, a solution could always be obtained for the structures studied, but by optimization of the value (by trial and error) the speed of solution could be increased by almost an order of magnitude.

3.5 Tolerance and mesh size calculations

The equations presented in the section 3.4 have been derived, for simplicity, assuming a constant mesh spacing in the vertical and horizontal directions. However, to use such a grid in practice would require an extremely large number of mesh points. This is because the error in the solution of a five point finite difference expansion is related to the square of the mesh size, and the fourth derivative of the function (in this case the voltage distribution). Near to discontinuities, the fourth derivative can become large, and thus the error increases. The boundary conditions for the Laplace equation solution contain several discontinuities, and the mesh size near these should be made small. Although a uniform mesh could be used to meet these requirements, this would require an excessive

number of mesh points where the solution was not changing rapidly. It was therefore necessary to use a non-uniform mesh, the design of the mesh depending on the specific situation.

Mesh design was manual, the criteria for accepting a certain mesh being that the calculated input and output current were within a specified tolerance (taken to be less than 1%) and that when the mesh size was doubled the calculated input current and homojunction and heterojunction output currents changed by less than the tolerance. This generally required approximately 40 mesh points in the horizontal direction and 20 mesh points in the vertical direction for a laser 2μm deep and 6μm wide (only half of the width is modelled).

The tolerance value for the convergence of the Laplace equation solution was chosen by taking a value and reducing it successively until the input and output currents changed by less than 1%. The problem of mesh design and tolerance are linked, so it is not possible to specify the exact value of the tolerance to meet the above criterion, but it was generally of the order of 10^{-4}.

3.6 Investigation of leakage current

The results presented in this section are for a laser with nominal parameters given in table 1. Results are presented for both the BRS and, where applicable, the CM laser. With the CM laser, the mesa angle is fixed by the crystal structure of the InP, and therefore the device depth and width are not independent. Also, since contact is made to the whole of the top of the mesa, it is not possible to vary the contact width without varying the device width. In those cases where a parameter cannot be varied independently comparison of results is of little value, and so results are not presented for the CM laser for varying the contact width, device width and depth.

One of the aspects of the BRS and CM lasers of interest is the leakage of current around the active layer. However, unless the current leakage is very high indeed (rendering the laser useless in a practical sense) then no appreciable leakage occurs until the laser is above threshold. The electrical model as presented in the above sections is only valid above threshold when the stimulated recombination term in the carrier diffusion equation is known, and this may only be found satisfactorily by a self-consistent model. Therefore, in order to model the above threshold electrical characteristics using the non self-consistent electrical model, it is necessary to make some assumptions about the laser behaviour.

It is well known that the active layer carrier density above threshold is clamped to near its threshold value due to the lasing action. If the threshold current of the device were known, then it would be possible to calculate the carrier density in the active layer from the carrier diffusion equation (3.3.12), assuming that at threshold the stimulated recombination could be neglected. However, with a purely electrical model there is no way of predicting device threshold.

For the rest of this chapter it has therefore been necessary to make what in the past has been a common assumption in leakage current calculations [6-9], that the carrier density is pinned at its threshold value, and that the carrier density is uniform throughout the active layer. This then allows above threshold leakage current calculations, using the model as presented in section 3.4. The nominal value of threshold carrier density is taken as $2x10^{18}cm^{-3}$, which corresponds closely with values calculated from experimental results, and has been used in other leakage current calculations [6].

3.6.1 Current distribution

Figures 3.5 and 3.6 show the variation of the injected current density across the active/homojunction plane of the nominal BRS and CM lasers for increasing levels of drive current. The figures show that the majority of current flows through the active region, with the (leakage) current density at the homojunction regions several orders of magnitude less than that in the active region. It is also clear from the figures that there are many similarities in the pattern of current density between the BRS and CM lasers.

The main features of the two graphs are a high current density across the active region, increasing towards the edge of the region. The current density then falls dramatically as the homojunction region is encountered, but increases along the width of the homojunction region. The increase in current density at the edge of the active region is less significant in the CM laser. It can also be seen that as the injected current is increased, the current density through the homojunction regions increases at a greater rate than the current density through the active layer.

For all values of injected current the leakage current is slightly lower in proportion to the active layer current in the CM laser compared to the BRS device. The differences in current distribution between the two lasers are entirely attributable to the difference in cladding layer geometry, all other aspects of the model are identical. This lower leakage current is seen to varying degrees in all the comparisons between BRS and CM lasers in this section, and it therefore seems that the trapezoidal shape of the CM cladding layer helps to focus the current into the active region.

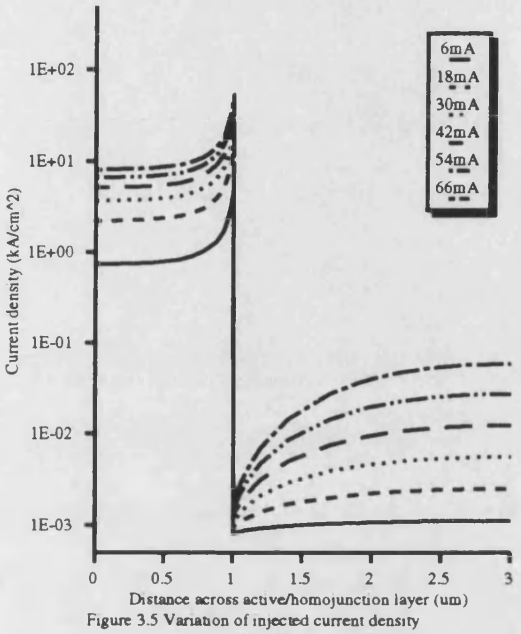

Figure 3.5 Variation of injected current density across the active/homojunction layer (BRS laser)

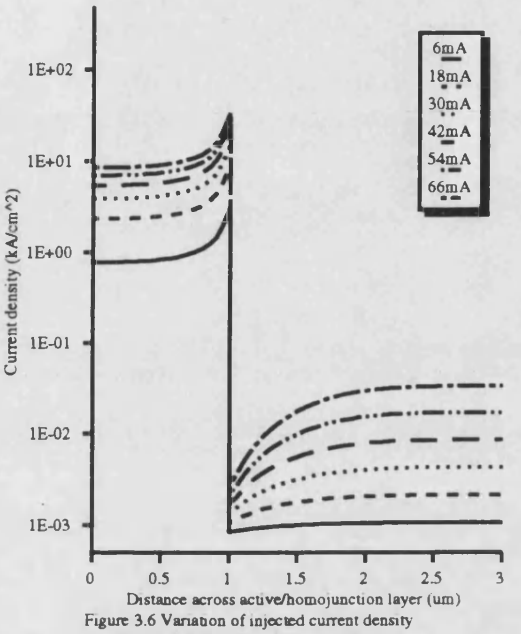

Figure 3.6 Variation of injected current density across the active/homojunction layer (CM laser)

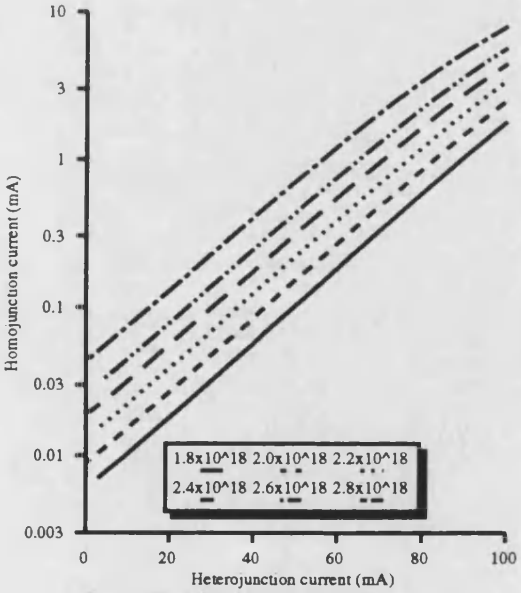

Figure 3.7 Homojunction leakage current versus heterojunction current with active layer carrier density as a parameter (BRS laser)

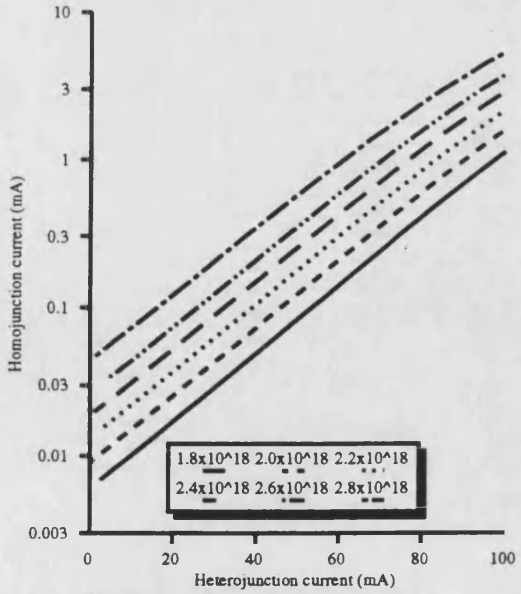

Figure 3.8 Homojunction leakage current versus heterojunction current with active layer carrier density as a parameter (CM laser)

3.6.2 The effect of carrier density

There is some uncertainty in the experimentally obtained values for the active layer carrier density, and changes in device geometry will effect the value of the carrier density at which lasing might be expected to take place. It is therefore necessary to examine the effect on the electrical model of changes in carrier density. Experimental studies have shown that it is reasonable to expect the carrier density to vary between 1.8 and 2.8×10^{18}, and the effect of this variation is shown for the BRS laser in figure 3.7 and for the CM laser in figure 3.8.

The figures show that the leakage current increases almost exponentially with hetero-junction current, although at higher levels of heterojunction current the relationship, which is shown in the figure on a logarithmic scale, becomes slightly sub-linear due to the effects of current spreading in the devices. It can be seen that although the carrier density has an effect on the leakage current, increasing the carrier density merely scales the leakage current by a fixed factor, i.e. the leakage increases as e^k, where k is a constant. However, at high values of carrier density and heterojunction current the relationship is slightly less clear, and the sub-linearity of the curves is increased.

Whereas it can be seen that the actual value of the leakage current is altered by the active layer carrier density, the trend remains the same for all of the values of carrier density studied. This may be expected, since the active layer voltage distribution changes only by a small amount with the expected values of carrier density variation.

The figures show that, even at a heterojunction current of 100mA, the leakage current is only a few percent of the total. It can also be seen that, at low values of heterojunction current, the results for the CM and BRS lasers are almost identical. However, at higher

heterojunction currents the leakage current is slightly lower in CM lasers, as was noted in the above section. This effect is a direct result of the different cladding layer geometries between the two devices.

3.6.3 The effect of contact stripe width

The effect on the leakage current in BRS lasers of altering the contact stripe width is shown in figure 3.9. The results are presented in two forms. Figure 3.9(a) shows the homojunction current, which in this model is considered to be the only contribution to the total leakage current, plotted against the heterojunction current (which is that proportion of the total current which contributes to light production). Figure 3.9(b) shows the rate of change in total drive current with drive voltage plotted against drive current, the I-dV/dI characteristic.

This graph is particularly useful since it can be obtained directly from experimental I-V characteristics. A change in slope in the I-dV/dI characteristic signifies a change in device resistance. The devices studied in this thesis incorporate forward biased homojunction regions, and a simple explanation for changes in device resistance may be found by considering the effects of these regions. Whilst the homojunction regions are not conducting there is only a single current path available, and any change in device resistance, which will be very slight, must be caused by alterations in the pattern of current spreading. The "turn on" of the homojunction regions provides a second, parallel current path through which the current may flow, by-passing the active region, and thus causing a change in the overall device resistance. Therefore a change in slope of the I-dV/dI characteristic may be taken as an indicator of the turn-on of the homojunction regions.

It can be seen from figure 3.9(a) that a narrower contact stripe width leads to a lower leakage current, although the effect is small. This effect can also be seen in figure 3.9(b).

At a stripe width of 1.0μm a slight change in slope of the characteristic can be detected at around 80mA, and this change in slope occurs at lower drive currents for wider contact widths. This indicates, as does figure 3.9(a), that the homojunction region is "turned on" at lower and lower drive currents as the contact width is increased.

The effect can be understood by considering the current spreading in the device. If the contact is narrower than the actual active layer width, then current is injected into the device directly above the active layer. For current to flow through the homojunction region, it must first spread out into the cladding layer. On the other hand, a contact wider than the active region will inject current above the homojunction region as well as the active region. It is therefore to be expected that the greater the stripe width, the greater the leakage current.

3.6.4 The effect of device geometry

The basic device geometry can be altered in several ways. In this section, the effects on the leakage current of changing device width and depth, and active region and regrown region widths are investigated. Figure 3.10(a) shows that the effect on the leakage current of altering the device width is strong, as would be expected. Figure 3.10(b) shows that, for devices of width greater than about 4μm, the point at which the homojunction regions become turned on does not alter significantly. The increased homojunction leakage current seen in figure 3.10(a) is therefore mainly due to the increased homojunction width in the wider devices.

Again, the exponential relationship between heterojunction and homojunction current seen in figure 3.10(a) appears to break down at high injection currents. The effect is

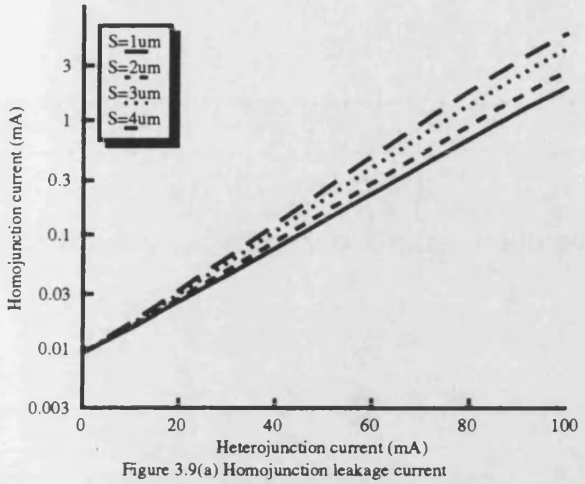

Figure 3.9(a) Homojunction leakage current versus heterojunction current with stripe width as a parameter (BRS laser)

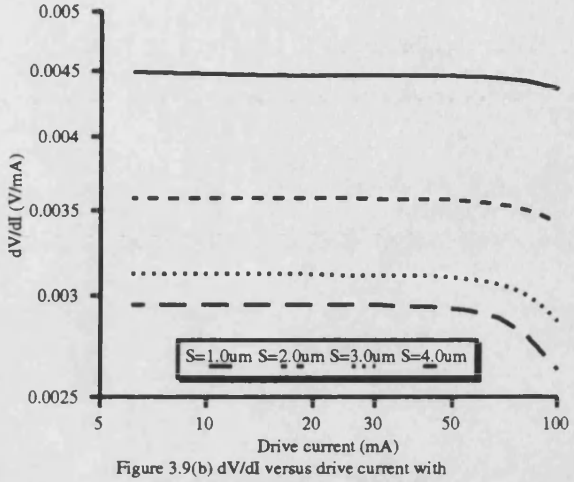

Figure 3.9(b) dV/dI versus drive current with stripe width as a parameter (BRS laser)

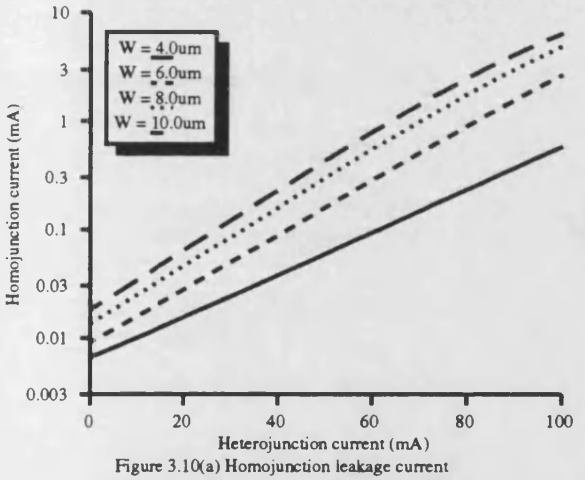

Figure 3.10(a) Homojunction leakage current versus heterojunction current with device width as a parameter (BRS laser)

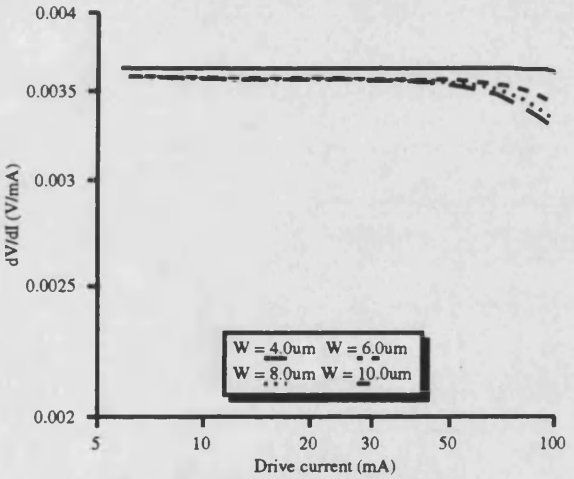

Figure 3.10(b) dV/dI versus drive current with device width as a parameter (BRS laser)

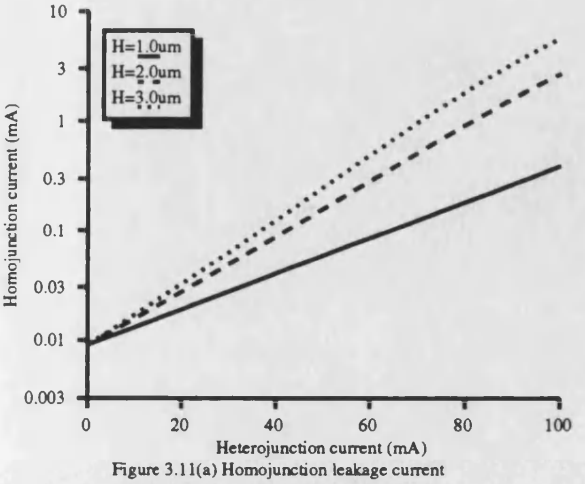

Figure 3.11(a) Homojunction leakage current versus heterojunction current with cladding layer depth as a parameter (BRS laser)

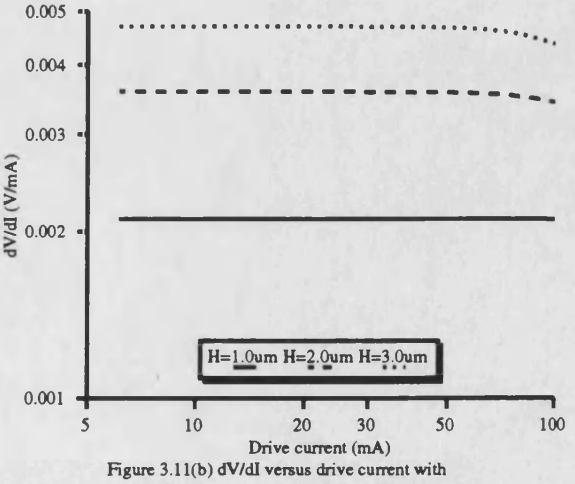

Figure 3.11(b) dV/dI versus drive current with cladding layer depth as a parameter (BRS laser)

most obvious at device widths greater than 8μm. It is to be expected that this proportional relationship would break down at greater device widths, due to the effects of current spreading in the device.

The effect of varying the device depth (i.e. the depth of the upper cladding layer) is shown in figure 3.11, which shows that the shallower the device, the lower the leakage current. This may again be explained in terms of the current spreading in the cladding region. In a shallower device there is less current spreading to the homojunction regions, and consequently less homojunction current.

The I-dV/dI characteristics of figure 3.11(b) show a lower initial value (indicating a lower device resistance) for shallow devices. The characteristics also show that, as the depth is decreased, the drive current at which the homojunction regions become turned on is increased, and by using a very shallow cladding layer the homojunctions do not become turned on even for heterojunction currents of 100mA. There is, however, a practical lower limit to the device depth of around 1μm which is set by the vertical optical field distribution in the laser.

The range of variation of the active region width is also set by the laser operating requirements. It is generally desirable to confine the laser to a single lateral mode, with the widest possible active region. Widths of 1 to 2 μm are routinely used. The effect on the homojunction current of altering the active region width is very strong, as can be seen in figures 3.12 for the BRS laser and 3.13 for the CM device. By decreasing the active region width whilst maintaining the same device width, the effective homojunction region width is increased, and the position of the homojunction relative to the stripe contact is also changed. Decreasing the active region width therefore has a similar effect to simultaneously increasing the contact stripe and homojunction region widths.

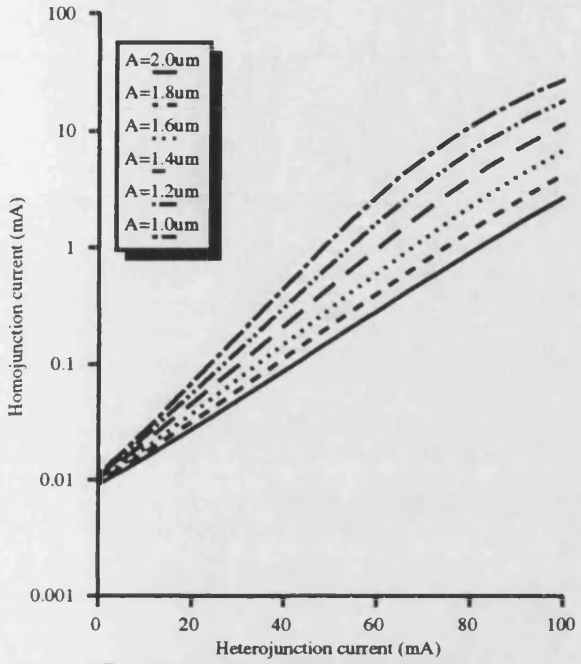

Figure 3.12(a) Homojunction leakage current versus heterojunction current with active width as a parameter (BRS laser)

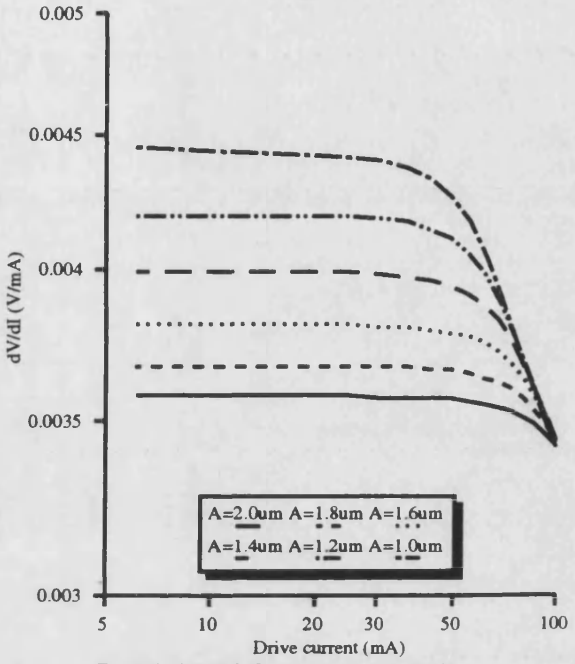

Figure 3.12(b) dV/dI versus drive current with active layer width as a parameter (BRS laser)

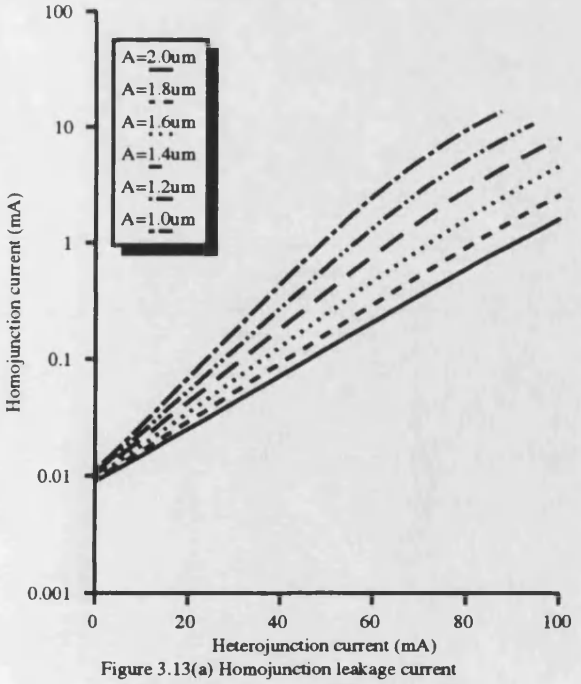

Figure 3.13(a) Homojunction leakage current versus heterojunction current with stripe width as a parameter (CM laser)

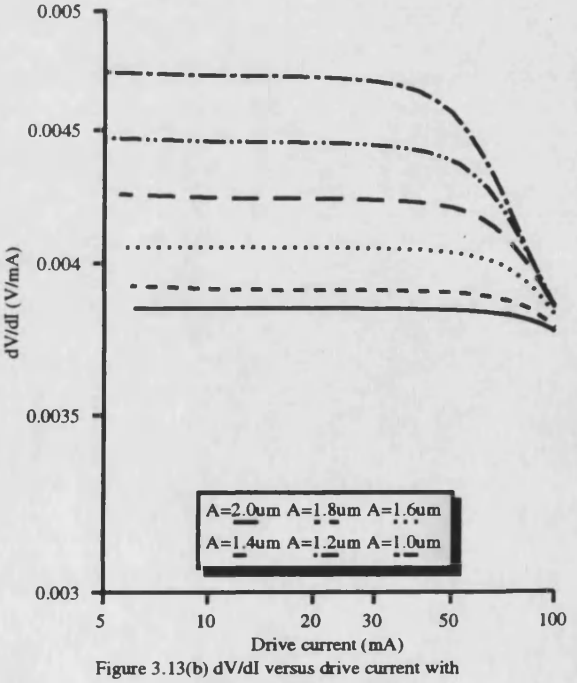

Figure 3.13(b) dV/dI versus drive current with active layer width as a parameter (CM laser)

It can be seen from the figures that a wide active region width is desirable from an electrical viewpoint, although this will be shown in chapter 6 to have a serious effect on the optical characteristics. Due to the current spreading, the homojunction regions become turned on at lower drive currents for narrower active widths, as shown in figures 3.12(b) and 3.13(b). Also, as seen previously, the exponential relationship between leakage and heterojunction current breaks down at high current injection for narrow device widths, indicating the effects of current spreading in the cladding region.

In the CM laser the active layer is etched away to the desired width using a selective wet chemical etch, and then buried in InP material that is regrown by mass transport or vapour phase epitaxy. The growth process for these lasers is described in detail in chapter 7. The width of the regrown homojunction region may be controlled by altering the length of the growth period. Although it is not possible to do this with the standard BRS laser shown in figure 3.1(b), lasers fabricated using the same techniques as for the CM devices, but having rectangular upper cladding layers have been produced. With these devices, which will be termed BRS lasers here due to their rectangular cladding layer cross section, it is also possible to vary the regrown width.

The effects of altering the width of the regrown region of the BRS and CM lasers are shown in figures 3.14 and 3.15. As might be expected, decreasing the width of the regrown region has the desirable effect of decreasing the leakage current. This is due to the fact that there is less area over which current leakage can take place, and therefore less leakage current may flow. It would appear that reducing the regrown region width to zero would eliminate the leakage current entirely. However, there is a lower limit placed on the width of the regrown region of around 0.5μm by two considerations. First, and most importantly, the InP is regrown to protect the active layer, and too thin a regrown

region can cause premature device failure [21]. Secondly, if the regrown region is too thin then this has an effect on the optical properties of the waveguide formed by the active region, as will be demonstrated in chapter 5.

3.6.5 The effect of doping density

The effect of altering the cladding layer doping density is demonstrated in figures 3.16 and 3.17. These show that there is a very large (three orders of magnitude) change in leakage current for an increase in doping level from $6x10^{17}$ to $2x10^{18}$. It can also be seen, from figures 3.16(b) and 3.17(b), that the homojunction regions do not become turned on within the range of current shown for doping densities greater than 10^{18}.

The cladding layer doping density has two effects on the parameters in the model. The first of these is to alter the conductivity of the region, the greater the doping density the greater the conductivity, and this alters the pattern of current spreading in the cladding region. The second effect is on the saturation current of the homojunction region, J_{sat}. This decreases with increasing doping density, thus decreasing the current flowing though the homojunction regions.

3.7 Discussion

It has be seen that both the CM and BRS lasers have very similar characteristics, as is to be expected due to their similar construction. However, the leakage current predicted by the non-self consistent electrical model is higher in the case of the BRS laser, indicating that the sloping mesa sidewalls of the CM device have a beneficial effect on the voltage and current distribution in the laser.

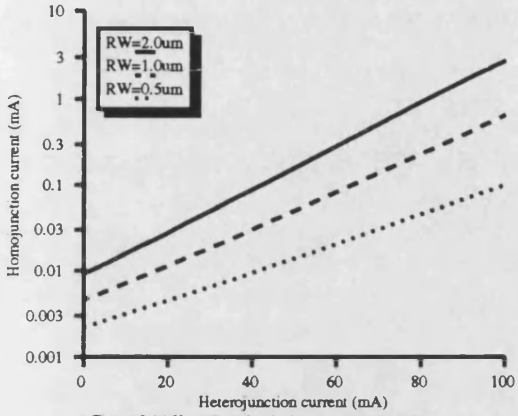

Figure 3.14 Homojunction leakage current versus heterojunction current with regrown width as a parameter (BRS laser)

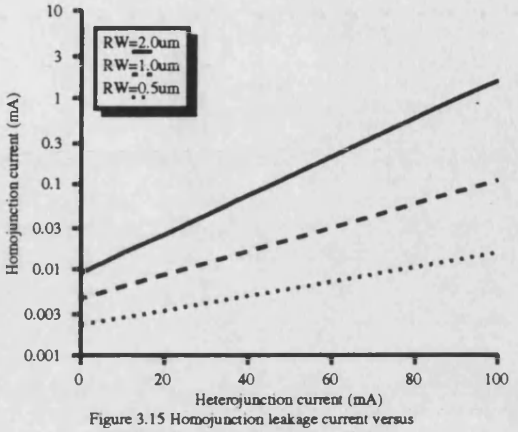

Figure 3.15 Homojunction leakage current versus heterojunction current with regrown width as a parameter (CM laser)

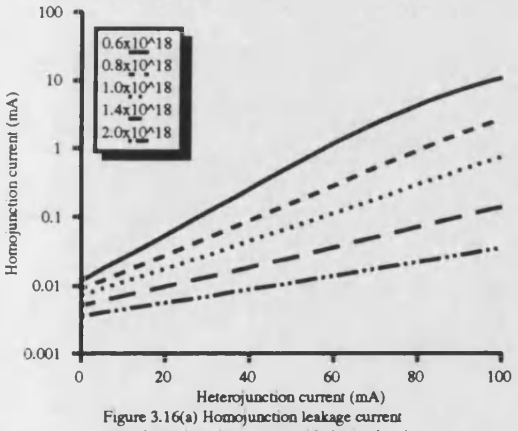

Figure 3.16(a) Homojunction leakage current versus heterojunction current with doping level po as a parameter (BRS laser)

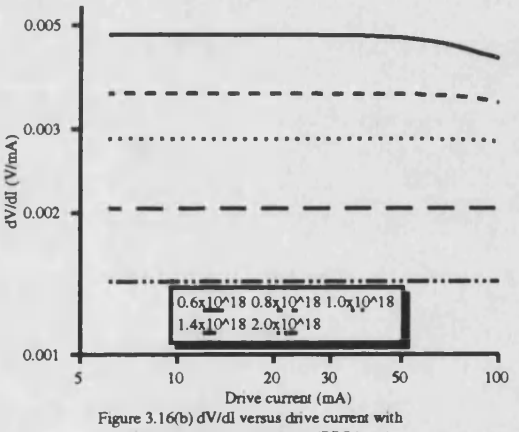

Figure 3.16(b) dV/dI versus drive current with doping level po as a parameter (BRS laser)

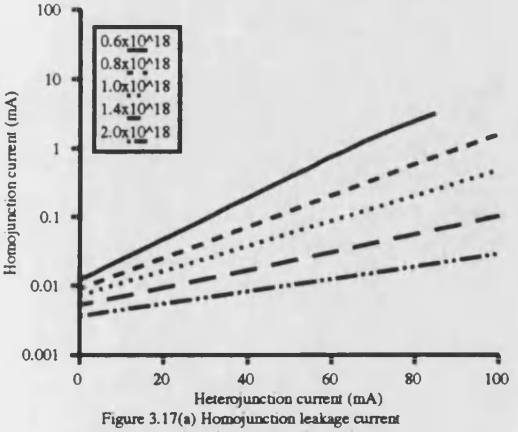

Figure 3.17(a) Homojunction leakage current versus heterojunction current with doping level po as a parameter (CM laser)

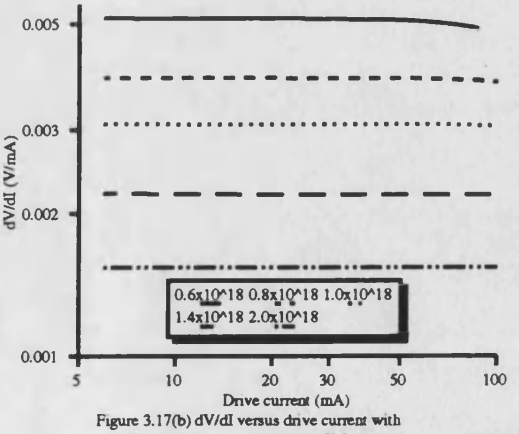

Figure 3.17(b) dV/dI versus drive current with doping level po as a parameter (CM laser)

The parameters that have the greatest effect on the leakage current are the doping level and the regrown and active region widths, followed by the device width and depth. The contract stripe width has little effect. It would therefore benefit the device manufacturer to fabricate devices with wide active layers, narrow regrown layers and high cladding layer doping densities, and to make narrow and shallow devices. This has been noted by other authors, and the historical trend has been to fabricate smaller and higher doped devices, following on from experimental and theoretical studies [8,9].

The electrical model presented in this chapter is the first step in the overall self-consistent model. From the current distribution in the laser it is possible to calculate the active layer carrier density, and therefore to obtain the waveguiding properties of the device. Finally, it is worth noting the close comparison between the results presented here and those obtained by Amman and Thulke [9] who have also studied the effects of leakage currents in the BRS laser.

The results presented in this chapter have assumed that in buried heterostructure lasers above threshold, the carrier density in the active layer is clamped at its threshold value, and it has been assumed that this value is uniform across the active layer. This assumption has been common in modelling the electrical characteristics of buried heterostructure lasers, however it will be shown in chapter 6 that this is not the case, and the carrier profile is affected by spatial hole burning and the high current injection at the active layer edges. The results have also assumed one value of carrier density, however it was shown that the actual value of carrier density, which will alter with device geometry, has a scaling effect on the leakage current. The results presented in this section are therefore only useful in predicting general trends, and a self-consistent approach will be required to obtain actual values.

	Parameter	Value	Units
Electrical model constants	μ_p	300	$cm^2V^{-1}s^{-1}$
	η	1.0	
	J_{sat}	$20/p_o$	$mAcm^{-3}$
	K_1	$3.53553x10^{-1}$	
	K_2	$4.95009x10^{-3}$	
	K_3	$1.48386x10^{-4}$	
Dimensions (see figure 3.2)	W	6.0	µm
	C	2.0	µm
	A	2.0	µm
	R	2.0	µm
	d	2.0	µm
	t	0.15	µm
	Length	300	µm
	α (BRS)	90°	
	α (CM)	45°	

Table 1. Parameters used in the electrical model

REFERENCES

[1] J.E.A.Whiteaway, "Theoretical analysis of current spreading in stripe-geometry injection lasers," IEE proc.I, vol 129, no. 3, pp.89-95, 1982

[2] G.Lengyel, P.Meissner, E.Patzak and K.-H.Zschauer, "An analytic solution of the lateral current spreading and diffusion problem in narrow oxide stripe (GaAl)As/GaAs DH lasers," IEE J.Quantum.Electron., vol QE-18, no. 4, pp.618-625, 1982

[3] T.Kumar, R.F.Ormondroyd, and T.E.Rozzi, "Interstripe coupling and current spreading in a subthreshold double heterostructure twin-stripe laser," IEEE J.Quantum Electron., vol. QE-20, no. 4, pp.364-373, 1984

[4] M.-C.Amann, B.Stegmuller, "Threshold current analysis of InGaAsP-InP ridge-waveguide lasers," IEE proc.J, no. 6, pp 341-348, 1986

[5] E.Baralis, A.Bianco, G.P.Bava, I.Montrosset, "Simplified hybrid optical model for RWL threshold current optimisitation," IEE proc.J, vol 134, no. 1, pp.16-21, 1987

[6] Z.L.Liau, J.N.Walpole, D.Z.Tsang and V.Diadiuk, "Characterisation of mass transported p-substrate GaInAsP/InP buried heterostructure lasers with analytical solutions for electrical and thermal resistances," IEEE J.Quantum Electron., vol. QE-24, no. 1, pp.36-42, 1988

[7] Z.L.Liau, and J.N.Walpole, "Prevention of current leakage in mass transported GaInAsP/InP buried heterostructure lasers with narrow transported regions," IEEE J.Quantum Electron., vol. QE-23, no. 3, pp.313-319, 1987

[8] Z.L.Liau, J.N.Walpole, and D.Z.Tsang, "Fabrication, characterisation, and analysis of mass-transported GaInAsP/InP buried heterostructure lasers," IEEE J.Quantum Electron., vol. QE-20, no. 8, pp.855-865, 1984

[9] M.C.Amann, and W.Thulke, "Current confinement and leakage currents in planar buried-ridge-structure laser diodes on n-substrate," IEEE J.Quantum Electron., vol. QE-25, no. 7, pp.1595-1602, 1989

[10] D.P.Wilt and A.Yariv "A self-consistent static model of the double- heterostructure laser," IEEE J.Quantum.Electron., vol 17, no. 9, pp.1941-1949, 1981

[11] K.B.Kahen, "Two-dimensional simulation of laser diodes in the steady state," IEEE J.Quantum.Electron., vol 24, no. 4, pp.641-651, 1988

[12] M.Ueno, S.Asada, and S.Kumashiro, "Two-dimensional numerical analysis of lasing characteristics for self-aligned structure semiconductor lasers", IEEE. J.Quantum Electron., vol. 26, no. 6, pp.972-981, 1990

[13] T.Kumar, R.F.Ormondroyd, and T.E.Rozzi, "A self-consistent model of the lateral behaviour of a twin-stripe injection laser," IEEE J.Quantum Electron., vol. QE-22, no. 10, pp.1975-1985, 1986

[14] M.S.Mock, "Analysis of mathematical models of semiconductor devices," Boole Press, Dublin, 1983

[15] T.L.Koch, L.A.Coldren, et al, "Low-threshold high speed 1.55μm vapour phase transported buried heterostructure lasers (VPTBH)," Elect.Lett., vol. 20, pp.856-857, 1984

[16] T.R.Chen, L.C.Chiu, A.Hasson, K.L.Yu, U.Koren, S.Margalit and A.Yariv, "Study and application of the mass transport phenomena in InP," J.Appl.Phys., vol. 54, no. 5, pp.2407-2412, 1983

[17] W.B.Joyce, "Carrier transport in double heterostructure active layers," J.Appl.Phys., vol. 53, no. 11, pp.7235-7239, 1982

[18] S.M.Sze, "Physics of semiconductor devices," 2nd edition, John Wiley and Sons, New York

[19] W.B.Joyce and R.W.Dixon, "Analytic approximations for the Fermi energy of an ideal Fermi gas," Appl.Phys.Lett., vol. 31, no. 5, pp.354-356, 1977

[20] L.A.Coldren, K. Furuya, B.I.Miller, "On the formation of planar-etched facets in GaInAsP/InP heterostructures," J.Electrochem.Soc., vol. 130, no. 9, pp.1919-1926, 1983

[21] H.Jung, E.G.Burkhardt, W.Pfister, "Reduction of degradation in vapor phase transported InP/InGaAsP mushroom stripe lasers," Appl.Phys.Lett., vol. 53, no. 14, pp.1230-1232, 1988

CHAPTER 4: OPTICAL WAVEGUIDES

4.1 Introduction

In order to be able to model the physical operation of the semiconductor laser, an understanding of the propagation of light constrained by a dielectric waveguide is required. The subject of waveguiding and propagation of light has been extensively studied, and is covered in several books [e.g. 1-7]. This chapter will only focus on the basics of propagation and waveguiding for one dimensional dielectric waveguides. The next chapter deals with the more realistic case of two dimensional guides, and explains the method used in the self-consistent model to solve for the guided modes of such a waveguide.

All lasers incorporate some form of waveguiding. With semiconductor lasers this is due to a change in the dielectric permittivity of the semiconductor material forming the device. For the double heterojunction structure, as discussed in chapter 2, the waveguide in the transverse direction is provided by the different dielectric constants of the materials forming the heterojunction. In the lateral direction light is guided either by a change in the imaginary part of the dielectric constant (gain guiding), or by a change in the real dielectric constant (index guiding) provided by a change of material in the lateral direction, or by a combination of both processes.

This chapter explains some of the basic optical theory that has been used in the analysis of the lasers considered in this thesis. It begins by deriving some fundamental relationships from Maxwell's equations. The wave equation is derived and solutions obtained for lossless and conducting media, showing how the propagation constant and gain/loss of the material are linked. The characteristic solutions of a one dimensional three-layer

slab waveguide are obtained and the modal cut-off conditions discussed. The differences between TE and TM modes are presented, and finally the power flow and confinement factor are examined.

4.2 Maxwell's equations

Light is part of the electromagnetic spectrum, and as such the distribution of an optical field is described by Maxwell's equations, which set out the relationships governing electric and magnetic fields. These equations are given below, where the bar symbol is used to denote a vector

$$\nabla \times \overline{E} = -\frac{\partial \overline{B}}{\partial t} \tag{4.2.1}$$

$$\nabla . \overline{D} = \rho \tag{4.2.2}$$

$$\nabla \times \overline{H} = \frac{\partial \overline{D}}{\partial t} + \overline{J} \tag{4.2.3}$$

$$\nabla . \overline{B} = 0 \tag{4.2.4}$$

The ancillary equations are written

$$\overline{B} = \mu \overline{H} \tag{4.2.5}$$

$$\overline{J} = \sigma \overline{E} \tag{4.2.6}$$

$$\overline{D} = \varepsilon \overline{E} \tag{4.2.7}$$

In the above equations $\overline{E}$ is the electric field vector, $\overline{H}$ is the magnetic field vector, $\overline{D}$ is the electric displacement vector, $\overline{B}$ is the magnetic flux density, $\overline{J}$ is the current density, ρ is the charge density, ε is the dielectric constant, μ the magnetic permeability, and finally σ is the conductivity. The materials considered in this thesis are non-magnetic,

and so the permeability may be replaced with μ_0, the permeability of free space. The materials are also considered source free, with ρ equal to zero, so equations (4.2.2) an (4.2.5) become

$$\nabla.\overline{D} = 0 \tag{4.2.8}$$

$$\overline{B} = \mu_0 \overline{H} \tag{4.2.9}$$

4.3 The wave equation

This chapter is concerned with the propagation of light, and thus solutions of Maxwell's equations are sought which define the electric and magnetic field components, $\overline{E}$ and $\overline{H}$, of the propagating field. Combining equations (4.2.1) and (4.2.9) one may obtain

$$\nabla \times \overline{E} = -\mu_0 \frac{\partial \overline{H}}{\partial t} \tag{4.3.1}$$

Applying the curl operator to equation (4.3.1) gives

$$\nabla \times (\nabla \times \overline{E}) = -\mu_0 \nabla \times \left[\frac{\partial \overline{H}}{\partial t}\right] = -\mu_0 \left[\frac{\partial}{\partial t}(\nabla \times \overline{H})\right] \tag{4.3.2}$$

If an arbitrary vector $\overline{A}$ is given, a standard result in vector algebra states that

$$\nabla \times (\nabla \times \overline{A}) = \nabla(\nabla.\overline{A}) - \nabla^2 \overline{A} \tag{4.3.3}$$

and by applying this result to equation (4.3.2) it can be seen that

$$\nabla(\nabla.\overline{E}) - \nabla^2 \overline{E} = -\mu_0 \left[\frac{\partial}{\partial t}(\nabla \times \overline{H})\right] \tag{4.3.4}$$

The first term in this expression is $\nabla(\nabla.\overline{E})$. Substituting equation (4.2.7) into (4.2.8) gives

$$\nabla.\varepsilon\overline{E} = 0 \tag{4.3.5}$$

In an homogeneous medium, ε is uniform, and so this term becomes $\varepsilon\nabla.\overline{E} = 0$, which implies that the first term in expression (4.3.4) is zero. Using this result, and substituting (4.2.3) into (4.3.4) gives the following result

$$\nabla^2\overline{E} = \mu_0\frac{\partial^2\overline{D}}{\partial t^2} + \mu_0\frac{\partial\overline{J}}{\partial t} \tag{4.3.6}$$

Finally, substituting the ancillary equations (4.2.6) and (4.2.7) into this result and assuming that the conductivity is independent of time, the wave equation is obtained

$$\nabla^2\overline{E} = \mu_0\varepsilon\frac{\partial^2\overline{E}}{\partial t^2} + \mu_0\sigma\frac{\partial\overline{E}}{\partial t} \tag{4.3.7}$$

To arrive at this result a source free, homogeneous medium has been assumed. There is a corresponding wave equation that may be derived for the magnetic field. Solutions to the wave equation show the distribution of the electric (magnetic) field over space and time. If the space dependence is assumed to be time independent, and thus the space and time dependence are separable, then one may write, for the electric field

$$\overline{E}(r,t) = \overline{E}(r)\Gamma(t) \tag{4.3.8}$$

Assuming a harmonic variation of $\overline{E}$ with respect to time, the solution for $\Gamma(t)$ is $\Gamma(t) = \exp(j\omega t)$ and substituting this into equation (4.3.7) one obtains the time independent wave equation

$$\nabla^2\overline{E}(r) = -\omega^2\mu_0\varepsilon\overline{E}(r) + j\omega\mu_0\sigma\overline{E}(r) \tag{4.3.9}$$

Again there is a corresponding wave equation for the magnetic field. Much of the rest of this chapter is concerned with the implications of this important result. It is worthwhile to examine the solutions of this equation under two often encountered special conditions,

unguided propagation in a lossless medium (an idealised case) and unguided propagation in a partially conducting medium. In the following two sections only the electric field is considered, but the analysis is equally applicable to the magnetic field.

4.3.1 Propagation in a lossless medium

Although light propagating in any real medium will experience loss, for practical purposes many media can be considered lossless, the most important cases in optics being free space propagation and propagation in passive waveguides. For the lossless case the conductivity is zero, i.e. $\sigma = 0$, and the medium is considered to have a dielectric permittivity relative to that of free space given by ε_r, so $\varepsilon = \varepsilon_0\varepsilon_r$, where ε_0 is the permittivity of free space. Under these conditions the time independent wave equation (4.3.9) may be written

$$\nabla^2\overline{E}(r) = -\omega^2\mu_0\varepsilon_0\varepsilon_r\overline{E}(r) \qquad (4.3.1.1)$$

To simplify the solution the field is assumed to propagate in the z-direction only, and to be polarised with a single electric field component, E_y, such that $\overline{E}(r) = (0, E_y, 0)$. This gives the one dimensional scalar wave equation

$$\frac{d^2E_y}{dz^2} = -\omega^2\mu_0\varepsilon_0\varepsilon_r E_y \qquad (4.3.1.2)$$

which has a general solution of the form

$$E_y = A\exp(-j\beta z) + B\exp(j\beta z) \qquad (4.3.1.3)$$

where z is the direction of propagation and β is the propagation constant of the unguided wave, defined as

$$\beta = \sqrt{\omega^2\mu_0\varepsilon_0\varepsilon_r} \qquad (4.3.1.4)$$

Now the velocity of light in a vacuum, c, is given by $c = 1/\sqrt{\mu_0\varepsilon_0}$, so β can be written as

$$\beta = (\omega/c)\sqrt{\varepsilon_r} = kn \qquad (4.3.1.5)$$

The term $\sqrt{\varepsilon_r}$ is called the refractive index, and is often given the symbol n, and the wave vector $k = \omega/c$ is defined such that for propagation in a uniform lossless dielectric medium $\beta = kn$. In the special case of free space propagation ε_r is unity and $\beta = k$. The actual, physical, solution of the wave equation, including the time dependence but considering only the forward propagating solution, can thus be written

$$E_y(r,t) = A\exp[j(\omega t - \beta z)] \qquad (4.3.1.6)$$

4.3.2 Propagation in a conducting medium

There are often cases when a medium cannot be considered lossless, for example light propagating in a semiconductor waveguide may be subject to scattering and absorption losses, or in the case of a laser the medium of propagation may have gain. It is thus necessary to consider the case when σ has a non-zero value. Again, a medium of dielectric constant ε_r, and an electric field polarised in the y direction are assumed. Where the analysis differs from the previous case is that the last term in the time independent wave equation (4.3.9) is no longer zero. The one dimensional time independent wave equation may thus be written

$$\frac{d^2E_y}{dz^2} = -\omega^2\mu_0\varepsilon_0\varepsilon_r E_y + j\omega\mu_0\sigma E_y \qquad (4.3.2.1)$$

If the two terms on the right hand side are combined, one may write, with reference to (4.3.1.2)

$$\frac{d^2E_y}{dz^2} = -\omega^2\mu_0\varepsilon_0\underline{\varepsilon}E_y \qquad (4.3.2.2)$$

where $\underline{\varepsilon}$ is a complex variable defined as

$$\underline{\varepsilon} = \varepsilon_r - j\left(\frac{\sigma}{\varepsilon_0\omega}\right) \qquad (4.3.2.3)$$

The solution to equation (4.3.2.2) is similar to that of equation (4.3.1.2), except that the propagation constant $\underline{\beta}$ is complex, and given by

$$\underline{\beta} = \omega/c\sqrt{\underline{\varepsilon}} \qquad (4.3.2.4)$$

The refractive index is defined, as in the previous section, as the square root of the dielectric constant, and the complex refractive index $\underline{n}$ is written

$$\underline{n} = \sqrt{\underline{\varepsilon}} = n + jK \qquad (4.3.2.5)$$

so that, from (4.3.2.3)

$$\varepsilon_r = n^2 - K^2 \qquad (4.3.2.6)$$

$$\varepsilon_i = -\frac{\sigma}{\varepsilon_0\omega} = 2nK \qquad (4.3.2.7)$$

where n and K are the real and imaginary parts of the refractive index respectively, and K is called the extinction coefficient. $\underline{\beta}$ may thus be written as

$$\underline{\beta} = k(n + jK) \qquad (4.3.2.8)$$

such that

$$Re(\underline{\beta}) = kn \qquad (4.3.2.9)$$

$$Im(\underline{\beta}) = kK \tag{4.3.2.10}$$

Thus the solution of equation (4.3.2.2), including the time dependence, can be written (with reference to equation (4.3.1.6))

$$E_y = A\exp(j(\omega t - \underline{\beta} z)) \tag{4.3.2.11}$$

or

$$E_y = \exp\{Im(\underline{\beta})z\} A exp\{j(\omega t - Re(\underline{\beta})z)\} \tag{4.3.2.12}$$

Comparing this to equation (4.3.1.6) it is seen that the solutions for the lossless and conducting cases differ by the factor $\exp\{Im(\underline{\beta})z\}$. Now, using equations (4.3.2.7) and (4.3.2.10), $Im(\underline{\beta})$ is given by

$$Im(\underline{\beta}) = -\sigma/(2\varepsilon_0 cn) \tag{4.3.2.13}$$

and thus it is proportional to σ. If σ is zero, the lossless case, (4.3.2.12) and (4.3.1.6) are equal as would be expected. If σ is positive then $Im(\underline{\beta})$ is negative, and the solution for E_y is a decaying travelling wave. This means that the material is absorptive. However, if σ is negative then the solution is a growing wave and the material has gain (and is called an active material).

A standard technique for measuring the gain or loss of a material is to shine a beam of light into the material and measure the intensity of the light some point in the material. The intensity of the light will vary exponentially along the material, and the material loss or gain can then be described in terms of the absorption (gain) coefficient, α of this exponential. The intensity of the light is related to the square of the field, and so the intensity at any point on the z-axis relative to a reference point at $z = 0$ is given by

$$|E_y(z)|^2 = |E_y(0)|^2 \exp(-\alpha z) \tag{4.3.2.14}$$

Comparing this with equation (4.3.2.12) it is easy to show that

$$\alpha = -2Im(\underline{\beta}) \qquad (4.3.2.15)$$

From equation (4.3.2.14) it can be seen that if α is positive then the medium is lossy, and if negative then the medium has gain. It can therefore be seen, from equation (4.3.2.15), that the sign of the imaginary part of the propagation constant determines whether the guide has loss or gain, and it's value determines the magnitude of the loss (gain). Thus, if $Im(\underline{\beta})$ is known, one can determine whether a laser is above or below threshold by comparing this term to the losses experienced by the light in the cavity.

Finally, from equations (4.3.2.5) to (4.3.2.10) it can be seen that the imaginary part of the refractive index is directly related to the gain of the medium, whereas the imaginary part of the permittivity is related to the gain via the real part of the refractive index. Therefore if a medium has gain, this gain has a direct effect on the refractive index and a more indirect effect on the permittivity.

4.4 The three layer slab waveguide

So far the propagation of light in media of infinite extent has been considered. With all lasers, confining structures are used to guide the light generated, and thus an understanding of such structures is required for modelling. It is instructive to consider the three-layer dielectric waveguide, as shown in figure 4.1. Although such a simple one dimensional guide structure is not directly used in semiconductor laser devices, the principles involved can be applied to more complex guide geometries, as will be shown in the next chapter. The three layer guide is taken to be infinite in the y-direction, such that $\partial/\partial y = 0$.

There are only a limited number of solutions to the wave equation which any particular waveguide will support, and these are called the modes. The modes of the slab waveguide may be classified by the polarisation of their constituent fields as either TE or TM modes.

TE modes, or transverse electric modes, do not have a component of electric field in the direction of wave propagation, whereas TM or transverse magnetic modes do not have a longitudinal magnetic field component.

4.4.1 Guided modes - TE

The assumption that $\partial/\partial y = 0$ implies that in the chosen co-ordinate system the only non-zero field components of the TE modes are E_y, H_x and H_z. $\overline{E}$ and $\overline{H}$ can thus be written

$$\overline{E} = E_y \overline{b} \qquad (4.4.1.1a)$$

$$\overline{H} = H_x \overline{a} + H_z \overline{c} \qquad (4.4.1.1b)$$

where $\overline{a}$, $\overline{b}$ and $\overline{c}$ are unit vectors along the x, y, and z directions respectively. If these equations are substituted into equation (4.3.1) and the components of like vectors equated, the following equations are obtained

$$\frac{\partial E_y}{\partial z} = \mu_0 \frac{\partial H_x}{\partial t} \qquad (4.4.1.2a)$$

$$\frac{\partial E_y}{\partial x} = -\mu_0 \frac{\partial H_z}{\partial t} \qquad (4.4.1.2b)$$

For convenience in writing the equations, the time and z- dependence of the fields, $\exp\{j(\omega t - \beta z)\}$, will be omitted, since this factor is common to all field quantities. Equation (4.4.1.2) may then be simplified to obtain

$$H_x = -\frac{\beta}{\mu_0 \omega} E_y \qquad (4.4.1.3a)$$

$$H_z = \frac{j}{\mu_0 \omega} \frac{\partial E_y}{\partial x} \qquad (4.4.1.3b)$$

Therefore, once the electric field component E_y has been obtained, the magnetic field components can be directly calculated from the above relations. The time independent wave equation (4.3.9) may be re-written using the work of section 4.3 and relationships that have already been defined for k and n as

$$\nabla^2 \overline{E} + k^2 n^2 \overline{E} = 0 \qquad (4.4.1.4)$$

For the three layer slab waveguide, infinite in the y-direction and with a TE mode propagating in the z-direction, this equation reduces to

$$\frac{\partial^2 E_y}{\partial x^2} + (n^2 k^2 - \beta^2) E_y = 0 \qquad (4.4.1.5)$$

which is often called the one dimensional scalar Helmholtz equation. This relationship holds for each region of the waveguide, so that for the three layer slab guide, shown in figure 4.1, the individual equations for the different regions become

$$\frac{\partial^2 E_{y3}}{\partial x^2} + (n_3^2 k^2 - \beta^2) E_{y3} = 0 \qquad x \geq 0 \qquad (4.4.1.6a)$$

$$\frac{\partial^2 E_{y1}}{\partial x^2} + (n_1^2 k^2 - \beta^2) E_{y1} = 0 \qquad 0 \geq x \geq -d \qquad (4.4.1.6b)$$

$$\frac{\partial^2 E_{y2}}{\partial x^2} + (n_2^2 k^2 - \beta^2) E_{y2} = 0 \qquad x \leq -d \qquad (4.4.1.6c)$$

For propagating modes, there are three physically possible types of field distribution which satisfy these equations, and these are shown in figure 4.2. The first case, at the top of the diagram, shows a guided mode, with the field decaying exponentially in either direction, and the field sinusoidal in the guiding region. This case occurs when

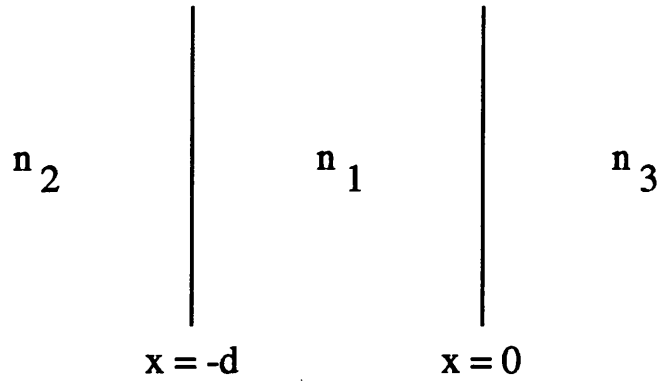

Figure 4.1 The three layer dielectric waveguide

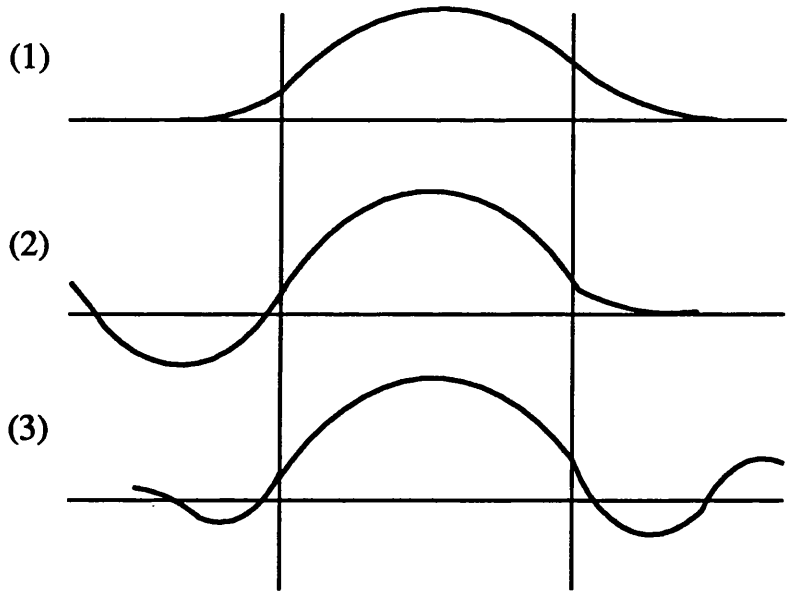

Figure 4.2 The three guided solutions. (1) shows a guided mode, (2) shows a 'substrate radiation' mode, an (3) shows a radiation mode.

$n_1 > \beta/k > n_2 \geq n_3$. The second case shows a mode sinusoidal in the guiding region and also in the positive x-direction, but exponential in the -ve x direction. This is often referred to as a substrate radiation mode, and occurs when $n_2 > \beta/k > n_3$. The final case is for $n_3 > \beta/k > 0$ and shows a radiation mode, with the field sinusoidal in all regions, and the energy radiating from the guiding region.

Solutions to equations (4.4.1.6) are sought which are guided modes, i.e. solutions for which the E_y component vanishes at $x = \pm\infty$. The solutions must also satisfy the boundary conditions of continuity of the tangential E and H fields at the two dielectric interfaces at $x = 0$ and $x = -d$. Thus E_y and H_z must be continuous at the interfaces. These conditions lead to the solutions

$$E_y = \begin{cases} A\exp(-\delta x) \\ A\cos\kappa x + B\sin\kappa x \\ (A\cos\kappa d - B\sin\kappa d)\exp[\gamma(x+d)] \end{cases} \quad \begin{matrix} x \geq 0 \\ 0 \geq x \geq -d \\ x \leq -d \end{matrix} \qquad (4.4.1.7)$$

where

$$\delta^2 = \beta^2 - k^2 n_3^2 \qquad (4.4.1.8a)$$

$$\kappa^2 = k^2 n_1^2 - \beta^2 \qquad (4.4.1.8b)$$

$$\gamma^2 = \beta^2 - k^2 n_2^2 \qquad (4.4.1.8c)$$

It can be seen from these relationships that the E_y component satisfies the one dimensional Helmholtz equation, (4.4.1.5), and is also continuous at the dielectric interfaces. The H_z component may be obtained from equations (4.4.1.7) and (4.4.1.3b) as follows

$$H_z = -j/\omega\mu_0 \begin{cases} \delta A\exp(-\delta x) \\ \kappa(A\sin\kappa x - B\cos\kappa x) \\ -\gamma(A\cos\kappa d - B\sin\kappa d)\exp[\gamma(x+d)] \end{cases} \quad \begin{matrix} x \geq 0 \\ 0 \geq x \geq -d \\ x \leq -d \end{matrix} \qquad (4.4.1.9)$$

Unlike equation (4.4.1.7) the equation for H_z does not, in itself, satisfy the continuity condition at the dielectric boundaries at $x = 0$ and $x = -d$. Imposing these conditions the following equations are obtained

$$\delta A + \kappa B = 0 \qquad (4.4.1.10a)$$

$$[\kappa\sin(\kappa d) - \gamma\cos(\kappa d)]A + [\kappa\cos(\kappa d) + \gamma\sin(\kappa d)]B = 0 \qquad (4.4.1.10b)$$

These two equations may be solved simultaneously to yield the solution

$$\delta[\kappa\cos(\kappa d) + \gamma\sin(\kappa d)] - \kappa[\kappa\sin(\kappa d) - \gamma\cos(\kappa d)] = 0 \qquad (4.4.1.11)$$

which may be written in a more useful form

$$\tan\kappa d = \kappa(\gamma + \delta)/(\kappa^2 - \gamma\delta) \qquad (4.4.1.12)$$

Recalling the definitions of δ,κ and γ (equation (4.4.1.8)) it can be seen that the above eigenvalue equation defines the allowed values of β for which the one dimensional wave equation is satisfied. From these equations it is possible to calculate how many modes a guide supports, and the propagation constants for each of these modes.

4.4.2 Guided modes - TM

For TM modes, the analysis is basically similar to that for TE modes. Indeed, in the general case, the derivation is identical. The field components for a TM mode are H_y, E_x and E_z, so that from Maxwell's equations, and assuming a time and z-dependence for all field components of $\exp[j(\omega t - \beta z)]$, the electric field may be found from the magnetic field (c.f. equation (4.4.1.3)) as

$$E_x = \frac{\beta}{\omega\varepsilon_0\varepsilon_r} H_y \qquad (4.4.2.1a)$$

$$E_z = -\frac{j}{\omega\varepsilon_0\varepsilon_r}\frac{\partial H_y}{\partial x} \qquad (4.4.2.1b)$$

The difference between the equations for the electric field (4.4.2.1) and for the magnetic field (4.4.1.3) lies in the fact that whilst μ_0 is constant over all regions of the waveguide, $\varepsilon_0\varepsilon_r$ is different for the three regions, and this must be taken into account in the boundary conditions for TM modes. Again, solutions are sought which are guided modes, so

$$H_y = \left.\begin{cases} A\exp(-\delta x) \\ A\cos\kappa x + B\sin\kappa x \\ (A\cos\kappa d - B\sin\kappa d)\exp[\gamma(x+d)] \end{cases}\right\} \quad \begin{matrix} x \geq 0 \\ 0 \geq x \geq -d \\ x \leq -d \end{matrix} \qquad (4.4.2.2)$$

If the derivation for the TE modes is followed, taking into account the change of ε_r across the guide, the following eigenvalue equation is obtained

$$\tan(\kappa d) = n_1^2\kappa(n_3^2\gamma + n_2^2\delta)/(n_2^2 n_3^2\kappa^2 - n_1^4\gamma\delta) \qquad (4.4.2.3)$$

4.4.3 Gain guiding

It was shown in section 4.3.2 that if the material in which the light is propagating has either loss or gain, then the refractive index of the material will be complex. In the previous two sections, however, it has been tacitly assumed that the waveguide medium is lossless, and that the waveguiding has therefore been caused by changes in the real part of the refractive index. It is also possible to have waveguiding in media whose real refractive index is the same, with the guiding action produced by changes in the imaginary part of the refractive index. Consider a medium with gain sandwiched between two layers with loss, with all three having the same real refractive index. In this case one may intuitively recognise that the central layer is more transparent and will thus guide an electromagnetic wave.

The theory that has been developed in the previous two sections is still valid for the complex case, if it is understood that all relevant parameters become complex. In particular the refractive index is complex, and in layer *i* of the waveguide it takes the form

$$\underline{n}_i = (n_i + jK_i) \qquad (4.4.3.1)$$

Consider, for simplicity, a three layer symmetric waveguide, i.e. $n_2 = n_3$. There are four possible combinations for the real refractive indices and extinction coefficients, which may be listed as

(a) $n_1 \geq n_2$; $\quad K_1 \geq K_2$

(b) $n_1 \geq n_2$; $\quad K_1 \leq K_2$

(c) $n_1 \leq n_2$; $\quad K_1 \geq K_2$

(d) $n_1 \leq n_2$; $\quad K_1 \leq K_2$

All of these possibilities will support guided modes [7], however not all of these modes will be stable solutions, i.e. solutions which are unaffected by perturbation. It can be shown [1] that a necessary, but not sufficient, condition for stability of guided modes propagating in material with loss or gain is that

$$n_1 K_1 - n_2 K_2 > 0 \qquad (4.4.3.2)$$

From this inequality several possibilities for stable guided modes can occur, and are listed as:-

(i) $K_1 = K_2$: In this special case equation (4.4.3.2) now reads $n_1 > n_2$, which is the previously stated condition for real index guiding

(ii) $n_1 = n_2$: Equation (4.4.3.2) now reads $K_1 > K_2$, which implies that there is a gain maximum in the central guiding region.

(iii) If $n_1 = n_2 + \Delta n$ where $\Delta n \ll n_1, n_2$ and $\Delta K = K_1 - K_2$ then equation (4.4.3.2) becomes

$$\frac{\Delta K}{K_1} + \frac{\Delta n}{n_2} > 0 \qquad (4.4.3.3)$$

This is a particularly interesting case, since it shows that either gain guided or index guided modes may be stable even in the presence of anti-guidance due to the opposite effect, providing the guiding action is strong enough. This may be the case in semiconductor lasers, where the presence of carriers in the active layer depresses the real part of the refractive index but gives rise to gain in the active layer. In the waveguides considered in this thesis the real index guiding is strong, and so the question of instability of the solution does not arise.

4.4.4 Cut off

The cut off point for a mode is defined as the point at which that mode is no longer confined by the waveguide. For a guided wave, the relationship between the indices is defined as $kn_1 \geq \beta > kn_2 \geq kn_3$. We may define a frequency ω at which $kn_2 = \beta$ $(k = \omega/c)$ and thus γ becomes zero. The field in the outer dielectric regions is therefore no longer a decaying exponential, as seen in figure 4.2, and the mode is no longer guided. The cut-off condition for a mode is therefore that

$$\beta = kn_2 \qquad (4.4.4.1)$$

If this condition is put into the eigenvalue equation for TE modes (4.4.1.12) the following equation may be obtained

$$\tan v = \sqrt{a-1} \qquad (4.4.4.2)$$

where the normalised parameters a and v are defined

$$a = \frac{n_1^2 - n_3^2}{n_1^2 - n_2^2} \quad >= 1 \qquad (4.4.4.3)$$

$$v = dk\sqrt{n_1^2 - n_2^2} \qquad (4.4.4.4)$$

The parameter a is often referred to as the asymmetry parameter, and for asymmetrical guides $a > 1$. The relationship between a and ν is shown in figure 4.3. It can be seen that for $a > 1$ there is a minimum value of ν, $\nu' = \tan^{-1}\sqrt{a-1}$ below which no mode propagates, i.e. the lowest order mode is cut-off. The number of modes such an asymmetric guide will support for a given ν is

$$M = In\left\{1 + \frac{\nu - \tan^{-1}\sqrt{a-1}}{\pi}\right\} \qquad (4.4.4.5)$$

where In is the integer truncation function of the term in braces, and $\tan^{-1}$ is restricted to the range 0 to $\pi/2$.

For symmetrical structures, $a = 1$, and the cut-off condition, equation (4.4.4.2), becomes $\tan\nu = 0$. This is satisfied for $\nu = 0, \pi, 2\pi$, etc., and it can be seen from figure 4.3 that there is no cut-off value of ν for the lowest order mode. The cut-off value of ν for the m^{th} transverse mode is thus $\nu = (m-1)\pi$. The number of modes supported by the symmetrical structure for a given ν is

$$M = In\left\{1 + \frac{\nu}{\pi}\right\} \qquad (4.4.4.6)$$

For TM modes, the cut-off condition, $\beta = kn_2$ reduces the eigenvalue equation (4.4.2.3) to

$$\tan\nu = n_1^2/n_3^2\sqrt{a-1} \qquad (4.4.4.7)$$

and the number of TM modes a three layer slab waveguide may support is therefore

$$M = In\left\{1 + \frac{\nu - \tan^{-1}(\sqrt{a-1}\,n_1^2/n_3^2)}{\pi}\right\} \qquad (4.4.4.8)$$

again, for symmetrical guides $a = 1$, and there is no cut-off value for the zero order mode.

4.4.5 Calculation of β for the symmetrical guide

The propagation constant of a mode is an important parameter for lasers, as was explained in section 4.3.2. This section describes how β may be obtained from the eigenvalue equations (4.4.1.12), (4.4.2.3) for the TE and TM modes of the three-layer symmetrical guide. The same principles may be applied to the asymmetric guide, but for the symmetrical guide the calculation of the propagation constant β is simplified by the fact that $n_2 = n_3$, ie $\delta = \gamma$. The eigenvalue equation for TE modes may be written

$$\tan \kappa d = \frac{2\kappa\gamma}{\kappa^2 - \gamma^2} \qquad (4.4.5.1)$$

This may be re-written, by use of the double-angle formula

$$\tan\left(2\frac{\kappa d}{2}\right) = 2\frac{\tan(\kappa d/2)}{1 - \tan^2(\kappa d/2)} = \frac{2\gamma/\kappa}{1 - (\gamma/\kappa)^2} \qquad (4.4.5.2)$$

which may then be re-arranged as a quadratic

$$\tan^2(\kappa d/2) + \{1 - (\gamma/\kappa)^2\} \tan(\kappa d/2) - 1 = 0 \qquad (4.4.5.3)$$

The roots of this quadratic equation are

$$\tan(\kappa d/2) = \frac{\gamma d}{\kappa d} \qquad (4.4.5.4a)$$

$$\cot(\kappa d/2) = -\frac{\gamma d}{\kappa d} \qquad (4.4.5.4b)$$

These equations give the even (4.4.5.4a), and odd (4.4.5.4b) modes of the symmetrical guide. Using the definitions of κ and γ it is a simple matter to show that

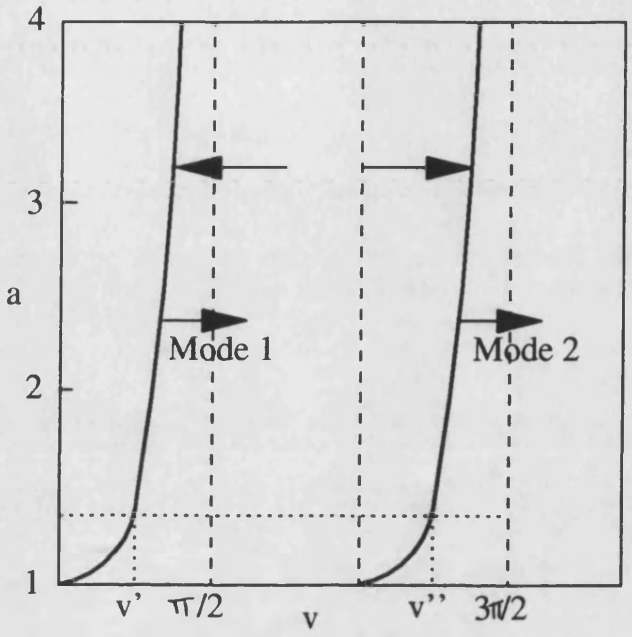

Figure 4.3 Relationship between the asymmetry parameter, a, and the normalised guide width, v, showing the cut-off conditions for the first and second modes. A waveguide geometry defined by a point to the right of each curve implies that the mode can propagate in the guide.

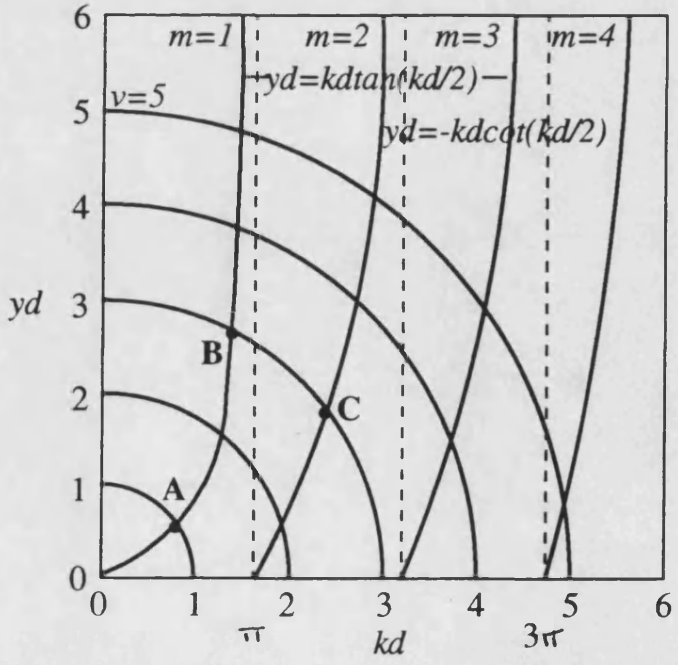

Figure 4.4 Plot of eigenvalue equations for even and odd TE modes

$$\kappa^2 d^2 + \gamma^2 d^2 = (n_1^2 - n_2^2)k^2 d^2 = \nu^2 \qquad (4.4.5.5)$$

Equations (4.4.5.4) and (4.4.5.5) represent two equations in two unknowns, and may be solved simultaneously to obtain κ and γ, and thus β may be found from (4.4.1.8). Equation (4.4.5.5) is the equation of a circle of radius ν, and the solutions for the even order modes involve the intersection of this circle with equation (4.4.5.4a). The solutions for the odd order modes are found from the intersection of the circle and equation (4.4.5.4b). A graphical solution is shown in figure 4.4.

It can be seen from the figure that, at low values of ν, $0 < \nu < \pi$, the curves only intersect at one point, and thus only one mode exists. Point A on the diagram is an example of such a point. The mode represented by this point is the first TE mode, and is designated TE_0. For this mode the parameter κ lies within the boundaries

$$0 < \kappa d < \pi \qquad (4.4.5.6)$$

and the mode has no zero crossings in the guiding region of the slab $0 \leq x \leq -d$.

If ν is increased, such that $\pi < \nu < 2\pi$, two intersections are obtained, e.g. points B and C, corresponding to two confined modes. B corresponds to $\kappa d < \pi$, and thus defines the propagation constant of the TE_0 mode. C, however, lies in the region

$$\pi \leq \kappa d \leq 2\pi \qquad (4.4.5.7)$$

The mode corresponding to this point has one zero crossing, and is called the TE_1 mode.

Both of these modes correspond to the same value of ν, which means that for fixed guide parameters, n and d, they correspond to the same frequency. Therefore, both modes may be excited simultaneously by the same input field, or may lase simultaneously at the same frequency. The TE_0 mode, however, corresponds to a greater value of γ, and is

therefore more highly confined, and has a larger value of β (from equation (4.4.1.8b)) than any higher order mode. It can be seen that, as ν is increased in steps of π, an increasing number of modes are allowed to propagate.

Again, the situation is very similar for TM modes. For a symmetrical guide, the eigenvalue may be written, with reference to (4.4.5.1), as

$$\tan \kappa d = \frac{2(n_2^2\kappa)(n_1^2\gamma)}{(n_2^2\kappa)^2 - (n_1^2\gamma)^2} \qquad (4.4.5.8)$$

The corresponding equations to (4.4.5.4) may then be written

$$\tan(\kappa d/2) = (n_1^2/n_2^2)\frac{\gamma d}{\kappa d} \qquad (4.4.5.9a)$$

$$\cot(\kappa d/2) = -(n_1^2/n_2^2)\frac{\gamma d}{\kappa d} \qquad (4.4.5.9b)$$

Now $n_1/n_2 > 1$, and therefore the solution for γ for the TM modes is less than that for the TE modes. This in turn implies that $\beta_{TM} < \beta_{TE}$. One consequence of this which is relevant to lasers is that the TM mode has less gain than the TE mode, since gain = $2\mathrm{Im}\beta$, and the TM mode is also less well confined to the region of interest, therefore lasing generally occurs in the TE, and not the TM, mode.

Whilst a graphical method enables easy visualisation of the solutions, for numerical calculations of the values of κ and γ a different approach is required. One such alternative method is to derive the eigenvalue equation, (4.4.1.12), in terms of the normalised frequency ν, and the normalised propagation constant b, which is defined as

$$b = \frac{(\beta/k)^2 - n_2^2}{n_1^2 - n_2^2} \qquad (4.4.5.9)$$

Using the definitions of b and v, the eigenvalue equation (4.4.1.12) may be written, with some rearranging

$$\tan(v\sqrt{1-b}) = \sqrt{\frac{b}{(1-b)}} \qquad (4.4.5.10)$$

or

$$v\sqrt{1-b} = \tan^{-1}\left[\sqrt{\frac{b}{(1-b)}}\right] + m\pi \qquad (4.4.5.11)$$

where m = 1, 2, 3, etc is the mode number. This equation is relatively easy to solve numerically using, for example, a Newton-Raphson approach.

4.4.6 Power flow and confinement factor

The time averaged power flow, P, is given by the integral across the guide of the z component of the Poynting vector S_z

$$P = \int_{-\infty}^{\infty} S_z dx = \frac{1}{2}\int_{-\infty}^{\infty} Re(E \times H^*)_z dx \qquad (4.4.6.1)$$

where H^* indicates the complex conjugate of H. For TE modes it is simple to show that S_z is given by

$$S_z = -\frac{1}{2} E_y H_x^* \qquad (4.4.6.2)$$

and, by use of the complex conjugate of equation (4.4.1.3a)

$$S_z = \frac{\beta}{2\mu_0\omega} |E_y|^2 \qquad (4.4.6.3)$$

Thus the total time averaged power of the mode is given by

$$P = \frac{\beta}{2\mu_0\omega}\int_{-\infty}^{\infty} |E_y|^2 dx \qquad (4.4.6.4)$$

The power may be calculated by splitting the integral over the three different dielectric regions, and solving in each region. Denoting the power in each region as P_i (i=1,2,3) and making use of equation (4.4.1.10a) one obtains

$$P_3 = \frac{\beta}{2\mu_0\omega}\left[\frac{A^2}{2\delta}\right] \qquad (4.4.6.5)$$

$$P_1 = \frac{\beta}{2\mu_0\omega}\left[\frac{A^2}{2\kappa}\right]\left[\frac{\kappa^2+\delta^2}{\kappa}\right]\left[d + \frac{\gamma}{\kappa^2+\gamma^2} + \frac{\delta}{\kappa^2+\delta^2}\right] \qquad (4.4.6.6)$$

$$P_2 = \frac{\beta}{2\mu_0\omega}\left[\frac{A^2}{2\gamma}\right]\left[\frac{\kappa^2+\delta^2}{\gamma^2+\kappa^2}\right] \qquad (4.4.6.7)$$

An important parameter in lasers is the confinement factor, Γ, which is defined for each region of the waveguide as the fraction of the total power confined to that region. In a laser it is important to know the fraction of the power confined to the active region, since this fraction of the power interacts with the carriers and produces stimulated emission. The confinement factor is defined as

$$\Gamma = \frac{\int_{x_1}^{x_2} |E_y|^2 dx}{\int_{-\infty}^{\infty} |E_y|^2 dx} \qquad (4.4.6.8)$$

which may be written, for the three layer slab waveguide, as

$$\Gamma = \frac{P_1}{P_1+P_2+P_3} \qquad (4.4.6.9)$$

4.5 Discussion

This chapter has examined optical fields and waveguiding in one dimensional guides, using the three layer guide as an example. The wave equation was derived from Maxwell's equations, and it was shown that propagation in conducting and lossless media may be considered in the same way, the only difference being that for the conducting case a complex propagation constant and refractive index are used. It was shown that the imaginary part of the propagation constant is directly related to the intensity loss or gain of the optical medium, and how this may be used to determine if a laser is above or below threshold.

The three layer slab waveguide was considered as an example of a one dimensional guide, and the eigenvalue equation derived for the modes. The modal cut-off point was established, and the solutions for β found in terms of the guide parameters and the frequency of the propagating field. The power of a mode was calculated, and thus the confinement factor was explained.

The chapter has mainly considered TE polarised modes. This is because TM polarised modes have a lower value of γ, and thus a lower value of β. This implies that the TM modes have a lower gain, and thus a semiconductor laser would require a greater pumping current to lase in a TM mode. Therefore, as can be experimentally verified, most semiconductor lasers are TE polarised. The general features of TM modes are the same as discussed here for TE modes.

REFERENCES

[1] M.J.Adams, "An introduction to optical waveguides", John Wiley, New York, 1981

[2] D.Marcuse, "Theory of dielectric optical waveguides", Academic Press, New York, 1974

[3] W.T.Tsang, (ed), "Semiconductors and semimetals", Vol. 22, Pt.E., Academic Press, New York, 1985

[4] H.J.Kressel, and J.K.Butler, "Semiconductor lasers and heterojunction LEDs", Chapters 4,5, Academic Press, New York, 1977

[5] G.H.B.Thompson, "Physics of semiconductor laser devices", Chapter 4, John Wiley, New York, 1980

[6] A.Yariv, "Optical Electronics", Chapter 13, Holt, Rinehart and Winston, New York, 1985

[7] D.Marcuse, "Light Transmission Optics", Van Nostrand Rienhold, New York, 1972

Chapter 5: THE WAVEGUIDE MODEL

5.1 Introduction

In the previous chapter the propagation of light in one dimensional dielectric waveguides was studied in detail. It was seen that if the waveguide has loss or gain then this implies that the refractive index, and thus the propagation constant, is complex. General methods were presented to obtain the value of this propagation constant for a three layer dielectric waveguide. In this chapter, it will be shown how the work of chapter 4 can be extended to two dimensional guides with complex dielectric constants, and a model the optical characteristics of buried heterostructure lasers will be developed.

All physically realisable dielectric waveguiding structures are three dimensional. However, it is often possible to reduce the problem of the solution of the wave equation to two dimensions, by assuming a sinusoidally varying field propagating along the longitudinal (z-) axis of the waveguide. This approximation was made in the previous chapter, where it was also assumed that the waveguide was invariant and infinite in extent in the transverse (y-) dimension, and thus the wave equation was reduced to one dimension. However, in semiconductor laser structures the dielectric constant often varies in both the transverse and lateral directions, and the two dimensional nature of the waveguide must be taken into account.

Whilst it is simple to formulate analytic equations to describe the three layer slab guide, and possible to extend this analysis to multi-layer one dimensional guides, an analytic solution is not possible for even the simplest two dimensional rectangular dielectric waveguide. This is due to the fact that it is not possible for an analytic solution to satisfy

all the boundary conditions for the E and H fields sustained by the guide. It is therefore necessary to use numerical methods or approximate analytic techniques to obtain a solution.

One of the basic requirements for lasing action is that the medium inside the optical cavity in which the light propagates must have gain. This means, as shown in chapter 4, that the propagation constant will be complex. In a semiconductor laser the optical gain is provided by the stimulated recombination of charge carriers, which generates photons in the cavity. Therefore, the permittivity of the active medium is related to the carrier density, via the gain parameters of the material. If the carrier distribution is known then the waveguiding properties of the laser can be found. However, to calculate the carrier density using the carrier diffusion equation, the optical field profile is required in the stimulated recombination term.

From the above statements, and the work of the previous chapters, it is apparent that the relationship of the refractive index to the carrier density in the active region means that the electrical and optical problems are coupled. The waveguide model must therefore include not only include the two dimensional nature of the waveguide, but also the effect of the carriers. Further, for all lasing modes the propagation constants (to determine the gain) and field distributions (to enable the calculation of the carrier density) must be found.

There are several methods of solving for the modes of two dimensional optical waveguides, perhaps the most commonly used is the Effective Index (EI) method [1] which is described in section 5.3. However, in the present work the chosen solution technique is the recently proposed Weighted Index [WI] method [2], which is described in section 5.4. The reasons for the selection of the WI over the EI method are (i) the improved accuracy of solution obtained from the WI method, and (ii) the difficulty of implementing

the EI method for the waveguide formed by the constricted mesa laser, where the outer waveguide regions are cut-off. The method of solution is discussed in section 5.5, and results are presented showing the effect of the guide geometry on the first and second modes.

The presence of carriers in the active layer alters both the real and complex parts of the dielectric constant. However, the Weighted Index method as presented in reference [2] and derived in section 5.4, cannot be applied to waveguides of complex permittivity. The reasons for this, and the derivation of the Weighted Index method in complex waveguides, are presented in section 5.6. Finally, results are given for the solution of the wave equation in guides of complex permittivity, showing that the effect of increasing the carrier density is to increase the gain of the guided modes, whilst the effect on the real part of the permittivity is relatively small.

5.2 Two dimensional waveguides

For a simple one dimensional dielectric waveguide, the light may be considered as being polarised in either TE or TM polarisations. However, this is no longer true for two dimensional rectangular dielectric waveguides. In this case the modes are hybrid (having both TE and TM components), but essentially TEM polarised, i.e. the axial components of the electric and magnetic fields are very much less than the transverse components. However, if it is assumed that the refractive index step between the core and the cladding layers is small, then the solutions can be classified approximately as either TE or TM. This chapter is concerned with the solutions for lasing modes, and therefore is constrained to TE-like modes for reasons presented in section 4.4.

Many methods have been used to solve the wave equation in rectangular dielectric waveguides and some of these are reviewed in references [3] and [4]. The difference

between the methods lies in the assumptions made, and the choice of method is usually determined by the required accuracy of the solution. Currently, the most accurate method of solution is generally considered to be the Vector Finite Element method [5]. Unfortunately, as might be expected, there is a trade off between the accuracy of the solution and the time taken to obtain it.

In this thesis the self-consistent modelling of laser diodes is considered. As will be seen in Chapter 6, the method of solution is iterative, requiring many iterations of the optical model for an optical solution, and several iterations of the overall model to converge to a final solution. For this reason a rapid solution to the waveguide problem is required. However, the accuracy of solution is also important, since the gain or loss of a mode is determined directly from the propagation constant, and this parameter therefore defines whether or not a mode is lasing. A further consideration in the model is the need to accurately calculate the optical field and propagation constant for all guided modes of the waveguide, even those near to cut-off.

Several approximate and rapid solution techniques are available. Probably the most frequently used of these is the Effective Index method [1] which is explained in the following section. A second method, the Weighted Index method, has been proposed recently as a rapid and accurate method [2], being more accurate [6] and only slightly slower than the EI method. This method is described in section 5.4, and it's extension to the case of complex permittivity is given in section 5.6. Both methods rely on describing a two-dimensional guide in terms of one dimensional equations.

5.3 The Effective Index method

The EI method was first derived for the case of an optical waveguide by Knox and Toulios [1]. The main importance of the method lies not in the accuracy of the solution

obtained (however this is often surprisingly accurate considering the bold assumptions made), but in the simplicity and speed of calculation; the method requires only a few solutions of the one dimensional wave equation, the number depending on the waveguide geometry. Because of this it has been widely adopted and applied to a vast range of optical waveguiding structures, including those of complex permittivity.

The principle of the EI method is illustrated in figure 5.1 for a the case of a rectangular waveguide. The guide of figure 5.1(a) is a buried ridge guide, with a core region of refractive index n_1 surrounded by cladding material of index n_2. It is assumed that the wave is well confined to the core and that the field decays exponentially in the cladding regions. The dielectric permittivity $\varepsilon(x,y)$ is assumed to vary slowly in the lateral x direction compared to its variation in the transverse y direction.

The basis of the method is that, if the above assumptions are valid, the two dimensional waveguide of figure 5.1(a) can be thought of as equivalent to the two one dimensional slab waveguides shown in figures 5.1(b) and 5.1(c). The wave equation is first solved in the waveguide of figure 5.1(b), and the propagation constant found is used to define an effective index which describes the transverse waveguiding. The effective index is then used as the refractive index of the core region of the lateral waveguide, figure 5.1(c), and the wave equation is solved in this waveguide to obtain a solution which approximately describes the lateral waveguiding of the two dimensional guide.

In section 4.4 the scalar Helmholtz equation was derived from Maxwell's equations for the one dimensional case (equation 4.4.1.5). The equation may be generalised to two dimensions as

$$\nabla^2 E(x,y) + [k_0^2 \varepsilon(x,y) - \beta^2] E(x,y) = 0 \qquad (5.3.1)$$

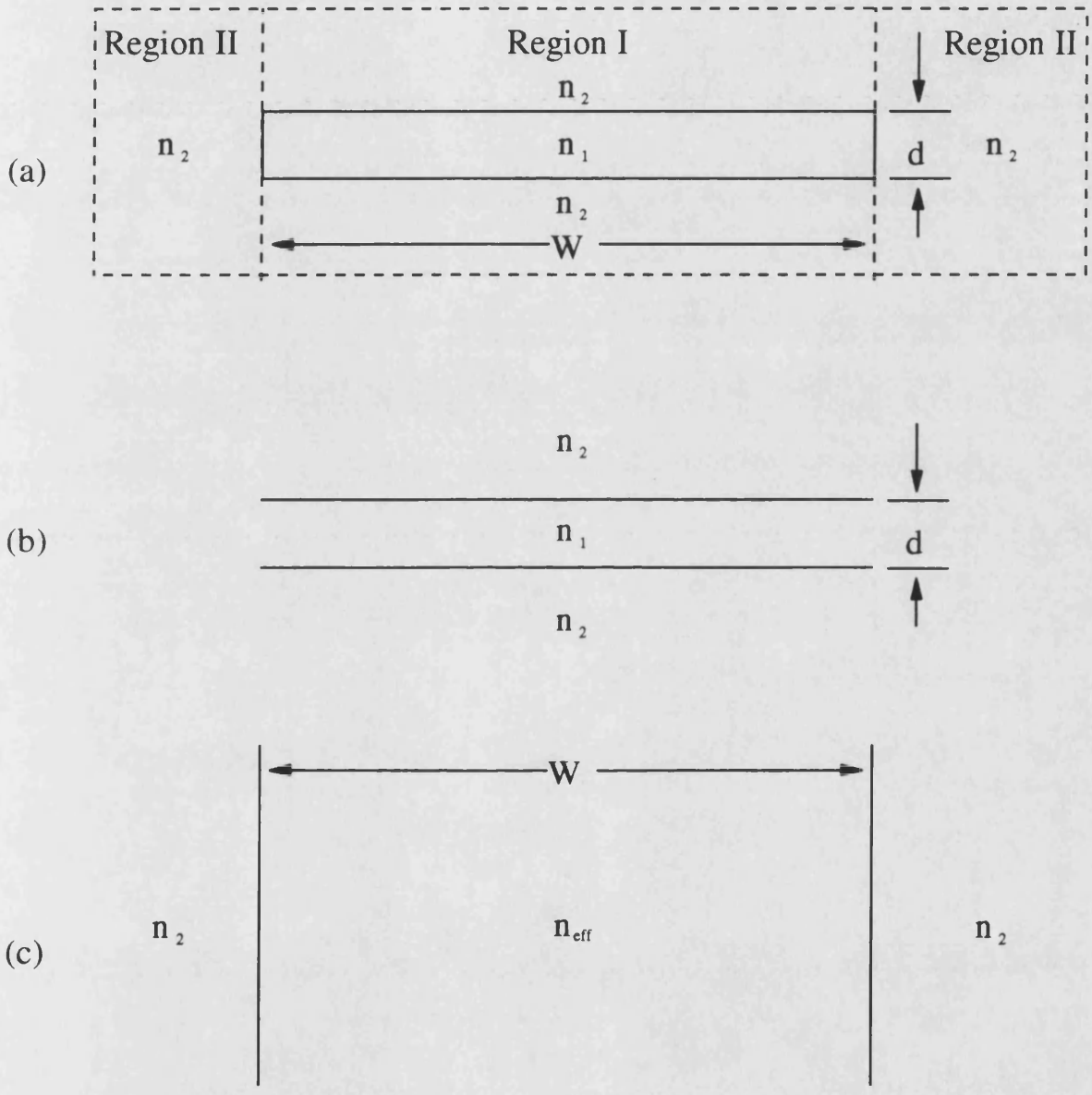

Figure 5.1. The Effective Index Method. (a) Buried ridge waveguide; (b) transverse slab waveguide of thickness d; (c) lateral slab waveguide with thickness W.

where k_0 is the wave number, ε the dielectric permittivity of the material and β the propagation constant. A sinusoidal field variation has been assumed in the longitudinal z direction, $\overline{E}(r) = E(x,y)\exp(j\beta z)$. Using the assumption that the variation of $\varepsilon(x,y)$ is slow in the lateral direction, the electric field may be approximated by

$$E(x,y) = F(x)G(x,y) \tag{5.3.2}$$

which may be substituted into equation (5.3.1) to obtain

$$\frac{1}{F}\frac{d^2F}{dx^2} + \frac{1}{G}\frac{\partial^2 G}{\partial y^2} + [k_0^2\varepsilon(x,y) - \beta^2] = 0 \tag{5.3.3}$$

where it has been assumed that $\partial^2 G/\partial x^2$ is negligible. The first step in the EI approximation is to solve for the transverse field $G(x,y)$ using the waveguide of figure 5.1(b), to obtain the effective propagation constant $\beta_{eff}(x)$ for each separate region of the waveguide, where

$$\frac{\partial^2 G}{\partial y^2} + [k_0^2\varepsilon(x,y) - \beta_{eff}^2(x)]G = 0 \tag{5.3.4}$$

An effective index for the guide may then be defined, where

$$n_{eff}(x) = \beta_{eff}(x)/k_0 \tag{5.3.5}$$

For the buried strip waveguide of figure 5.1 there are three separate regions in the lateral direction. However, the waveguide is degenerate (all indices are the same) in the regions marked II, and so the effective index in these regions is equal to the bulk index. The effective index calculated for region I is used as the refractive index of the core region of the lateral guide (figure 5.1(c)), and the lateral field distribution, $F(x)$, may be obtained from

$$\frac{d^2F}{dx^2} + [\beta_{eff}^2(x) - \beta^2]F = 0 \qquad (5.3.6)$$

From the solution of the two equations (5.3.4) and (5.3.6) the transverse and lateral modes of the laser may be found. It should be noted that to obtain the TE solutions of the rectangular waveguide, it is necessary to use the TE solutions for the first waveguide and the TM solutions of the second. The method is very rapid (requiring in this case only two solutions of the one dimensional wave equation) and has reasonable accuracy, however it relies on several approximations which may not be valid. Most notably, the method breaks down for modes near to cut-off (where much of the optical field extends outside the core region and into the cladding regions) and for structures whose outer slab regions are cut-off.

A schematic of the CM laser is given in figure 5.2(a). This structure can be approximated for waveguiding purposes by the structure shown in figure 5.2(b), where it has been assumed that the field decays sufficiently to be neglected at the sloping mesa edges. This simplifies the structure and, provided that the core region is sufficiently far from the sloping edge of the mesa, should not reduce the accuracy of the solution. It can be seen from the figure that the two outer slab regions consist of an InP/air/InP 'guide', which, because of the relative indices of the component parts, will not support any guided modes and are therefore cut-off. Also, in the structures analysed in this work, the second order mode is often near to cut-off. It would therefore appear that the effective index method would be a poor choice in this case.

It is, however, possible to analyse this structure by the EI method, by considering the complementary waveguide of 5.2(c). Using this technique, waveguiding in CM lasers with no regrowth (so called "mushroom stripe" lasers) was analysed by Amann [7], who compared the results obtained by the EI method to those obtained by a more accurate

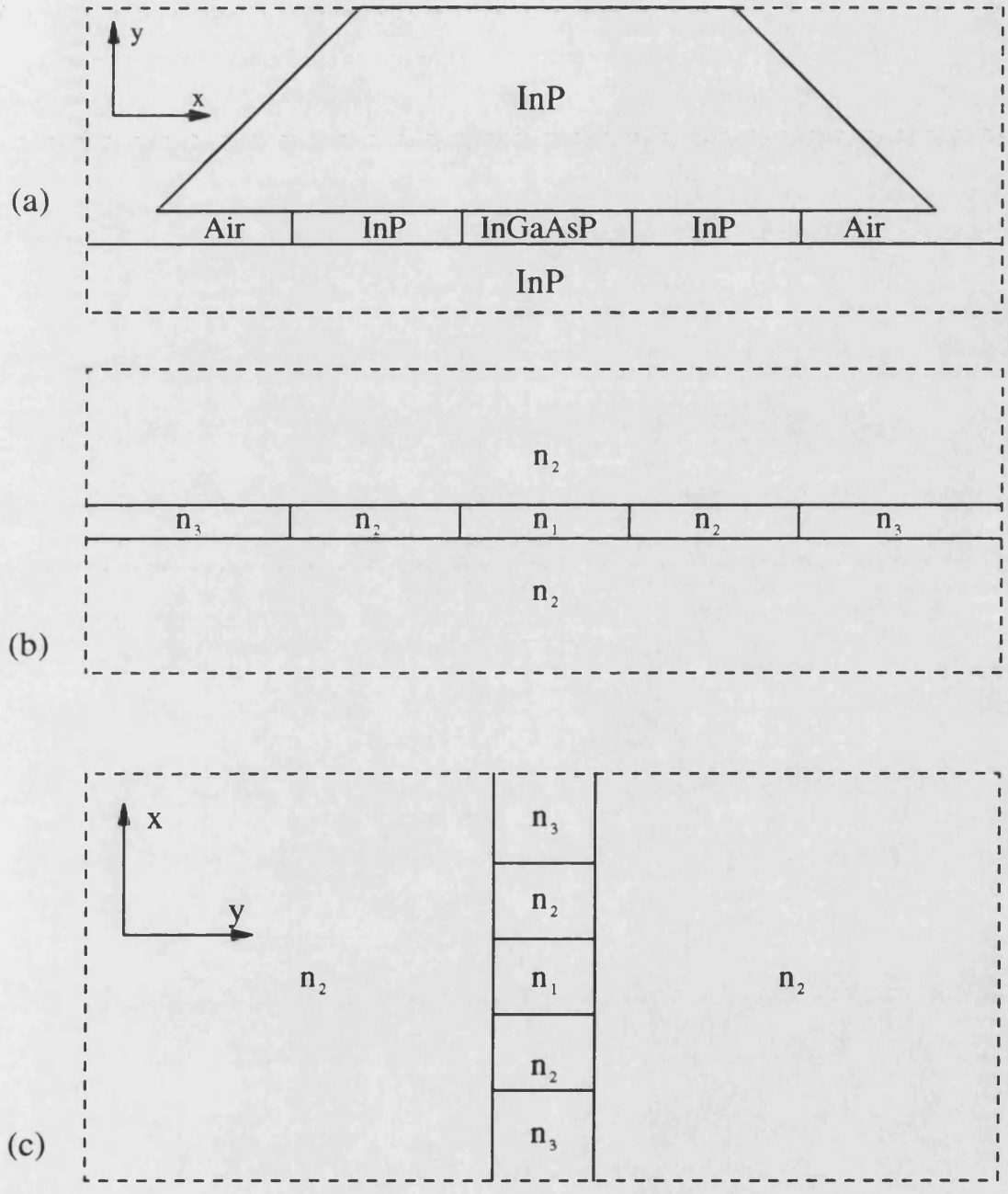

Figure 5.2. (a) The constricted mesa laser. (b) The equivalent waveguide (c) The waveguide model needed to apply the EI method.

technique. Amman's analysis shows that the EI method does indeed provide very poor solutions for guides of width less than 3μm, even for the fundamental mode. Such lack of accuracy in a self-consistent model will lead to inaccuracies in both electrical and optical solutions. A more accurate, but still rapid method was required, and the WI method, which is explained in the next section, was chosen as fitting both the criteria.

5.4 The Weighted Index method

The Weighted Index method was proposed by Kendall *et al* in 1987 [5], and like the Effective Index method assumes that the field may be split into two components. The weighted index method is an iterative technique, and obtains the best separable solution to the scalar Helmholtz equation. For the WI method, the separation used is

$$E(x,y) = F(x)G(y) \tag{5.4.1}$$

Substituting this into the scalar Helmholtz equation, (5.3.1), gives

$$G\frac{d^2F}{dx^2} + F\frac{d^2G}{dy^2} + \{k_0^2\varepsilon(x,y) - \beta^2\}FG = 0 \tag{5.4.2}$$

Multiplying (5.4.2) by G and integrating with respect to y one obtains

$$F''\int_{-\infty}^{+\infty} G^2 dy + F\int_{-\infty}^{+\infty} G''G\,dy = F\beta^2\int_{-\infty}^{+\infty} G^2 dy - F\int_{-\infty}^{+\infty} G^2 k_0^2\varepsilon(x,y)dy \tag{5.4.3}$$

where F'' is d^2F/dx^2 and G'' is d^2G/dy^2. Without loss of generality, the fields in the x and y directions may be normalised using $\int F^2dx = 1$, $\int G^2dy = 1$, which implies an overall normalisation $\iint E^2dxdy = 1$. Simplifying (5.4.3) using the normalisation condition, and rearranging, it can be shown that

$$F'' + F\int_{-\infty}^{+\infty} G^2 k_0^2 \varepsilon(x,y)dy = F\left[\beta^2 - \int_{-\infty}^{+\infty} GG''dy\right] \tag{5.4.4a}$$

A similar equation may be found for G, where

$$G'' + G\int_{-\infty}^{+\infty} F^2 k_0^2 \varepsilon(x,y)dx = G\left[\beta^2 - \int_{-\infty}^{+\infty} FF''dx\right] \tag{5.4.4b}$$

These are two, coupled, one dimensional scalar wave equations, which may be written in the form

$$F'' + Fk_x^2 = F\alpha_1^2 \tag{5.4.5a}$$

$$G'' + Gk_y^2 = G\alpha_1^2 \tag{5.4.5b}$$

It can be seen, by comparison of coefficients between equations (5.4.4a,b) and (5.4.5a,b), that the propagation constants $\alpha_{1,2}$ and "index" terms $k_{x,y}$ in equation (5.4.5) are related to (or weighted by) the field in the direction perpendicular to the direction of solution. For each equation, if the permittivity distribution and the field in the direction perpendicular to the direction of solution is known, $k_{x,y}$ may be calculated, and thus the respective $\alpha_{1,2}$ may be found for each mode supported. From this it is possible to calculate the modal propagation constant, β, by differentiation of the field. However, we seek a solution for β in terms of the individual propagation constants, $\alpha_{1,2}$, and other terms that are more readily evaluated. Multiplying (5.4.4a) by F, integrating with respect to x and using the normalisation condition $\int F^2 dx = 1$, gives

$$\beta^2 = \int_{-\infty}^{+\infty}\int_{-\infty}^{+\infty} F^2 G^2 k_0^2 \varepsilon(x,y)dxdy + \int_{-\infty}^{+\infty} FF''dx + \int_{-\infty}^{+\infty} GG''dy \tag{5.4.6}$$

(the same equation is obtained by multiplying (5.4.4b) by G and integrating with respect to y). Substituting the values of α_1^2 and α_2^2 into (5.4.6) gives

$$\beta^2 = \alpha_1^2 + \alpha_2^2 - \int_{-\infty}^{+\infty}\int_{-\infty}^{+\infty} F^2 G^2 k_0^2 \varepsilon(x,y)\,dxdy \tag{5.4.7}$$

In other words, β can be obtained from the individual propagation constants, the index distribution, and the fields.

If a piecewise constant distribution is assumed for ε, as shown in figure 5.3(a) for the CM waveguide, such that the guide is divided into a grid of p regions in the x-direction and q regions in the y-direction, with the permittivity in each region being designated ε_{pq}, one may write, with reference to equations (5.4.4) and (5.4.7)

$$\frac{d^2F}{dx^2} + F\left\{\sum_q w_{yq} k^2 \varepsilon_{pq}\right\} = F\alpha_1^2 \tag{5.4.8}$$

$$\frac{d^2G}{dy^2} + G\left\{\sum_p w_{xp} k^2 \varepsilon_{pq}\right\} = G\alpha_2^2 \tag{5.4.9}$$

$$\beta^2 = \alpha_1^2 + \alpha_2^2 - \sum_p \sum_q w_{xp} w_{yq} k^2 \varepsilon_{pq} \tag{5.4.10}$$

where the weights, w_{xp} and w_{yq} are defined as

$$w_{xp} = \int_{x_p}^{x_{p+1}} F^2 dx \tag{5.4.11}$$

$$w_{yq} = \int_{y_q}^{y_{q+1}} G^2 dx \tag{5.4.12}$$

These equations are identical to equations (21), (22), and (23) of reference [2], which have been derived using a variational method. The solution technique is illustrated in figure 5.3 for the CM laser, and proceeds as follows. Initially a distribution for one of the weighting terms, e.g. w_{xp}, must be assumed. A sensible choice would be $\int F(x)^2 dx = 1$

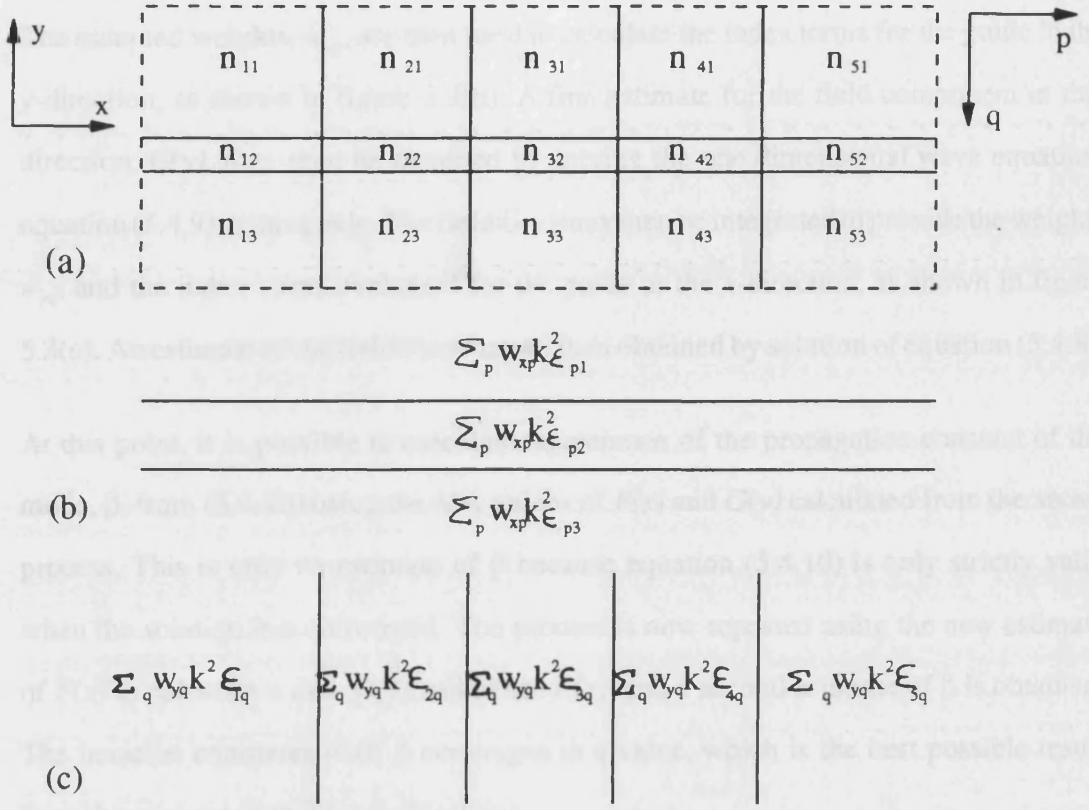

Figure 5.3. The Weighted Index method. (a) The equivalent waveguide for the CM/BRS laser. (b) The waveguide in the y-direction. (c) The waveguide formed in the x-direction.

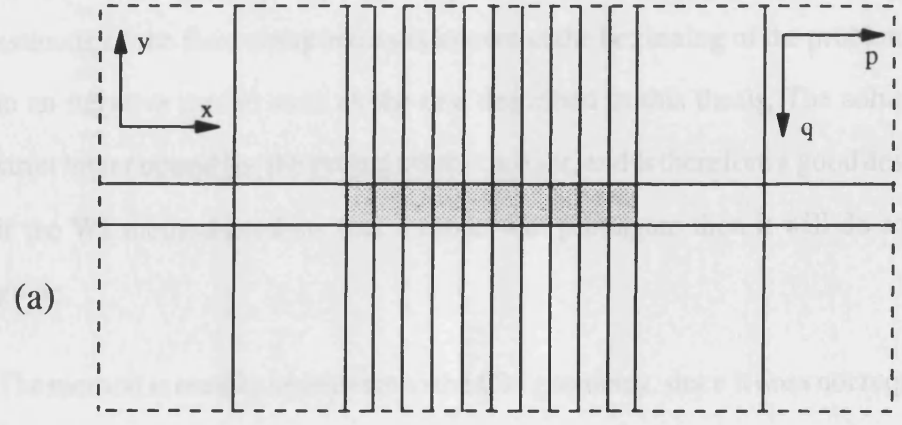

Figure 5.4 The weighted index model for the CM/BRS laser. In the active layer (shaded) the refractive index distribution is approximated a series of sections with their permittivity fixed by the carrier density.

in the core region and 0 elsewhere (remembering that $F(x),G(y)$ are normalised variables). The assumed weights, w_{xp}, are then used to calculate the index terms for the guide in the y-direction, as shown in figure 5.3(b). A first estimate for the field component in this direction, $G(y)$, may then be obtained by solving the one dimensional wave equation, equation (5.4.9) in this guide. The field $G(y)$ may then be integrated to provide the weights w_{yq}, and the index terms evaluated for the guide in the x-direction, as shown in figure 5.3(c). An estimate of the field $F(x)$ may be then obtained by solution of equation (5.4.8).

At this point, it is possible to calculate an estimate of the propagation constant of the mode, β, from (5.4.10) using the new values of $F(x)$ and $G(y)$ calculated from the above process. This is only an estimate of β because equation (5.4.10) is only strictly valid when the solution has converged. The process is now repeated using the new estimate of $F(x)$ to calculate a new $G(y)$ and hence $F(x)$, and a second estimate of β is obtained. The iteration continues until β converges to a value, which is the best possible result from the trial solution $E(x,y)=F(x)G(y)$.

Solution is rapid and requires very little computational time. In fact, the main computational effort is in the solution of the one dimensional scalar wave equations and simple integrations to calculate the weights. The solution is especially rapid when a good estimate of the field components is known at the beginning of the problem, as is the case in an iterative model such as the one described in this thesis. The solution provides a strict lower bound for the propagation constant, and is therefore a good design parameter; if the WI method predicts that a mode will propagate then it will do so in a practical guide.

The method is readily applicable to the CM geometry, since it does not require evaluation of the propagation constants of the cut-off outer slab guides as is the case with the EI method. The WI method also degrades slowly near to cut off of modes because the optical

field in all regions is taken into account in the analysis. The degradation of the solution is due to the fact that near to cut off the field distribution is no longer well described by a separable solution. The method is therefore well suited to the requirements of the self-consistent model, satisfying both the requirements of speed and of accuracy. The next section describes how the WI method was implemented.

5.5 The waveguide solution

The WI method relies on the solution of the scalar Helmholtz equation in one dimensional waveguides. In order to apply the method, the wave equation solution must be able to provide the optical field distribution and the propagation constant of the mode which is sought. Because the permittivity in the active layer depends on the carrier distribution, which is a complex function of distance, the wave equation is non-linear. The carrier density equation is solved by a finite difference technique, and hence the carrier density is only known at discrete points. The active layer permittivity is likewise only known at these points, and a numerical method of solution is required.

For the WI method, the waveguide must be split into rectangular regions with constant permittivity within each region. Outside the active layer the permittivity is set by the bulk permittivity of the material in that region. Inside the active region the model assumes that the active layer is split into many rectangular sections of depth equal to that of the active region, and width set by the finite difference mesh used to calculate the carrier density. In each of these sections the refractive index distribution is determined from the carrier density, and is assumed to be constant within the section.

A schematic diagram of the two dimensional waveguide used in the modelling of the optical properties of the BRS and CM lasers is shown in figure 5.4. The model ignores the effects of the metallisation and the sloping sidewalls of the CM laser, an assumption

which is valid if the confining layers are thick and the distance between the edge of the active layer and the sloping sidewalls is sufficient (approximately 0.5μm). The sloping sidewalls could be accounted for in the WI solution by assuming a staircase profile for the permittivity, but this would increase the complexity of the model and the time to obtain a solution for little or no gain in accuracy.

5.5.1 Wave equation solution technique

The WI method requires the solution of the one dimensional wave equation

$$\frac{d^2E(x)}{dx^2} + [k_0^2\varepsilon(x) - \beta^2]E(x) = 0 \qquad (5.5.1.1)$$

in multi-layer slab waveguides. This is a standard eigenvalue problem which results in a set of solutions, $E_1(x)$, $E_2(x)$, $E_3(x)$, etc. which represent the distributions of the optical modes corresponding to the discrete values of β for which the solution is valid. Several numerical techniques are available which could provide a solution of the wave equation, the method of solution which has been chosen is the shooting method. This method is readily applied to non-linear equations if a good initial estimate of the eigenvalue to be obtained is known, and can be used to solve simultaneously for the optical field and the propagation constants of the modes.

In the shooting method an initial estimate of the eigenvalue (in this case β_{m1}) is required, and this may be found either by prior knowledge of the problem or by some other technique. Using this estimate of the eigenvalue, the wave equation is solved by an initial value solution technique, with the boundary conditions at one edge of the region being

used as initial conditions. The solution at the other edge of the region is compared to the boundary condition to be applied there, and the discrepancy between the calculated and desired boundary value used to improve the initial guess of the eigenvalue.

In the following derivation a uniform mesh is assumed for simplicity of explanation, however the solution method uses an adaptive grid, of varying mesh size, to provide an accurate solution. Let the region of interest, $0 \le x \le h_x(M-1)$ be discretised into *(M-1)* elements each of length h_x. The symmetry of the problem is used to halve the required mesh size. At the boundary nodes it is assumed that the boundary conditions

$$(dE/dx)\,|_{x=0} = 0: \quad (dE/dx)\,|_{x=h_x(M-1)} = 0 \quad (even \quad modes) \qquad (5.5.1.2)$$

$$(dE/dx)\,|_{x=0} = 0: \quad E\,|_{x=h_x(M-1)} = 0 \quad (odd \quad modes)$$

exist. It is also reasonable to assume, in this problem, that the optical field has decayed to a small value at the initial node corresponding to $x = 0$ i.e. $E = 10^{-4}$.

The initial value solution technique employed in this work to solve the wave equation is the Runge-Kutta method. The accuracy of the wave equation solution determines the accuracy of the eigenvalue obtained, and since this value is important in determining whether a mode is lasing, a high degree of accuracy is required. A fourth order method is used to provide a local truncation error of order h^5 and an estimate of the error. This estimate of the error may be used to obtain in an adaptive mesh scheme to reduce the error to the order of h^6. This is a standard technique and is described in, for example, reference [7].

The Runge-Kutta solution is stepped through the solution interval and the calculated boundary condition at the boundary node of the region is compared to the known boundary condition here, namely $dE(hx(M-1))/dx = 0$ for even modes or $E(hx(M-1)) = 0$ for odd modes.

If the calculated boundary condition does not agree with the desired value within an acceptable tolerance, then a second value of β, β_{m2}, close to the original value is chosen and the set of calculations repeated. If the boundary condition is not satisfied for this new value of β then a further estimate of β is made using the following strategy

$$\frac{[dE(hx(M-1))/dx]}{\Delta\beta} = \frac{[dE(hx(M-1))/dx]\,|_{\beta=\beta_{m1}} - [dE(hx(M-1))/dx]\,|_{\beta=\beta_{m2}}}{\beta_{m1}-\beta_{m2}} \qquad (5.5.1.3)$$

and

$$\beta_{m3} = \beta_{m2} - \left[\frac{[dE(hx(M-1))/dx]_{\beta=\beta_{m2}}}{\{\Delta dE(hx(M-1))/dx\}/\Delta\beta}\right] \qquad (5.5.1.4)$$

From this point, the new estimate of β is made automatically by expression (5.5.1.4) and the entire set of calculations for $E_m(x)$ are repeated until the boundary conditions at node M are met. The technique is insensitive to boundary locations and is efficient, and the mesh size choice is automated.

The initial estimate of the eigenvalue for the fundamental mode is taken as the highest value of dielectric constant, for the first order mode the initial estimate is taken as the eigenvalue calculated for the fundamental mode. In the self-consistent model subsequent solutions use the value calculated from the previous iteration, and the solution is therefore faster. The WI method requires totally separate solutions for the fundamental and first order modes, i.e. both the lateral and the transverse field distributions must be calculated separately for each mode, unlike the EI method. At all stages a check is made to ensure that the solution is converging to the correct mode.

As with all numerical methods, it is important to determine the tolerance within which the solution should be obtained. For the weighted index method, two waveguides are solved, one in the horizontal and one in the vertical direction, Each of these waveguides has different dimensions, and therefore requires a different step size. The solution technique employs adaptive step sizes, limiting the error to within a fixed tolerance, and the solution can therefore be made very accurate. The required tolerance of the solution is limited by the expected accuracy of the Weighted Index method, which is estimated from the tables of reference [3] as 10^{-4}. To achieve this accuracy of final solution, the tolerance of the waveguide solutions was therefore limited to $<10^{-6}$.

The program for the weighted index method follows the lines of the solution technique outlined in section 5.3. A flow chart of the actual program is shown in figure 5.5. The integration of the functions to obtain the weights is carried out numerically, as an integral part of the Runge-Kutta solution method.

5.5.2 Results for guides of real permittivity

There has only been one published study of waveguiding in CM lasers [8]. This concentrated on the case where the regrown InP regions around the active layer, which are formed by mass transport or vapour phase epitaxy of InP, are of zero width, the so called "mushroom stripe" configuration. This study demonstrated the fact that the EI method gives poor results in such structures, and showed that the fundamental (zero order) mode becomes cut-off for guides of less than 0.5μm. If the regrown region is assumed to be of infinite extent, the structure becomes a simple buried ridge, as used in the BRS laser. There have been previous studies of waveguiding such devices e.g. [9],[10], again showing that the accuracy of the EI method may not be sufficient for laser design,

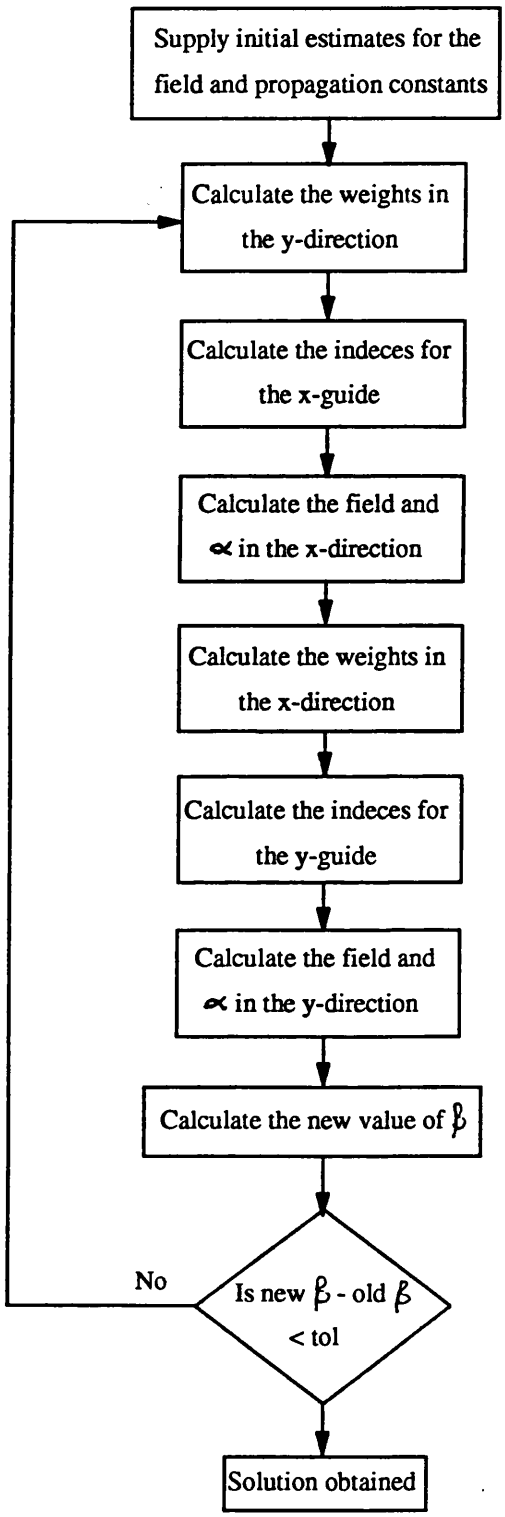

Figure 5.5. Flow chart of the weighted index solution

however, it has been shown [6] that in such structures the WI method produces very good results. So far, however, no studies have been conducted to examine the effect of the regrown region width on the waveguiding properties of the CM laser.

This section presents results from the WI model showing the effect on the propagation constant and confinement factor of altering the waveguide dimensions. All results assume no carriers are present in the active layer, and therefore all the permittivities are assumed to be real, and are fixed at the bulk values. The undercut in the laser is assumed to be filled with a protective SiO_2 coating, and the cladding layers are assumed to be semi-infinite in extent, as is the regrown region unless otherwise stated. The relevant refractive indices and nominal values of the waveguide parameters are shown in table 5.1.

Figure 5.6 shows the effect of the width of the regrown regions of the CM laser on the normalised propagation constant (β/k), and figure 5.7 the effect on the mode confinement, for the fundamental and first order modes. Both parameters are bounded by the values obtained at one extreme for a guide with no regrown region, and at the other by a guide with a fully regrown region (i.e. the buried ridge waveguide). It can be seen that for regrown widths greater than 0.5μm and guide widths greater than 0.5μm the effect of the regrown width on the mode characteristics is minimal, and the propagation constant takes the value for a fully buried guide. For regrown widths below 0.5μm the propagation constant begins to drop, and the confinement rise with decreasing regrown width, as the field penetrates into the $Si0_2$ region.

As would be expected, the effect on the propagation constant and confinement is more noticeable for the first order mode and for narrower guides, where the mode is initially less confined to the active region. However, it can be seen from figure 5.6(b) that for regrown widths greater than 0.5μm the effect of the regrown width on the propagation

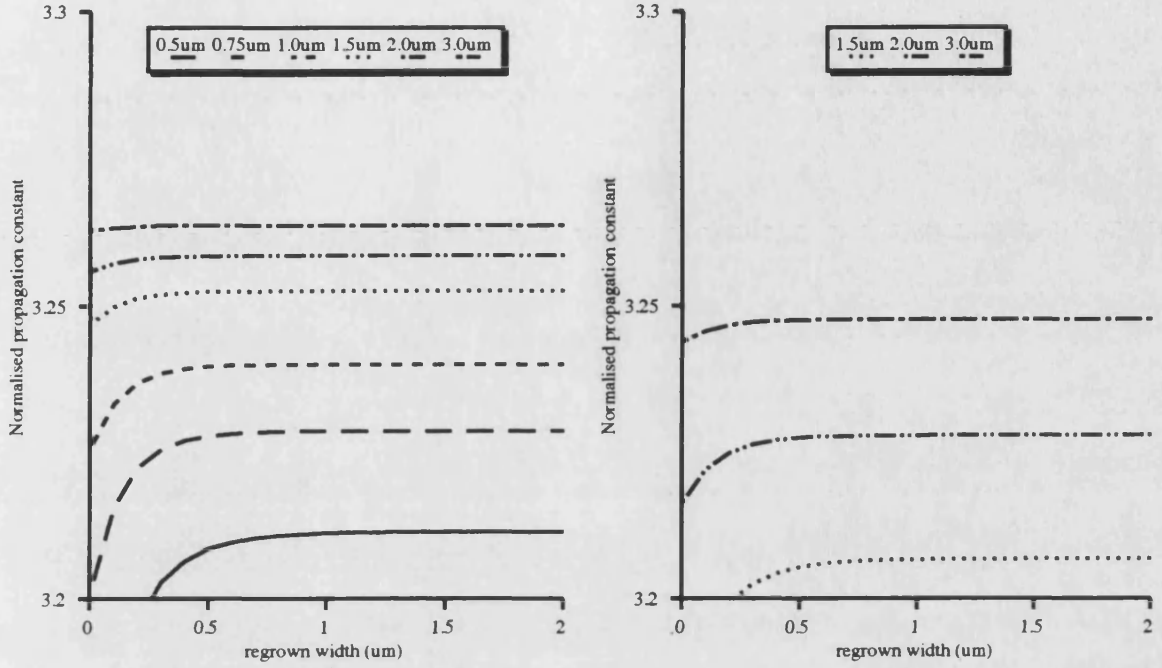

Figure 5.6 Normalised propagation constant vs regrown layer width with active layer width as a parameter. (a) TE00 (b) TE01

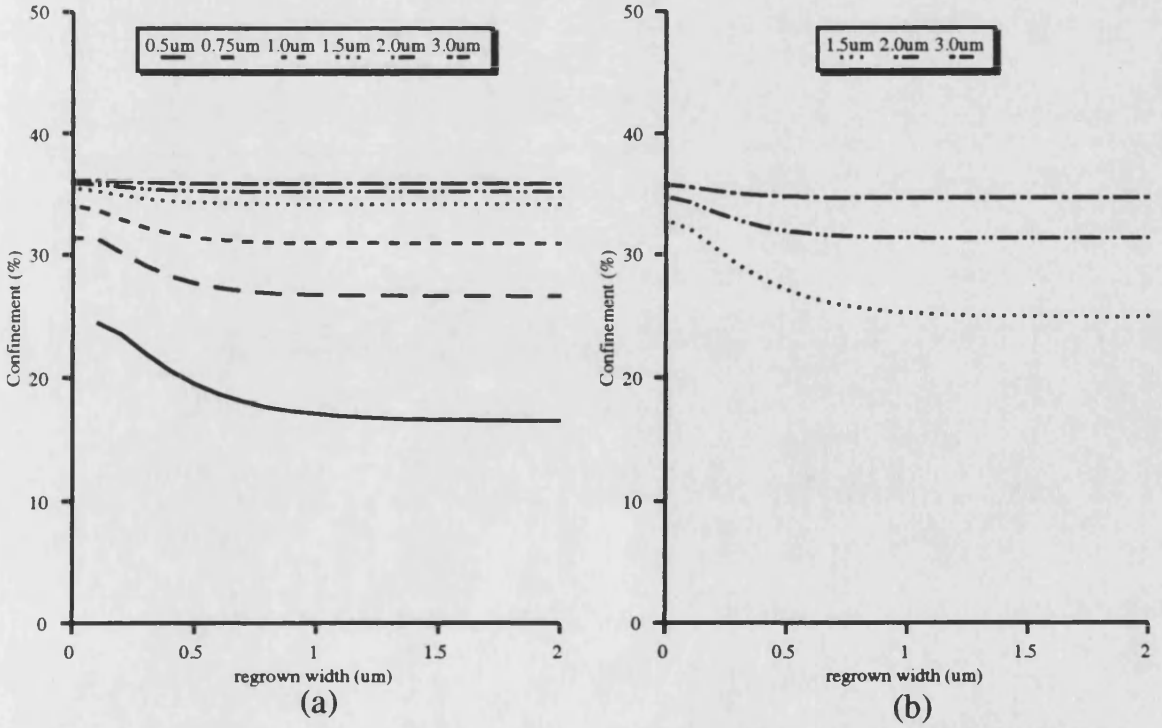

Figure 5.7 Confinement factor vs regrown layer width with active layer width as a parameter. (a) TE00 (b) TE01

constant of the first order mode is negligible, and from figure 5.7(b) that the effect on the confinement factor is small above a regrown width of 0.8μm. Therefore, unless the regrown region is extremely thin, the effects of the surrounding SiO_2 region can be ignored, but for very narrow (<0.8μm) regrown regions the effect must be included. Devices are sometimes fabricated with very narrow regrown regions in order to decrease the leakage current, and it is therefore necessary to be able to include the effects of the regrown region in the optical model.

For the rest of this chapter it is assumed that the regrown region is sufficiently wide to be able to ignore the SiO_2 region, and the modelling is therefore equally applicable to the BRS and CM laser structures. The effect on the propagation constant and mode confinement of varying the active layer width is shown in figures 5.8 and 5.9. Again the fundamental and first order modes are shown. It might be expected that for wide active region widths the propagation constant and confinement factor would tend towards the value for a one dimensional slab waveguide. However, the figures show that even for guides 3μm wide, the propagation constant, although tending towards the asymptotic value, is still increasing. This demonstrates that the guide must be treated in all calculations as a two dimensional guide.

The confinement curves of figure 5.9, unlike those for the propagation constant, tend towards their asymptotic values at reasonable values of guide width, the increase in confinement slowing rapidly as the guide width approaches 1.5μm for the fundamental mode and 2.0μm for the first order mode. Figure 5.9b also shows the cut-off widths of the first order mode are all below 1.6μm for active depths above 0.1μm indicating that it is possible to fabricate guides which will support only the fundamental mode, but for only very narrow guide widths.

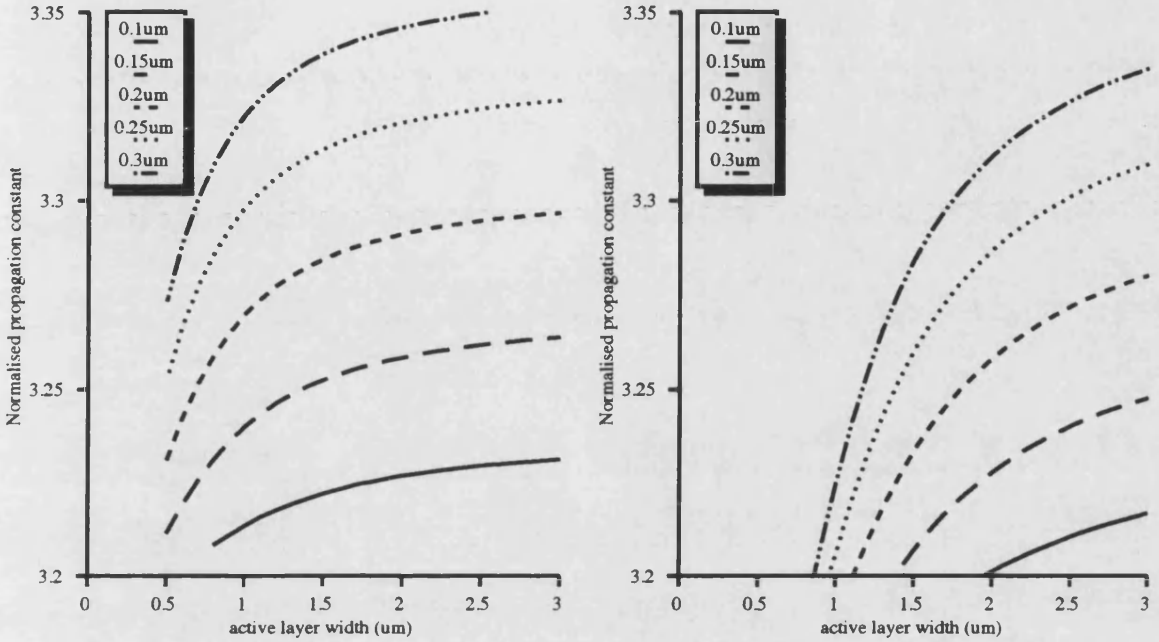

Figure 5.8 Normalised propagation constant vs active layer width with active layer depth as a parameter. (a) TE00 (b) TE01

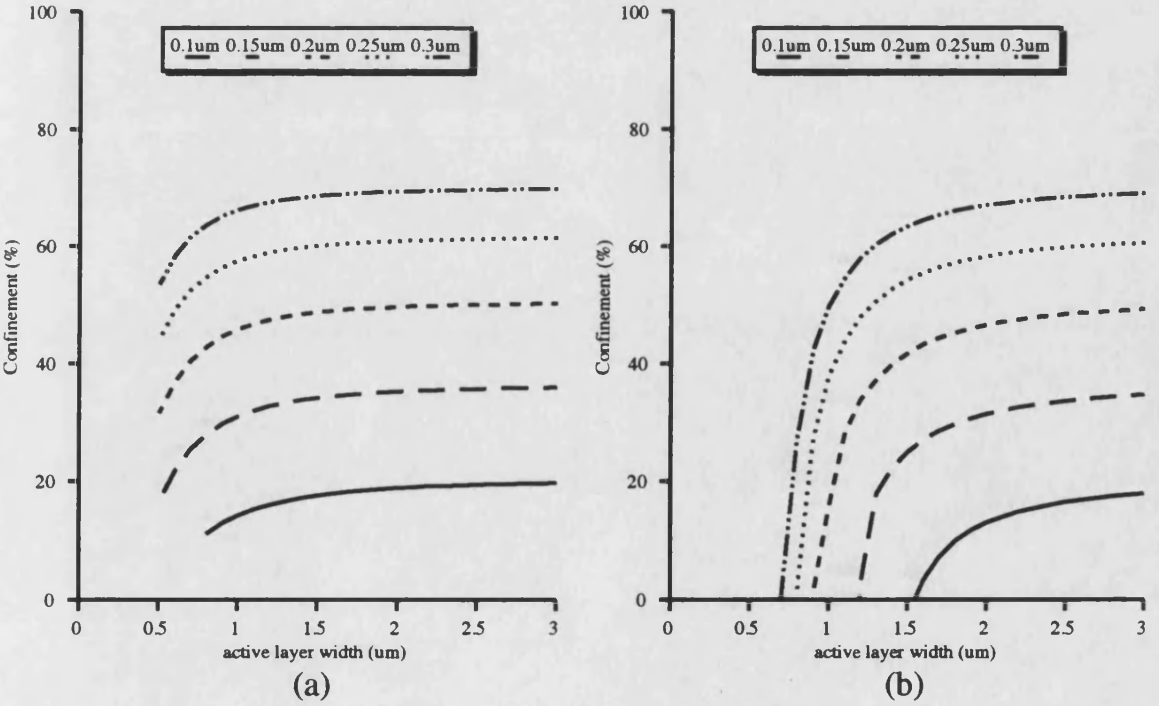

Figure 5.9 Confinement factor vs active layer width with active layer depth as a parameter. (a) TE00 (b) TE01

The data of figures 5.8 and 5.9 is replotted in figures 5.10 and 5.11 to show more clearly the effects of guide depth variations. The effect of guide depth on propagation constant and guide width is more marked than the effect of guide width, and both characteristics fail to reach their asymptotic values within a depth of 0.4μm. Again the first order mode is seen to propagate in narrow guides providing that the depth is sufficient. For a nominal guide depth of 0.15μm the first order mode will propagate for guides wider than 0.8μm. The first order mode may therefore play an important part in the lasing characteristics of devices, even if they have quite narrow active widths.

The intensity distribution of the fundamental and first order modes are shown in figure 5.12 for a waveguide of 2μm width and 0.15μm depth. The dotted region in the figure shows the waveguide layer. It can be seen that the field is almost totally confined to the guide region in the lateral direction, but extends for some distance in the transverse direction. The figure also shows pictorially the difference in confinement between the fundamental and first order modes that was seen in figures 5.9 and 5.11.

5.6 Waveguides with complex permittivity

In the previous section, all refractive indices were assumed to be real. However, it is necessary for the waveguide model to cope with the situation where carriers are present in the active region. The presence of carriers depresses the real part of the refractive index and also introduces a complex contribution. In section 4.4.3 gain guiding was considered, and it was noted that the theory for slab waveguides is equally applicable to waveguides of real or complex permittivity. However, the WI method has not previously been applied to situations where the refractive index is complex, and variational methods, of which the WI method is an example, have been criticised as not being valid for complex waveguides [4], although recently published [11] and unpublished

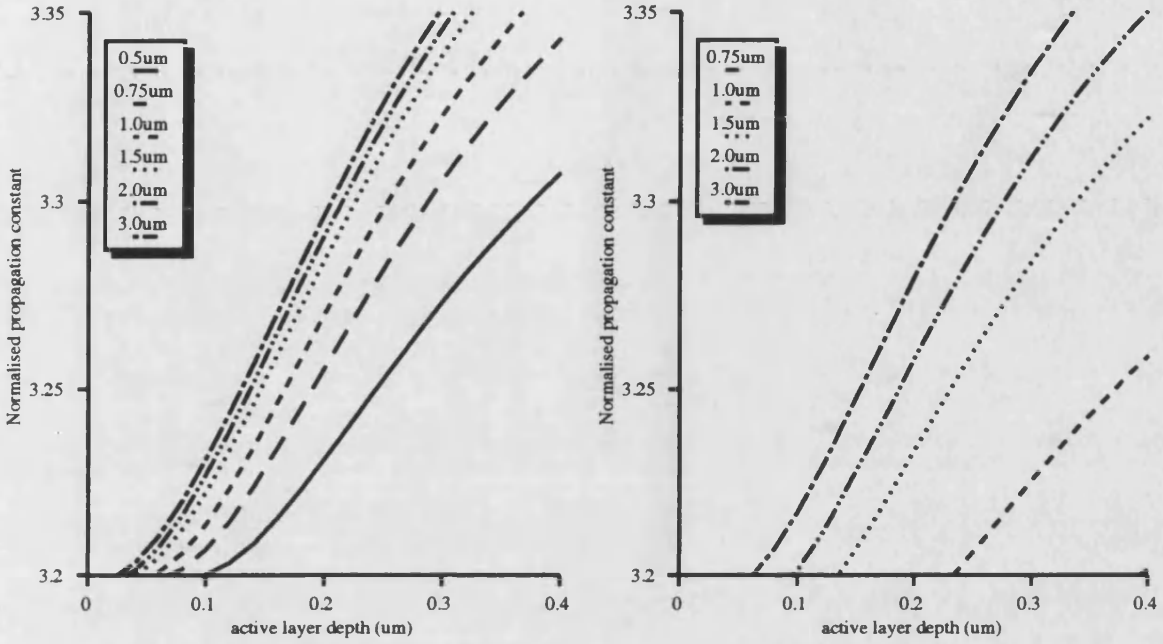

Figure 5.10 Normalised propagation constant vs active layer depth with active layer width as a parameter. (a) TE00 (b) TE01

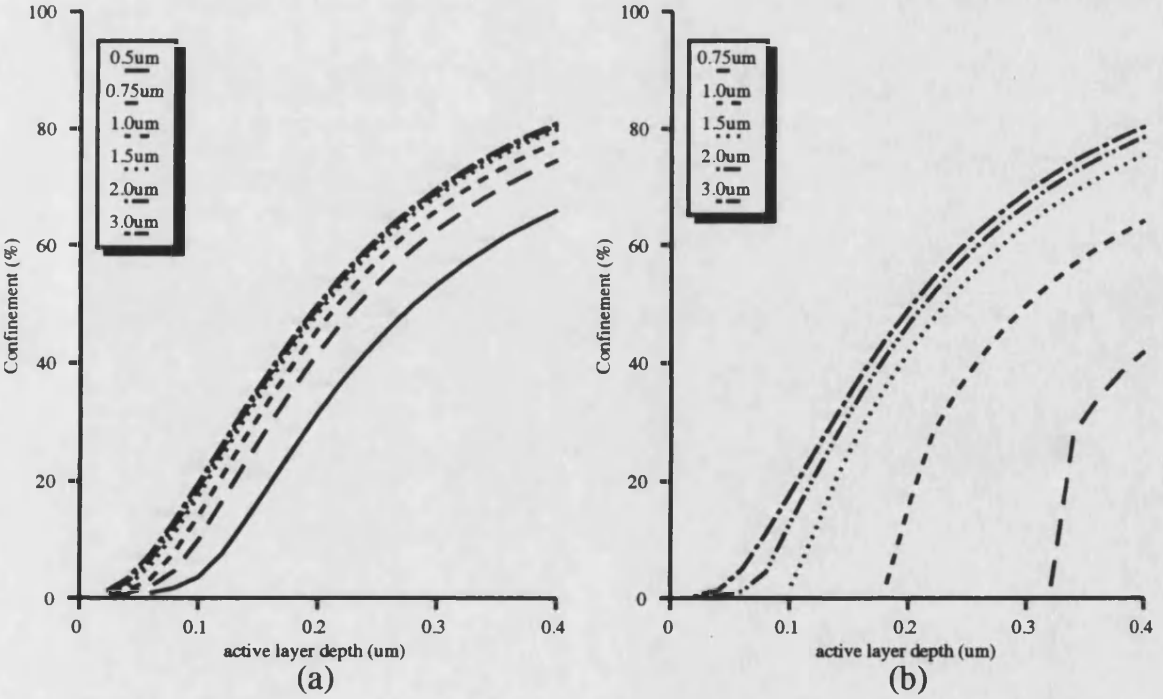

Figure 5.11 Confinement factor vs active layer depth with active layer width as a parameter. (a) TE00 (b) TE01

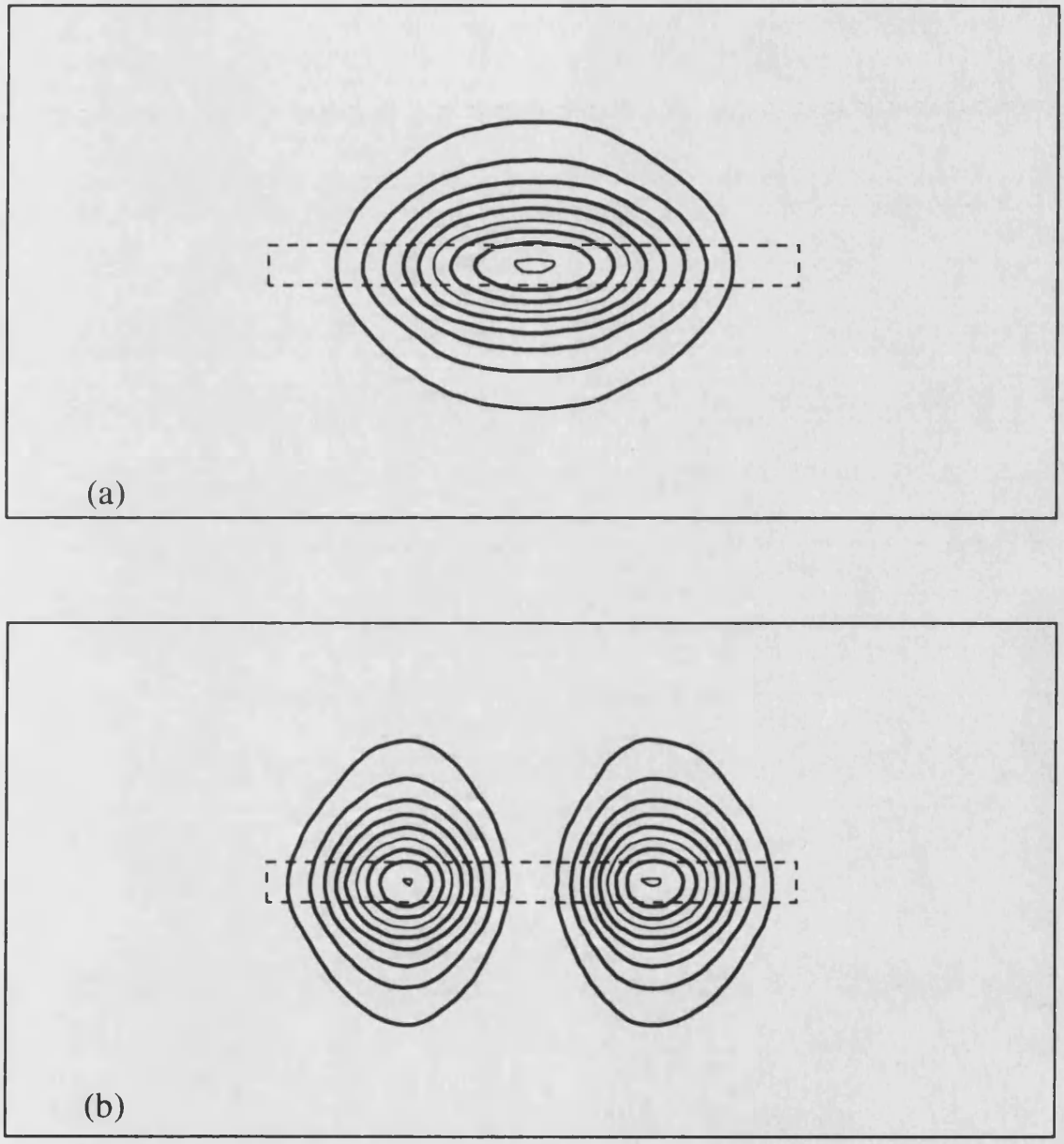

Figure 5.12 Intensity patterns for the fundamental (a) and first order (b) lateral modes. The contours are each represent one tenth of the intensity. The dotted line represents the waveguide region.

results have shown that such methods can provide accurate results. The WI method presented in this work avoids the use of the Rayleigh quotient, and therefore the criticisms of [4] are not applicable.

5.6.1 The complex Weighted Index method

Whereas other solution techniques such as the EI and finite element methods have been applied to waveguides with complex permittivities in the past, and are know to produce valid results, questions have been raised as to the validity of the WI method. This section demonstrates the validity of the Weighted Index method when derived for the case where the permittivity is complex. In the complex case, the field components E, F, and G are all complex, as is the propagation constant. The derivation follows the lines of section 5.4, and the derivation given here relies on this previous work. The field is again split into x and y components, such that

$$E(x,y) = F(x)G(y) \tag{5.6.1.1}$$

and using this separation, the wave equation may be written

$$G\frac{d^2F}{dx^2} + F\frac{d^2G}{dy^2} + \{k_0^2\varepsilon(x,y) - \beta^2\}FG = 0 \tag{5.6.1.2}$$

In section 5.4, equation (5.6.1.2) was multiplied by G and integrated with respect to y. Previously a normalisation of the form $\int AA\,dx = 1$ was used for the field components. With complex fields, this leads to the requirement that the complex part of the field integrates to zero, which is clearly wrong. Bearing this in mind, we chose to multiply equation (5.6.1.2) not by G, but by the complex conjugate of G, G^*. Integrating with respect to y gives

$$F''\int_{-\infty}^{+\infty} GG^* dy + F\int_{-\infty}^{+\infty} G''G^* dy = \tag{5.6.1.3}$$

$$F\beta^2\int_{-\infty}^{+\infty} GG^* dy - F\int_{-\infty}^{+\infty} GG^* k_0^2\varepsilon(x,y)dy$$

The normalisation condition must now be modified to take into account the different multiplication factor. The fields in the x and y directions are normalised using $\int FF^* dx = 1, \int GG^* dy = 1$, which implies an overall normalisation $\iint EE^* dxdy = 1$. This normalisation condition does not set any extra limits on the complex part of the field, as was the case previously. Following the derivation of section 5.4, equation (5.6.1.3) is simplified using the normalisation condition, and rearranged to obtain

$$F'' + F\int_{-\infty}^{+\infty} GG^* k_0^2\varepsilon(x,y)dy = F\left[\beta^2 - \int_{-\infty}^{+\infty} G'G^{*\prime} dy\right] \tag{5.6.1.4a}$$

A similar equation may be found for G, where

$$G'' + G\int_{-\infty}^{+\infty} FF^* k_0^2\varepsilon(x,y)dx = G\left[\beta^2 - \int_{-\infty}^{+\infty} F'F^{*\prime} dx\right] \tag{5.6.1.4b}$$

These are two, coupled, one dimensional scalar wave equations, which may be written in the form of equations (5.4.5a,b). Once again, we wish to find a solution for β, which may be obtained, c.f. equation (5.4.7) as

$$\beta^2 = \alpha_1^2 + \alpha_2^2 - \int_{-\infty}^{+\infty}\int_{-\infty}^{+\infty} FF^* GG^* k_0^2\varepsilon(x,y)dxdy \tag{5.6.1.5}$$

Finally, if a piecewise constant distribution is assumed for ε, as before, such that the guide is divided into a grid of p regions in the x-direction and q regions in the y-direction,

with the index term in each region set as ε_{pq}, then identical equations to equations (5.4.8) to (5.4.10) may be written. However, the weighting terms are subtly different, being obtained from

$$w_{xp} = \int_{x_p}^{x_{p+1}} FF^* dx \tag{5.6.1.6}$$

$$w_{yq} = \int_{y_q}^{y_{q+1}} GG^* dx \tag{5.6.1.7}$$

The equations for the weights deal with real variables, as AA^* must always be real, and the integrations are simple to perform mathematically. The Weighted Index may therefore be applied to waveguides of complex permittivity, but only if the change is made to the normalisation condition.

5.6.2 Results for guides of complex permittivity

Up to the present time, no results have been published for the WI method used in waveguides of complex permittivity. Such guides have, however, been analysed by other techniques [e.g. 10], and it is therefore useful to compare the results obtained from the complex WI method with those of reference [10]. Figures 5.13 and 5.14 show such a comparison, where the dotted lines show the data of figures 6 and 7 of reference [10]. It can be seen from the figres that there is very close agreement between the results of the complex WI method and complex finite element method. The figures also show that if the loss in the cladding region of the waveguide is only one order of magnitude less than the gain of the guiding region, then the loss has a minimal effect on the mode gain. It is assumed in all the following work that the loss of the cladding regions is negligible

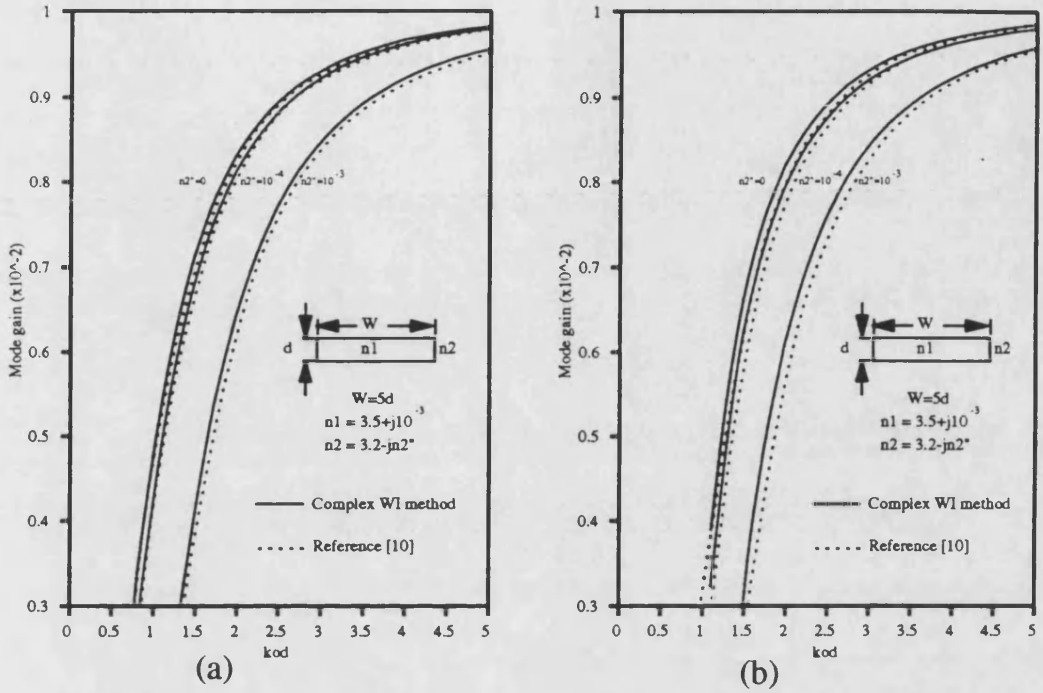

Figure 5.13 A comparison of the modal gain calculated by the complex weighted index method and the finite element method of reference [10]. (a) TE00 (b) TE01

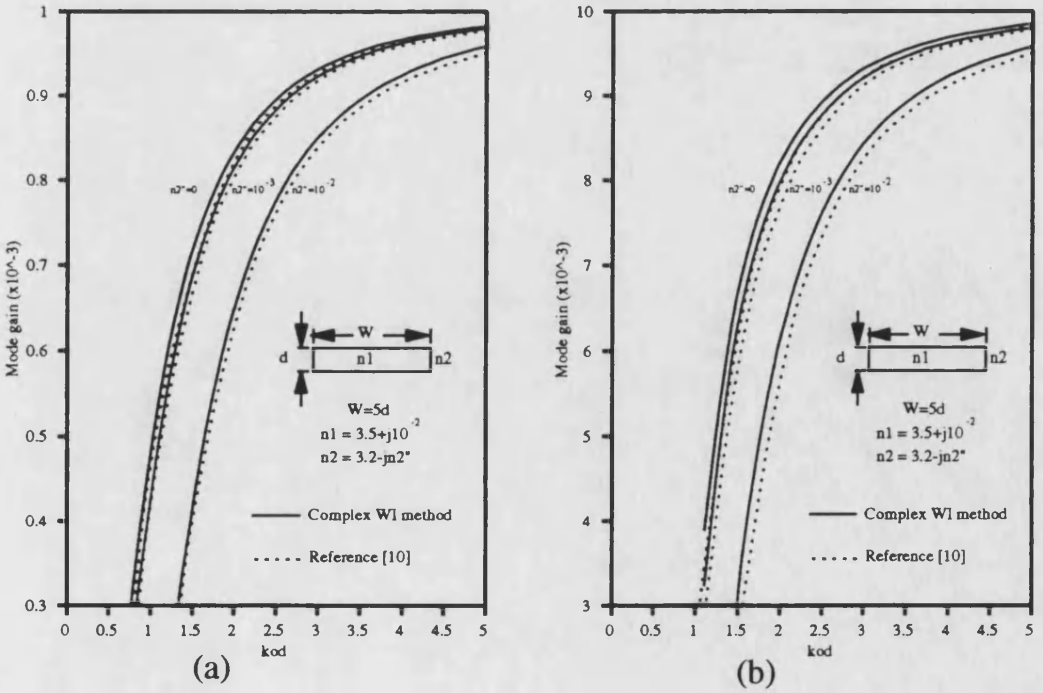

Figure 5.14 A comparison of the modal gain calculated by the complex weighted index method and the finite element method of reference [10]. (a) TE00 (b) TE01

The gain in semiconductor lasers is provided by the stimulated recombination of carriers, and the carriers have an effect not only on the imaginary part of the refractive index, but also on the real refractive index. In the rest of this section the WI method as derived in section 5.6.1 is applied to CM waveguides where the active layer material is assumed to have a permittivity related to the carrier density by

$$\varepsilon(x) = \left(n_a + \frac{an(x)}{2k_0} R + j \frac{g(x)}{2k_0} \right)^2 \qquad (5.6.2.1)$$

where n_a is the bulk refractive index of the active layer, $n(x)$ is the carrier density in the active layer, R is the ratio of real refractive index dependence on the carrier density, and is negative. The local optical gain is assumed to be a linear function of carrier density, $g(x) = an(x) - b$, where a and b are gain constants.

As with the modelling of leakage current in chapter 3, the simplifying assumption is made here that the lasing action pins the carrier density to a fixed value, which is assumed to be uniform across the active region. The guide geometry and index profile is otherwise the same as in section 5.5.2 and given in table 1, and full regrowth of material around the active region is assumed. Results are presented in this section showing the dependence of the real part of the propagation constant, and of the optical gain, on carrier density and guide geometry. The optical gain is found from twice the imaginary part of the propagation constant, as was demonstrated in section 4.3.2.

Figure 5.15 shows the effect of varying the carrier density on the real part of the normalised propagation constants of the fundamental and first order modes. It can be seen that increasing the carrier density decreases the real part of the propagation constant. This is a result of the depression of the real part of the active layer permittivity caused by the presence of carriers, which is seen in equation (5.6.2.1) (R is negative). The effect on the calculated real part of the permittivity of both modes is quite small, as can be seen

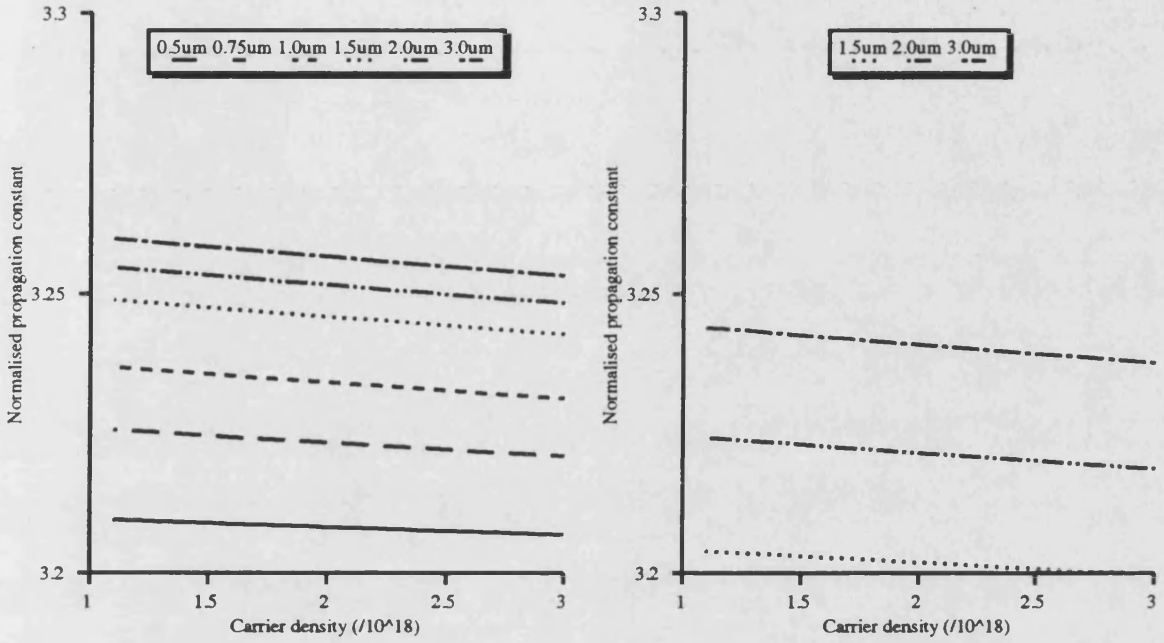

(a) (b)

Figure 5.15 Normalised propagation constant vs carrier density with active layer width as a parameter. (a) TE00 (b) TE01

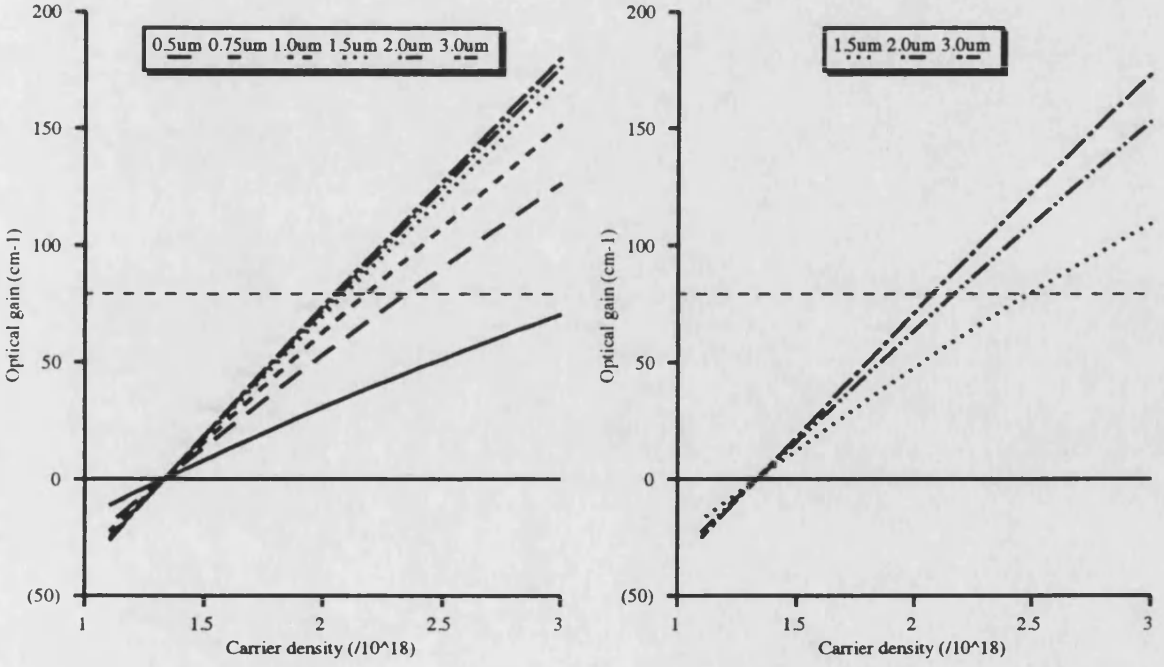

(a) (b)

Figure 5.16 Optical gain vs carrier density with active layer width as a parameter. (a) TE00 (b) TE01

from figure 5.15. This effect can, however, play an important part in the determination of the number of propagating modes. For example, it can be seen that, for the first order mode propagating in a guide of 1.5μm width, the propagation constant at a carrier density of $3x10^{18}cm^{-3}$ falls below that of the surrounding InP material, indicating that the mode is very close to cut-off.

Although the effect of the carriers on the real part of the propagation constant of the mode is small, figure 5.16 shows that as the carrier density is increased, the optical gain alters significantly. The change from negative (loss) below a carrier density of about $1.3x10^{18}cm^{-3}$ to gain occurs at the same point for all guide widths and for both modes. This is consistent with a first order perturbation analysis (as given for example in [12]) which shows that the modal optical gain, G, in such a buried ridge guide with constant local gain in the active region is given approximately by $G \approx \Gamma g = \Gamma(an(x) - b)$, where Γ is the confinement factor of the mode to the active region. Thus when the local gain is zero then the modal gain will also be zero.

The curves of figure 5.16 appear at first glance to be linear, however they are slightly sublinear, an effect which is more apparent for the first order mode. This can again be seen from the perturbation theory, since the confinement of the mode to the active cavity falls slightly with increasing carrier density due to the decrease in the real refractive index with carrier density. Figure 5.16 also shows that the narrower the active layer width, the higher is the carrier density required to obtain a certain gain. However, for the fundamental mode this effect is only significant for guides below 1.5μm wide, between 1.5μm and 3.0μm there is very little change.

The difference between the gain of the fundamental and second modes is often used in laser design to ensure that only one mode will lase, the second mode not having sufficient gain to overcome the cavity losses. The difference between the gains of the two modes

becomes more significant with decreasing guide width, and this means that narrower guides tend to support only a single lasing mode, despite the fact that the guide can allow more than one mode to propagate.

A typical figure for the overall cavity loss (internal losses and mirror losses) of an InP/InGaAsP buried heterostructure laser is $80cm^{-1}$ [13]. This level of gain is shown on figure 5.16 by the dashed horizontal line. It can be seen from the figure that the difference between the carrier densities required by the two modes at such a gain becomes appreciable for guides of width less than 2μm. This fact is used in laser design, and cavity widths of 2μm or less are most often used in buried heterostructure designs.

Figure 5.17 shows the effect of increasing carrier density on the real part of the propagation constant for variations of active layer depth. It can be seen that, again, the change in the real part of the refractive index is quite small. Figure 5.18 shows the effect on the optical gain. The cross over point between gain and loss is again fixed, for reasons stated previously, and as with figure 5.16 the difference between the gain for the various active depths increases with carrier density.

It can be seen from figure 5.18 that the gain can be increased by a factor of four by increasing the depth from 0.1μm to 0.3μm, a fact which is again related to the increased mode confinement for deeper active layers. It would seem that this could be of benefit in obtaining threshold laser gains at lower carrier injection, and therefore lead to lower threshold currents. However, an increase in the active region depth means that a greater current density is required to obtain the same carrier density. There is therefore an optimum value of active layer depth which will result in a minimum threshold current.

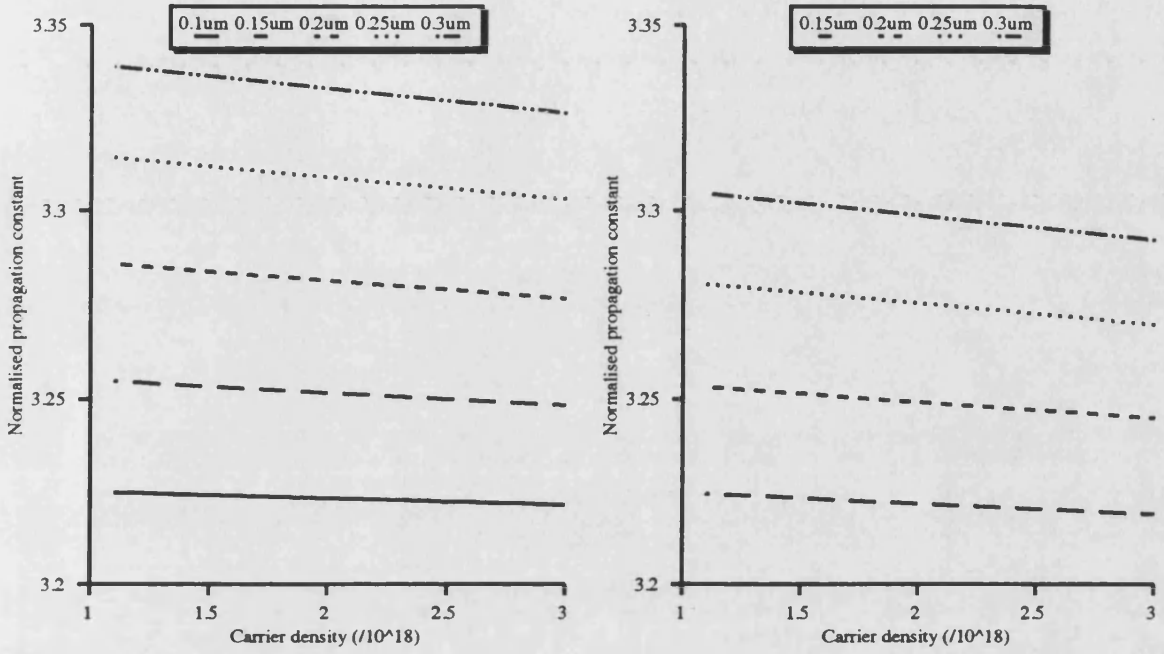

(a) (b)

Figure 5.17 Normalised propagation constant vs carrier density with active layer depth as a parameter. (a) TE00 (b) TE01

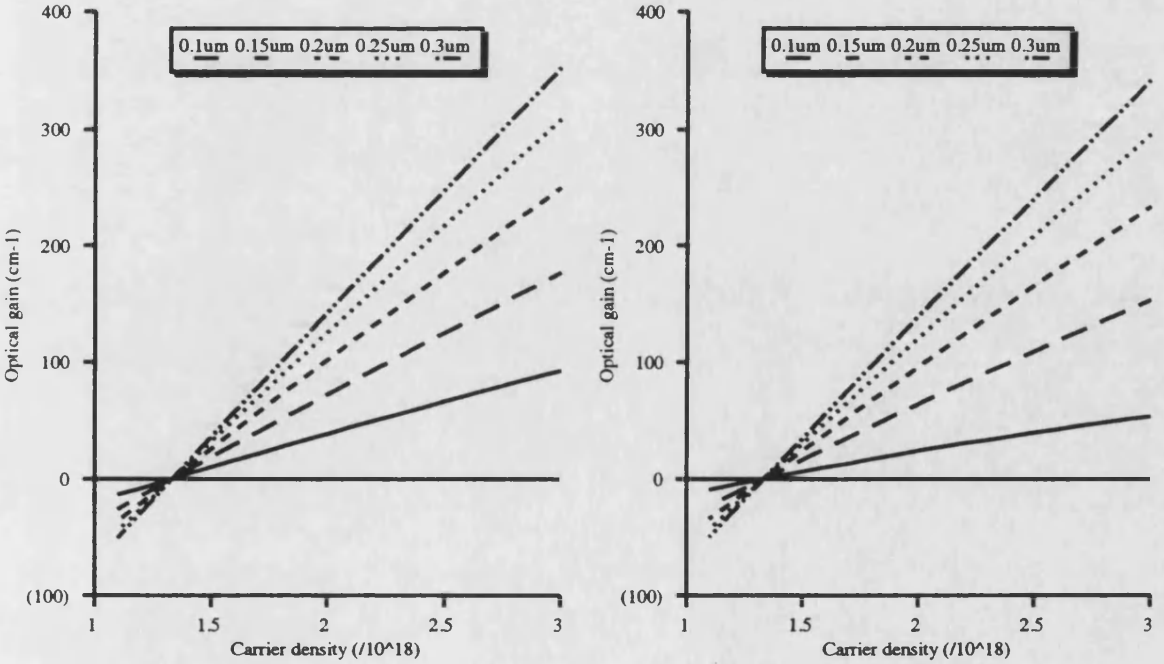

(a) (b)

Figure 5.18 Optical gain vs carrier density with active layer depth as a parameter. (a) TE00 (b) TE01

5.7 Discussion

It has been seen in this chapter that the solution of two dimensional guides is considerably more involved than the solution for one dimensional guides, and requires numerical or approximate analytical methods. Because of the requirement for speed of solution in the overall self-consistent model, there is a limited choice of solution techniques possible. In many self-consistent models, the Effective Index method is used, however this is difficult to apply in the CM geometry, and the accuracy of the EI method in this case has been shown to be low. It was therefore decided to use the Weighted Index method in the waveguide model, because it gives a high level of accuracy for a relatively small amount of computational effort. The Weighted Index method, however, has not been used previously to analyse complex waveguides, and it has been necessary to adapt the method to this situation.

From an analysis of the CM waveguide geometry, it can be seen that for very narrow waveguides (<0.75μm) and narrow regrown widths (<0.8μm) the effect of the regrown width must be taken into account. It is rare to find active region widths less 1.0μm because of the problems that this causes in coupling the light out of the waveguide, but such narrow regrown widths are used in an attempt to limit the leakage current in these devices, and the effect of the regrown width must therefore be included in the model. The analysis of the guiding structures shows that the propagation constant and confinement factor depends on both active depth and width. The dependence on the active width shows that whilst the propagation constant tends towards the value for an infinitely wide guide, this value is not reached for guides below 3μm, and the structure must therefore be analysed in two dimensions.

If the carrier density across the active layer is assumed to be uniform, then the dependence of both the real and imaginary parts of the propagation constant on carrier density is

shown to be nearly linear for fixed guide dimensions, an observation which is well explained by first order perturbation theory. If a uniform carrier profile is assumed, the carrier density required for threshold can be obtained from the figures as in the region of $2x10^{18}cm^{-3}$, assuming a cavity loss of $80cm^{-1}$, although the actual figure depends on waveguide depth and to a lesser extent width.

The results presented in this chapter assume uniform carrier density, but the shooting method used in the wave equation solution enables solution of guides with non uniform carrier density. The waveguide model developed in this chapter can therefore be used without any changes in the overall self-consistent model. The electrical and optical models are linked by the carrier density, and in order to couple the two models the carrier density must be calculated self-consistently. The overall self-consistent model is explained in the following chapter.

	Parameter	Value	Units
Optical constants	λ	1.3	μm
	n_{InP}	3.2	
	$n_{InGaAsP}$	3.52	
	n_{SiO_2}	1.5	
	a	$3x10^{-16}$	cm^2
	b	400	cm^{-1}
	R	-3	
Waveguide dimensions	active width	2.0	μm
	active depth	0.15	μm

Table 5.1. The parameters used in the optical waveguide modelling

REFERENCES

[1] R.M.Knox and P.P.Toulios, "Integrated circuits for the millimeter through optical frequency range", Proceedings of the MRI symposium on submillimeter waves", 1970, Polytechnic Press, Broklyn, pp 497-516

[2] P.C.Kendall, M.J.Adams, S.Ritchie, and M.J.Robertson, "Theory of calculating approximate values for the propagation constants of an optical rib waveguide by weighting the refractive indices", IEE Proc.A, Sept 1987, vol 134, no 8, pp 699-702

[3] T.M.Benson, P.C.Kendall, M.S.Stern, and D.A.Quinney, "New results for rib waveguide propagation constants", IEE Proc J, April 1989, vol 136, no. 2, pp 97-102

[4] J.Buus, "Principles of semiconductor laser modelling", IEE Proc.J. Feb 1985, vol 132, no 1, pp 42-51

[5] B.M.A.Rahman, and J.B.Davies, "Finite-element analysis of optical and microwave problems", IEEE Trans., 1984, MTT-32, pp 20-28

[6] D.A.Roberts and M.S.Stern, "Accuracy of method of moments and weighted index method", Electron. Lett., 1987, vol. 23, pp. 784-785

[7] C.F.Gerald and P.O.Wheatly, "Applied Numerical Ananlysis", Fourth ed., Addison Wesley, Reading, Mass., 1989

[8] M.C.Amann, "Waveguiding analysis of mushroom stripe laser diodes", IEE Proc J, Feb 1988, Vol 135, no. 1, pp 68-73

[9] S.Seki, T.Yamanaka,, and K.Yokoyama, "Two-dimensional analysis of optical waveguides with a nonuniform finite difference method", IEE Proc J, April 1991, Vol 138, no. 2, pp 123-127

[10] K.Hayata, M.Koshiba, and M.Suzuki, "Lateral mode analysis of buried heterostructure diode lasers by the finite element method", IEEE JQE, 1986, Vol 22, no. 6, pp 781-788

[11] M.I.Oksanen and I.V.Lindell, "Complex valued functionals in variational analysis of waveguides with impedance boundaries," IEE Proc J, 1989, vol 136, pp 281-288

[12] G.P.Agrawal, and N.K.Dutta, "Long-wavelength semiconductor lasers", chapter 2, 1986, Van nostrand Reinhold, New York

[13] J.E.Bowers, B.R.Hemenway, T.J.Bridges, E.G.Burkhardt, "26.5 GHz bandwidth InGaAsP lasers with tight optical confinement", Electron. Lett., 1985, vol. 21, pp 1090-1091

CHAPTER 6: THE COMBINED MODEL

6.1 Introduction

This chapter presents the overall self-consistent model of both the electrical and optical properties of buried heterostructure lasers. The literature on partially self-consistent models of lasers is quite extensive, and a review paper by Buus [1] covers most of the models produced up to 1985. Up to this time fully self-consistent models of the static electrical and optical properties of lasers were rare, most models made a number of assumptions about the electrical properties of the laser to enable the authors to use analytic formulations for the current distributions, and all models assumed a one dimensional or quasi one dimensional optical field distribution.

Such assumptions, however, can severely limit the applicability of the model. More fully self-consistent models [2-6] have generally solved the electrical field problem in two dimensions, using either the Laplace or Poisson equations to solve for the current spreading. It is still common practice to use the Effective Index method to solve for optical fields [2-4], although more recently there has been a move towards solving the optical field problem in two dimensions, often by finite difference or finite element methods [5]. Many models now claim to be applicable over a broad range of laser structures [2,4,5], although the assumptions made in each model vary depending on the parameters which the model is examining. It is therefore rarely possible to compare the results of models, and although there have been several excellent models of lasers produced, none have general applicability.

In this work a model of the static properties of one specific class of buried heterostructure lasers (the details of which were given in chapter 3) is presented. The class is quite broad,

and the model may be easily applied to lasers of widely varying geometries, ranging from the buried ridge structure of figure 6.1(a), with a very narrow active layer and narrow regrown regions (which has been used to obtain record modulation bandwidths of 24 GHz at room temperature [7]) to the broad area stripe geometry laser shown in figure 6.1(b), which is a simple double (not buried) heterostructure device, and including a variety of structures (constricted mesa, etched stripe, double stripe etc.) which can be fabricated from double heterostructure wafers. Wide variations in active layer and cladding layer geometries can be accommodated, as can index guiding, gain guiding and all combinations of the two.

There have been several recently published models of semi-conductor lasers, some of which can handle some of the above structures. The difference between these models and the model described in this thesis is twofold. First, it is believed that so far no fully self consistent model of buried heterostructure lasers has been developed elsewhere. Secondly, the only other study to consider multi-lateral mode operation in a self-consistent fashion [6] uses a very restricted electrical model, and does not examine the case of predominantly index guided lasers, where the problem of multi-lateral mode operation is most important.

Previous chapters have discussed, separately, the current leakage and optical field problems in CM and BRS lasers. Up to this point, however, it has been assumed that the carrier density is fixed at the threshold value across the entire active layer, and the threshold value of carrier density has been taken from experimental studies. In order to model accurately the above threshold behaviour of semiconductor lasers, it is necessary to couple self-consistently the models for the electrical and optical properties. This requires the determination of the effect of the interaction of the photons of the optical field with the active layer carriers, and the effect that this has on the current distribution and optical field in the laser.

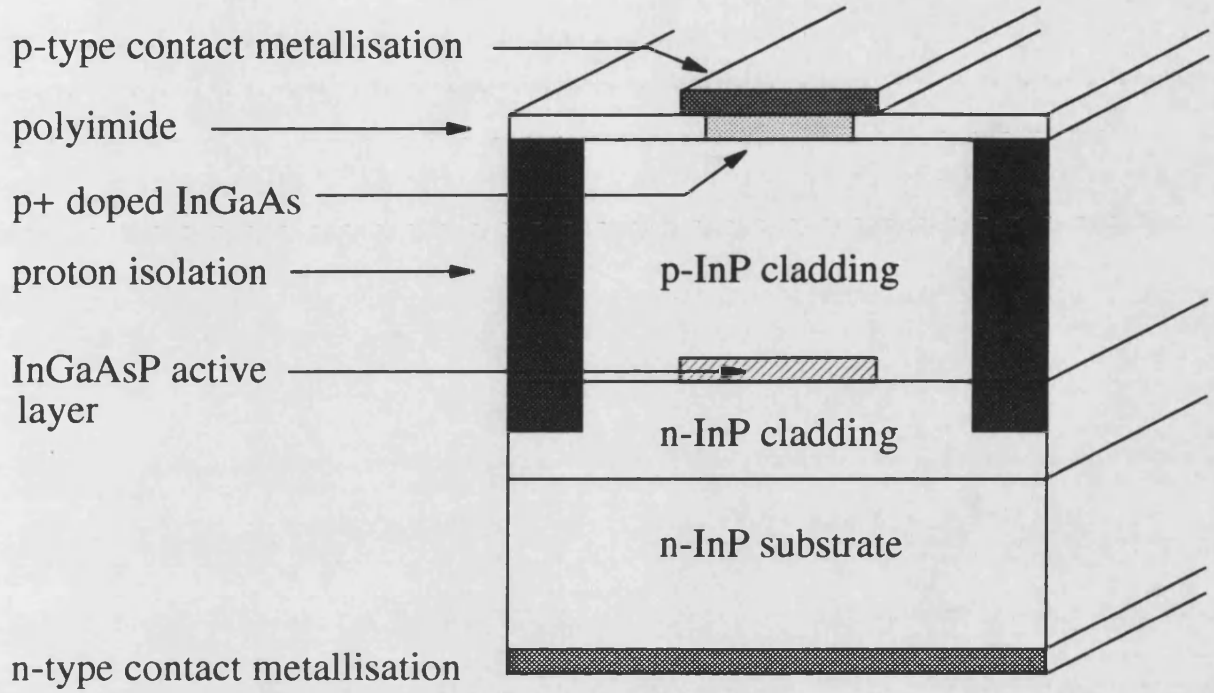

Figure 6.1(a) The buried ridge structure laser

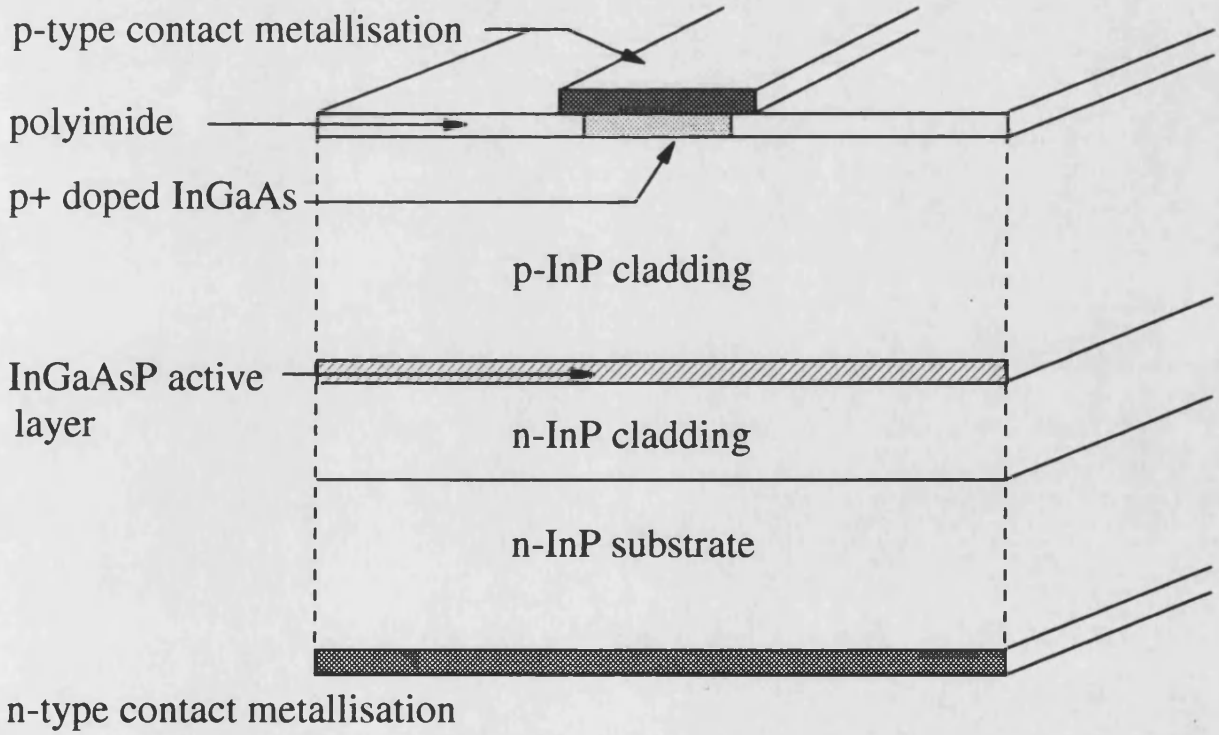

Figure 6.1(b) The stripe geometry laser

The next two sections of this chapter explain the alterations to the electrical and optical models required to combine the two models in a self consistent scheme. The theoretical background to the model is then presented, detailing the assumptions made and the equations used in the modelling. The self-consistent solution scheme is described, and results are given for a wide range of different situations. Finally conclusions are drawn about the model and its applicability.

6.2 Calculation of carrier density

In common with most other authors [2-5] it has been assumed that the variations in carrier density and current density in the z-direction may be averaged over, and they are therefore assumed to be uniform. The active layer is, generally, very narrow in practical devices (0.1 to 0.25μm) and when modelling laser characteristics the assumption is invariably made that the carrier density is uniform across the depth of the active layer. Under these assumptions the electron density distribution, $n(x)$, is given by the one-dimensional diffusion equation detailing the generation and recombination of carriers [8]

$$D_e \frac{d^2 n(x)}{dx^2} + \frac{J_{active}(x,d)}{qt} = R_{Stim}(n) + R_{Spon}(n) + R_{NR}(n) \qquad (6.2.1)$$

where D_e is the effective diffusion coefficient, t the active layer thickness, and the terms on the right hand side of the equation represent the recombination of carriers due to stimulated, spontaneous and non-radiative processes. This equation was introduced in chapter 3, but since with the electrical model there is no way of calculating the stimulated recombination term, a constant lateral carrier density distribution was assumed for the calculations. Knowledge of the carrier density is crucial to the self-consistent model, and thus the diffusion equation must now be solved.

For buried heterostructure lasers, the active layer is surrounded on all sides by material of a different bandgap. Thus, at the sides of the active region a heterojunction is formed in the lateral direction. This heterojunction forms a carrier blocking barrier, since it will not become "turned on" at the values of electrical field that occur in the lateral direction. The diffusion equation (6.2.1) must be solved, therefore, subject to the boundary condition of zero carrier flow across the lateral heterojunction. This important property of buried heterostructure lasers has been ignored by other authors [2,13-15], however it has significant implications for the laser performance, notably in respect of the leakage current.

The spontaneous recombination coefficient is taken here as linearly dependant on the carrier density, being related to the hole and electron concentrations by

$$R_{Spon}(n) = (B_0 - B_1 n(x)) n(x) p(x) \qquad (6.2.2)$$

where B_0 and B_1 are constants. In long wavelength materials, non-radiative recombination due to Auger processes becomes important, and must be included in the model. The spontaneous and non-radiative recombination terms used in this model come from a study by Olshanski [9], who examined recombination mechanisms in CM lasers. This work suggested that the non-radiative recombination can be adequately described by a single Auger term, and a second term which must be introduced to explain anomalous behaviour at low carrier densities

$$R_{NR}(n) = Cn(x)p^2(x) + Dn^z \qquad (6.2.3)$$

Here, C is the Auger recombination constant and D and z are constants determined from the experimental data. It is suggested that an increase in the parameter D may be used to account for the difference in device performance as the device ages [9]. The hole density in the active layer is calculated, assuming an active layer doping of p_a as

$$p(x) = n(x) + p_a \tag{6.2.4}$$

Radiative recombination is related to the photon density in the active layer and the optical field distribution. If a normalised optical field distribution is defined as

$$\Psi(x,y) = \frac{|E(x,y)|^2}{\int_{-\infty}^{+\infty}\int |E(x,y)|^2 \, dxdy} \tag{6.2.5}$$

then the stimulated recombination term is given by

$$R_{Stim} = g(x)\frac{c}{\eta_o}\sum_M \{\Psi_M(x,y) S_{A_M}\} \tag{6.2.6}$$

where $g(x)$ is the optical gain, c/η_0 is the group modal velocity in the cavity and S_A is the photon density per unit cross sectional area, and the summation is carried out over the lasing modes. This recombination term is one of the coupling terms between the optical and electrical field problems.

When these equations (6.2.2-6) are substituted into the diffusion equation it can be seen that the equation is non-linear, depending on terms in n^2, n^3 and n^z. Due to the complexity of the equation, and the fact that the current density injected into the active layer, which is a source term in the equation, is only specified at points given by the solution of the Laplace equation in the upper cladding layer, a numerical method of solution is required.

The chosen method of solution is to use a quasi-linearization technique to linearize the equation. If this linearized equation is written in finite difference form it is tri-diagonal in form, and is readily solved using fast and efficient matrix methods. This linearized

solution may then be used to obtain an improved estimate of the carrier distribution, and an iterative scheme is used to obtain the final solution. The solution method is given in Appendix 2.

6.3 The lasing condition applied to the optical model

In chapter 5, the Weighted Index method was developed for two dimensional waveguides with complex permittivity. It was shown how the optical field distributions and propagation constants of all guided modes of the waveguide can be found. This forms the basis of the optical model. The propagation constant determines the optical gain of the mode, as was shown in chapter 4. The optical field profile is required in the stimulated recombination term of the carrier density equation (as seen in equation (6.2.5)), and the carrier profile in the active layer sets the optical field via the permittivity distribution. The permittivity is given by

$$\varepsilon(x) = \left(\eta_a + \frac{an(x)}{2k_0}R + i\frac{g(x)}{2k_0}\right)^2 \qquad (6.3.1)$$

where η_a is the bulk refractive index of the active layer, and R the ratio between real and carrier dependant imaginary part of the refractive index.

The optical model, however, is considerably more complicated than just the determination of the optical fields and propagation constants. One of the requirements of a laser is that the optical gain of all lasing modes are equal to the losses experienced in the optical cavity by the modes. The optical gain of a mode, G_M, is given by $2Im(\beta)$, and to a good level of approximation, this is given by the two dimensional overlap integral of the gain coefficient and the mode profile

$$G_M = \int\int_{-\infty}^{+\infty} g(x,y)\Psi(x,y)dxdy \tag{6.3.2}$$

For a steady state lasing mode, this gain must compensate for the losses experienced by the mode in a round trip around the cavity. This condition may be written as

$$G_M = \alpha_m + \alpha_i \tag{6.3.3}$$

Here α_m is the mirror loss and α_i is the internal loss in the laser cavity, including free-carrier, scattering and absorption losses. The internal loss is taken as a constant, whereas the mirror loss is averaged over the cavity length, L_c, and obtained from the mirror reflectivity, R, as

$$\alpha_m = \frac{1}{L_c}\ln\left(\frac{1}{R}\right) \tag{6.3.4}$$

The only way to alter the propagation constant of the modes, and thus the optical gain, is to alter the waveguide in which the mode propagates. Within the confines of a fixed optical cavity, this can only be done by altering the carrier density in the active layer. If the current injected into the active layer is fixed, then the controlling variables in the carrier density equation (6.2.1) are the photon densities S_A of each lasing mode, which enter the equation via the stimulated recombination term. By suitable adjustment of the photon densities of all lasing modes, it is possible to alter the carrier density and hence permittivity such that the gains of all lasing modes are equal to the losses.

Due to the non-linear nature of the carrier diffusion equation, the solution for each mode depends on the other modes, and a simple super-position of solutions will not satisfy the equation. An efficient scheme for obtaining the photon density of a single mode was suggested by Kumar [3] and is used here, extended to deal with the general case of any

number of lasing modes. The method uses the Newton-Raphson technique to alter the photon densities of each mode to relax an initial guess of the photon densities towards a solution. A description of the method is given in Appendix 3.

In the overall scheme, the solution of the optical problem is preceded by a solution of the electrical problem. Initially the laser is assumed to be below threshold, and thus the photon densities of all modes are zero. The optical solution proceeds as follows:

(1) Using the injected current distribution provided by the Laplace equation solution, the carrier density is obtained from equation (6.2.1). It is then possible to determine the permittivity distribution in the active layer that this carrier density implies, and thus to solve the wave equation and obtain the field profile and propagation constants of the guided modes of the waveguide.

(2) The gains of all guided modes, determined from the propagation constants, are then compared to the cavity loss. If the gain of any mode is greater than the loss, then the laser is above threshold, and the solution continues. If not, the laser is below threshold, and the electrical solution describes the laser behaviour, ignoring spontaneous emission. If the laser is above threshold, then any mode for which the gain is greater than or equal to the threshold value is assumed to be lasing at this stage in the iteration. It is possible for a mode to appear to be lasing at one stage in the iteration, but to fall below threshold at a later stage. Similarly it is possible for a mode to begin to lase at some subsequent stage in the iteration.

(3) For all lasing modes, it is then necessary to fix the gain equal to the losses. This is done by altering the photon density in the carrier diffusion equation, and resolving the equation to obtain the new carrier density that this photon density

implies. An initial guess of the photon densities of each lasing mode is supplied by the program, and this guess is improved using the multi-dimensional Newton-Raphson technique described in Appendix 3.

This process alters the carrier density profile in the active layer, and strictly speaking, every time the carrier density is altered, the fields and propagation constants of the lasing modes should be re-calculated to enable calculation of the gain. Solution of the wave equation is time consuming, and in general the change in the optical field is small at each subsequent iteration. The modal gains must be determined several times during the Newton-Raphson solution, and at this point in the solution loop it is therefore useful to calculate the gain from the approximate equation (6.3.2), and use the field distribution calculated in step (2).

(4) Stage (3) alters the carrier density, and this alters the permittivity and hence the optical field distribution. It is therefore necessary to re-calculate the optical field profiles and propagation constants of all lasing modes by a full solution of the wave equation, as per stage (1). Having done this, the gains of the lasing modes are again compared to the losses. If they are within a tolerable error, and no other guided mode now has a gain greater than the threshold value, a solution has been obtained. If not, the solution is repeated from stage (2) using the new optical field distribution.

During the iteration process, especially when the solution is very close to the point at which the next highest order mode begins to lase, the multi-dimensional Newton-Raphson routine can sometimes give a negative value for the photon density of the higher order mode. This is obviously not a physically possible solution, and it is therefore

not allowed. It is found that, in such a situation, it is invariably possible to obtain a solution with a lower number of lasing modes, and the negative photon density appears to be due to numerical instability in the iteration loop.

6.4 The self-consistent model

In this section the equations describing the overall self-consistent model of the electrical and optical fields in buried heterostructure lasers are given. The models for the electrical and optical components are similar to those used in chapters 5 and 6, the difference being in the way that the carrier density in the active layer is treated. It is the carrier density that couples the two models, and must be treated in a self-consistent way between them.

6.4.1 The current spreading and carrier density problem

The p-type confining region is taken to be homogeneous and passive, and thus the two dimensional potential distribution is given by a solution of Laplace's equation

$$\nabla^2 V(x,y) = 0 \qquad (6.4.1.1)$$

subject boundary conditions on the current flow at the edges of the region. The current may be obtained from the solution of Laplace's equation as

$$J(x,y) = -\sigma \nabla V(x,y) \qquad (6.4.1.2)$$

where σ is the conductivity of the p-type region, which is related to the electronic charge, q, the hole mobility μ_p and the p-type doping p_0 by

$$\sigma = q\mu_p p_0 \qquad (6.4.1.3)$$

From these relations the total current injected into the device may be obtained by integrating the current density injected across the contact (or any plane parallel to the contact)

$$I = \int J(x,y)\,|_{y=c}\, dx \tag{6.4.1.4}$$

This is solved numerically using the trapezoidal rule method. The contact is taken to be an equipotential surface, and the boundary conditions at the insulating boundaries are given by

$$\overline{J}(x,y).\overline{n} = 0 \tag{6.4.1.5}$$

where $\overline{n}$ is the unit vector normal to the boundary. In common with others the homojunction regions are assumed to operate in the low-injection regime, and to be abrupt junctions. The current at any point on the homojunction boundary may be represented by the Shockley equation

$$J(x,d)\,|_{homojunction} = J_{sat}\left[\exp\left(\frac{qV(x,d)}{\eta kT}\right) - 1\right] \tag{6.4.1.6}$$

where J_{sat} is the saturation current density, η is the ideality factor, k the Boltzmann constant and T is the temperature.

At the heterojunction boundary the Shockley equation may not be applied, because the lasing action at the junction clamping the carrier density near to the threshold value. The Shockley equation also relies on Boltzmann statistics, which are not valid at the high carrier densities required for lasing. The injected current acts as a source of carriers into the active region, and the electron distribution in the active layer, $n(x)$, may be found from the carrier diffusion equation [8]

$$D_e \frac{d^2 n(x)}{dx^2} + \frac{J_{active}(x,d)}{qt} = R_{Stim}(n) + R_{Spon}(n) + R_{NR}(n) \qquad (6.4.1.7)$$

where D_e is the effective diffusion coefficient, t the active layer depth, and the terms on the right hand side of the equation represent the recombination of carriers due to stimulated, spontaneous and non-radiative processes. This equation is solved subject to the condition of zero electron leakage across the lateral heterojunction. The spontaneous and non-radiative recombination rates are given by [9]

$$R_{Spon}(n) = (B_0 - B_1 n(x)) n(x) p(x) \qquad (6.4.1.8)$$

$$R_{NR}(n) = Cn(x)p^2(x) + Dn^z \qquad (6.4.1.9)$$

In these equations B_0 and B_1 are constants, C is the Auger coefficient and the term $Dn^z(x)$ is an expression introduced by Olshanski *et al* [9] to explain anomalous behaviour at low currents. $p(x)$ is the hole concentration which, for an active layer with a p-type doping of p_a is given by

$$p(x) = n(x) + p_a \qquad (6.4.1.10)$$

The electron and hole concentrations set the quasi-Fermi level separation, and this in turn sets the active layer voltage. The separations are given by

$$F_{1/2}\left[\frac{F_c(x) - E_c(x)}{kT}\right] = \frac{n(x)}{N_c} \qquad (6.4.1.11)$$

$$F_{1/2}\left[\frac{E_v(x) - F_v(x)}{kT}\right] = \frac{p(x)}{N_v} \qquad (6.4.1.12)$$

where $F_{1/2}(\Phi)$ is the Fermi integral, F_c and F_v are the quasi-Fermi levels of electrons and holes respectively, E_c and E_v are the energies of the conduction and valence band edges

in the active region, and N_c and N_v the conduction and valence band density of states in the active layer. The solution of the Fermi integral is obtained using the approximate analytic expansions [10].

$$F_c(x)-E_c(x)=kT\left\{\ln\left(\frac{n(x)}{N_c}\right)+K_1\left(\frac{n(x)}{N_c}\right)+K_2\left(\frac{n(x)}{N_c}\right)^2+K_3\left(\frac{n(x)}{N_c}\right)^3+\cdots\right\} \quad (6.4.1.13)$$

$$E_v(x)-F_v(x)=kT\left\{\ln\left(\frac{p(x)}{N_v}\right)+K_1\left(\frac{p(x)}{N_v}\right)+K_2\left(\frac{p(x)}{N_v}\right)^2+K_3\left(\frac{p(x)}{N_v}\right)^3+\cdots\right\} \quad (6.4.1.14)$$

The constants K_1, K_2, and K_3 are given in table 1. The potential difference across the active region may then be found from the electron and hole densities

$$V(x,d)=\frac{1}{q}[(F_c-E_c)+(E_v-F_v)+E_g] \quad (6.4.1.15)$$

where E_g is the bandgap of the active layer material.

6.4.2 The optical problem

If the light is assumed to propagate in the z-direction, with time and axial dependence taken as $\exp\{i(\omega t-\beta z)\}$, then the two dimensional scalar Helmholtz equation, which describes the distribution of the optical field under these conditions, may be derived from Maxwell's equations as

$$\nabla^2 E(x,y)+\{k_o^2\varepsilon(x,y)-\beta^2\}E(x,y)=0 \quad (6.4.2.1)$$

where $E(x,y)$ is the optical field distribution, $\varepsilon(x,y)$ the complex relative permitivity, k_0 the wave number and β the modal propagation constant. In the active layer the complex relative permitivity is dependant on the carrier density, and is given by

$$\varepsilon(x) = \left(\eta_a + \frac{an(x)}{2k_0}R + i\frac{g(x)}{2k_0}\right)^2 \qquad (6.4.2.2)$$

The local gain, $g(x)$, is assumed to be linearly dependant on the carrier density

$$g(x) = an(x) - b \qquad (6.4.2.3)$$

where a and b are gain constants. Solution of the wave equation is by the Weighted Index method [11]. This method is ideally suited to device modelling, being is both more accurate than the commonly used effective index method and faster than other solution techniques (e.g. the finite element method [5], beam propagation method [6] etc.). Speed of solution is an important factor in self-consistent models, where the optical problem is only part of the model, and may need to be solved many times in the course of the overall solution. The method, as derived in reference [11], is not directly applicable to waveguides of complex permittivity due to the normalisation condition used, but was derived for this case in chapter 5.

In the steady state, the lasing condition may be written

$$G_M = \alpha_m + \alpha_i \qquad (6.4.2.4)$$

where α_m is the mirror loss and α_i the cavity losses. The modal optical gain is given by $2\mathrm{Im}(\beta)$, and this can be shown to be approximately

$$G_M = 2Im\beta_M \approx \int\int_{active} g(x)\Psi_M(x,y)dxdy \qquad (6.4.2.5)$$

where $\Psi(x,y)$ is the normalised intensity distribution given by equation (6.4.5)

The optical and electrical problems are linked by the stimulated recombination term in the carrier diffusion equation (6.2.1). This term is given by

$$R_{Stim} = g(x)\frac{c}{\eta_o}\sum_M \{\Psi_M(x,y)S_{A_M}\} \qquad (6.4.2.6)$$

where c/η_0 is the group modal velocity in the cavity and S_A is the photon density per unit cross sectional area. The summation is over the lasing modes. The output power from each facet is given by

$$P = \frac{1}{2}\alpha_m h\upsilon \frac{c}{\eta_0} A L_c \sum_M S_{A_M} \qquad (6.4.2.7)$$

where $h\upsilon$ is the energy of the mode and A the active layer lateral cross-sectional area $A = Wt$.

6.5 Solution technique

A flow chart summarising the solution scheme used in the self-consistent model is shown in figure 6.2. All equations are solved numerically, using the finite difference technique, and the usual precautions have been taken to ensure computational stability and accuracy. All the solution techniques that use iteration have checks employed in the solution loops to ensure that the solution is converging. Where possible, to check the accuracy of the program, each equation requiring a separate solution technique was solved in the first instance by two different methods. The fastest method of solution was used in the actual program, provided the accuracy was sufficient.

The solution of the finite difference equations uses a non-uniform grid to help speed up the solution. The same precautions to ensure good grid design as for the electrical model were employed. The grid design was again manual, however, when the diffusion equation is included in the model it is found necessary to increase the number of points in the

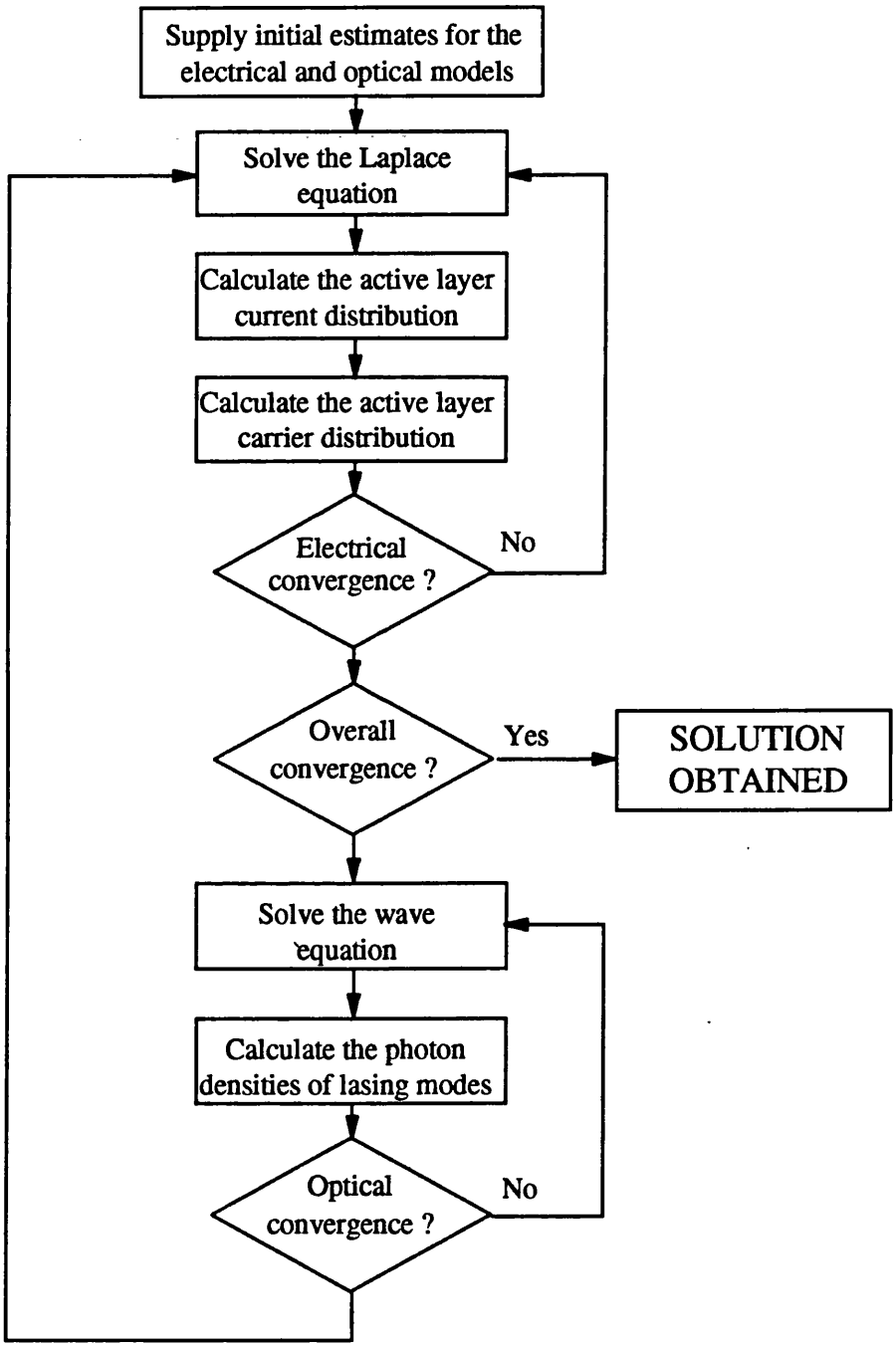

Figure 6.2 Flow chart of the self-consistent method

lateral grid to ensure the accuracy of the overall equation solution. The grid design depended on the shape of the laser being modelled, but generally there were around 60 points in the x direction and 20 in the y direction. The optical solution uses an adaptive Runge-Kutta technique [12] to determine the grid, with the grid size set by the allowable global error of the fields F(x) and G(y).

The general solution technique is as follows:

(1) The first step in the model is to assume a voltage applied to the top equipotential contact, and to solve Laplace's equation (6.4.1.1) subject to the boundary conditions given in equations (6.4.1.2-15). This is achieved by an iterative solution technique, and on the first iteration an active layer voltage is assumed and equations (6.4.1.1) to (6.4.1.6) are solved. The active layer injection current, $J(x,d)$, is then calculated and equation (6.4.1.7) is solved to give the carrier density in the active layer that this current distribution implies. Initially $S_A=0$ is assumed for all modes. The active layer voltage distribution may then be calculated from equations (6.4.1.11-15) and compared to the voltage initially assumed. If the two are within a specified tolerance then a solution for the electrical problem has been obtained, and this solution provides a first estimate of the carrier density in the active layer. If not then this step is repeated using the new active layer voltage until convergence is obtained.

(2) The calculated carrier density distribution is used to determine the refractive index distribution from equation (6.4.2.2). The complex two dimensional Helmholtz equation (6.4.2.1) is then solved by the Weighted Index method for the guided modes, obtaining the field profiles and propagation constants for each mode. The modal gains, $2Im(\beta_M)$, obtained from the waveguide solution, are compared to

the cavity loss given by equation (6.4.2.4). If, on the first iteration, none of the modal gains is greater than the losses, then the laser is below threshold and the solution is halted.

(3) If the gain of any mode is greater than, or equal to, the cavity losses, then that mode is considered to be lasing. The requirement is that the gain of each lasing mode is equal to the losses, and the modal gains are adjusted by altering the photon densities, S_A, in the diffusion equation (6.4.1.7) using the method of Appendix 3. This changes the carrier density, and thus the gain, $g(x)$, which in turn alters the modal gains via the approximate expression (6.4.2.5). The photon density must be calculated for each lasing mode, but this process is complicated by the non-linear nature of the diffusion equation, which means that altering the photon density of one mode will change the gain of the other. A multi-dimensional Newton-Raphson root finding technique is employed to obtain solutions for the photon densities.

(4) Using the approximate expression for modal gain in step (3) speeds the solution, but means that the Helmholtz equation is not re-solved during the calculation of the photon densities. However, the carrier density is affected by this process, and thus the refractive index profile is changed. It is therefore necessary to re-solve the Helmholtz equation with the new refractive index profile, and thus to obtain the new optical field distribution and gains for the lasing modes. This and subsequent solutions of the Helmholtz equation are rapid because a good initial estimate of the propagation constants is available from the previous iteration. If the calculated value of gain for each lasing mode is within a specified tolerance of the cavity loss then the optical solution has converged, and the solution proceeds to step (5). If not, the optical solution is repeated from step (2), and iteration continues until convergence is obtained.

(5) The carrier profile obtained from the optical solution sets a new active layer voltage, and the electrical problem must therefore be re-solved using this new value. The model iterates between electrical and optical problems until the carrier profile at the start and finish of the optical model converges to within a specified tolerance.

Despite using such a complex iteration scheme, very few convergence problems were encountered. Three separate tolerance values were necessary to limit the errors in the overall solution to a tolerable value, these being for the Laplace equation, active layer carrier density, and gains of the modes. Other tolerance values (i.e. for the diffusion equation, wave equation and Weighted Index solution) were set at the limit of the computational accuracy. It was found that to obtain a solution of the diffusion equation consistent with the current spreading problem in the upper confining region, the Laplace equation had to be solved to within a very fine tolerance level, the average error at any node was required to be limited to less than 10^{-7}. Convergence of the Laplace equation was not a problem, however such a fine tolerance required more computing time than would otherwise have been required.

The only convergence problems encountered were when dealing with cladding regions with very high doping levels ($>1.5x10^{18}$) where the resistivity of the layer was very low. In such cases, a small variation in active layer voltage distribution causes quite a large change in injected current. It was possible to obtain a situation where, if a relatively poor guess of the active layer carrier density was used, the solution to Laplace's equation would give far too high (or too low) an injected current into the active layer. This would lead to the diffusion equation solution giving a poor estimate of the carrier density, and therefore the subsequent Laplace equation obtaining a low or high value of active layer current. This could lead to oscillations in the electrical solution.

The problem was rare and it was almost always possible to overcome the oscillations by using an average of the two carrier density distributions obtained by the two extreme cases. It had been anticipated that problems might arise due to the two modes competing for carriers, and therefore causing oscillation between solutions with one and two modes lasing. This did not occur in the present model, the only problem with the optical solution was that of rogue solutions having a negative photon density for the higher order lasing mode. In such a case a solution was invariably possible with just a single mode lasing, as explained in section 6.3.

Using the above iteration scheme, modified to prevent oscillations in the solution, it was possible to solve for the current spreading, carrier density and optical modes of the solution to within a fine tolerance. Solutions were obtained for the injected current density and output light power which would vary only in the fourth significant figure for changes in the assumed initial conditions.

6.6 Results

The basic structure used in the modelling is a BRS laser with a two micron wide active layer, two micron wide contact stripe and overall width of 6 microns, as shown in figure 6.3. The advantage of using the BRS structure as a basis for the modelling is that it is possible to vary the geometrical parameters of the structure independently, whereas with the CM laser the device height, width and contact width are interrelated. A basic doping level of $8x10^{17}$ cm^{-3} has been used in most of the calculations, since this is in the range of dopings used in practical devices, and it is the doping level recommended in the previous studies of current spreading in BRS and CM lasers [13-15]. Other basic parameters used in the simulation, unless otherwise stated, are given in table 1.

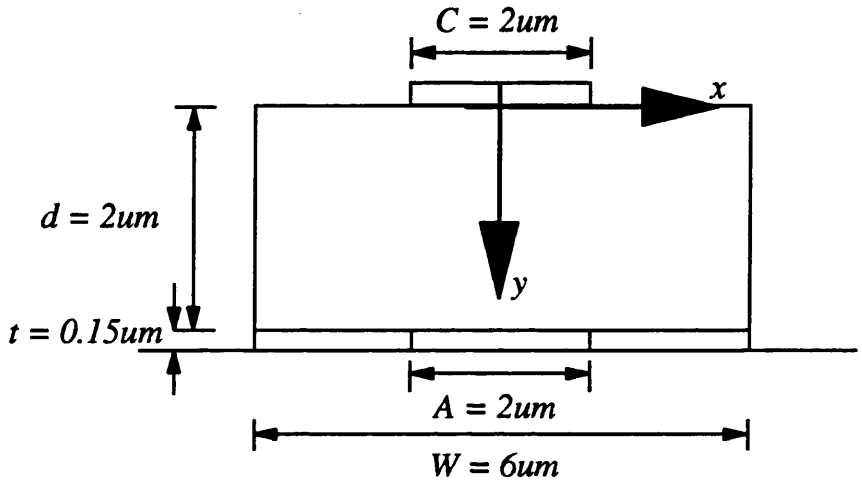

Figure 6.3 Schematic diagram of the BRS structure laser to be modelled

The parameters used in the computer model reported here are all obtained from the literature and no attempt has been made to fit parameters to obtain solutions which better represent the experimental situation. However, where the value of a parameter (such as the gain parameters) varies widely in the literature, a representative value has been used to represent the laser structures under investigation. The gain parameters used here are identical to those used in several other laser models [e.g.3,4], and close to those found experimentally in studies on the CM laser [16]. Wherever possible, the values of parameters are obtained from experimental results for relevant laser structures.

The only external boundary condition on the problem is the voltage applied to the upper p-type contact, however, in experimental situations the lasers are generally driven from current, rather than voltage sources. The current injected into the device can be obtained from equation (6.4.1.4). Above threshold the I-V characteristic is substantially linear if the leakage current is small, and it is therefore possible to use the injected current as boundary condition if the I-V curve for the particular laser structure is known. This may be done by calculating two points on the I-V curve, near to threshold, and using these to extrapolate the value of voltage required to produce a certain current. This has been done for most of the characteristics presented here, and has been automated in the program. Where the characteristic varies substantially from the linear, i.e. where the homojunction leakage current is significant, the program recalculates the voltage to obtain the correct value of current.

The model can solve for any number of lasing modes. However, since for practical devices it is desirable to limit lasing to only the fundamental mode, the model only solves self-consistently for the first two lasing modes. This enables the model to be used to study whether a device will support more than one lasing mode, and reduces the time taken to obtain a solution. An experimental study on CM lasers [17] found that for some device geometries lasing in two modes does occur, but lasing in three modes was never

observed. It is relatively easy, but time consuming, to check whether higher order guided modes are lasing, simply by solving for the mode using the WI method and comparing the calculated gain to the cavity loss. In the cases where this was done it was found that, in agreement with the experimental observations, a third lasing mode would not be supported.

6.6.1 The basic BRS laser

The basic BRS laser is shown in figure 6.3. This device structure is useful to demonstrate the various problems associated with relatively wide active layers and those associated with relatively low p-type cladding layer doping. The graph of light production per facet against drive current (the light-current or L-I curve) obtained from the model for such a device, and with dimensions and doping level as given in table 1, is shown in figure 6.4.

The figure shows that the laser has a low threshold current, of around 12mA, which is in excellent agreement with experiments carried out by several groups on this and related structures [13-15]. The calculated external quantum efficiency of 24% per facet is again in excellent agreement with experiment [15]. The very sharp transition from zero light production to lasing shown in figure 6.4 is due to the neglect of the amplified spontaneous emission in the model, but this effect only makes a noticeable difference around threshold. It can be seen that, although the curve is virtually linear at low injected current densities, it becomes sub-linear at high injected current. Although at this cladding layer doping level the effect is not very noticeable, it can be seen by comparing the calculated curve to the guide line drawn on figure 6.4, which has been extrapolated from the initial slope of the curve. Again, this sublinearity of the light-current characteristic is observed experimentally. Even this degree of sublinearity can have a grave effect in applications

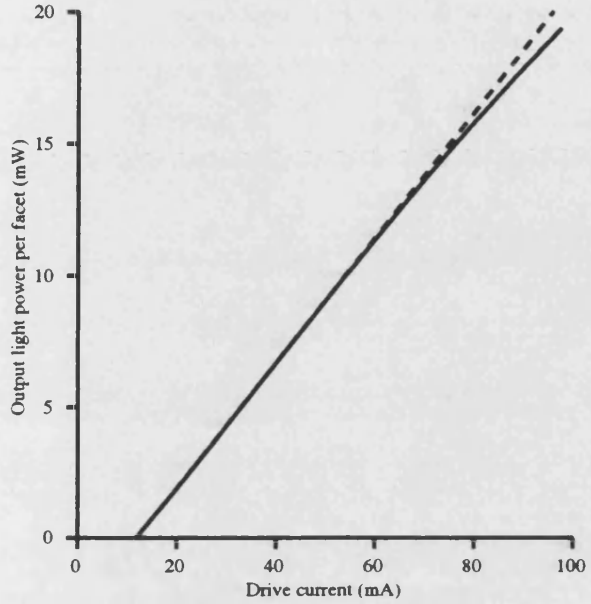

Figure 6.4 The variation of output light power with drive current. The dotted line shows a linear relationship as a guide to the eye.

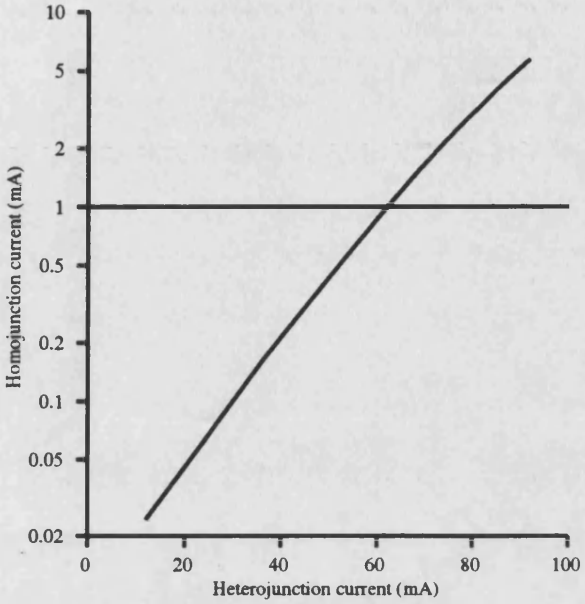

Figure 6.5 Homojunction leakage current versus heterojunction current for the standard BRS laser.

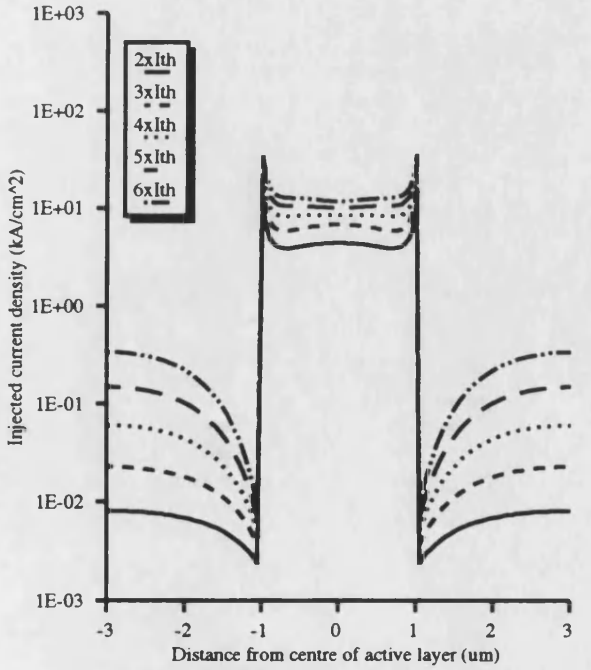

Figure 6.6 The variation of current injection across the active/homojunction layer

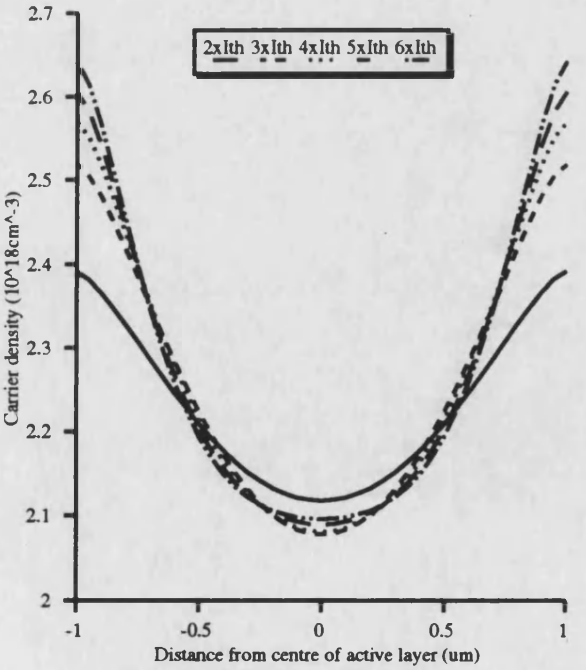

Figure 6.7 The variation of carrier density across the active layer

(such as cable television) which are very sensitive to signal distortion.

The sub-linear behaviour is consistent with the non self-consistent electrical modelling of chapter 3. It was shown that, as the injected current is increased, a fraction of the current can by-pass the active region and flow through the homojunction regions. This fraction increases with injected current. The homojunction current does not contribute towards the light produced, and so it is to be expected that as the drive current is increased, the light-current characteristic will become increasingly sub-linear. The relationship between homojunction current and heterojunction current can be seen from figure 6.5. The figure shows that, as with the non self-consistent electrical model, the relationship between the two currents is nearly exponential in nature, although at the values of injected current in the figure, the homojunction current is only a small fraction of the hetero-junction current.

The calculated distribution of the current injected into the heterojunction/homojunction plane is shown in figure 6.6. This shows that very little current is injected into the homojunction regions, in order to make the leakage current visible on the graph a log-arithmic scale has been used. It can be seen that in this laser the majority of the leakage current occurs far from the active region, near the edges of the device. Figure 6.6 also shows that, as is to be expected, as the current injected into the device is increased the pattern of current distribution in the active layer alters.

The current density spikes at the edges of the active region indicate the extent of the current crowding in the device. This is mainly due to the effects of the lateral hetero-junction and the fact that the homojunction regions are not conducting to any real extent, forcing almost all the current injected into the device to flow through the active region. The pattern of current injection across the bulk of the active layer alters from near threshold, where the curve is slightly convex, to well above threshold, where it becomes

concave. This effect is mainly caused by the change in the carrier distribution in the active layer and the consequent alteration of the current distribution in the laser as the current is increased.

The carrier density across the active region is shown in figure 6.7. It can be seen from the figure that at an injected current of twice the threshold current the carrier density is relatively flat, varying from around 2.4×10^{18} cm^{-3} at the edges of the region to 2.15×10^{18} cm^{-3} near the centre. The dip in the carrier profile is caused by the effects of stimulated recombination, the non-uniform current injection into the active layer, and carrier diffusion. In the centre of the active region the stimulated recombination is greatest, since the optical field is greatest at this point. As the current injected into the device is increased, the carrier profile alters, most noticeably at the edges of the device. Here, the current injection is greatest and the optical field strength least, so the carrier density increases, whereas in the centre of the region the carrier density becomes clamped by the lasing action, changing only slightly in response to the alterations in optical field profile.

Figure 6.8 shows the normalised optical field strength plotted against distance across the device. The curves for two and three times threshold current are nearly identical, and cannot be separated on the scale at which the diagram is drawn. This indicates that the predominant guiding mechanism is real index guiding, i.e. there is little focussing of the beam as is found for gain guided devices [6]. As the injected current is increased to a value of four times threshold current, it is found that the second lateral mode has begun to lase, and the overall optical field profile alters in response to this.

The reason for the lasing of this second mode is the increased gain seen by this mode due to the high carrier density near the edges of the active region. Although the mode is still predominantly guided by the real index variation between the cladding and active

regions, the overlap between the carrier profile and first order mode increases with increased carrier density. This means that the gain seen by the mode increases, and at some point the gain becomes sufficient for it to be equal to the losses in the cavity, and the mode therefore begins to lase.

At four times threshold current the strength of the second mode is not sufficient to cause a dip at the centre of the field profile, however, due to the nature of the first order mode profile the overall field shape is widened. As the injected current is increased, the gain of the second mode also increases, and the power carried by this mode relative to the fundamental mode increases, causing a dip in the field profile. Increasing the current increases this dip. This has a knock on effect on the carrier profile, and thus the current profile, with the carrier density in the centre of the active layer increasing as the relative optical field strength here decreases, as seen in figure 6.7.

Figure 6.9 shows the relative photon densities of the two lasing modes. It can be seen that the photon density of the fundamental mode increases virtually linearly up to the point at which the first order mode begins to lase. The slope of the curve then suddenly alters, keeping the sum of the two lasing modes as a linear function of current. It can be seen that, as the current is increased above the threshold for the first order mode, the photon density of this mode initially increases relative to the fundamental mode, such that, at a certain value of injected current the first order mode will be the predominant lasing mode, provided that no further modes begin to lase.

It can be seen from figure 6.9 that the sub-linear behaviour shown in figure 6.4 does not coincide with the onset of the second lasing mode, and there is no kink in the L-I curve at the point at which the second mode begins to lase. However, as seen from the guide lines on the figure, the sublinear nature of the overall light-current curve is mainly due to the sublinearity of the photon density characteristic for the first order mode (this effect

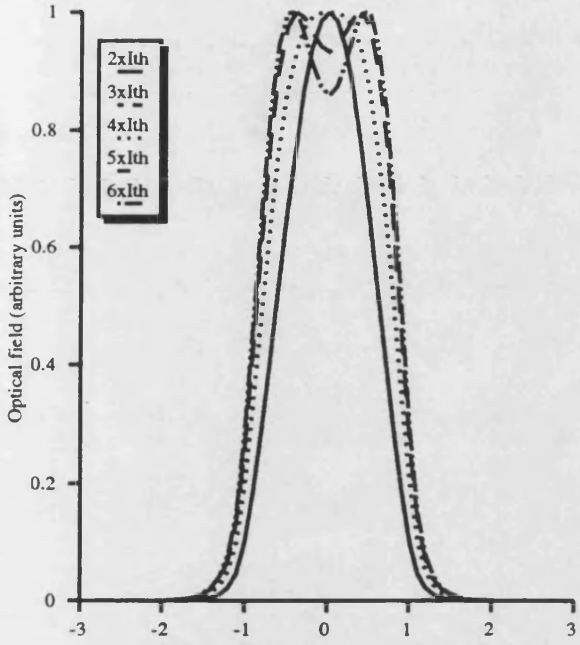

Figure 6.8 Variation of the normalised optical field across the active/homojunction plane

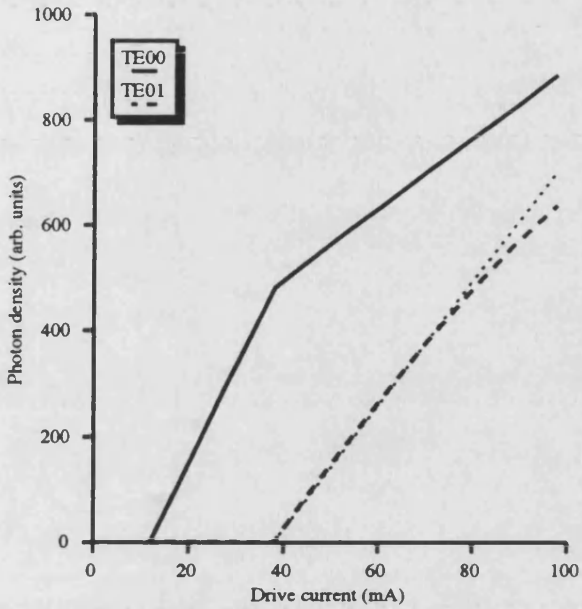

Figure 6.9 The variation of photon density with drive current. The dotted line shows a linear relationship as a guide to the eye.

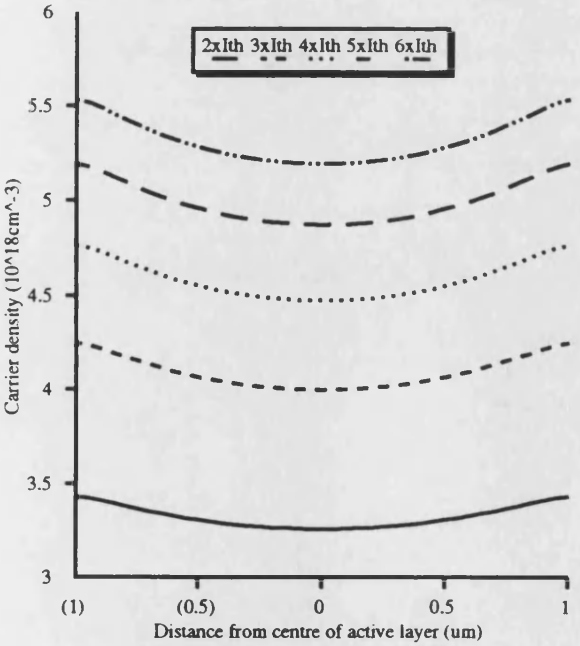

Figure 6.10 The variation of carrier density across the active layer when stimulated recombination is ignored.

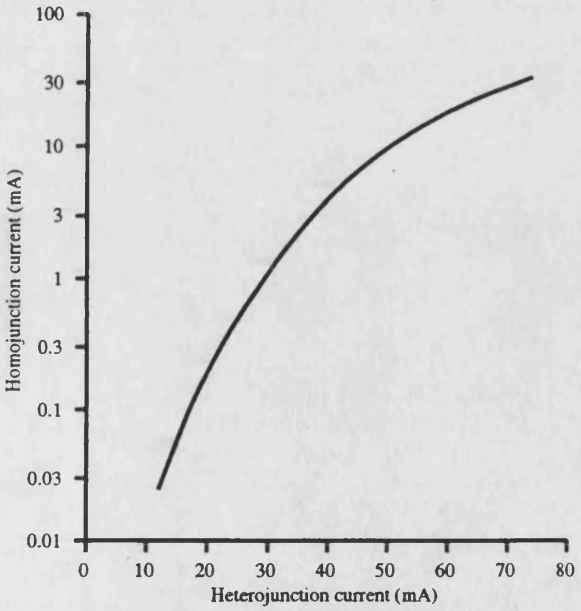

Figure 6.11 Homojunction leakage current versus heterojunction current when no stimulated recombination is allowed.

is seen more clearly in figure 6.20, where the lower doping level allows greater current leakage and thus sub-linarity). The reason for this is examined in greater detail in section 6.6.4, where it is shown that it is the current leakage that is responsible for the non-linear nature of the L-I curve, and not the second lasing mode.

6.6.2 The effect of stimulated recombination

The carrier density profiles of figure 6.7 show that the carrier density becomes pinned near to its threshold value across the active layer, although at the edges of the active region, where the optical field is lowest, there is less carrier pinning. If the optical field were not present, then the carrier density would not be pinned, and would continue to rise with drive current. This effect is shown clearly in figure 6.10, which plots the distribution of the carrier density across the active layer for various drive currents, assuming that no stimulated recombination occurs.

Ignoring the stimulated recombination effectively means that there is no light production in the cavity, and therefore no threshold current. For comparison purposes, the carrier density has been plotted assuming that the threshold current would be the same as for figure 6.7. It can be seen from figure 6.10 that whilst the carrier density is no longer pinned near to its threshold value, the carrier density profile does still dip in the centre, although not to such an extent as is seen in figure 6.7. Since there is no stimulated recombination, the dip must be caused by current crowding at the edges of the active layer, and by carrier diffusion.

Comparison of figures 6.10 and 6.7 shows the effect of the inclusion of the optical model on the carrier profile. The effect on the calculated leakage current in the device is just as great, and the graph of heterojunction versus homojunction current, assuming no stimulated recombination, is shown in figure 6.11. It can be seen, by comparing figure

6.11 with figure 6.5, that if the stimulated recombination is ignored, the increased active layer carrier density leads to greatly increased leakage current. The linear relationship between heterojunction and homojunction current is also lost as a greater current flows through the homojunctions. These two figures, 6.10 and 6.11, show the crucial effect of the stimulated carrier recombination on the electrical characteristics of the BRS laser.

6.6.3 The effect of the second lasing mode

The model outlined in this chapter includes, in a self consistent fashion, the effects of several lasing modes. This type of fully self-consistent treatment of the optical problem only been carried out by one other author [6], and in this case a highly simplified electrical model was used. Most other models of the lasing characteristics of semiconductor devices only include the effect of a single lateral optical mode. However, it has been observed experimentally for buried heterostructure lasers that lasing does occur in more than one lateral mode [17], due to the strong real index guiding provided. It is therefore instructive to observe the effects of the second lasing mode on the laser characteristics by comparison to the case when only a single optical mode is allowed to lase.

It is simple, from the model, to limit lasing to a single mode, and this has been done for the results presented in this section. The carrier profile across the active layer in such a case is shown in figure 6.12, where carrier profiles are presented for five different values of injected current. When compared to figure 6.7, which shows the same characteristic for the case where lasing is allowed in the second mode, it can be seen that there are considerable differences in the carrier profiles. The variation in carrier density across the active region is greater than that for the double moded case, because with only a single optical mode there is greater optical field in the centre of the active region, but less at the edges, and hence the carrier density at the active layer edges is not clamped

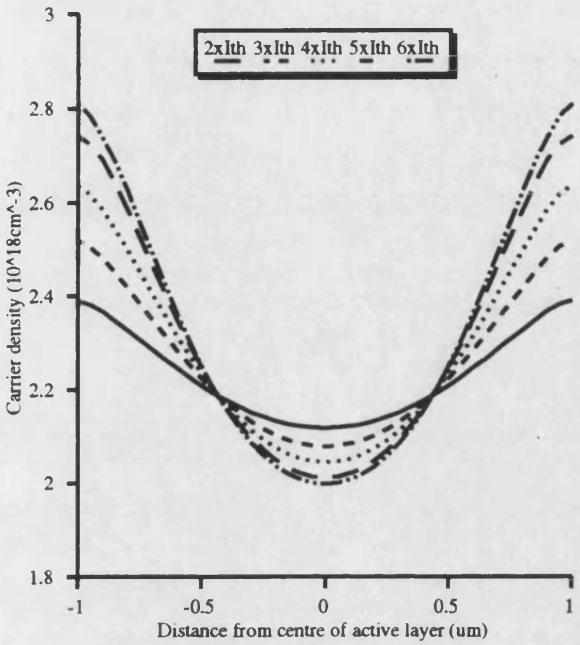

Figure 6.12 The variation of carrier density across the active layer when only a single mode is allowed to lase

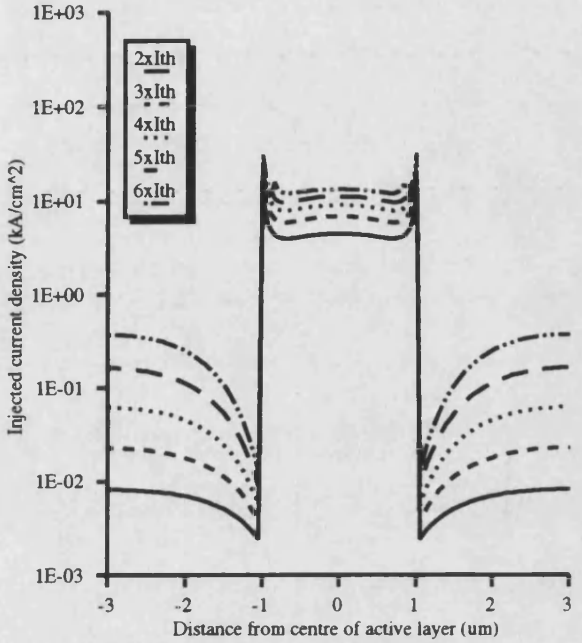

Figure 6.13 The variation of current injection across active/homojunction layer when only a single mode is allowed to lase

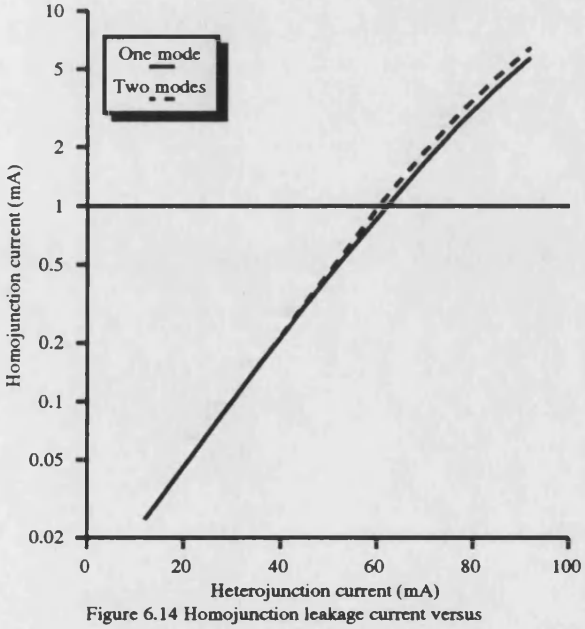

Figure 6.14 Homojunction leakage current versus heterojunction current showing the effect of a second lasing mode.

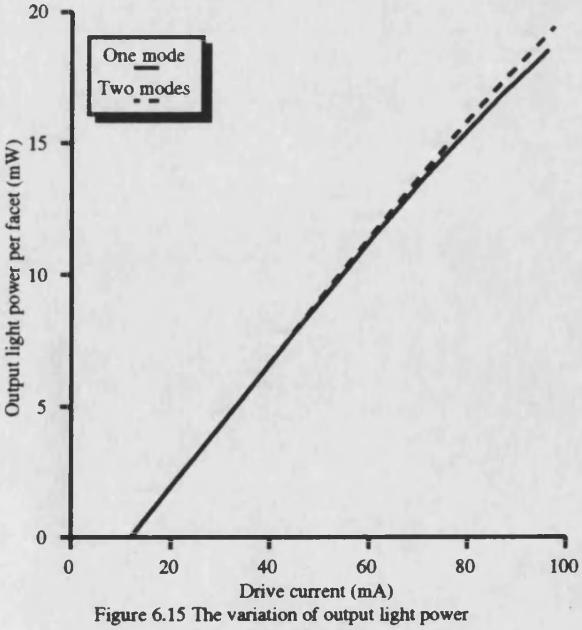

Figure 6.15 The variation of output light power with active layer current showing the effect of a second lasing mode

by the lasing action.

The pattern of current density in the device also differs, due to the lack of the second lasing mode, and this is shown in figure 6.13. The change of the curve in the centre of the active region from convex to concave, as seen in figure 6.6 for the case where two lasing modes are allowed, no longer occurs. This indicates that the change in current distribution is due to the effects on the stimulated recombination of the second lasing mode.

The effect on the leakage current of allowing only the fundamental mode to lase is seen in figure 6.14. It can be seen that by allowing only a single mode to lase, the leakage current is over-estimated slightly. The main reason for this is that the carrier density at the edges of the active layer is increased by the single mode assumption, as seen in figure 6.12. This increases the voltage at the edges of the active layer, with the consequence that the voltage across the homojunction region will be increased, and therefore the leakage will be higher.

The result of the single mode assumption on the light-current characteristic is shown in figure 6.15, which also shows, for comparison, the L-I curve obtained when two modes are allowed to lase. It can be seen that, due to the over-estimation of the leakage current, the curve for the single mode case shows greater sublinearity. Although the effect may appear slight, it has already been noted that such slight variations can render the laser useless for certain applications.

The point at which the second lateral mode begins to lase can be an important design parameter. The second mode alters the beam width, changing the coupling of the light out of the device, and will have a turn on transient which may affect the modulation performance. It can also be shown that the dynamic performance of lasing devices is related to the carrier profile across the active layer [18], which is significantly altered if

the second lasing mode is ignored. The inclusion of the second lateral mode in the model therefore alters the laser performance, and the inclusion of the second mode in the model will lead to a more accurate assessment of the device characteristics, and enable the structures which do not support a second mode to be identified.

6.6.4 The effect of doping variations

It was seen in chapter 3 that the simple, non self-consistent model predicted that leakage current through the homojunction regions can be reduced to negligible levels by increasing the doping level of the p-type upper cladding layer. In this section the influence of the doping level of the upper cladding layer on both the calculated electrical and optical characteristics is investigated. The effect of the doping level on the overall light versus current characteristic of the device is shown in figure 6.16. The figure shows the effect of increasing the cladding doping level from $5.0x10^{17}cm^{-3}$ to $2.0x10^{18}cm^{-3}$. It can be seen that the characteristics become increasingly linear, indicating that the leakage current is indeed reduced. Above a doping level of about $1.1x10^{18}cm^{-3}$ (not shown on the figure) the curves become virtually linear, whilst at the lowest doping level investigated, $5.0x10^{17}cm^{-3}$, there is considerable leakage as evidenced by the sublinearity of the curve.

It has been observed from experiments [15] carried out on CM and other lasers that increasing the doping level of the upper cladding layer has the effect of increasing the threshold current of the lasers. This effect, however, is not seen in figure 6.16. The p-type dopant which is used in the InP/InGaAsP lasers studied here is Zn, which can be used to obtain very high doping levels. One of the characteristics of this dopant is that it is very mobile. The lasers studied here have regrowth stages, with the BRS laser the active region stripe is defined on the wafer, and then the upper cladding layer grown over it.

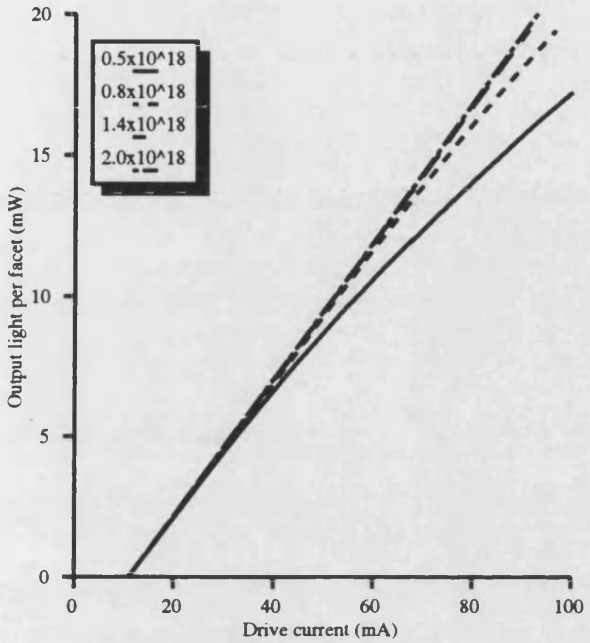

Figure 6.16 Variation of output light power with drive current, with cladding layer doping level as a parameter. Undoped active layer.

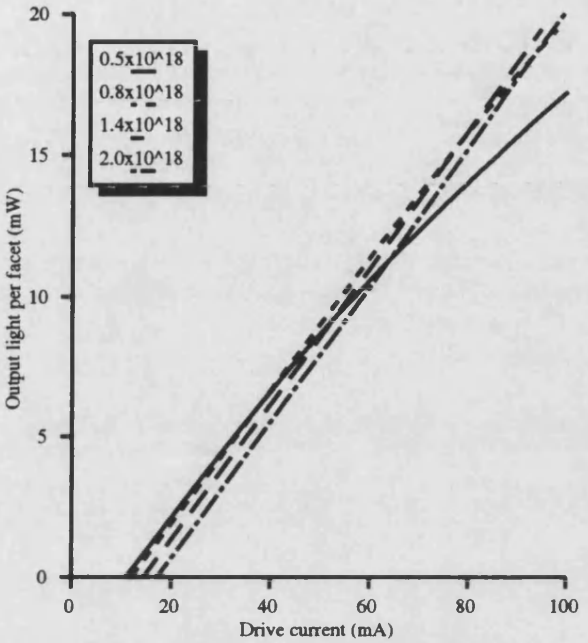

Figure 6.17 Variation of output light power with drive current, with cladding layer doping level as a parameter.

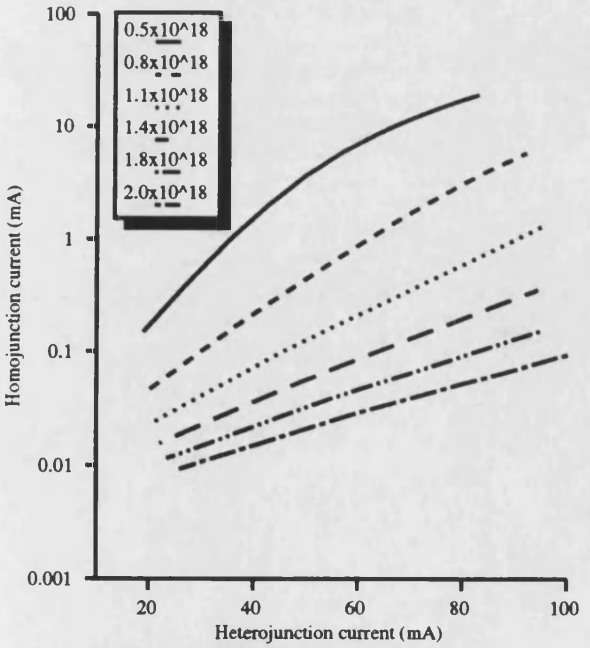

Figure 6.18 Homojunction leakage current versus heterojunction current with p-doping level as a parameter.

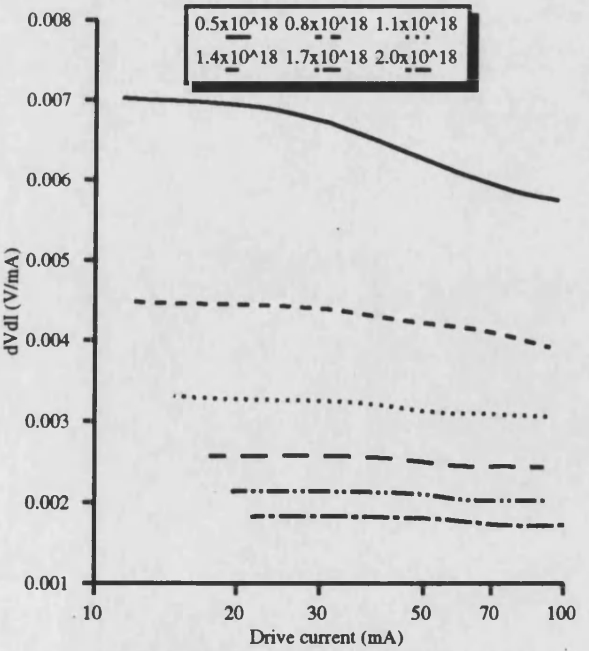

Figure 6.19 dVdI versus drive current with cladding layer doping as a parameter

is defined on the wafer, and then the upper cladding layer grown over it. With the CM laser, the regrowth of material to bury the active layer is by either mass transport or vapour phase epitaxy, both of which are relatively high temperature processes.

The simplicity of the structures studied here is an advantage in the fabrication process, however it means that the highly doped cladding region is in direct contact with the nominally undoped active region during the re-growth processes. It is therefore reasonable to assume that the doping of the cladding layer migrates into the thin active layer. In the model, this means that the doping of the active layer, p_a, is equal to the doping of the cladding layer, p_o. The calculated light versus current characteristics, assuming that the dopant migrates, are shown in figure 6.17. It can be seen that the threshold current does indeed now increase with doping level, as observed experimentally. This shows strong evidence to suggest that the p-type doping from the upper cladding region in the actual devices migrates into the active layer. The cladding and active layer doping levels are therefore assumed to be identical in all the results presented in this chapter, with the exception of figure 6.16.

The effect of the doping level on leakage current is seen in figures 6.18 and 6.19. In figure 6.18 the homojunction current is plotted against the heterojunction current, and figure 6.19 shows the I-dV/dI characteristic which was introduced in chapter 3. It can be seen that the calculated leakage current pattern is similar to that obtained from the non self-consistent electrical model in chapter 3 (figures 3.16(a) and 3.17(a)). As found in chapter 3, the leakage current curves are sub-linear at high values of heterojunction current, indicating the effects of current spreading in the cladding layer. However, the degree of sublinearity seen in figure 6.18 is greater than that of figure 3.14, and the predicted leakage currents are higher.

The I-dV/dI characteristic shown in figure 6.19 also shows the same basic form as that calculated from the electrical model of chapter 3 (figures 3.16(b) and 3.17(b)). The calculated change in slope of the characteristic, indicating turn on of the homojunction regions is, however, less in the self-consistent model than in the non self-consistent electrical model. In the cases where a significant homojunction current flows (i.e. doping levels less than $1.1x10^{18}cm^{-3}$), the change in slope of the characteristic can be seen.

The electrical model used in the self-consistent model is identical in all respects, apart from the calculation of the active layer carrier density, to the electrical model of chapter 3. In chapter 3 a fixed, uniform carrier density was assumed in the active layer, whereas the effects of carrier diffusion and stimulated recombination are included in the self-consistent model and used to calculate the carrier density in the active region. The main differences between the characteristics calculated from the two models are due to two consequences of the calculation of the active layer carrier density. First, the level of the carrier density calculated by the self-consistent model is generally higher than that used for the electrical only simulation. Secondly, the spatial hole burning in the carrier profile across the active layer, caused by stimulated recombination, carrier diffusion and non-uniform current injection into the active layer, alters the current spreading in the cladding region.

Figures 6.18 and 6.19 indicate that the effects of stimulated recombination and carrier diffusion, which are taken into account in the full self-consistent model, are of importance in calculating the form of the electrical properties of the device. Also, as was demonstrated in chapter 3, the value of the carrier density chosen in the electrical model has an important effect in determining the actual value of leakage current calculated, and the value of the carrier density can only be found from the fully self-consistent model.

Since it is the actual value of leakage current that is of interest when manufacturing a device, it can be seen that the self-consistent model is a much more accurate predictor of the electrical characteristics than the more simple electrical model of chapter 3.

The photon densities of the first two lasing modes are shown in figure 6.20 plotted against drive current, with the cladding (and active) layer doping density as a parameter. It can be seen that the slope of the fundamental mode photon density curves change dramatically when the second lasing mode appears, as has been seen previously. Figure 6.20 also shows that the sublinearity of the light-current curve is mainly due to changes in the behaviour of the first order and not the fundamental mode. For doping densities below $1.1x10^{18}cm^{-3}$ the IL characteristic is sublinear, but the sublinearity is most noticeable at the lowest doping level studied, $5.0x10^{17}cm^{-3}$. It can be clearly seen from figure 6.20 that at this doping density, whilst the curve for the fundamental mode consists of two virtually straight line segments, the curve for the first order mode is substantially sub-linear, and cuts across the characteristics for the higher doping densities.

The fact that the sub-linear L-I characteristic is not caused by the presence of the second lasing mode is demonstrated by comparing the results of figures 6.20 and 6.17. In figure 6.17 it can be seen that the L-I curves become linear for increasing doping, whereas figure 6.20 shows that for all doping levels examined two modes are lasing. The sublinearity is therefore not due to the second lasing mode, but to the leakage current that is by-passing the active layer.

The model includes a great deal of interaction between the electrical and optical characteristics, and the reason why the leakage has a greater effect on the first order mode photon density is not clear. One possible explanation for this effect may be found by considering the fact that the first order mode requires a high carrier density at the edges of the active region for lasing. When the homojunction regions become conducting the

current distribution alters, and a proportion of the current that would otherwise be injected into the edges of the active region (and generate carriers here) flows through the homojunctions. This effect is more pronounced at the edges of the active region than at the centre, and hence when the homojunction regions begin to conduct the effect on the first order mode is greater than on the fundamental mode.

It can also be seen from figure 6.20 that the threshold current for the fundamental mode increases less with increasing doping density than the threshold current for the first order mode. Therefore, as the doping density increases, the range of current over which the laser will operate in a single lateral mode increases substantially. The explanation for the increase in threshold of the first order mode relative to that of the fundamental mode is again related to the carrier distribution in the active layer.

Again, due to the complex interactions involved, it is not possible to be precise about the reason for this effect, but a major contributing factor will be that the increased doping level decreases the resistivity of the cladding region. This means that at higher doping levels there is a more uniform distribution of current in the device, and therefore less current crowding at the edges of the active layer. There is therefore a more uniform current distribution injected into the active layer, and the carrier distribution in the active layer is thus flatter, with less carriers at the edges of the active region. This in turn leads to there being less optical gain at the edges of the active region, and the threshold of the first order mode is increased.

This combination of the two effects described above, that of increased threshold for the first order mode and greater sublinearity of the L-I characteristic due to leakage, can be seen in figure 6.21. The figure shows the normalised optical field profile across the active/homojunction plane of the laser at a drive current of six times the threshold current. From the figure the relative contributions of the fundamental and first order lasing modes

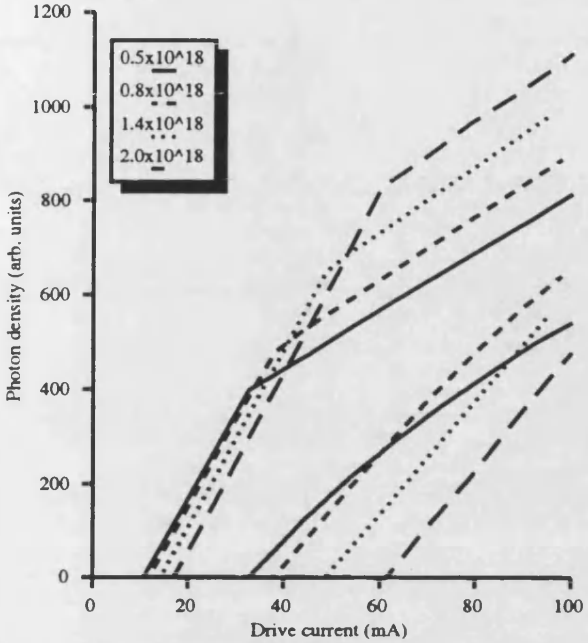

Figure 6.20. Variation of the photon density of the TE00 and TE01 modes versus drive current, cladding layer doping density as a parameter.

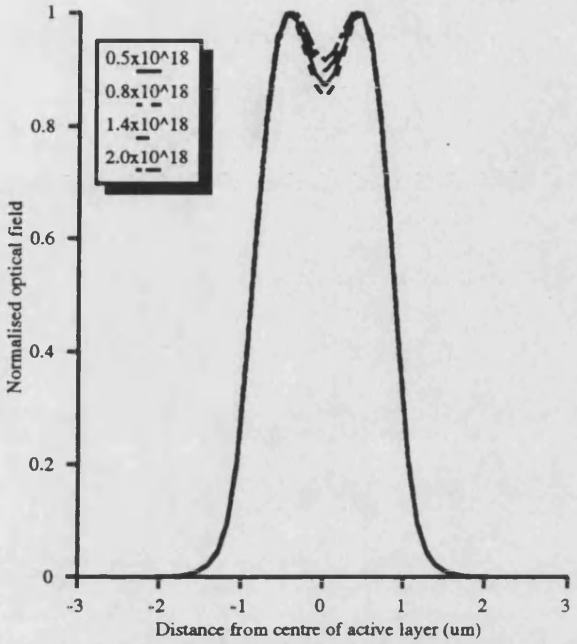

Figure 6.21 Normalised optical field across the active/homojunction plane at six times threshold current, with doping level as a parameter

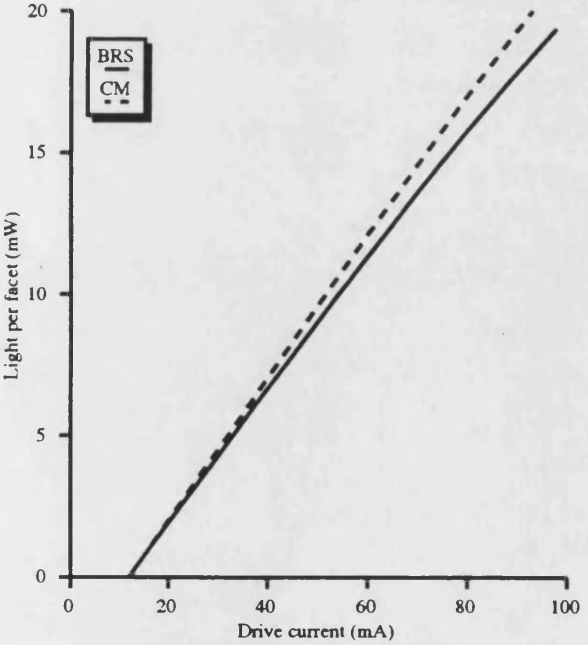

Figure 6.22. The variation of output light power with drive current, with device structure as a parameter.

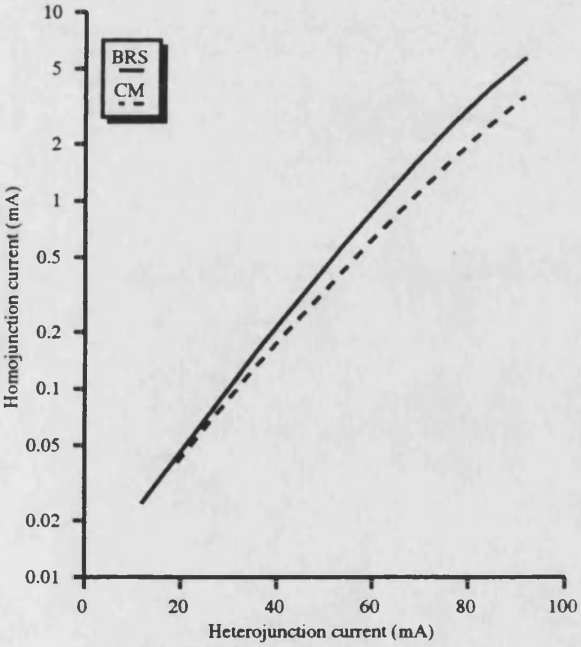

Figure 6.23. Homojunction leakage current versus heterojunction current, with laser structure as a parameter.

can be seen. The trend, as would be expected from the increased threshold of the first order mode with doping, is that increasing the doping level results in a less significant contribution of the second lasing mode. However, due to the effect of the leakage current reducing the power carried by the first order mode, at a doping level of $5.0x10^{17}cm^{-3}$ the contribution of this mode as a fraction of the overall power is less than at a doping level of $8.0x10^{17}cm^{-3}$.

The p-type doping level of the upper cladding region therefore has a much more complex effect than might have been assumed from the simple electrical or optical models. The doping level does, as anticipated, reduce the leakage of current through the homojunction regions. It also has the unfortunate effect of increasing the threshold current of the device, due to leakage of dopant into the active region. An unexpected benefit of increasing the doping level above that required for linearity of the L-I characteristic is that the tendency of the device to lase in more than one lateral mode is reduced.

6.6.5 The CM laser

It was noted in chapter 3, when the electrical characteristics of the BRS and CM structures were modelled in a non self-consistent fashion, that the difference between the two devices was small. The main difference that was noticed was that the leakage current in the CM device was lower than in the BRS laser. With the self-consistent model, the only differences are in the electrical model, the optical problem is the same for both devices, since the optical field decays to a very small fraction of its original intensity near the sloping mesa walls and these are therefore not included in the optical model.

Figure 6.22 shows a comparison between the light vs current characteristics calculated for the two different laser structures, each with identical dimensions. It is assumed that, as in chapter 3, the mesa angle of the CM laser is 45°. It can be seen that the two curves

are of the same form, the threshold current is identical in each case and the curves are substantially linear. The curve for the CM laser, however, shows a very slightly higher quantum efficiency relative to that of the BRS, and also lower leakage, as evidenced by the more linear characteristic.

A comparison of the leakage currents in the two devices is shown in figure 6.23. It can be seen from this figure, as predicted from figure 6.22 and the non self-consistent modelling of chapter 3, that the leakage current is indeed slightly lower in the CM than the BRS laser. It would therefore appear that the current is focussed into the active layer by the sloping mesa sidewalls, as was found in chapter 3. The CM laser therefore offers slightly better performance than the BRS laser, which, together with its lower parasitics, increases its suitability for high bandwidth applications.

6.6.6 The effect of dimensional variations

It has been demonstrated, in chapters 3 and 5, that the variation of the device dimensions has a great effect on both the electrical and optical properties of buried heterostructure lasers. One of the main uses of a model such as the one presented here is to analyse the effects of various dimensional changes and to obtain an optimized device structure. Such alterations to device geometry are difficult and expensive to carry out experimentally. The model has therefore been used to examine the effects of changes in the device geometry on the static performance of the laser devices. In the following two sections, unless otherwise stated, the nominal device dimensions and doping levels are as given in table 1.

6.6.6.1 Active layer depth

The active layer depth has an effect on both the electrical and optical properties of the device. The confinement of the optical mode to the active layer, and hence the stimulated recombination, depends critically on the active layer depth, whilst the generation of carriers in the active layer, and hence the electrical properties of the device, are also depth dependant. These two factors operate in opposition, and it can be shown, using a simple analysis (e.g. [19]) that there should be an optimum active layer depth which produces a minimum threshold current.

Figure 6.24 shows the effect on the calculated threshold current of varying the active layer depth between 0.1 and 0.2μm. As expected, there is an optimum value of depth which gives the lowest threshold, and the threshold current is below 12mA for active layer depths between 0.125 and 0.15μm. In practice, due to variations in the growth of the wafer, the active layer depth will vary across a wafer, but with modern processing technology it is possible to control the active layer depth between these limits. For many reported devices, the active layer depth used is around 0.15μm, corresponding to the minimum threshold, although there has been a tendency recently to increase the active layer depth to improve the optical confinement, at the expense of laser threshold.

The modelled light-current characteristics for lasers with active layer depths varying between 0.1 and 0.2μm are shown in figure 6.25. The figure shows that the sub-linearity of the LI characteristic, as well as the threshold current, varies with depth, indicating that the leakage current is influenced by device depth. This is to be expected, since the carrier generation term in the carrier diffusion equation depends on active layer depth, as does the radiative recombination term, though more indirectly (the optical field is

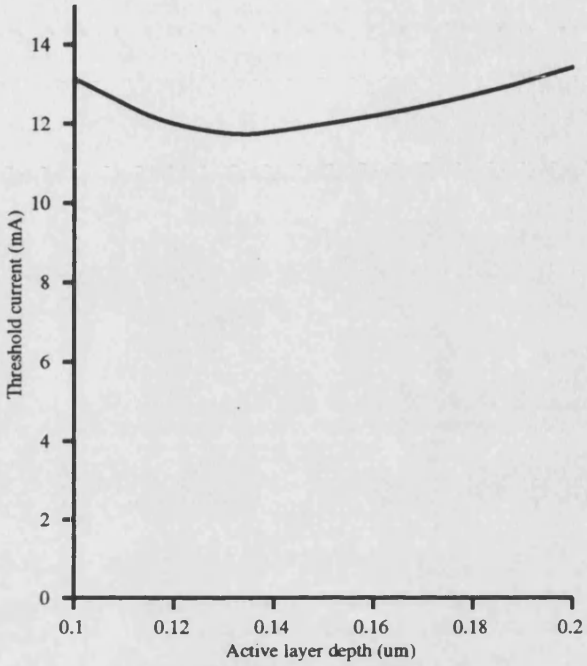

Figure 6.24 The variation of threshold current with active layer depth

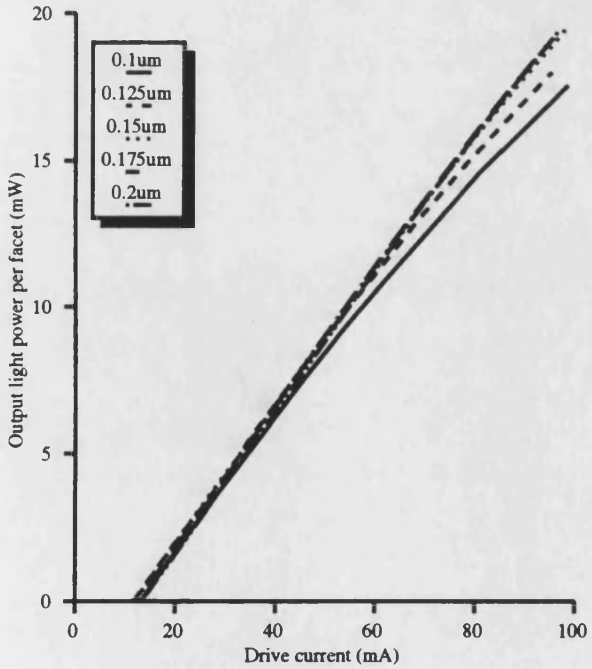

Figure 6.25 The variation of output light power with active layer depth as a parameter.

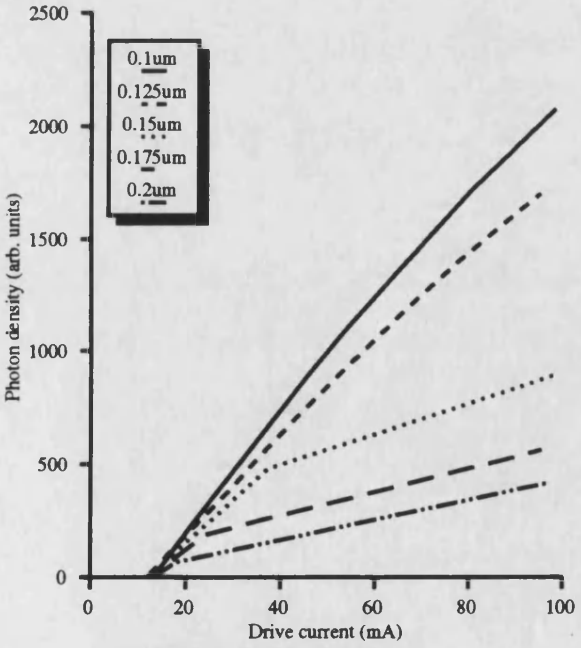

Figure 6.26 Variation of photon density of the TE00 mode with current, with active layer depth as a parameter

better confined with a deeper active layer). It can be seen that increasing the active layer depth, from 0.1μm to 0.15μm, has quite a large effect on reducing the leakage current, whereas a further increase in depth to 0.2μm has a limited effect on leakage.

The effect of the active layer depth on the mode structure of the laser is shown in figure 6.26. The figure shows that, at an active layer depth of 0.15μm the characteristic is clearly multi-moded, as evidenced by the abrupt change in slope of the photon density characteristic of the fundamental mode, where the first mode begins to lase. However, at a depth of 0.125μm the characteristic shows only one lasing mode. The main reason for this effect is that the active layer depth alters the confinement of the optical modes in the transverse direction. Reducing the confinement will reduce the gain experienced by the mode, and at some point the gain will be reduced sufficiently to inhibit lasing. Further reduction of the active layer depth will result in the mode being cut-off. The reduction in confinement is greater for the first order mode than the fundamental mode, and the differential gain between the modes is therefore altered by the active depth, as was seen in chapter 5.

It can therefore be seen that the active layer depth has an effect on the threshold current, leakage current and mode structure of the laser. For a minimum threshold current, a depth of 0.125 to 0.15μm must be used. However, at one end of this range, 0.125μm, the leakage current is high, whereas at the other end the laser operates in several lateral modes. The two effects, therefore, are not complimentary, and with this particular laser geometry an active layer depth may be defined to limit either leakage or multimode operation, but not both effects.

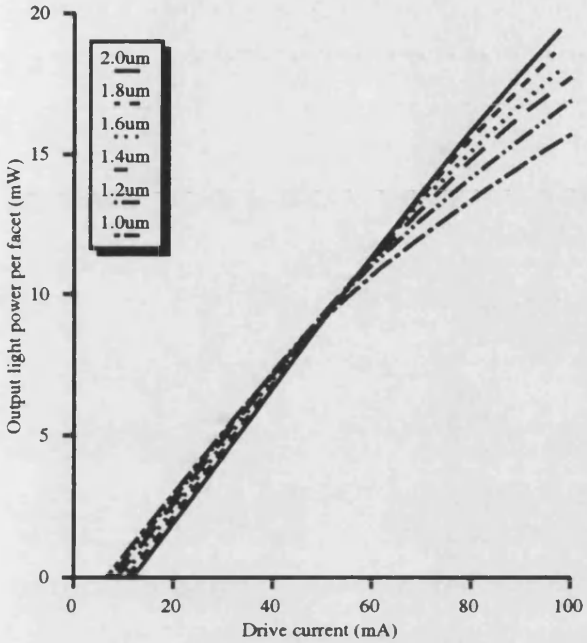

Figure 6.27 The variation of output light power with drive current, with active layer width as a parameter

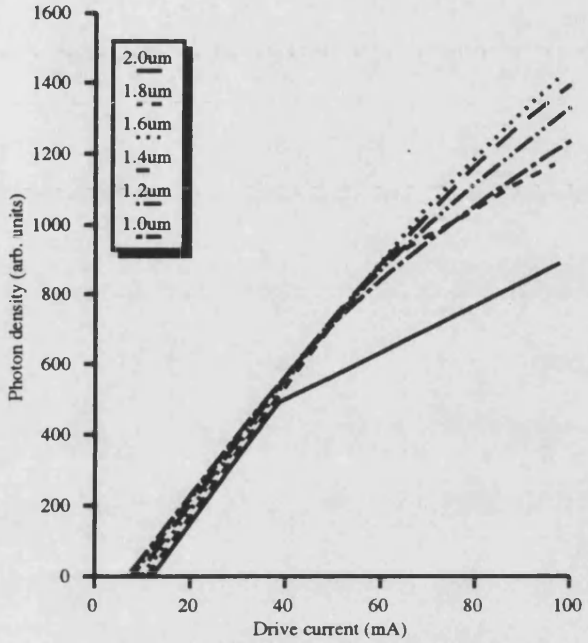

Figure 6.28 Variation of photon density of the TE00 mode with current, with the active layer width as a parameter.

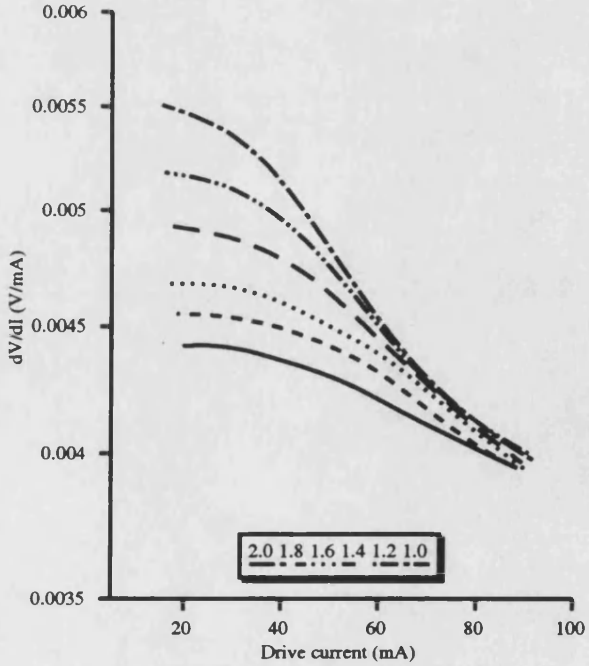

Figure 6.29 dV/dI versus drive current with active layer width as a parameter

photon density of the mode therefore falls off.

Figure 6.28 is useful to demonstrate two important points. First, with an active layer cross section of 1.6μm x 0.15μm the first order mode is still guided by the waveguiding structure of the laser. However, figure 6.28 shows clearly that this mode does not lase, at least at currents up to 100mA. This demonstrates that single mode operation can be obtained in active regions which support higher order modes. Secondly, the leakage current is low (from figure 6.27) at active layer widths of 2.0 and 1.8μm, where two modes are lasing, but increases at lower device widths. This shows again that there is no relationship between the second lasing mode and the sublinearity of the characteristic.

The change in overall device resistance (dV/dI) against injected current is shown in figure 6.29. This characteristic was presented in chapter 3 for the electrical model, and is readily obtained from experimental measurements. The overall form of the characteristic is similar to that of figures 3.12(b) and 3.13(b) of chapter 3, however the actual values are different, which is to be expected since in chapter 3 a simple fixed active layer carrier density was taken, and the actual value of this carrier density was unknown. Figure 6.29, however, does not show such the clear cut change in slope that was seen in chapter 3. This is probably due a change in current distribution caused by the varying active layer carrier distribution seen, for example, in figure 6.7.

6.7 Discussion

In this chapter a self-consistent model for the static lasing characteristics of buried heterostructure lasers has been presented. The model uses the work presented in chapter 3 for the electrical model and chapter 5 for the optical model, and these are modified to

include the lasing condition, and to enable the calculation of the carrier density in the active layer. The model has been used to analyse both the BRS and CM laser structures, and the results from this analysis have been presented.

The model is capable of calculating experimentally observable characteristics, such as optical field profile, light-current and dV/dI characteristics. It is also possible to calculate characteristics which would be difficult or impossible to obtain experimentally, such as carrier and current profiles in the device, the relationship between heterojunction and homojunction leakage current, and the proportion of the power carried by each of the lasing modes. These characteristics are invaluable in explaining the effects seen in the observable parameters, and are one of the important features of the model.

It was seen that the inclusion of the second lasing mode in the model is important, since the calculated characteristics from the model are altered by the inclusion of the mode. The effect of the doping level was investigated, and it was seen that the effect of altering the doping level is greater than might be expected by the separate electrical and optical modelling carried out in the previous chapters. The leakage current is reduced by increasing the doping level, but the threshold current of the laser is also increased, due to migration of the cladding layer dopants into the active layer. By increasing the cladding layer doping level the threshold of the second lasing mode is also increased relative to the laser threshold. This means that for higher doped devices there is a greater range of currents over which the laser will operate in a single lateral mode.

The differences between the two device geometries under investigation, the CM and BRS lasers, was examined. It was seen that there was little difference between the two lasers, but as anticipated from the electrical modelling, the leakage current was slightly lower for the CM laser. The reason for this effect must lie in the geometry of the cladding region, which directs the current in different directions in the two lasers.

The effects on the laser output of varying the active region dimensions was investigated. It was seen that there is an optimum value of active layer depth that will produce a minimum threshold current. Unfortunately, this depth does not correspond to the value at which single lateral mode operation is ensured, and therefore some other means of ensuring this is required. Reducing the active layer width will provide a means of limiting the laser to single lateral mode operation, however narrow active layers can cause problems with coupling of the light out of the device and into the fibre. If one were designing a laser there is therefore a compromise to be made, and the model presented here would be an excellent design tool to ensure good laser performance.

	Parameter	Value	Units
Electrical constants	D_e	10	cm^2s^{-1}
	B_0	$1.1x10^{-10}$	cm^3s^{-1}
	B_1	$1.2x10^{-29}$	cm^6s^{-1}
	C	$3.3x10^{-29}$	cm^6s^{-1}
	D	$1.9x10^{17}$	$cm^{-1.44}s^{-1}$
	z	0.52	
	N_c	$3.4x10^{17}$	cm^{-3}
	N_v	$1.5x10^{19}$	cm^{-3}
	E_g	0.954	eV
	μ_p	100	$cm^2V^{-1}s^{-1}$
	η	1	
	J_{sat}	20/*po*	cm^{-2}
	K1	$3.53553x10^{-1}$	
	K2	$-4.95009x10^{-3}$	
	K3	$1.48386x10^{-4}$	
	K4	$-4.42563x10^{-6}$	
Optical constants	λ	1.3	μm
	n_{InP}	3.2	
	$n_{InGaAsP}$	3.52	
	a	$3x10^{-16}$	cm^2
	b	400	cm^{-1}
	reflectivity	0.35	
	cavity loss	50	cm^{-1}
	R	-3	
Dimensions (see figure 6.3)	W	6.0	μm
	C	2.0	μm
	A	2.0	μm
	d	2.0	μm
	t	0.15	μm
	Length	250	μm

REFERENCES

[1] J.Buus, "Principles of semiconductor laser modelling," IEE proc J, vol. 132, no. 1, pp.42-51, 1985

[2] D.P.Wilt and A.Yariv "A self-consistent static model of the double-heterostructure laser," IEEE J.Quantum.Electron., vol 17, no. 9, pp.1941-1949, 1981

[3] T.Kumar, R.F.Ormondroyd and T.E.Rozzi, "A self-consistent model of the lateral behaviour of a twin-stripe injection laser," IEEE J.Quantum Electron., vol. QE-22, no. 10, pp.1975-1985, 1986

[4] K.B.Kahen, "Two-dimensional simulation of laser diodes in the steady state," IEEE J.Quantum.Electron., vol 24, no. 4, pp.641-651, 1988

[5] M.Ueno, S.Asada and S.Kumashiro, "Two-dimensional numerical analysis of lasing characteristics for self-aligned structure semiconductor lasers", IEEE. J.Quantum Electron., vol. 26, no. 6, pp.972-981, 1990

[6] P.Meissner, E.Patzak and D.Yevick, "A self-consistent model of stripe geometry lasers based on the beam propagation method," IEEE J.Quantum.Electron., vol. 20, no. 8, pp.899-905, 1984

[7] E.Meland, R.Holmstrom, J.Schlafer, R.B.Lauer and W.Powazinik, "Extremely high-frequency (24GHz) InGaAsP diode lasers with excellent modulation efficiency," Electron.Lett., vol. 26, no. 21, pp182-184, 1990

[8] W.B.Joyce, "Carrier transport in double heterostructure active layers," J.Appl.Phys., vol. 53, no. 11, pp.7235-7239, 1982

[9] R.Olshanski, J.LaCourse, T.Chow and W.Powazinik, "Measurement of radiative, Auger, and nonradiative currents in 1.3μm InGaAsP buried heterostructure lasers," Appl.Phys.Lett., vol. 50, no. 6, pp 310-312, 1897

[10] W.B.Joyce and R.W.Dixon, "Analytic approximations for the Fermi energy of an ideal Fermi gas," Appl.Phys.Lett., vol. 31, no. 5, pp.354-356, 1977

[11] P.C.Kendall, M.J.Adams, S.Ritchie and M.J.Robertson, "Theory for calculating approximate values for the propagation constants of an optical rib waveguide by weighting the refractive indices," IEE Proc. A, vol. 134, no. 8, pp.699-702, 1987

[12] C.F.Gerald, and P.O.Wheatley, "Applied numerical analysis," fourth edition, Addison-Wesley publishing, New York, pp 356-363, 1989

[13] M.C.Amann, and W.Thulke, "Current confinement and leakage currents in planar buried-ridge structure laser diodes on n-substrate," IEEE J.Quantum Electron., vol. QE-25, no. 7, pp.1595-1602, 1989

[14] Z.L.Liau, and J.N.Walpole, "Prevention of current leakage in mass transported GaInAsP/InP buried heterostructure lasers with narrow transported regions," IEEE J.Quantum Electron., vol. QE-23, no. 3, pp.313-319, 1987

[15] Z.L.Liau, J.N.Walpole, and D.Z.Tsang, "Fabrication, characterisation, and analysis of mass-transported GaInAsP/InP buried heterostructure lasers," IEEE J.Quantum Electron., vol. QE-20, no. 8, pp.855-865, 1984

[16] C.B.Su and V.Lanzisera, "Effect of doping level on the gain constant and modulation bandwidth of InGaAsP semiconductor lasers," App.Phys.Lett., vol. 45, no. 12, pp.1302-1304, 1984

[17] H.Burkhard and E.Kuphal, "Three and four layer LPE InGaAs(P) mushroom stripe lasers for λ=1.30, 1.54 and 1.66μm," IEEE J.Quantum.Electron., vol. 21, no. 6, pp.650-657, 1985

[18] N.Chinone, K.Aiki, M.Nakamura and R.Ito, "Effects of lateral mode and carrier density profile on dynamic behaviours of semiconductor lasers," IEEE J.Quantum.Electron., vol. 14, no. 8, pp.625-631, 1978

[19] G.H.B.Thompson, "Physics of semiconductor laser devices," John Wiley and sons, New York, 1980

CHAPTER 7: CONCLUSIONS AND FURTHER WORK

7.1 Introduction

This thesis has considered, in depth, the modelling of buried heterostructure semiconductor laser devices. It has been seen that in order to model the characteristics of diode lasers accurately, both the electrical and optical characteristics of the device must be considered. A self consistent model has been developed from the basic building blocks of the electrical model given in chapter 3 and the optical model of chapter 5. This self consistent model has been used to examine the lasing properties of various device structures, focussing specifically on the buried ridge structure (BRS) and constricted mesa (CM) lasers.

The investigation of these laser structures has examined the above-threshold characteristics, and concentrated on the twin problems of current leakage around the active layer, and multi-lateral mode operation. It has been shown that both of these problems can be alleviated by proper design. The important parameters in limiting current leakage have been shown to be the upper p-type cladding layer doping level and the ratio of active width to device width, the dominant parameter being the doping level. To limit the multimode operation it is necessary to have a relatively narrow and thin active region, and it has been shown in this work that the required width is less than the often quoted value of 2μm.

7.2 The electrical model

The electrical model, developed in chapter 3, considered the problem of current spreading in buried heterostructure lasers. The model does not account for the effects of carrier

recombination due to the presence of an optical field in the active layer, and it is therefore only valid up to threshold. In order to model the above-threshold characteristics (in a non self-consistent fashion) it was necessary to assume that the carrier density in the active layer becomes clamped at its threshold value. A value of carrier density ($2.0x10^{18}cm-3$) was chosen, within the range found in previous experimental and theoretical studies [1,2], and the carrier density was assumed to take this value throughout the width of the active layer. It was shown that the actual value of carrier density only has a multiplicative effect on the leakage current.

The electrical modelling concentrated on examining leakage currents around the active layer of above threshold buried heterostructure lasers. From the model it was possible to see several trends. As would be expected, increasing the ratio of active layer width to homojunction width decreased the ratio of leakage current to total current. However, the depth of the cladding region and the contact width were found to have only a small influence on the leakage current. The main influence on the leakage current was found to be the cladding layer doping level, with increasing doping levels dramatically reducing the homojunction leakage current.

Using the model it was possible to simulate the I-V characteristics of devices, and thus to calculate the I-dV/dI characteristic, both of which can be obtained experimentally. From these, it can be seen that the I-dV/dI characteristic can be used to examine directly the effect of the leakage current. Above threshold, a deviation in the characteristic shows the onset of current leakage. This could be a powerful experimental tool where other direct experimental methods cannot be used.

7.3 The optical model

The investigation of the optical characteristics used the Weighted Index method to model the waveguiding of the lasers. The standard WI method could not be applied directly to waveguides of complex permittivity, and the method was therefore generalised to account for complex permittivities by modifying the normalisation condition used. The optical modelling shows that, for buried heterostructure lasers of normal dimensions, neither the propagation constant nor the confinement factor achieve the asymptotic values for one dimensional waveguides which would be reached for guides of infinite width. It is therefore necessary to account for the two dimensional nature of the waveguides, and the WI method is ideal for use in such situations, being both rapid and accurate compared with other approximate techniques available.

The modelling of the optical characteristics of waveguides takes account of the carriers present in the active layer. The carrier injection depresses the real part of the refractive index, and increases the imaginary component, thus altering the waveguiding properties. The waveguide gain and propagation constant were examined for the case of uniform carrier density across the width of the active layer. It was seen that in this case, for normal guide dimensions, the relationship between carrier density and waveguide gain was nearly linear. It was shown that for typical waveguide geometries and internal losses, threshold carrier densities of around $2x10^{18}cm^{-3}$ are required for the lasing condition to be met.

7.4 The self-consistent model

The results of the self-consistent model show that the carrier density is not uniform across the active layer as was assumed in the non self-consistent modelling of the electrical and optical properties. Indeed, the carrier density profile across the active layer alters with

increasing injected current, active layer dimensions and the p-type cladding layer doping concentration. The non-uniform distribution of carriers is due to two main factors. The primary factor is spatial hole burning of the carriers caused by increased stimulated recombination in the region of high optical field. A further reason for the non-uniform carrier distribution is the current crowding in the device, which alters the current injection into the active layer and thus the carrier distribution.

The self consistent model shows that the leakage current is underestimated by the simpler electrical only model of chapter 3. This is due to two factors. The self-consistent model predicts a higher active layer carrier density than has been used in the electrical model, leading to higher leakage currents. Secondly, the carrier density varies across the active layer. The spatial hole burning and current crowding cause the carrier density at the edges of the active region to be higher than at the centre. This implies that the voltage across this part of the active layer increases, and this in turn requires that the voltage across the homojunction regions is increased. The increased homojunction voltage results in increased current passing through the homojunction regions and therefore greater leakage current.

The carrier density alters the refractive index in the active layer, altering its waveguiding properties. The change of the carrier profile caused by spatial hole burning and current crowding alters the gain profile across the active layer, and this means that a second optical mode may have sufficient gain to lase. The presence of the second lasing mode does not lead to a kink in the light-current characteristic, due to the well defined index guiding of the laser, but it can cause problems with the modulation and coupling performance of the devices.

The inclusion of the second optical mode in the model enables investigation of the point at which this mode begins to lase, and the structures in which a second mode is prevented

from lasing. It was demonstrated that it is possible to ensure lasing in only the fundamental mode by reducing the active layer width, or depth, sufficient to reduce the confinement of the second mode below a certain required value. It was also shown that the threshold current of the second lasing mode can be increased by increasing the doping density of the upper cladding layer. Other effects of the increased doping are to reduce the leakage current, and increase slightly the laser threshold current.

Without the inclusion of the second mode, it was found that the leakage current predicted by the model is artificially increased, due to the increased spatial hole burning in the centre of the active region. The self-consistent model therefore provides a more accurate picture of the laser characteristics than would be obtained from a single mode model. This fact demonstrates again that a self-consistent approach is required to obtain an understanding of what might otherwise seem to be anomalous behaviour.

7.5 Suggested further work

The model developed in this thesis has so far only been applied to the BRS and CM laser geometries. However, it would be possible to use the model, with suitable changes to the boundary conditions, in a wide range of laser structures, such as multiple stripe, ridge and rib waveguide lasers. The optical waveguide model is generally applicable to any waveguide structure where the two dimensional scalar wave equation is valid, and can be used to study waveguides where the predominant guiding is by gain guiding, index guiding, or a combination of both. The electrical model is more restricted, and the conditions in which the model is valid are given in chapter 3.

It would be possible to extend the model in several ways, although some of these would require extensive further work. One of the main problems in the practical operation of

laser devices is the temperature dependence of the output characteristics. Mass transported lasers are particularly prone to high temperature dependence, possibly because of the diffusion of dopants during the mass-transport process [3]. The temperature spreading in thermally conductive devices is well described by the Laplace equation, and the program already incorporates a Laplace equation solving routine. Temperature spreading from an external heat-sink would therefore be relatively simple to incorporate into the model.

The generation of heat inside the laser, and the effects of the temperature on the laser parameters are, however, not so simple to model. Such heating effects are caused by Ohmic heating and carrier recombination effects. Heat generation in the active layer has been previously investigated for other laser structures, and it has been found that this cannot be ignored [4]. The temperature dependence of the electrical properties of the BRS laser has also been studied previously [2], in this case the temperature dependence of the parameters was included in the model by simple analytic expressions. However, in the self consistent model it is the temperature dependent optical gain parameters that are the most critical, and the modelling of these parameters is not simple.

The gain parameters of the laser are also dependant on the doping level in the active layer. The most significant addition that would be required is an accurate model of the effect of temperature and doping levels on these gain parameters. Such a model has been published and the results tabulated in a convenient form [5], however the values of the parameters obtained from this theoretical model are only within an order of magnitude of those obtained from experiment. There appears to be a problem in obtaining a simple theoretical model of optical gain that agrees well with experimental values, probably due to inaccuracies in the band parameters used in theoretical modelling. The temperature modelling of the device may therefore be difficult.

InGaAsP lasers are well known for operating in more than one longitudinal mode, although this is almost always ignored in self-consistent modelling. A more accurate model would do well to include the effect of the longitudinal modes, since these will almost always be present in devices of reasonable length. If account is being taken of longitudinal modes, the phase relationships between the modes must be considered, and for consistency the longitudinal variations in carrier density and optical field should also be included. However, this would make the program far more complex, since the optical model would have to be significantly changed, and both the forward and backward propagating waves must be accounted for. Despite this, it would be possible to use an electrical model similar to that used in this work.

7.5.1 Temporal characteristics

Whilst this thesis has only examined static properties of lasers, the work carried out may have implications for the dynamic response of lasers. Several models of the temporal characteristics of CM and similar lasers have been constructed, and many of these predict that the relaxation oscillation peak at around resonance can be damped by spatial hole burning of carriers across the active layer, as well as by inclusion of all the longitudinal modes [4,6,7]. However, up to the present time this has been speculative, since no self-consistent model of the devices has been available, and therefore no accurate carrier profiles have been available.

The model used by Morton [4] employs a damping factor which is calculated by assuming a $\cos^2$ distribution of carriers across the active layer. This is used, via a series of approximations, to obtain a damping ratio. However, as can be seen from the results of chapter 6, the carrier distribution can vary widely, and a simple $\cos^2$ approximation is not a good one. From the present work, the exact carrier profile can be obtained for any

applied current, and hence a better, current dependant value of damping ratio found. This could then be included in the temporal model to improve the prediction of the time dependant response.

7.5.2 DFB lasers

Modelling of DFB lasers has, in general, not achieved the sophistication of Fabry-Perot laser models in terms of self-consistent electrical and optical models, due to the far greater complexity of such devices. In order to model DFBs, it is necessary to include the effect of longitudinal variations of optical field and carrier density. The model presented in this thesis could therefore not be applied to DFB lasers as it stands, however some features of the model do make it particularly suitable for extension to the DFB case. One of the important results from the present work that has a bearing on the DFB case is that spatial variations in the carrier density affect the leakage. It has also been found experimentally that current leakage is higher in DFB lasers than Fabry-Perot devices, and this may be due in part to the variation of carrier density along the length of DFB lasers.

The electrical model, in particular, can be easily extended to three dimensions, requiring only an extension of the finite difference scheme to a further dimension. Care should be taken, however, with the applicability of the model. It is often the case with DFBs that a waveguide layer of different bandgap is incorporated into the structure. Such a layer adds a further heterojunction into the structure, which is not easily accounted for in the model as it stands.

The optical model would require much greater complexity than the model used in this thesis. The simple two dimensional scalar wave equation is no longer applicable in the DFB case, and the full wave equation must be solved for both forward and backward

travelling waves by a more complex (and thus time consuming) method. One feature of the present model that is, however, ideal for modelling DFB lasers is that the carrier profile across any portion of the active layer fixes both the electrical and optical properties at that part of the device. Any self-consistent model for DFBs would be extremely large, and by using only the carrier density profile at any point to fully define all the properties of the device at that point, computer storage could be minimised.

7.6 Device Fabrication

The buried heterostructure laser has many desirable properties which can be exploited, and one of the initial aims of this work was to fabricate buried heterostructure constricted mesa lasers. Although this objective was not met due to financial constraints, much work was carried out in examining the relevant literature and in the design and purchasing of equipment to facilitate the device fabrication. Most buried heterostructure devices, however, require the growth of material over non-planar substrates. Material growth is an expensive and complicated process, requiring a great deal of investment in both equipment and personnel. It was therefore decided to use the mass transport process to bury the active layer.

Mass transport is relatively simple in comparison to other growth techniques, and requires relatively cheap and easy to operate equipment. It is therefore ideal for the production of buried heterostructure lasers at facilities such as Bath, where clean room facilities are available, but the need for material growth, or the financial resources, are not. A possible fabrication process for constricted mesa lasers that could be used at Bath is summarised in the following paragraphs, and illustrated in figure 7.1.

The initial step is to deposit a masking layer of SiO_2 on the upper (p-type) cladding layer of a double heterostructure wafer, grown by any of the standard growth techniques. Stripe

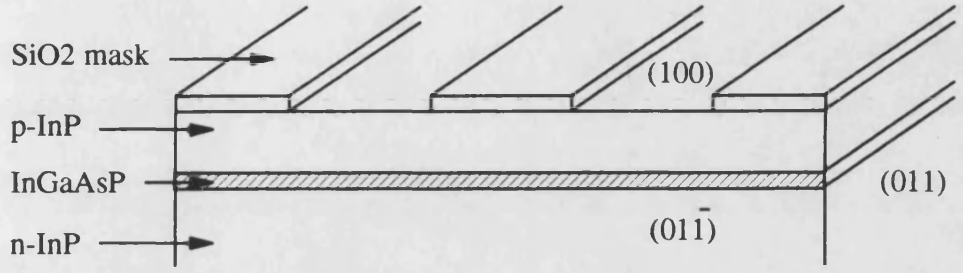

(a) Masked double heterostructure wafer

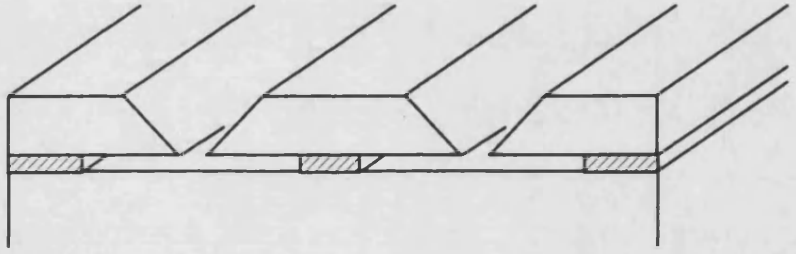

(b) Selective chemical etching

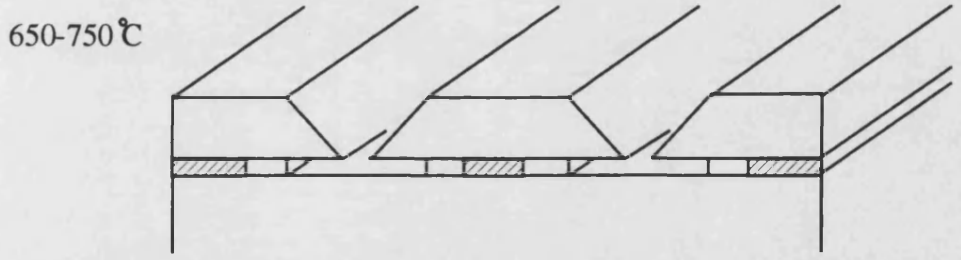

(c) Regrowth of InP

Figure 7.1 Schematic diagrams showing the fabrication of the constricated mesa laser by the mass transport process.

openings are formed in the SiO_2 masking layer using standard photolithographic techniques, as shown in figure 7.1(a). There then follow three chemical wet etch stages to define the mushroom shape of figure 7.1(b). In the first of these, the material not protected by the mask is etched away using a selective etchant which stops at the active layer. This wet etch acts preferentially along the crystal planes to form V-shaped grooves. The masking layer is removed in a second etch step, and finally the active layer is etched away to the desired width using a preferential etch.

The next fabrication step is to regrow InP material around the active layer to form a buried heterostructure. The proposed technique for this is mass transport, which has been used with success by several groups [e.g. 1,3,7]. Mass transport is a particularly simple regrowth technique, requiring only a suitable liquid phase epitaxy type furnace, a supply of hydrogen gas, and a source of phosphorus (either from PH_3 or an InP cover slice). The wafer is loaded into the furnace and heated to around 670°C in the presence of the hydrogen and phosphorous, and the material of the wafer redistributes to bury the active layer, as seen in figure 7.1(c).

After the regrowth process, contacts are made to the wafer on the n and p sides, and the wafer diced to produce devices. Devices may be fabricated from wafers with an InGaAs p^+ capping layer to aid contacting to the upper p-type cladding layer, or may undergo a further processing step before metallisation to Zn dope the upper cladding layer, again to improve the contact.

The only step in this fabrication process which cannot be carried out using the facilities already present at Bath is the mass transport of the InP. In this process material from the device wafer redistributes itself in such a way as to smooth out defects on the surface and fill cavities. The structure of the CM laser is such that the technique can be used to bury the active layer. The process must be carried out at high temperature in a clean

atmosphere in which phosphorus and hydrogen are present. The method for obtaining phosphorus is either by the addition of PH_3 to the reactor atmosphere, or by covering the wafer with a cover slice of InP (from which the phosphorus outgasses) in close proximity to the device wafer. Due to the safety problems involved with use of PH_3, the second method was chosen.

A laboratory facility was designed and much of the equipment necessary to carry out the mass transport process was purchased. The main components required were a furnace, furnace tube, gas handling equipment, connecting pipework and control circuitry for the furnace and gasses. A schematic diagram of the design of the laboratory is shown in figure 7.2. Care was taken to ensure that the hydrogen gas was handled in a safe fashion, it was to be housed in a gas cabinet which was to be constantly vented (the cabinet also housed a supply of nitrogen to flush the furnace and reduce the amount of hydrogen required by the fabrication process). The ceiling was also to be sealed, and a room vent was provided. The furnace tube was fabricated to enable the temperature control thermocouple to be close to the wafers, and to enable easy access to the tube for the wafers.

Due to lack of funds, the mass transport laboratory was never completed, and no devices were produced. The main components required for the laboratory were, however, purchased and there remains little to be done to complete the laboratory.

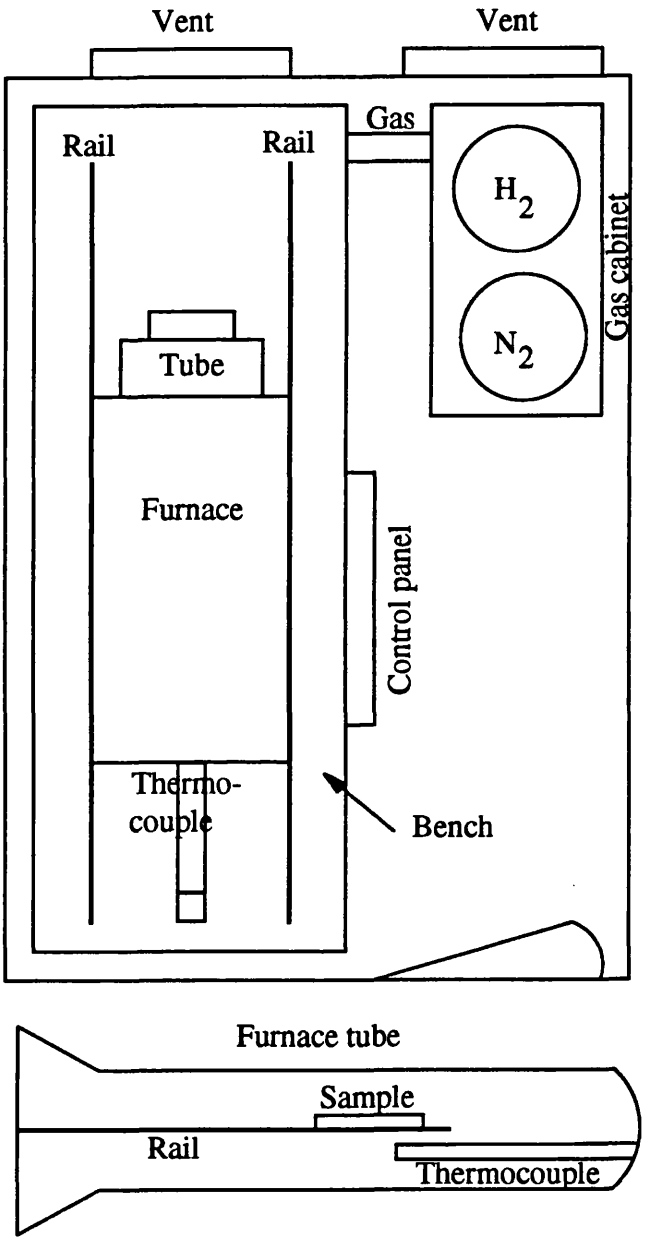

Figure 7.2 The mass transport laboratory, with exploded view of the furnace tube.

REFERENCES

[1] Z.L.Liau, J.N.Walpole, and D.Z.Tsang, "Fabrication, characterisation, and analysis of mass-transported GaInAsP/InP buried heterostructure lasers," IEEE J.Quantum Electron., vol. QE-20, no. 8, pp.855-865, 1984

[2] M.C.Amann, and W.Thulke, "Current confinement and leakage currents in planar buried-ridge structure laser diodes on n-substrate," IEEE J.Quantum Electron., vol. QE-25, no. 7, pp.1595-1602, 1989

[3] T.R.Chen, L.C.Chiu, A.Hasson, K.L.Yu, U.Koren, S.Margalit and A.Yariv, "Study and application of the mass transport phenomena in InP," J.Appl.Phys., vol. 54, no. 5, pp.2407-2412, 1983

[4] P.A.Morton, "The dynamics of directly modulated semiconductor laser diodes," PhD Thesis, University of Bath, 1988

[5] H.Ghafoori-Shiraz, "Temperature, bandgap-wavelength, and doping dependence of peak-gain coefficient parabolic model parameters for InGaAsP/InP semiconductor laser diodes," IEEE J.Lightwave Technol., vol. 6, no. 4, pp.500-506, 1988

[6] R.S.Tucker, "High-speed modulation of semiconductor lasers," IEEE J.Lightwave Technol., vol. 3, no. 6, pp.1180-1192, 1985

[7] J.E.Bowers, B.R.Hemenway, A.H.Gnauck, D.P.Wilt, "High speed InGaAsP constricted-mesa lasers," IEEE J.Quantum.Electron., vol. 22, no. 6, pp.833-842, 1986

APPENDIX 1: BOUNDARIES AT AN ANGLE BY THE FINITE DIFFERENCE METHOD

When analyzing the current spreading in the constricted mesa laser, sloping insulating boundaries are encountered. In this appendix the finite difference formulae for calculating the voltage at any point on such a boundary are presented. A rectangular grid can always be arranged such that the sloping boundary falls on node points, leaving two of the five node points outside the boundary. Referring to figure A1.1, the problem is to calculate the value of the voltage at the two nodes lying outside the boundary, in order that the five point finite difference form of the Laplace equation ($\nabla^2 V = 0$) may be applied. To calculate the voltages at the external nodes, the boundary condition must be applied, and in this case the boundary condition is that of zero current flow across the boundary.

In the case of the left sloping boundary shown in figure A1.1, the points which fall outside the mesa are *V(p,q-1)* and *V(p-1,q)*. If the internal grid has a node spacing of h_x in the horizontal direction and h_y in the vertical direction, then the points *V(p,q-1)* and *V(p-1,q)* are chosen to be at these distances from the centre node, giving a regular rectangular grid for which $h_y/h_x = \tan\alpha$. Applying the boundary condition, the component of current from the four nodes at $(p \pm 1, q \pm 1)$ into the node at (p,q) in the direction perpendicular to the boundary must be zero, and thus

$$\frac{V(p-1,q)-V(p,q)}{h_x}\sin(\alpha)+\frac{V(p,q-1)-V(p,q)}{h_y}\cos(\alpha) \qquad \text{(A1.1)}$$

$$=\frac{V(p+1,q)-V(p,q)}{h_x}\sin(\alpha)+\frac{V(p,q+1)-V(p,q)}{h_y}\cos(\alpha)$$

Rearranging equation (A1.1) gives

$$\tan^2\alpha[V(p+1,q)-V(p-1,q)] = [V(p,q-1)-V(p,q+1)] \qquad \text{(A1.2)}$$

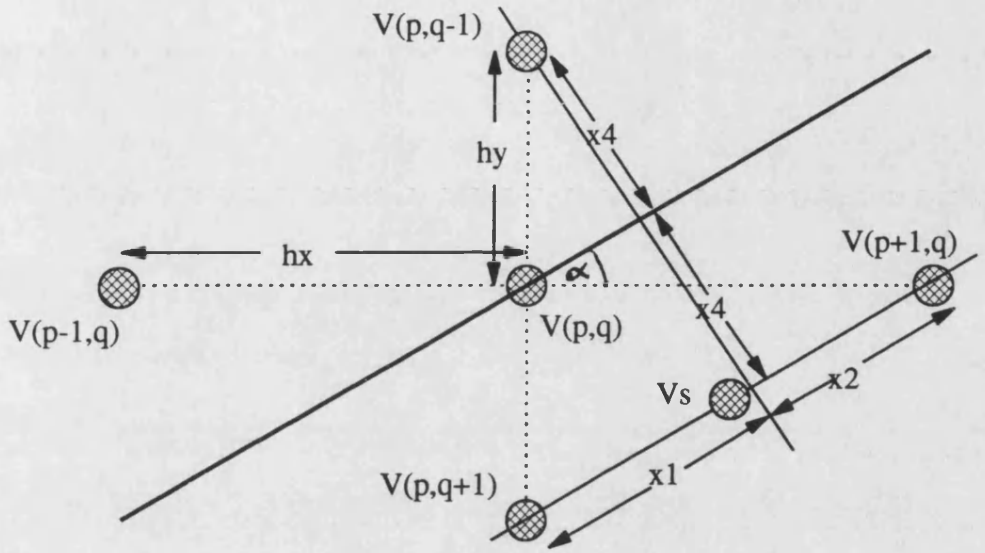

Figure A1.1 Schematic diagram of a boundary at an angle

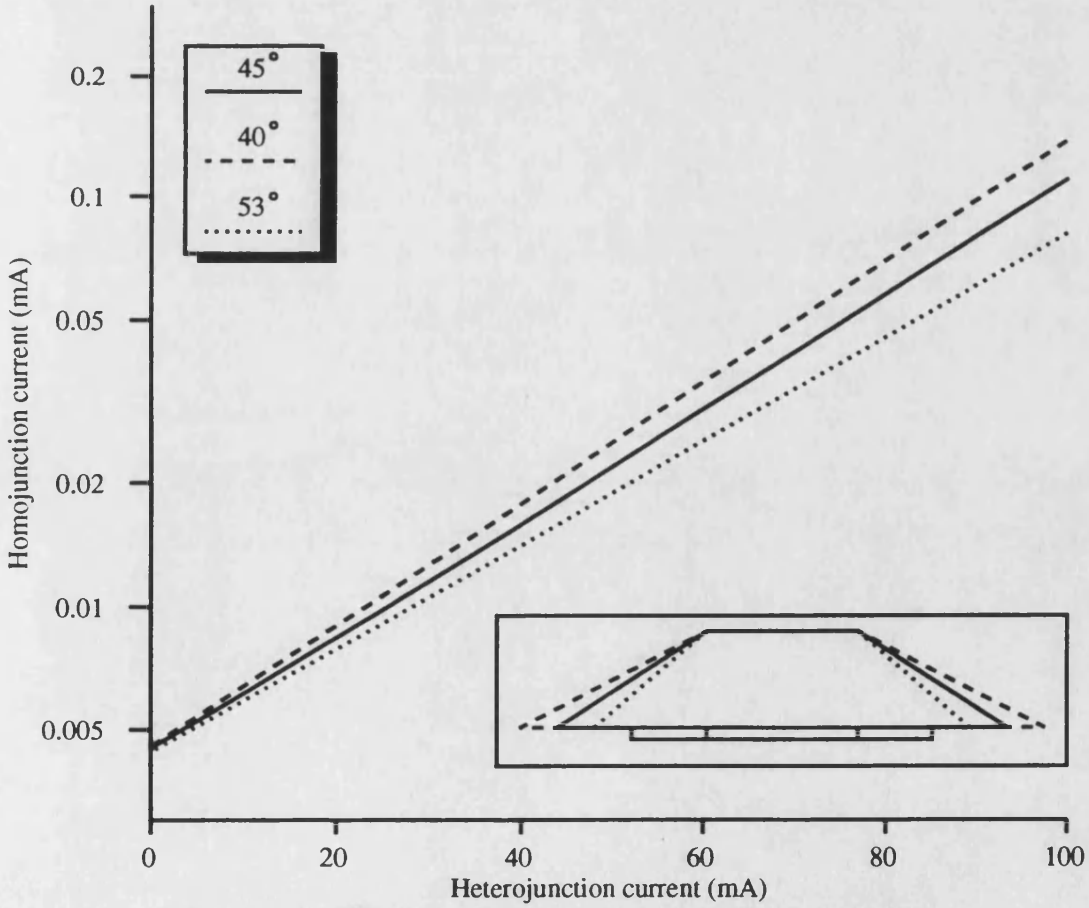

Figure A1.2 Homojunction leakage current versus heterojunction current for CM lasers. The lasers are illustrated in the inset diagram.

For the special case of $\alpha = 90°$, a vertical boundary, it can be seen that equation (A1.2) gives the well known boundary condition

$$V(p-1,q) = V(p+1,q) \tag{A1.3}$$

and for the case of $\alpha = 0°$, which relates to a horizontal boundary, equation (A1.2) gives

$$V(p,q-1) = V(p,q+1) \tag{A1.4}$$

However, equation (A1.2) will in general not yield sufficient values for the external nodes, because there are two unknowns and only one equation. In order to obtain values for both the external nodes, it is necessary to calculate one of the two unknowns in terms of the two known values. One way to do this is to interpolate the voltage at the point *Vs*, shown in figure A1.1. From this, *V(p,q-1)* can be calculated immediately; both nodes lie on the perpendicular to the boundary and are at the same distance from it, therefore the two voltages at these nodes are equal. From the figure it can be seen that

$$x_1 = 2h_y \sin\alpha \tag{A1.5}$$

and

$$x_1 + x_2 = h_y / \sin\alpha \tag{A1.6}$$

thus

$$x_2 = \frac{h_y(1-2\sin^2\alpha)}{\sin\alpha} \tag{A1.7}$$

Interpolating the voltage at *Vs* between *V(p+1,q)* and *V(p,q+1)* gives

$$V_s = V(p,q+1) + \frac{V(p+1,q) - V(p,q+1)}{x_1 + x_2} x_1 \qquad \text{(A1.8)}$$

$$= V(p,q+1)\frac{x_2}{x_1 + x_2} + V(p+1,q)\frac{x_1}{x_1 + x_2}$$

$$= V(p,q+1)(1 - 2\sin^2\alpha) + V(p+1,q)2\sin^2\alpha$$

Since *Vs* and *V(p,q-1)* are at the same distance from the boundary, and lie on a perpendicular to it, then *Vs* = *V(p,q-1)*, and

$$V(p,q-1) = (1 - 2\sin^2\alpha)V(p,q+1) + 2\sin^2\alpha V(p+1,q) \qquad \text{(A1.9)}$$

Using equations (A1.2) and (A1.9) the values of the voltage at the node (*p-1,q*) may be found as

$$V(p-1,q) = (1 - 2\cos^2\alpha)V(p+1,q) + 2\cos^2\alpha V(p,q+1) \qquad \text{(A1.10)}$$

The analysis is restricted to $0° \le \alpha \le 90°$, for other angles the same analysis may be used, with the grid rotated. The angle of the sloping insulating boundary of the CM laser is close to 45°, and for this specific angle equation (A1.9) gives

$$V(p,q-1) = V(p+1,q) \qquad \text{(A1.11)}$$

and from equation (A1.10)

$$V(p,q+1) = V(p-1,q) \qquad \text{(A1.12)}$$

This boundary condition can also be obtained by observing that for a 45° boundary, $V_s = V(p+1,q)$.

To obtain the solution for the voltage at the point (*p,q*), the Laplace equation must be solved. Recall that the five point central difference form of Laplace's equation may be written

$$\frac{V(p-1,q)+V(p+1,q)-2V(p,q)}{h_x^2} \qquad \text{(A1.13)}$$

$$+\frac{V(p,q-1)+V(p,q+1)-2V(p,q)}{h_y^2}=0$$

which may be re-arranged to give the voltage at node (p,q) in terms of the voltage at the four neighbouring nodes

$$V(p,q)=\frac{1}{2}\frac{h_x^2h_y^2}{h_x^2+h_y^2}\left[\frac{V(p-1,q)+V(p+1,q)}{h_x^2}+\frac{V(p,q-1)+V(p,q+1)}{h_y^2}\right] \qquad \text{(A1.14)}$$

The voltage at a node on the boundary may thus be found from equation (A1.14) by substituting the values of voltage at the exterior nodes *V(p-1,q)*, and *V(p,q-1)* from equations (A1.9) and (A1.10). The actual values of the two possible mesa angles are 40° and 53°. Simulations of the current spreading in trapezoidal regions with such angles have been carried out, and it has been found that there is little difference between the two possible mesa angles and the chosen angle of 45°.

As an example, figure A1.2 shows a comparison between the leakage currents obtained for CM lasers of 2μm depth, 2μm contact width, a regrown width of 1μm and an active layer width of 2μm. Other parameters for the simulation are identical to those used for the nominal CM laser in chapter 3. It can be seen that there is little difference between the three curves, justifying the use in the simulations of an angle of 45°.

APPENDIX 2: SOLUTION OF THE CARRIER DENSITY EQUATION

The carrier diffusion equation described in chapters 3 and 6 is non-linear, and is solved by the quasi-linearization method which is outlined in this appendix. Consider the non-linear second order differential equation

$$y'' = f(x, y, y') \tag{A2.1}$$

This can be written as

$$\Phi(x, y, y', y'') = y'' - f(x, y, y') = 0 \tag{A2.2}$$

The values of y after the j^{th} and $(j+1)^{th}$ iterations are denoted by y_j and y_{j+1}, and for both of these $\Phi=0$. The j^{th} iteration gives

$$y_j'' - f(x, y_j, y'_j) = 0 \tag{A2.3}$$

For the $(j+1)^{th}$ iteration, if the difference between values on successive iterations is small, then a first order Taylor's series expansion gives

$$\Phi(x, y_{j+1}, y'_{j+1}, y''_{j+1}) = \Phi(x, y_j, y'_j, y''_j) + \left(\frac{\partial \Phi}{\partial y}\right)_j (y_{j+1} - y_j) \tag{A2.4}$$

$$+ \left(\frac{\partial \Phi}{\partial y'}\right)_j (y'_{j+1} - y'_j) + \left(\frac{\partial \Phi}{\partial y''}\right)_j (y''_{j+1} - y''_j) + \cdots = 0$$

or

$$-\left(\frac{\partial f}{\partial y}\right)_j (y_{j+1} - y_j) - \left(\frac{\partial f}{\partial y'}\right)_j (y'_{j+1} - y'_j) + (y''_{j+1} - y''_j) = 0 \tag{A2.5}$$

Finally, substituting y''_j from equation (A2.3) into equation (A2.5) gives the general formula

$$y''_{j+1}-\left(\frac{\partial f}{\partial y'}\right)_j y'_{j+1}-\left(\frac{\partial f}{\partial y}\right)_j y_{j+1}=f(x,y_j,y'_j)-\left(\frac{\partial f}{\partial y'}\right)_j y'_j-\left(\frac{\partial f}{\partial y}\right)_j y_j \qquad \text{(A2.6)}$$

Equation (A2.6) is now in a linear form, and can be solved by standard finite difference techniques. The application of this method to the solution of the carrier diffusion equation is now described.

The diffusion equation, equation (6.4.1.7) may be written, substituting for the values of the recombination parameters from equations (6.4.1.8), (6.4.1.9) and (6.4.2.8)

$$D_e\frac{d^2n(x)}{dx^2}+\frac{J(x,d)}{qt}=(an(x)-b)\frac{c}{\eta_0}\sum_M\{\Psi_M(x,y)S_{A_M}\}+ \qquad \text{(A2.7)}$$

$$(B_0-B_1n(x))n(x)(n(x)+p_a)+Cn(x)(n(x)+p_a)^2+Dn(x)^2$$

Applying the quasi linearization technique requires a slight re-arrangement of the equation. If n'' denotes d^2n/dx^2, then

$$f(x,n_j)=n''_j=1/D_e\{K_1+K_2n_j+K_3n_j^2+K_4n_j^3+K_5n_j^2\} \qquad \text{(A2.8)}$$

where the constants K_1 to K_5 are defined as

$$K_1=-b\frac{c}{\eta_0}\sum_M\{\Psi_M(x,y)S_{A_M}\}-\frac{J(x)}{qt} \qquad \text{(A2.9)}$$

$$K_2=a\frac{c}{\eta_0}\sum_M\{\Psi_M(x,y)S_{A_M}\}+B_0p_a+Cp_a^2 \qquad \text{(A2.10)}$$

$$K_3=B_0-B_1p_a+2Cp_a \qquad \text{(A2.11)}$$

$$K_4=C-B_1 \qquad \text{(A2.12)}$$

$$K_5=D \qquad \text{(A2.13)}$$

The derivative of equation (A2.8) with respect to n_j is given by

$$f'(x,n_j) = 1/D_e\{K_2 + 2K_3 n_j + 3K_4 n_j^2 + zK_5 n_j^{(z-1)}\} \tag{A2.14}$$

The linearized equation is given by (A2.6) as

$$n''_{(j+1)} - f'(x,n_j)n_{j+1} = f(x,n_j) - f'(x,n_j)n_j \tag{A2.15}$$

The standard three point central difference formula for a function defined on a regular grid with grid spacing h gives the second derivative at any grid node, p, as

$$\frac{d^2n(x)}{dn^2}\Big|_{n=n_p} = \frac{n_{p+1} - 2n_p + n_{p-1}}{h^2} \tag{A2.16}$$

Using this formula, equation (A2.15) may be written in finite difference form as

$$\frac{\{n_{j+1}\}_{(p+1)} - 2\{n_{j+1}\}_{(p)} + \{n_{j+1}\}_{(p-1)}}{h^2} \tag{A2.17}$$

$$-f'(x,\{n_j\}_{(p)})\{n_{j+1}\}_{(p)} = f(x,\{n_j\}_{(p)}) - f'(x,\{n_j\}_{(p)})\{n_j\}_{(p)}$$

remembering that the subscript j refers to the iteration and the subscript p to the node in the finite difference approximation to the function. Finally this equation may be written as

$$\{n_{j+1}\}_{(p+1)} - \left[2 + h^2 f'(x,\{n_j\}_{(p)})\right]\{n_{j+1}\}_{(p)} + \{n_{j+1}\}_{(p-1)} \tag{A2.18}$$

$$= [f(x,\{n_j\}_{(p)}) - f'(x,\{n_j\}_{(p)})\{n_j\}_{(p)}]h^2$$

This equation is a linear finite difference equation, and the matrix produced by the set of finite difference equations describing the function is tri-diagonal. Such a system of equations may be solved by Gaussian elimination and back substitution, and a

tri-diagonal matrix may be stored using only a small amount of computer memory since only three columns in any row are non-zero. The solution implemented by such a scheme is rapid and economical of computer storage.

APPENDIX 3: THE METHOD OF CALCULATING PHOTON DENSITY

The optical model described in section 6.3 requires the photon densities of all lasing modes, this appendix explains the method used to calculate the photon densities. In order for a mode to lase, the gain of the mode, determined from the complex part of its propagation constant, must exactly equal the round trip cavity losses experienced by that mode. A critical parameter in determining the waveguiding properties of the laser is the dielectric constant in the active layer, and this depends upon the active layer carrier density. Calculation of the active layer carrier density relies on the values of the photon densities of the lasing modes via the stimulated recombination term in the carrier diffusion equation. Therefore, by altering the photon densities of the lasing modes it is possible to alter the waveguiding in the active layer. This will alter the gain of each guided mode, and the aim is to adjust the photon densities in such a way as to ensure that the gain of all lasing modes is equal to the cavity losses.

Considering initially only a single lasing mode, if the initial guess for the photon density of this mode gives a value for the modal gain which is greater than the cavity loss, then expression (6.3.2) suggests that the local gain, $g(x)$, and hence the carrier density, must be reduced in order that condition (6.3.3) may be met. To achieve this, the value of the initial estimated photon density must be increased in order to increase the stimulated recombination and thus depress the carrier density (and hence modal gain). Similarly, if the initial guess for the photon density gives a modal gain that is too low, a new photon density must be chosen which is below the initial value in order to reduce the stimulated recombination term.

The problem can be considered as finding a solution to a set of non-linear equations, and a Newton-Raphson approach is applied to the problem. For a single mode, the problem is that of obtaining the root of the equation

$$f(S_0) = G_0 - \alpha_C = 0 \tag{A3.1}$$

where α_C is the total round trip cavity loss (including mirror losses), S_0 is the photon density of the mode, and G_0 is the calculated gain of the mode. An improved estimate of the photon density, S_0^{k+1}, may be obtained from the previous estimate, S_0^k, via the Newton-Raphson formula

$$S_0^{k+1} = S_0^k - f(S_0^k)/f'_0(S_0^k) \tag{A3.2}$$

where f'_0 is the derivative of the function with respect to S_0. For the complex series of equations that link S_0 to G_0 it is not possible to obtain an analytic solution for the derivative. The derivative is therefore obtained numerically from

$$f'_0(S_0) = \frac{\Delta f}{\Delta S_0} = \frac{G_0 - \alpha_C - (G_0^\delta - \alpha_C)}{S_0 - (S_0 - \delta S_0)} = \frac{G_0 - G_0^\delta}{\delta S_0} \tag{A3.3}$$

where G_0^δ is the gain obtained when the photon density of $S_0 - \delta S_0$ is used, and δS_0 is a small increment to S_0. The improved estimate of the photon density for a single mode is thus

$$S_0^{k+1} = S_0^k - (G_0^k - \alpha_C)\left[\frac{\delta S_0^k}{G_0^k - (G_0^k)^\delta}\right] \tag{A3.4}$$

Equation (A3.4) can be used to iteratively improve an estimate of the photon density in order to relax the modal gain to within a specified tolerance of the cavity loss. However, this equation is restricted to a single lasing mode, whereas two lasing modes are considered in this thesis. The photon density of each lasing mode is taken into account in the carrier density equation, and thus increasing or decreasing the photon density of one mode will alter the gain of the other mode. The Newton-Raphson method can be generalized to a system of equations, and it is therefore possible to use this technique to solve for the photon densities of all lasing modes.

For the case of two lasing modes, the two equations to be solved can be written

$$f(S_0, S_1) = G_0 - \alpha_C = 0 \tag{A3.5}$$

$$g(S_0, S_1) = G_1 - \alpha_C = 0 \tag{A3.6}$$

The form of the Newton-Raphson equation required for solution of two simultaneous equations on the k^{th} iteration is

$$\begin{bmatrix} f'_0(S_0^k, S_1^k) & f'_1(S_0^k, S_1^k) \\ g'_0(S_0^k, S_1^k) & g'_1(S_0^k, S_1^k) \end{bmatrix} \begin{bmatrix} \Delta S_0^k \\ \Delta S_1^k \end{bmatrix} = -\begin{bmatrix} f(S_0^k, S_1^k) \\ g(S_0^k, S_1^k) \end{bmatrix} \tag{A3.7}$$

In the above equations f'_0, g'_0 refer to the partial derivatives of the functions with respect to S_0, and f'_1, g'_1 refer to the partial derivatives with respect to S_1. As for the single mode case, the derivatives are evaluated numerically. Equation (A3.7) is solved by Gaussian elimination, and then an improved estimate of the root (S_0, S_1) may be obtained from

$$\begin{bmatrix} S_0^{k+1} \\ S_1^{k+1} \end{bmatrix} = \begin{bmatrix} S_0^k \\ S_1^k \end{bmatrix} + \begin{bmatrix} \Delta S_0^k \\ \Delta S_1^k \end{bmatrix} \tag{A3.8}$$

Iterations continue until both G_0 and G_1 are relaxed within a specified tolerance of the cavity loss.

LIST OF PUBLICATIONS

P.C.R.Gurney and R.F.Ormondroyd: "Self-consistent modelling of current leakage effects in an n-substrate InP/InGaAsP constricted mesa laser", Conference Proceedings of the Semiconductor Integrated Opto-Electronics Conference, Cardiff, UK, April 1991

P.C.R.Gurney: "Self-consistent modelling of semi-conductor lasers", UCINA Workshop on Semiconductor Device Modelling, (Invited Paper), Bath, UK, June 1991

P.C.R.Gurney and R.F.Ormondroyd: "Fully self-consistent modelling of an integratable buried heterostructure InP/InGaAsP laser diode", Conference Proceedings of SPIE OE/FIBRES '91, Boston, USA, September 1991

P.C.R.Gurney and R.F.Ormondroyd: "Detailed self-consistent modelling of the lateral optical fields in an n-substrate constricted-mesa laser for microwave modulation applications", Conference Proceedings of the IEE International Conference on Computation in Electromagnetics, London, UK, November 1991